SUSTAINABLE CARBON NANOMATERIALS: DELVING INTO ITS BIOMOLECULAR INTERACTIONS, RESPONSES AND APPLICATIONS

Ph.D. Thesis

By

PRANAV

DEPARTMENT OF METALLURGY ENGINEERING & MATERIALS SCIENCE

INDIAN INSTITUTE OF TECHNOLOGY INDORE

AUGUST 2020

SUSTAINABLE CARBON NANOMATERIALS: DELVING INTO ITS BIOMOLECULAR INTERACTIONS, RESPONSES AND APPLICATIONS

A THESIS

Submitted in partial fulfillment of the
requirements for the award of the degree
of
DOCTOR OF PHILOSOPHY

by

PRANAV

DEPARTMENT OF METALLURGY ENGINEERING AND MATERIALS SCIENCE

INDIAN INSTITUTE OF TECHNOLOGY INDORE

AUGUST 2020

INDIAN INSTITUTE OF TECHNOLOGY INDORE
CANDIDATE'S DECLARATION

I hereby certify that the work which is being presented in the thesis entitled **Sustainable carbon nanomaterials: Delving into its biomolecular interactions, responses and applications** in the partial fulfillment of the requirements for the award of the degree of **DOCTOR OF PHILOSOPHY** and submitted in the **DEPARTMENT OF METALLURGY ENINEERGING & MATERIALS SCIENCE, INDIAN INSTITUTE OF TECHNOLOGY INDORE**, is an authentic record of my own work carried out during the time period from JUNE 2016 to AUGUST 2020 under the supervision of Dr. Shaikh M. Mobin, Associate Professor, Indian Institute of Technology Indore. The matter presented in this thesis has not been submitted by me for the award of any other degree of this or any other institute.

Pranav
21/8/2020

Signature of the student with date
PRANAV

This is to certify that the above statement made by the candidate is correct to the best of my knowledge.

M. Shaikh

August 27, 2020

Signature of Thesis Supervisor with date

Dr. Shaikh M. Mobin

PRANAV has successfully given his Ph.D. Oral Examination held on.: March 19, 2021

Signature of Chairperson (OEB)	Signature of External Examiner	Signature of Thesis Supervisor
Date: 19/3/2021	Date: 19/3/2021	Date: March 19, 2021
Signature of PSPC Member #1	Signature of PSPC Member #2	Signature of Convener, DPGC
Date: 19.03.2021	Date: 19/3/21	Date: March 19, 21

Signature of Head of Discipline
Date: 19/3/2021

ACKNOWLEDGEMENTS

I would like to acknowledge and extend my deepest gratitude for suggestions, help, guidance and continuous support offered by numerous people for completing this thesis in current form.

At the outset, I would like to express gratitude to my advisor Dr. Shaikh M. Mobin for leading from the front and be a pillar during academic and research activities, providing all necessary facilities along with his expertise, motivation and tireless support for all these years. Special mention goes to the freedom he offered for trying new things and smoothly executing the research efforts. My sincere appreciations for his enormous efforts towards getting the work published in journals of international repute. I must thank him for giving me international research exposure by facilitating my participation in schools and conferences both in India and abroad. I owe him a lot.

I sincerely express my gratitude to my PSPC members Prof. Rajneesh Misra and Prof. Sarika Jalan for closely monitoring my research progress and helping me with their suggestions and comments on regular basis. I would like to thank Late Dr. Suprabha Nayar and Dr. Shilpee Jain who gave me the initial chance in the research world and inspired me to do PhD.

I am thankful to the staff of my discipline i.e. metallurgy engineering and materials science, discipline of chemistry and discipline of bioscience and biomedical engineering, IIT Indore for their support during my research work. I am hugely appreciative to the staff members of SIC, IIT Indore Mr. Kinny Pandey, Mr. Ghanshyam Bhavasar, Mr. Nitin Upadhyay and Mr. Ravindra Kumar for their help to perform the necessary characterization. I am also thankful to ACMS, IIT Kanpur, SAIF IIT Bombay, C-MET Pune and MNCF, CeNSE, IISc for characterization facilities. Furthermore I am

thankful to Dr. Tridib Kumar Sharma, Prof. Anindya Dutta for DLS and TCSPC measurement.

Special thanks to my group members Dr. Vinay Sharma, Dr. Anoop Saini, Dr. Sanjay Verma, Dr. Ajeet Singh, Mrs. Navpreet, Dr. Pratibha, Dr. Khursheed, Mrs. Richa, Ms. Shagufi, Ms. Neha, Mr. Ravinder, Mr. Praveen, Mr. Pawan, Mr. Kaushik for their needful suggestions during experiments and writing of the manuscripts and thesis. Also I would like to thank Mr. Ankit, Mr. Anubhav, Mr. Vishal, Mr Vaibhav and Mr.Achyuth for their suggestions during my work.

Nothing can be successful without having bunch of friends so I want thank my friends Mr. Nitish, Mr. Ashish, Mr. Aanand, Mr. Amritanshu, Ms. Jaya, Ms. Shruti, Mrs. Neha and Mr. Prem. They all were always behind me and gave me all kind of support and suggestions.

Last, but not the least, I would like to thank my family. No words can express my heartfelt gratitude towards my parents, my sister Mrs. Jayanti and brother in law Mr. Rakesh Pandey for their, endless love, unconditional support and tireless encouragement. My special thanks to Miss. Inshiya Pandey, Mr. Aanav Singh and all my extended family members for their moral support and encouragement all these years.

I dedicate this thesis to everyone who has directly or indirectly helped me throughout research work.

(Pranav)

DEDICATED TO MY FAMILY

TABLE OF CONTENTS

ABSTRACT

The investigation embodied in the thesis entitled "SUSTAINABLE CARBON NANOMATERIALS: DELVING INTO ITS BIOMOLECULAR INTERACTIONS AND RESPONSES" was initiated in June 2016 in the Discipline of Metallurgy Engineering & Materials Science, Indian Institute of Technology Indore.

The objectives of this thesis are exploration of graphene and carbon dot synthesis by employing green source, its biomolecular interactions, responses and suitability for biomedical applications.

The focal points of the thesis are as follows-

1. **Direct exfoliation of graphite to graphene using a sustainable source.**
2. **Investigation of biocompatibility and protein interactions on exfoliated graphene.**
3. **Exploration and applicability of c-dots for graphene exfoliation, its stabilization and biological activity.**
4. **Green synthesis of c-dots for optical sensing of biomolecules, physical entity and bioimaging.**
5. **Modulation of fluorescence performance of c-dots through functional group tuning.**

This thesis comprises seven chapters. It begins with a general introduction to the topic and literature review (**Chapter 1**), followed by exploring gelatin as an exfoliating and stabilizing agent for direct exfoliation of graphite, its colloidal stability and biocompatibility (**Chapter 2**), the effect of lateral size and concentration of graphene nanoflakes on protein adsorption and cellular compatibility (**Chapter 3**) applicability of carbon dots for direct exfoliation

of graphite and its antibacterial application (**Chapter 4**) and biosensing ability and fluorescence modulation through surface functional group tuning in carbon dots **(Chapter 5-6)**. The thesis outlines the future perspective especially focusing on sustainable carbon nanomaterials and their biomedical applications in **Chapter 7**.

The introductory chapter (**Chapter 1**) of the thesis illustrates the brief background and literature review of the basics of carbon nanomaterials especially emphasis on graphene & carbon dots has been discussed. The recent advances in the area of graphene production and their challenges have been provided. Afterwards, insights about its stability, cytocompatibility & protein adsorption have been given. Furthermore, carbon dots were explored for graphene exfoliation, biosensing, and bioimaging purposes furthermore various innovative ways to modulate the fluorescence performance of carbon dots having been discussed with recent literatures.

Chapter 2 describes the direct exfoliation of graphite using gelatin followed by; the effect of exfoliation conditions such as temperature, pH, Graphite to gelatin ratio and total particle concentration on graphene yield is examined. The exfoliated graphene dispersion was checked for its colloidal stability. Interestingly, compared to temperature~30^{o}C the higher graphene production was observed on increasing the temperature to 60^{o}C. Moreover, the exfoliated graphene was found to be highly bio and hemocompatible even at high concentration upto 10 mg/mL. All these findings open a more environmentally route to exfoliate graphite to graphene using a sustainable resource for many biological applications which so far was ignored and will enhance its applicability in a more practical capacity. This improved synthetic route will help in the easy functionalization of graphene and will remould its biomedical application.

Chapter 3 highlights Ggel nanosheets having different lateral sizes for protein adsorption with Bovine serum albumin (BSA) and fetal bovine serum (FBS) proteins. The protein adsorption showed concentration and lateral size-dependent behavior with exfoliated Ggel nanosheets. Also, the

adsorption behaviors were different with two different proteins. BSA showed the least adsorption with Ggel7 (least lateral size) and highest adsorption with Ggel1 (highest lateral size) at a concentration of 50 µg/mL whereas when concentration increased i.e. 200 µg/mL adsorption behavior were almost similar irrespective of lateral size. However, with FBS adsorption behavior was different. Furthermore, hydrodynamic diameter gets enhanced with Ggel nanosheets after protein adsorption. The fluorescence spectrum of proteins gets quenched after Ggel incubation suggesting non-radiative charge transfer between proteins and 2D nanosheets. Circular dichroism reveled because of Ggel nanosheets the proteins showed decrease in its ellipticity however the secondary structure remained intact. Moreover, these exfoliated sheets showed excellent cytocompatibility and hemocompatibility activity. The present work describes that protein adsorption nature gets vary with different proteins. However, no oxidative defects in these Ggel nanosheets provides advantages in terms of cytocompatibility and will be useful in designing graphene and its composite for biomedical applications.

Exploring 0D carbon nanomaterials i.e. carbon dots as a stabilizing agent for 2D materials offers lots of potential in the area of solar cells, drug delivery, biosensing etc. In **Chapter 4** we explored sustainable source "*Cannabis Sativa*" engineered carbon dots (N@CSDs) as an exfoliant for direct exfoliation of Gr into G (GN@CSDs). The present method opens a new avenue towards exploring a zero- dimensional carbon material (0D) for exfoliating Gr (3D) to G (2D). High-temperature sonication (~60^{o}C) facilitates the exfoliation process by disrupting π-π interactions between Gr sheets. The N@CSDs stabilizes the exfoliated sheets via electrostatic interaction into GN@CSDs. The Raman spectroscopy confirms successful exfoliation and formation of few- layer graphene sheets whereas atomic force microscopy reveals the presence of N@CSDs onto the GN@CSDs sheets. GN@CSDs shows excellent stability over a month under various

harsh conditions confirming the role of N@CSDs in the stabilization process. Interestingly, GN@CSDs exhibit antibacterial nature by hindering the growth of bacteria.

Encouraged by the *cannabis sativa* derived carbon dots having multifunctional property motivated to further explore them for sensing and bio-imaging purpose especially owing to the green synthesis route. In **Chapter 5**, the present work focuses on *cannabis sativa* derived carbon dots co-doped with nitrogen and sulphur (**N-S@CsCD**) as a nanosensor. The **N-S@CsCD** exhibits the distribution of size in the range of 4-6 nm and shows the excitation independent emission behaviour with emission wavelength around 414 nm. XPS spectra confirmed the presence of heteroatom doping by nitrogen and sulphur with a concentration of 10.71 and 1.94%, respectively. **N-S@CsCD** shows excellent stability with pH, time and salt concentration. Interestingly, **N-S@CsCD** exhibits reversible temperature responsive fluorescence "turn-off" behaviour. Further, **N-S@CsCD** also shows selective fluorescence "turn-off" behaviour in the presence of vitamin B_{12} (VB_{12}) with a limit of detection value of 7.87 µg/mL. The fluorescence life time of **N-S@CsCD** with and without VB_{12} was similar, which infers the sensing behaviour was purely static. Moreover, **N-S@CsCD** shows biocompatible and non-toxic behaviour with very high cell viability. The fluorescent nature of **N-S@CsCD** was further evaluated for intracellular imaging.

High quantum yield and fluorescence life time are the major problems associated with the carbon dot system. Doping and surface passivation method was used to modulate the fluorescence performance of carbon dots however these methods still did not solve the purpose. Thus in **Chapter 6** we synthesized heteroatom (nitrogen, boron, and fluorine) co-doped carbon dots (CNBF) was synthesized (using citric acid as a primitive carbon source. Further, CNBF was reduced with different concentrations of sodium borohydride ($NaBH_4$) leading to the synthesis of rCNBF1, rCNBF2, and

rCNBF3. The distinct optical characteristics of CNBF, rCNBF1, rCNBF2 and rCNBF3 were studied using different spectroscopic techniques. The quantum yield and fluorescence lifetime of the reduced forms rCNBF1, 2 and 3 were 39.14%; 41.73%; 44.61 and 13.30 nS, 13.52 nS, 14.21 nS, respectively which was higher than CNBF having quantum yield of 35.73% and 11.98 nS. Apparently, it was observed the energy bandgap of rCNBF was higher than CNBF suggesting the functional group modification due to reduction which tuned the optical behaviour. Afterwards using transmission electron microscope (TEM) morphologies of CNBF and rCNBF were studied. This study opens a new avenue in designing fluorescent materials using functional group modifications having potential emerging applications.

Chapter 7 outlines the future perspective of this work. Especially exploring direct exfoliated graphene for biomedical application, protein adsorption studies, carbon dot stabilized graphene for antibacterial applications and carbon dot fluorescence modulation for biosensing and subcellular targeting.

LIST OF PUBLICATIONS

1. **P. Tiwari**, N. Kaur, V. Sharma, H. Kang, J. Uddin, and S. M. Mobin, Cannabis sativa-derived carbon dots co-doped with N–S: highly efficient nanosensors for temperature and vitamin B12 , New J. Chem, 2019, 43, 17058-17068.

2. **P. Tiwari**, V. Sharma, N. Kaur, K. Ahmad, and S. M. Mobin, Sustainable Graphene Production: New Insights into Cannabis sativa Engineered Carbon Dots Based Exfoliating Agent for Facile Production of Graphene , ACS Sustainable Chem, 2019, 07, 13, 11500-11510 .

3. **P. Tiwari**, N. Kaur, V. Sharma and S. M. Mobin, High-yield graphene produced from the synergistic effect of inflated temperature and gelatin offers high stability and cellular compatibility, Phys.Chem.Chem.Phys., 2018, 20, 20096.

4. **P.Tiwari**, N. Kaur, V.Sharma and S.M. Mobin, "A spectroscopic investigation of Carbon-dots and its reduced state towards fluorescence performance. Journal of Photochemistry & Photobiology, A: Chemistry., 2020, 403, 112847-112856.

5. N. Kaur, V. Sharma, **P.Tiwari**, A.K. Saini and S.M. Mobin, "Vigna radiata" based green C-dots: Photo-triggered theranostics, fluorescent sensor for extracellular and intracellular iron (III) and multicolor live cell imaging probe, Sensors & Actuators: B. Chemical, 2019, 291, 275-286.

6. V. Sharma, N. Kaur, **P.Tiwari** and S.M. Mobin, Multifunctional fluorescent "Off-On-Off" nanosensor for Au3+ and S2− employing N-S co-doped carbon–dots, Carbon., 2018, 139, 93-103.

7. V. Sharma, N. Kaur, **P.Tiwari** and S.M. Mobin, Full color emitting fluorescent carbon material as reversible pH sensor with multicolor live cell imaging, Journal of Photochemistry & Photobiology, B: Biology., 2018, 182,137-145.

8. V. Sharma, **P. Tiwari** and S.M.Mobin, Sustainable carbon-dots: recent advances in green carbon dots for sensing and bioimaging, J.Mater.Chem.B., 2017, 5, 8904.

9. N. Kaur, **P. Tiwari**, K. Kapoor, A.K. Saini, V. Sharma and S.M.Mobin, Metal Organic Framework based Antibiotic Release and Antimicrobial Response: An Overview. CrystEngComm., 2020, 22, 7513-7527.

BOOK CHAPTER

1. V. Sharma[#], **P.Tiwari**[#] and S. M. Mobin (2019), Carbon Nanolights as Optical Nanosensors for Water Contaminants. Nano-sensors for Environmental Applications, Springer-Nature, 2020 Vol.- 43, ISBN:978-3-030-38100-4. (#- equal contribution)

Conferences/Workshop attended and oral/poster presentation

1. **Poster Presentation** at Nanobioteck-2017, organized by AIIMS-Delhi held at Thiruvananthapuram, India, December 02-05, 2017.
2. **Poster Presentation** at RSC-IIT Indore symposium on Advances in chemical sciences held at IIT Indore, India, January 04, 2018.
3. **Poster Presentation** at International conference on Complex and Functional Materials, held at, Kolkata, India, December 12-17, 2018.
4. **Poster Presentation** in 3rd Asian Conference on Chemosensors & Imaging probes, held at Amritsar, India, November 06-09, 2019.
5. **Poster Presentation** and hands on training at FCS-2019 (National Workshop on fluorescence and raman spectrometer), held at TIFR Hyderabad, India, December 02-07, 2019.
6. **Poster Presentation** at Gordon Research seminar Colloidal, Macromolecular and Polyelectrolyte Solutions (GRS) held February 01-02, 2020 at Four Points Sheraton in Ventura, CA United States.
7. **Poster Presentation** at Gordon Research Conference Colloidal, Macromolecular and Polyelectrolyte Solutions (GRC) held February 02-07, 2020 at Four Points Sheraton in Ventura, CA United States.
8. **Participated** in GIAN course on "Inorganic chemistry of imaging: Magnetic resonance and optical imaging with coordination complexes" held during January 08 - 12, 2018 conducted by Prof. Janet R. Morrow, University at Buffalo, USA at IIT Indore.

LIST OF ABBREVIATIONS

SEM	Scanning electron microscope
XPS	X-ray Photo electron spectroscopy
TEM	Transmission electron microscope
PXRD	Powder X-ray diffraction
FT-IR	Fourier transform - Infrared spectroscopy
TGA	Thermogravimetric analysis
UV	Ultraviolet
KBr	Potassium bromide
DLS	Dynamic Light Scattering
D_H	Hydrodynamic Diameter
CD	Circular Dichroism
LOD	Limit of detection
RT	Room temperature
MTT	3-(4,5-dimethylthiazol-2-yl)-2,5-

	diphenyltetrazolium bromide
MCF–7	Breast cancer cell line
HeLa	Cervical cancer cell line
C-dot	Carbon-dots
Gr	Graphite
G	Graphene
Gel	Gelatin
AFM	Atomic Force Microscopy
SH	Sonication with heating
BSA	Bovine serum albumin
FBS	Fetal Bovine Serum
RBC	Red blood cells
N@CSDs	Nitrogen doped C-dots
GN@CSDs	Nitrogen doped C-dots stabilized Graphene
N-S@CsCD	N-S heteroatom-doped carbon dots

VB_{12}	Vitamin B_{12}
$NaBH_4$	Sodium Borohydride
MEM	Minimum essential medium
CNBF	Nitrogen, boron and fluorine codoped C-dots
QS	Quinine sulphate
WHO	World Health Organization
K_r	Radiative transition rate constant
K_{nr}	Non-radiative transition rate constant
MIC	Minimum inhibition concentration
MBC	Minimum bactericidal concentration
E. coli	*Escherichia coli*
(°)	degree
Å	Angstrom
nm	Nanometer

LIST OF SCHEMES

LIST OF FIGURES

LIST OF TABLES

LIST OF ANNEXURES

CHAPTER 1

Introduction

Nanoparticles (NPs) are believed to be derived from millions of years and are continuously used in our lives [1]. However, Richard Feynman introduced the idea of nanotechnology in his popular speech "There is plenty of room at the bottom" in 1959. The term "nanotechnology" was coined by Norio Taniguchi at the University of Tokyo in 1971. According to the National Nanotechnology Initiative (NNI), USA "nanotechnology" is defined as material having size in the range (1-100 nm).

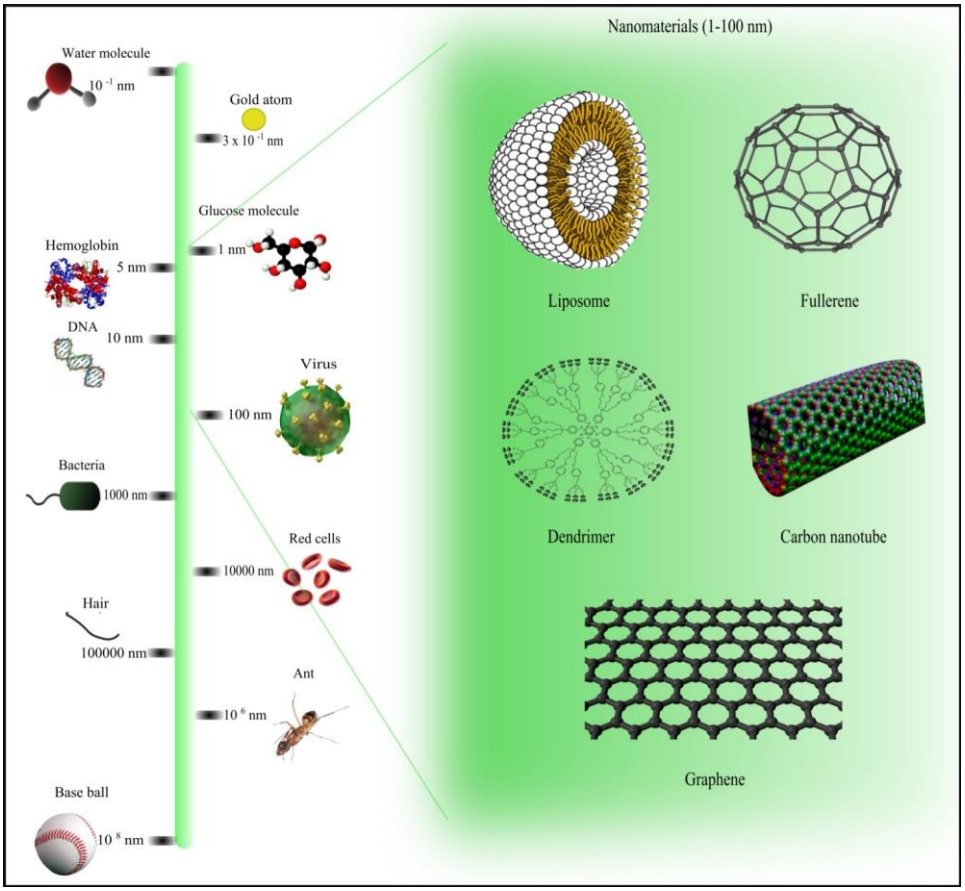

Figure 1.1. Comparison of nanoparticles based on size w.r.to other common materials. [1]

NPs and nanostructured materials have shown significant potential in technological advancements owing to their tunable physicochemical characteristics like melting point; wettability; electrical; thermal

conductivity arising due to the quantum confinement effect [2]. The extraordinary properties at the nanoscale level are unusual for two major reasons: (i). very high surface to volume ratio which leads to an increase in its surface area (ii). at nanolevel because of quantum confinement effect, the wave nature of electron dominates affecting the optical, magnetic & electronic properties of materials [3,4]. Generally, all the nanoparticles/ nanomaterials can easily be classified into three different categories: Inorganic, organic and hybrid. The inorganic nanomaterials include metallic nanoparticles (like gold, silver, iron oxide etc. based nanomaterials). Polymeric nanomaterials, carbon nanomaterials come under organic nanomaterials category. The hybrid nanomaterials ensembles engineered nanomaterials such as DNA-Carbon nanotube arrays; nanocomposites of inorganic-organic nanomaterials etc. [5,6].

The last decade has seen significant boom in nanotechnology research and its applications. Presently nanotechnology based products are used in almost every field like electronics like in NEMS systems; nanobatteries; supercapacitors, agriculture-food: sensors for food-borne pathogens; pesticide detections, healthcare-medicines: ultrafast disease detection kits; diabetic pads; smart bandages etc. [7–12]. The carbon nanomaterials and their composite have lead the nanotechnology based research especially encompassing antibacterial, anticancer, targeted drug delivery, bioimaging, diagnosis, bio-sensing and intracellular monitoring [13,14].

1.1. Carbon-based nanomaterials

Carbon, the third most abundant substance present in the universe. Carbon is the basis of DNA and thus provided the basis for life on earth. Based on carbon hybridization can be in sp^3; sp^2 & sp^1 states, it forms a large range of crystalline and dispersed structures [15]. Carbon nanomaterial represents an excellent material family with high potential in various fields such as nanoelectronics; hydrogen production; sensing; delivery of drugs

etc. Based on dimension carbon nanomaterials can be divided into three parts i.e. The 2D form is called graphene, the 1D form is known as the carbon nanotube (CNT) and the 0D form is called fullerenes (Figure 1.2) [16].

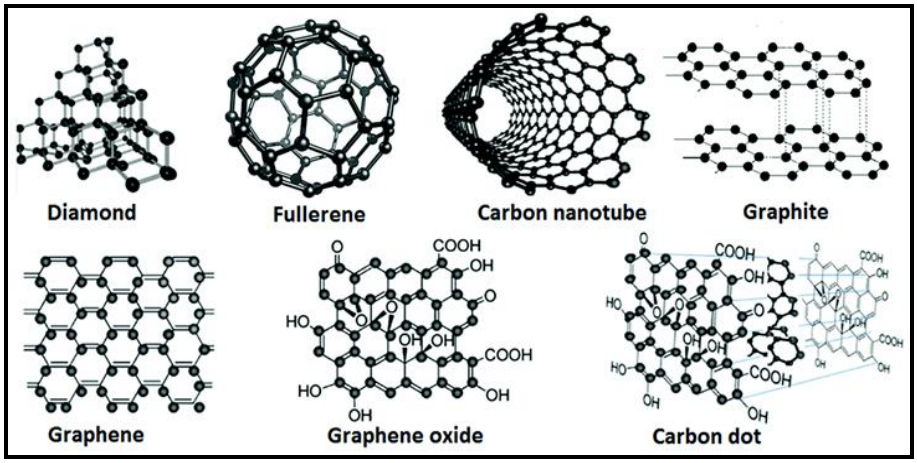

Figure 1.2. Representative images of various types of carbon nanomaterials. [16]

The Fullerenes, better known as "Buckyball", have a cage-shaped cylinder made of six sp^2 carbon atoms in 1985 [17]. CNTs are defined as twisted shell of sp^2 hybridized hexagonal ring of carbon atom. CNTs have shown attractive electrical properties similar to metal and semiconductors [18].

1.2. Graphene

Graphene a flat monolayer of carbon atoms consisting of hexagonally arranged sp^2 hybridized carbon atoms [19]. Graphene is known as the thinnest material and known as the basic building block for constructing other graphitic form of carbon materials thus, known as the mother of all graphitic forms of materials (Figure **1.3**) [19].

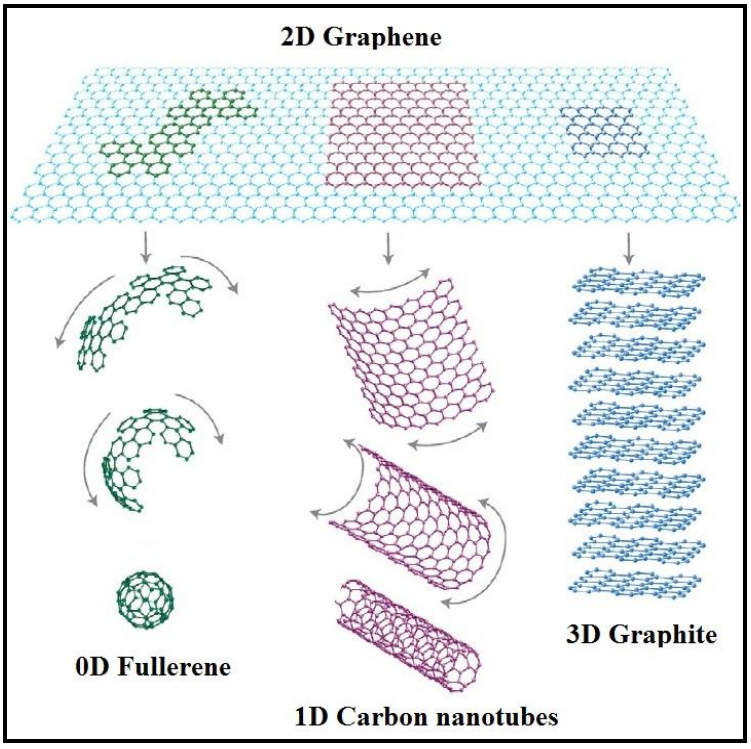

Figure 1.3. Graphene as mother of all forms of carbon materials. [19]

1.2.1. Properties of Graphene-

- **Structure-** Graphene having crystalline allotrope exhibits 2-dimensional property. Its structural stability arises due to its sp^2 hybridization and tightly packed carbon atoms. The σ- bonds are responsible for high strength whereas π-bonds are responsible for notable electronic properties. Graphene sheets exhibit diffraction at (002) graphitic plane. Furthermore, the electron diffraction pattern of graphene sheet exhibited honeycomb lattice [21].
- **Electronic-** Monolayer graphene behaves like semi metal and their conduction-valence band meet at dirac points. The electron propagating in graphene lattice losses their mass thus producing quasi-particles [22]. At ambient condition graphene electron mobility is around 15000 $cm^2V^{-1}s^{-1}$. The high electron mobility translates to ballistic transport property in graphene. Also, the graphene charge carrier follows dirac-like equation [23].

- **Optical-** Graphene is transparent in nature and it absorbs around 2.3% of light intensity. Monolayer graphene does not exhibit any colour [24].
- **Mechanical-** Graphene emerges as one of the impregnable material known. Experimentally it has been shown that graphene breaking strength is greater than steel by almost 200 times with the tensile strength of 130 GPa [25]. The monolayer graphene possesses strength of 120 GPa. The presence of defects like dislocations significantly reduces its mechanical strength. However, despite having excellent mechanical strength graphene sheets are brittle in nature [26].
- **Thermal-** Thermal transport in graphene arises from phonon. The monolayer graphene exhibited around 10 times higher thermal conductivity than copper [27].

1.2.2. Synthesis of Graphene- Various methods were used so far to produce graphene and have stimulated significant publications and patents in recent years. Bottom-Up and top-down are two main fabrication method for graphene production [28,29]. The chemical vapor deposition (CVD) and epitaxial growth comes under the bottom up fabrication method in which on metal substrate hydrocarbons gets arranged and form carbon/graphene layers. In top down method the graphitic layer gets peeled off.

- **Bottom up method-** The bottom up synthesis route involves epitaxial growth on silicon carbide (SiC) and CVD [30]. In the epitaxial method, the SiC gets heated to very temperature (~ 1100^{o}C) under low pressure (~10^{-6} torr). Due to high temperature, silicon sublimation occurs from SiC surfaces and leads to graphitization of additional carbon atoms on substrate. This method leads the production of large areas of monolayer and few layers graphene on insulating substrates [30]. The CVD method leads to graphene growth over metal substrate because of

carbonaceous material pyrolysis occurs at high temperature (Figure **1.4**) [31,32]. The bottom up method gives excellent quality graphene however, the disadvantages like high cost of production; use of sophisticated instruments limits their applicability.

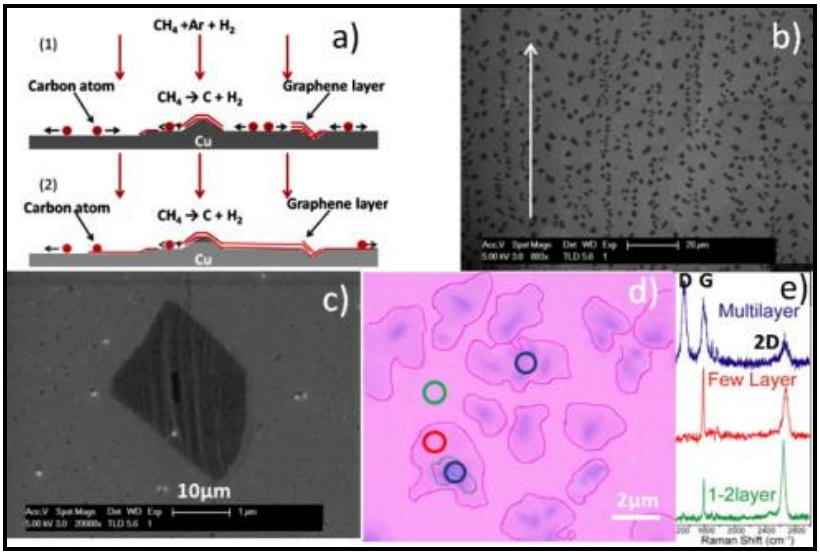

Figure 1.4. A production mechanism for CVD graphene growth on Cu. [32]

- **Top down method-** The top down method of graphene synthesis involves disruption of van der forces to get graphene sheets from the bulk graphitic layer (Figure **1.5**). Common top-down methods are micromechanical cleavage; modified hummers method and direct exfoliation method. The popular micromechanical method involves the famous scotoch® tape based graphene production for which Novoselov and Geim got Nobel Prize [33]. This method involves using adhesive tape to obtain graphene from graphitic layers. However, the method was inefficient for mass production and produces multilayer graphene. Modified Hummers method has gained significant attention in graphene synthesis. In this method, the graphite powder reacts with $KMnO_4$ and $NaNO_3$ in concentrated H_2SO_4. Afterwards H_2O_2 was used for the reduction and leads to synthesis of rGO. Because of oxidation the interlayer spacing in graphite gets increased and forms graphene. Further, the

oxygen functional group converts the hydrophobic graphite oxide into hydrophilic character. The exfoliated sheets possess very high oxygen functionality and lead to very high structural and oxidative defects [34]. The direct exfoliation method of graphene synthesis involves disruption of π-π interaction due to surface tension lowering. The direct exfoliation occurs either using surfactant or solvent. The surfactant leads to stable graphene dispersions because of electrostatic repulsive forces between the exfoliated sheets [35].

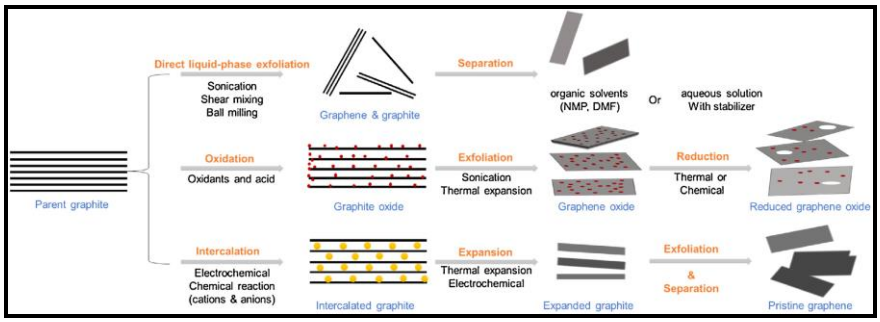

Figure 1.5. The graphene production method via top-down approach. [35]

1.2.3. Applications- Graphene after its discovery has shown tremendous interest because of very high electron mobility; mechanical flexibility and distinctive optical characteristics. Graphene and its derivative offer applications ranges from solar cells; biosensors, drug delivery etc.

- **Biomedical applications**- The biomedical application of graphene and its composite have grown rapidly in recent years. The significant expectations from graphene in biomedical applications arise because of amazing mechanical property; biocompatibility; excessive surface area. Graphene oxide and reduced graphene oxide can easily be used for drug delivery because their excellent water dispersibility. Graphene based drug delivery platform involves incorporation/ attachment of drug molecules through covalent and/or π-π interactions (Figure **1.6**). Many researchers

have fabricated various heterostructure either through spin coating, electrospinning etc using graphene. The fabricated heterostructures were used for tissue engineering purposes. However, cytocompatibility is one the major concern which may hamper the biomedical applicability of graphene [36].

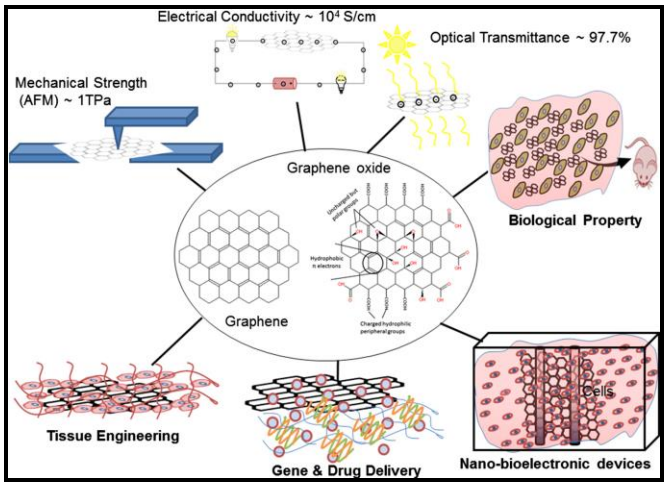

Figure 1.6. Graphene based material for biomedical applications. [36]

Graphene and graphene based materials cytocompatibility significantly depends on their concentrations along with physical and chemical properties. Mendes *et al*.[37] performed the toxicity study of different sized nano-sized GO flakes (size 89 nm and 277 nm) on HeLa and J7742 (microphage) cell lines shown in Figure **1.7**. The obtained result demonstrated that when NGO flakes of both size ranges incubated for 12 hrs, flakes with larger size showed more cell death w.r.to smaller size at a similar concentration. However, when the incubation time was increased decrease in cellular viability was observed with both the sizes suggesting no influence of size and concentration towards cellular viability. Further through TEM they observed that NGO flakes were internalized in both the cell lines. Due to internalization morphological changes were observed.

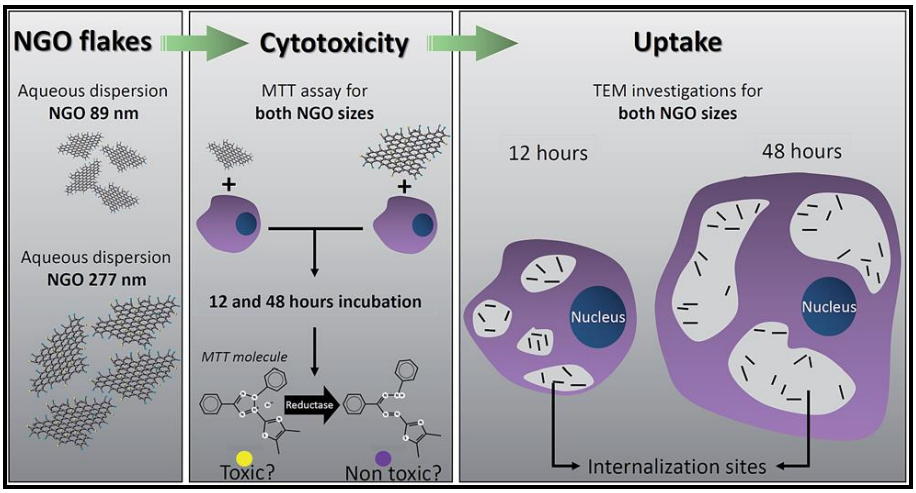

Figure 1.7. Schematic representation of size dependent toxicity. [37]

To implement graphene into commercial products, its safety concern needed to be addressed. Vranic *et al*. [38] investigated two critical parameters i.e. lateral dimension of graphene with and without protein coating along with its pulmonary impact. S-GO and 1-GO having different lateral sizes were produced using modified hummers method. Afterwards, by exploiting their intrinsic fluorescence nature, their cellular response was investigated using confocal live cell imaging (Figure **1.8**). Both types of nanoflake gets internalized however, GO type having larger lateral size damages cells w.r.to. smaller lateral sized graphene. This arises because of higher plasma membrane interaction which leads to an increase in ROS level; pro-inflammatory condition and ultimately enhanced toxicity. Also, they checked the serum protein coating effect and observed that higher lateral sized flakes coated with serum protein didn't entirely nullify the inflammatory responses with toxicity inferring the importance of lateral dimension towards biological responses.

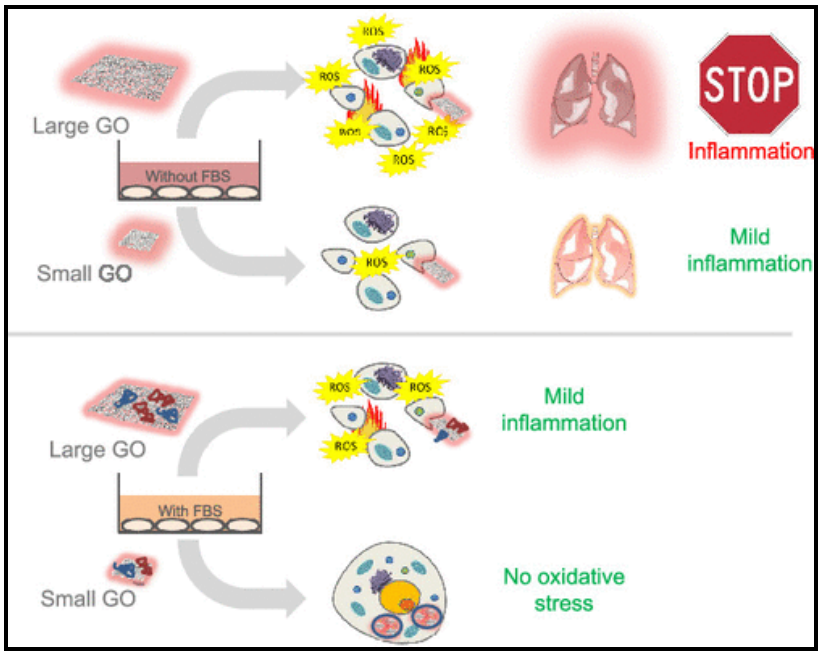

Figure 1.8. Effect of lateral size and serum coating on cellular toxicity. [38]

Sousa *et al*. [39] investigated the role of covalent functionalization. GO was covalently functionalized with D-mannose. Afterwards, they checked the toxicity towards human red blood cells. Due to mannosylation i.e. GO functionalized with D-mannose exhibited improved blood compatibility and lower hemolysis w.r.to. unfunctionalized GO shown in Figure **1.9**.

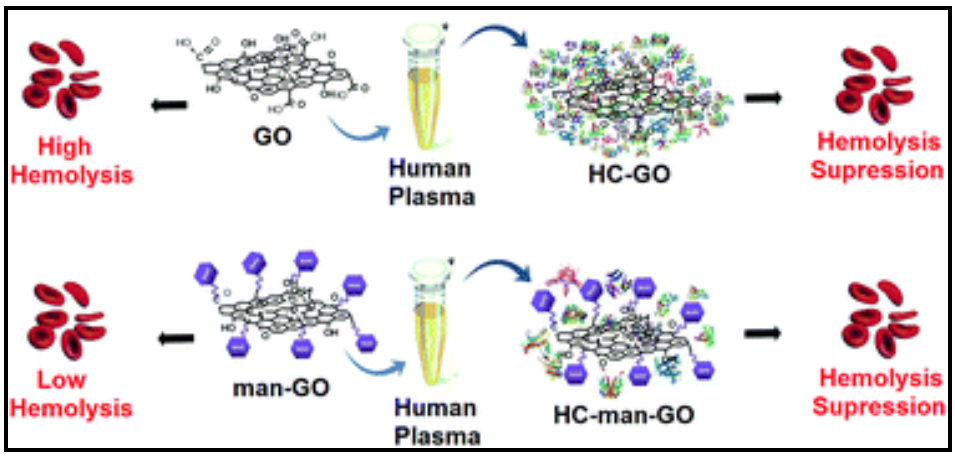

Figure 1.9. Effect of covalent functionalization on blood cells. [39]

1.2.4. Direct exfoliation of Graphene- Challa *et al*. [40] investigated aqueous phase exfoliation using eatable proteins and a kitchen blender. Bovine serum albumin (BSA) and haemoglobin proteins were chosen initially. The exfoliation efficiency was different with each protein and BSA showed maximum exfoliation efficiency of 4 $mgmL^{-1}h^{-1}$ and a yield of 7 mg mL^{-1} (Figure **1.10**). Graphene exfoliation occurs by shear force generated from kitchen blender and BSA acts as a stabilizing agent. Characterizations from raman spectrometer and transmission electron microscope reveled formation of 3-5 defect free graphene layers with a lateral size of 0.5 µm. The exfoliated sheets were stable at different physiological conditions (i.e. pH; temperature; biological fluid). These finding initiated to explore directly exfoliated graphene as an alternative over conventional hummers method for graphene production.

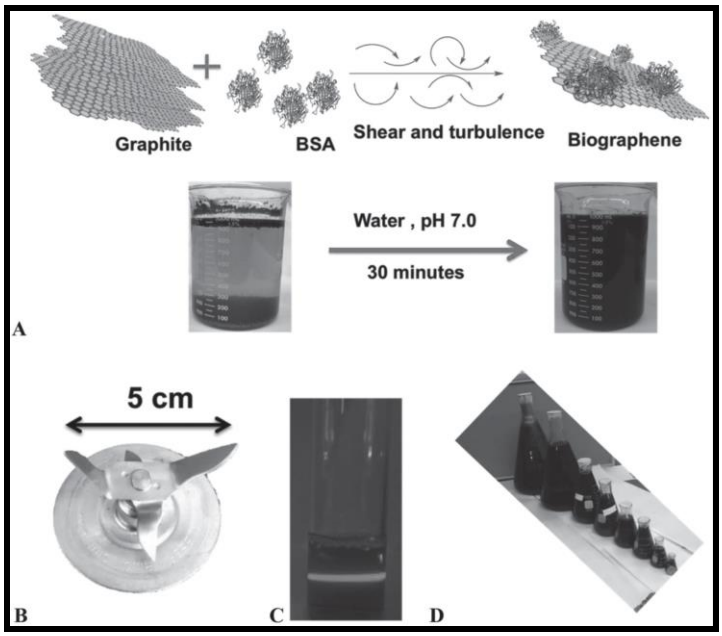

Figure 1.10. (a) Shear exfoliation of graphite using bovine serum albumin (b) types of blades used to generate turbulence (c) visualization of graphene formed by laser light scattering (d) Scalability of the method. [40]

Khademhosseini *et al*. [41] proposed a green approach to produce graphene dispersion through sonication from graphite powder in BSA solution shown in figure **1.11**. Quality of exfoliated sheets was determined from raman spectroscopy; transmission electron micrograph, XPS etc. Further, *ab inito* calculation reveled molecular interaction between BSA and graphene. Graphene dispersion then demonstrated for making conductive hydrogel-graphene system.

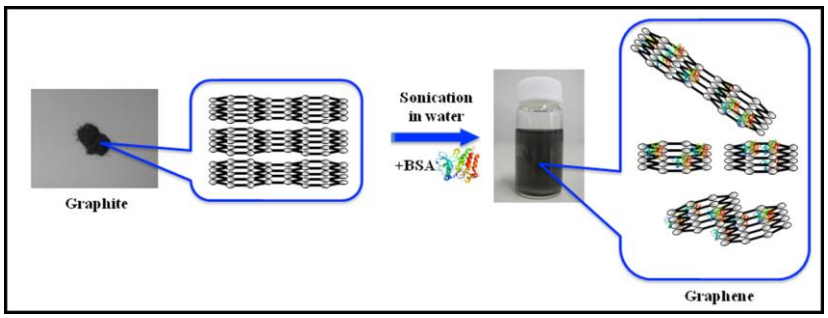

Figure 1.11. Direct exfoliation of graphite to graphene using BSA. [41]

Lee *et al*. [42] exfoliated 2D sheets in an aqueous solution without stabilizing agent. The exfoliation and dispersion occur just by elevating the sonicating bath temperature which originates because of the dissipation of sonic energy (Figure **1.12**). Afterwards, they demonstrated that exfoliated sheets can be used for inkjet printing on the different flexible substrate.

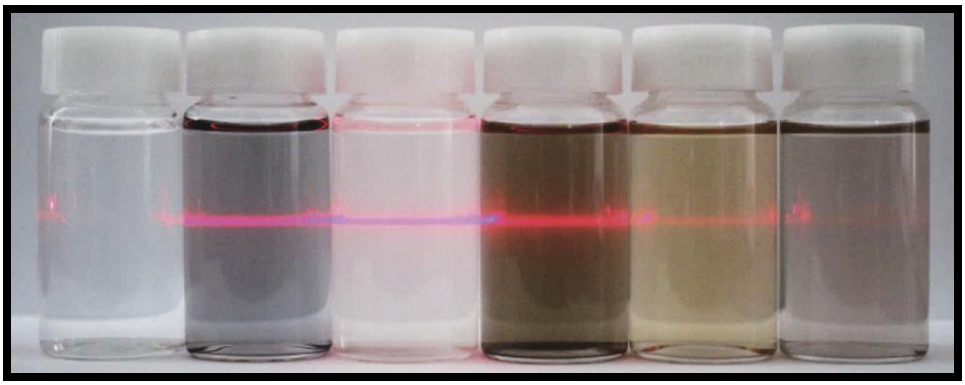

Figure 1.12. Photographs of 2D materials dispersed in water. [42]

Bai *et al*. [43] exfoliated graphene in a natural honey medium (MEG) by applying mechanical exfoliation with a yield of ~91%. Afterwards, the exfoliated sheets were dispersed in PVA matrix. Gel spinning technique was used to fabricate the PVA/MEG nanocomposite fibers and different thicknesses of nanofibers were achieved just by varying the MEG concentration. In addition to that PVA/MEG nanofibers showed cytocompatible nature towards PBMC cells and bactericidal behavior with both the type of bacteria's. The PVA/MEG nanofibrous system had the potential to be used as a surgical suture (Figure **1.13**).

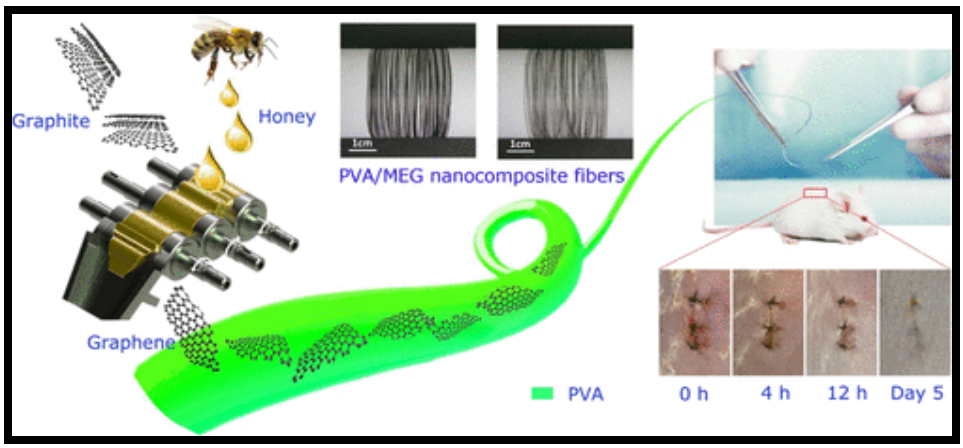

Figure 1.13. Mechanically exfoliated graphene nanocomposite fibers as medical suture. [43]

1.3. Carbon dots (c-dots)

Xu *et al*. [44] accidentally discovered fluorescent carbon nanoparticles from electrophoretic purification of SWCNT. Afterwards, Sun *et al*. [45] delineate the carbon nanoparticle synthesis with size less than 10 nm called carbon dots (c-dots). After its finding c-dots have emerged as a fascinating material owing to their remarkable fluorescence attributes like multicolor emission, up-conversion, excellent fluorescence quantum yield, very good aqueous solubility and excellent biocompatibility. Based on carbon source c-dots synthesis can be classified as green and chemically synthesized c-dots.

1.3.1 Chemically synthesized c-dots

In recent years, different chemical sources such as citric acid [46] PEG [47], ammonium citrate [48], benzene [49], phenylenediamine [50], and thiourea [51] etc. were used for c-dots synthesis. So far different synthetic routes have been used to synthesize these c-dots which includes solvothermal [52], hydrothermal [53], pyrolysis [54], electrochemical [55], ultrasonication [56], laser ablation [57] and chemical oxidation [58] etc.

Tan *et al*. fabricated c-dots from citric acid and polyethylenimine by hydrothermal treatment at 110°C for 2 h (Figure **1.14**). As synthesized c-dots exhibited small size-range of 3-6 nm with mean size around 4.5 nm calculated from TEM image also the presence of amino functional groups at c-dot surface increases its colloidal stability [59].

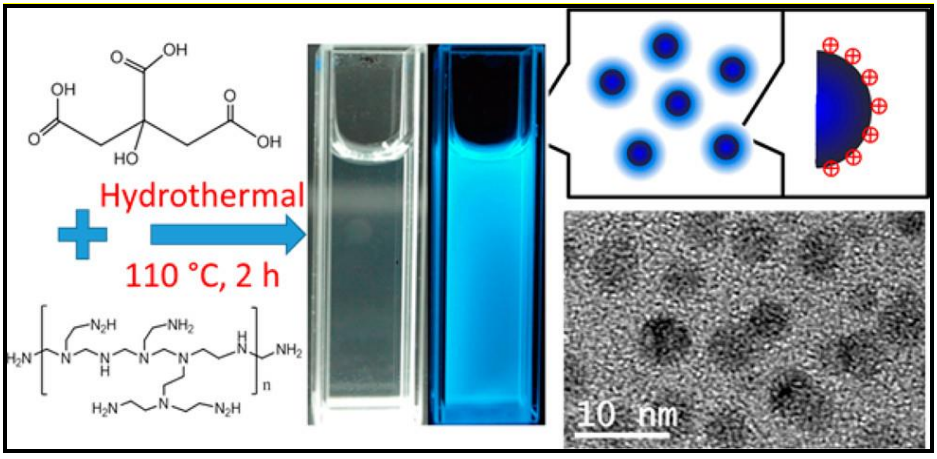

Figure 1.14. C-dots fabrication using citric acid and polyethylenimine. [59]

1.3.2 Ways to improve fluorescence properties of c-dots

- **Passivation-** Du *et al*. [60] created fluorescent carbon nanoparticles using laser irradiation in organic solvents of carbon powder (Graphite powder). Briefly due to pulse laser treatment graphite powder heated to the plasma state. Afterwards because of condensation carbon nanoparticles formed. Further reaction with PEG_{200N} the surface of carbon nanoparticles gets oxidized leads to

appearance of carboxylate groups on carbon nanoparticles surface and ultimately improved fluorescence behavior. In another work Park *et al*. [61] synthesized polydopamine based fluorescent c-dots and passivated its surface by polyethylenimine (FDA: PEI).

- **Doping-** Naumov *et al*. [62] synthesized N-GQDs & NS-GQDs from glucosamine hydrochloride as starting material by bottom-up approach (Figure **1.15**). As synthesized graphene quantum dots exhibited very high quantum yield (22-60%) as well as optical transitions.

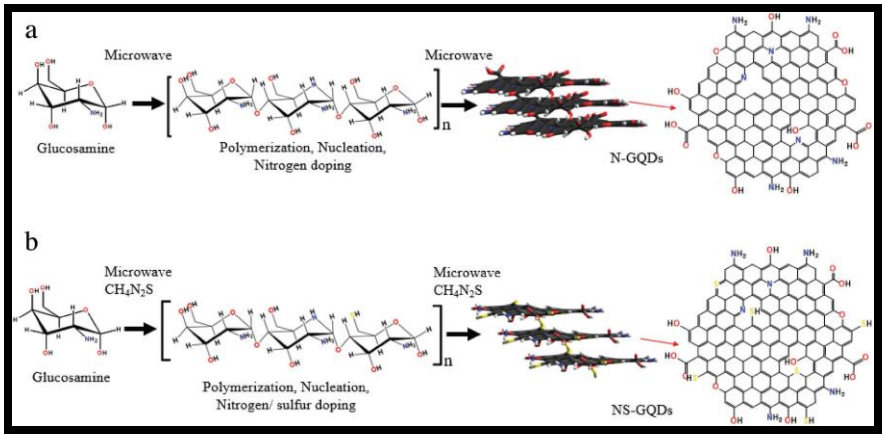

Figure 1.15. Schematic representation of the (a) N-GQDS and (b) NS-GQDs. [62]

However due to passivation the particle size of as-formed c-dots gets increased and heteroatom doping effect in fluorescence performance is still under investigation. Thus, a new strategy based on the reduction reaction of synthesized c-dots was developed for improving their fluorescence performance.

- **Reduction-** Zheng *et al*. [63] explored the reduction pathway for tuning fluorescence characteristics (quantum yield, life time) of c-dots. The original c-dots exhibited quantum yield of 1.55% and emission wavelength at 520 nm. Whereas when c-dots gets reduced by $NaBH_4$ quantum yield increased to 7.25% and blue shift in emission wavelength i.e. 450 nm was observed. Interestingly by changing the reducing agent source to $LiAlH_4$

quantum yield of 7.44% and the emission wavelength was observed at 345 nm. Thus, recognizable enhancement in fluorescence nature was observed for reduced c-dots w.r.to. c-dots. Fluorescence modulation through the reduction pathway is easy to go without affecting the size of c-dots.

1.3.2 Sustainable c-dots

Employing sustainable carbon source to synthesize c-dots offers advantages like low cost, abundant presence, reducing chemical exposure, reduces waste and the possibility of scaling-up. Thus, sustainable c-dots are synthesized from "green carbon sources" i.e. either naturally occurring or processed from natural products. Liu *et al.* did the pioneering work by using grass as a carbon source to synthesize c-dots [64]. Hsu *et al.* synthesized c-dots from coffee grounds as sloe carbon precursor with a quantum yield of 3.8% and diameter 5±2 nm [65]. Liu *et al.* reported c-dot fabrication from grass by employing hydrothermal treatment at 180°C. Afterwards, the resultant c-dots were doped with nitrogen. The elemental study confirmed the presence of carbon 41.54 wt%, nitrogen 4.23 wt%, hydrogen 4.18 wt% and oxygen 50.05 wt% with quantum yield of 6.2%. The study revealed temperature dependent particle size and quantum yield tuning [64].

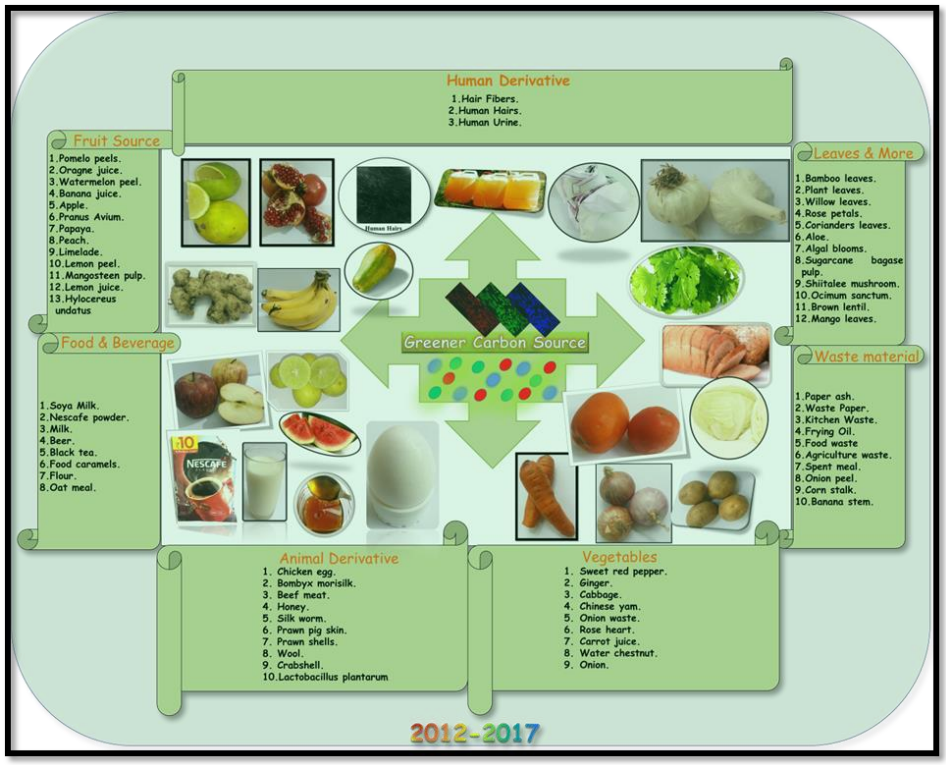

Figure 1.16. Illustration of sustainable sources derived c-dots. [66]

Synthesis of c-dots using green precursors has seen significant attention in order of its facile, cheap and environment favorable method with engrossing properties (Figure **1.16**).

Sahu *et al*. [67] used orange juice as the sole carbon precursor to synthesis c-dots at low temperature (~120^{o}C) with a quantum yield of 26% and particle size range 1.5- 4.5 nm in diameter (Figure **1.17**).

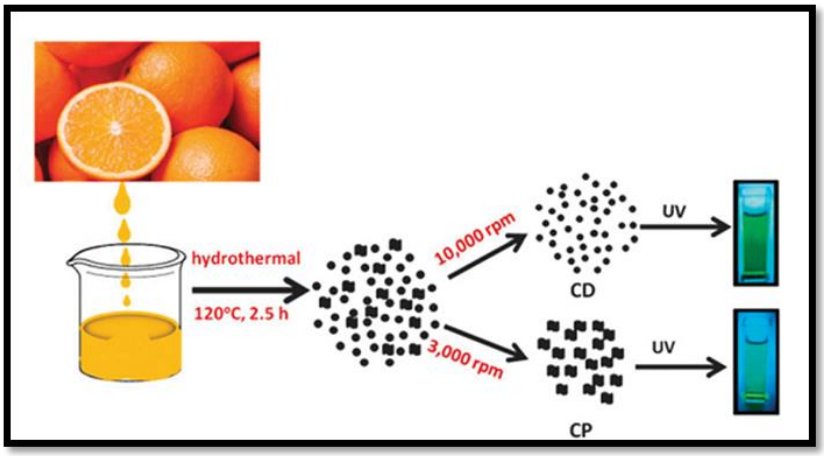

Figure 1.17. Hydrothermal synthesis of c-dots using orange juice. [67]

After using fruits, people have explored plant and plant derived c-dot. Cabbages derived c-dots were synthesized by Kim *et al* [68], cabbages were crushed using a domestic fruit juicer before the synthesis condition. The c-dots were collected after centrifugation and dialysis (Figure **1.18**). The major elements i.e. carbon; nitrogen and oxygen were around 66.5%, 4.61% and 28.73%, respectively and a quantum yield of 16.5% was found.

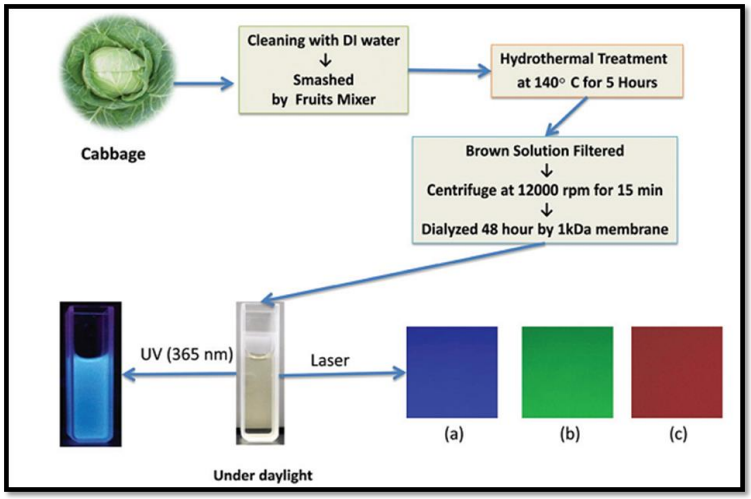

Figure 1.18. Cabbage derived hydrothermally synthesized c-dots. [68]

Kumawat *et al*. [69] synthesized red emissive graphene quantum dots using mangifera indicia as a carbon source (mGQDs). The size of as synthesized mGQDs was in the range of 2 to 8 nm with wavelength independent emissive behaviour in the range of 650 & 750 nm. Moreover, these mGQDs showed excellent biocompatibility on L929 cell lines upto the concentration of 0.1 mg/mL and intracellular temperature sensing ability under live cellular conditions (Figure **1.19**).

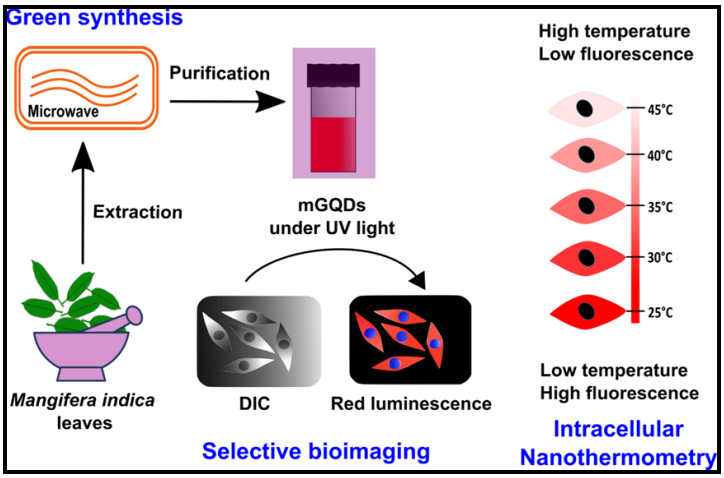

Figure 1.19. *Mangifera indica* derived graphene quantum dots showing selective bioimaging and intracellular nanothermometry applications. [69]

A range of plant leaves such as camphor, lotus, ginkgo pine, palm, bamboo, maple and osmanthus, pyrolyzed at the temperature 250-400°C within nitrogen condition. The optimum temperature for carbonization was 350°C suggesting that at a lower temperature the carbonization process was incomplete. The maximum quantum yield of 16.4%, 15.3% and 11.8% for the oriental plane, lotus and pine leaves were observed. Furthermore, by doing plasma treatment and microwave irradiation of these pyrolyzed leaves fluorescence enhancement was observed. It was stated that because of radiation treatment results in monodisperse and uniform size of these particles which ultimately led to higher fluorescence intensity [70] (Figure **1.20**).

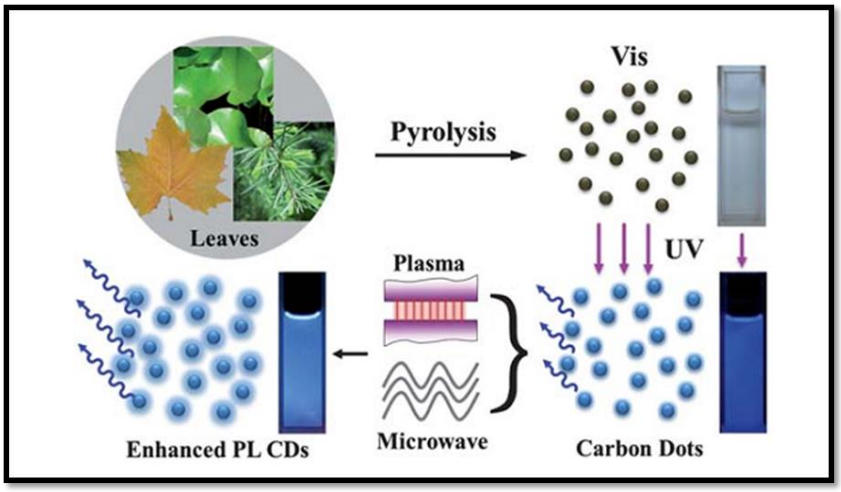

Figure 1.20. Plant leaf used c-dots synthesis. [70]

1.3.3 Calorimetric sensing

The excellent optical attributes (like enhanced quantum yield, wavelength tuned fluorescence etc.) of c-dots makes them a perfect candidate for calorimetric sensing. Attributes like small size, easy functionalization makes these c-dots very reactive which leads to change in their fluorescence characteristics and can be explored for calorimetric sensing applications [71].

Guo *et al*. [72] prepared blue emitting c-dots from human hair's thermal treatment. As synthesized c-dots selectively sense the Hg^{2+} with a limit of detection value of 10 nM by showing fluorescence turn-off behavior. In another report by Xu *et al*. [73] monodispersed blue emitting N-CDs were used for label free sensors to discriminate proteins (Figure **1.21**).

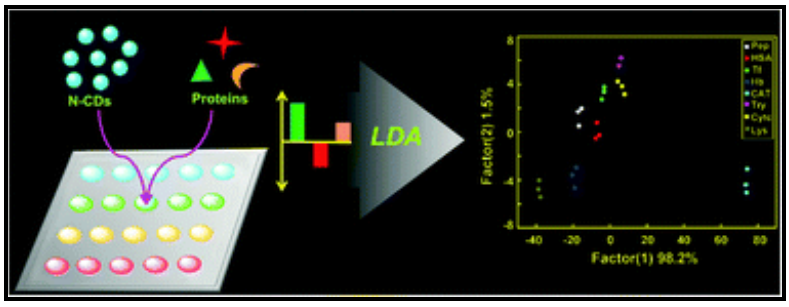

Figure 1.21. Schematic representation of label free sensor array for protein discrimination. [73]

Omer *et al*. [74] performed thermal sensing from B,N-co-doped c-dots with the sensitivity of 1.8%^{o}C in the temperature range 0-90^{o}C with excellent recovery. C-dots exhibited outstanding sensing nature with metals ions, biomolecules and physical entity suggesting its versatile nature for designing next generation sensing devices.

1.3.4 Bioimaging

C-dots having fluorescent nature offer an extra edge over standard dyes for cellular imaging purposes especially in terms of excellent photo stability, aqueous stability, cytocompatibility and easy cellular uptake. The present section mainly focuses on the application of c-dots for bioimaging purposes. Neto *et al.* [75] examined biomass wastes i.e. cow manure obtained c-dots for MCF-7 cell line bioimaging. Interestingly, the c-dots showed specific staining capability. In addition to looking at its effectiveness, bioimaging studies were also performed on MDA-MB-231, Caco-2, DU145 and found a similar trend. Gopinath *et al.* [76] synthesized c-dots using coriander leaf as a carbon precursor. Afterwards, bioimaging was performed on A549 and L-132 cell lines. Further to investigate the nuclear localization the cells were counterstained with Hoechst33342 dye. As no overlapping between c-dots (green fluorescence) & Hoechst (blue fluorescence) signalled that c-dots were distributed in the cytoplasm region and could not penetrate the nuclear membrane (Figure **1.22**).

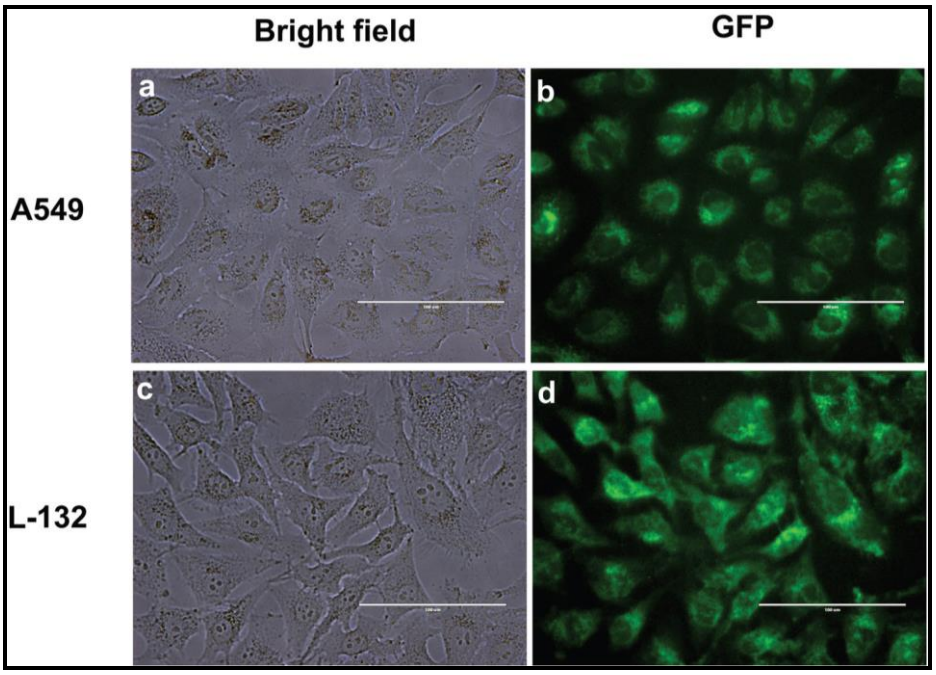

Figure 1.22. Representative fluorescence imaging of A549 and L-132 cells incubated with 0.5 mg mL^{-1} CDs. [76]

C-dots have already proven itself a useful material over contemporary fluorescent materials (inorganic quantum dots, organic dyes etc.) for cellular-subcellular imaging and sensing applications owing to their extraordinary properties. Further with development in green synthesis approach especially for synthesizing c-dots truly makes them a next generation material.

1.3.5 Carbon dot mediated synthesis of nanostructured materials

C-dots have shown lots of applications in the area of synthesis of different nanomaterials owing to the presence of various functional groups on its surface. Liu *et al*. [77] synthesized silver nanoparticles (AgNPs) from fluorescent c-dots as stabilizing and reducing agent. Further, the synthesis of AgNPs depends upon pH values i.e. at higher pH values c-dots exhibited higher reducing activity for AgNPs synthesis. In another report Li *et al*. [78] synthesized carbon quantum dots with PEI. Afterwards, as synthesized carbon quantum dots showed excellent reducibility towards

the synthesis of Ag-carbon quantum dots composite. Apart from acting as reducing agents for synthesizing metal nanoparticles c-dots have shown potential to stabilize 2D materials owing to their small size which helps in retaining the inherent structures of 2D materials. Huang *et al.* [79] demonstrated c-dots dispersing and reducing the ability for graphene and for synthesizing MnO_x-graphene hybrid nanocomposite. C-dots interacted with graphene sheets via π-π interaction and get it oxidized for making MnO_x particles on graphene sheets (Figure **1.23**).

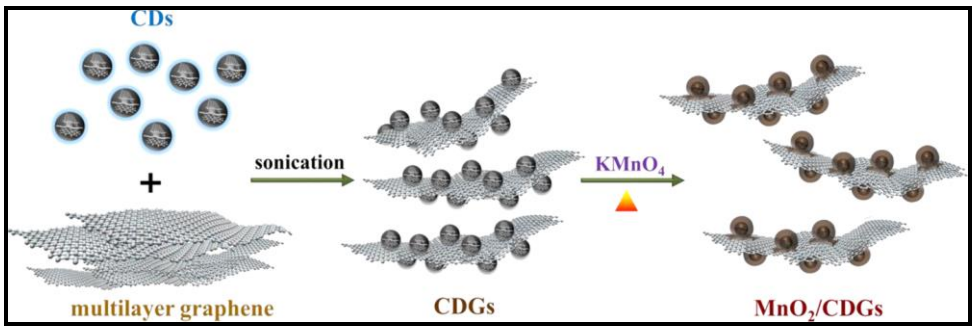

Figure 1.23. Schematic representation CDs based reductant and stabilizing agent. [79]

1.4. Scope of Present Work

The aforementioned discussion culminates about carbon nanomaterials (graphene & c-dots). The present thesis work highlights the development of graphene and c-dots by employing structure-property relationship and green synthesis approach. The motivation is to investigate these carbon nanomaterials for biocompatibility, colloidal stability, antibacterial activity, protein corona formation, optical sensing and live cell imaging along with exploring the functional group tuning for the modulation of fluorescence performance in these c-dots.

The focal points of thesis work are as follow-

1. **Direct exfoliation of graphite to graphene using a sustainable source.**
2. **Investigation of biocompatibility and protein interactions on exfoliated graphene.**
3. **Exploration and applicability of c-dots for graphene exfoliation, its stabilization and biological activity.**
4. **Green synthesis of c-dots for optical sensing of biomolecules, physical entity and bioimaging.**
5. **Modulation of fluorescence performance of c-dots through functional group tuning.**

1.5. References

[1] S. Wagner, A. Gondikas, E. Neubauer, T. Hofmann, F. von der Kammer (2014), Spot the Difference: Engineered and Natural Nanoparticles in the Environment—Release, Behavior, and Fate, Angewandte Chemie International Edition., 53, 2398–12419 (DOI: https://doi.org/10.1002/anie.201405050)

[2] O.D. Neikov, N.A. Yefimov, Chapter 9 - Nanopowders, in: O.D. Neikov, S.S. Naboychenko, N.A. Yefimov (Eds.), Handbook of Non-Ferrous Metal Powders (Second Edition), Elsevier, Oxford, 2019: pp. 271–311 (DOI: https://doi.org/10.1016/B978-0-08-100543-9.00009-9)

[3] I. Khan, K. Saeed, I. Khan (2019), Nanoparticles: Properties, applications and toxicities, Arabian Journal of Chemistry., 12, 908–931 (DOI: https://doi.org/10.1016/j.arabjc.2017.05.011)

[4] M.A. Gatoo, S. Naseem, M.Y. Arfat, A. Mahmood Dar, K. Qasim, S. Zubair (2014), Physicochemical Properties of Nanomaterials: Implication in Associated Toxic Manifestations, BioMed Research International., 2014, e498420 (DOI: https://doi.org/10.1155/2014/498420)

[5] S.K. Kulkarni (2015), Types of Nanomaterials and Their Properties, in: S.K. Kulkarni (Ed.), Nanotechnology: Principles and Practices, Springer International Publishing, Cham., 199–239 (DOI: https://doi.org/10.1007/978-3-319-09171-6_8)

[6] Classification of Nanomaterials, in: Nano- and Biomaterials, John Wiley & Sons, Ltd, 2017: pp. 27–56 (DOI: https://doi.org/10.1002/9783527807024.ch2)

[7] S. Saha, P. Samanta, N.C. Murmu, T. Kuila (2018), A review on the heterostructure nanomaterials for supercapacitor application, Journal of Energy Storage., 17, 181–202 (DOI: https://doi.org/10.1016/j.est.2018.03.006)

[8] A. Tan, R. Jeyaraj, S.F. De Lacey (2017), Nanotechnology in neurosurgical oncology, in: A.B. Mathur (Ed.), Nanotechnology in Cancer, William Andrew Publishing., pp. 139–170 (DOI: https://doi.org/10.1016/B978-0-323-39080-4.00007-0)

[9] J. Lu, Z. Chen, Z. Ma, F. Pan, L.A. Curtiss, K. Amine (2016), The role of nanotechnology in the development of battery materials for electric vehicles, Nature Nanotechnology., 11, 1031–1038 (DOI: https://doi.org/10.1038/nnano.2016.207)

[10] L.R. Khot, S. Sankaran, J.M. Maja, R. Ehsani, E.W. Schuster (2012), Applications of nanomaterials in agricultural production and crop protection: A review, Crop Protection., 35, 64–70 (DOI: https://doi.org/10.1016/j.cropro.2012.01.007)

[11] A. Kaphle, P.N. Navya, A. Umapathi, H.K. Daima (2018), Nanomaterials for agriculture, food and environment: applications, toxicity and regulation, Environ Chem Lett., 16, 43–58

(DOI: https://doi.org/10.1007/s10311-017-0662-y)
[12] M.M. Mihai, M.B. Dima, B. Dima, A.M. Holban (2019), Nanomaterials for Wound Healing and Infection Control, Materials., 12, 2176
(DOI: https://doi.org/10.3390/ma12132176)
[13] M. Notarianni, J. Liu, K. Vernon, N. Motta (2016), Synthesis and applications of carbon nanomaterials for energy generation and storage, Beilstein J. Nanotechnol., 7, 149–196
(DOI: https://doi.org/10.3762/bjnano.7.17)
[14] O. Zaytseva, G. Neumann (2016), Carbon nanomaterials: production, impact on plant development, agricultural and environmental applications, Chemical and Biological Technologies in Agriculture., 3, 17
(DOI: https://doi.org/10.1186/s40538-016-0070-8)
[15] I.A.S. Edwards, Chapter 1 - Structure in Carbons and Carbon Forms, in: H. Marsh, I.A.S. Edwards, R. Menendez, B. Rand, S. West, A.J. Hosty, K. Kuo, B. McEnaney, T. Mays, D.J. Johnson, J.W. Patrick, D.E. Clarke, J.C. Crelling, R.J. Gray (1989), Introduction to Carbon Science, Butterworth-Heinemann., pp. 1–36 (DOI: https://doi.org/10.1016/B978-0-408-03837-9.50006-3)
[16] Q.L. Yan, M. Gozin, F. Qi. Zhao, A. Cohena, Si.-Pi. Pang (2016), Highly energetic compositions based on functionalized carbon nanomaterials, Nanoscale., 8, 4799
(DOI: https://doi.org/10.1039/C5NR07855E)
[17] H.W. Kroto, J.R. Heath, S.C. O'Brien, R.F. Curl, R.E. Smalley (1985), C 60 : Buckminsterfullerene, Nature., 318, 162–163
(DOI: https://doi.org/10.1038/318162a0)
[18] A. Eatemadi, H. Daraee, H. Karimkhanloo, M. Kouhi, N. Zarghami, A. Akbarzadeh, M. Abasi, Y. Hanifehpour, S.W. Joo (2014), Carbon nanotubes: properties, synthesis, purification, and medical applications, Nanoscale Research Letters., 9, 393
(DOI: https://doi.org/10.1186/1556-276X-9-393)
[19] A.K. Geim, K.S. Novoselov (2007), The rise of graphene, Nat Mater., 6, 183–191 (DOI: https://doi.org/10.1038/nmat1849)
[20] R.C. Haddon (2013), Graphene – The Mother of Two-Dimensional (2-D) Materials, Acc. Chem. Res., 46, 2191–2192
(DOI: https://doi.org/10.1021/ar4002203)
[21] Z. Zhen, H. Zhu (2018), 1 - Structure and Properties of Graphene, in: H. Zhu, Z. Xu, D. Xie, Y. Fang (Eds.), Graphene, Academic Press., pp. 1–12 (DOI: https://doi.org/10.1016/B978-0-12-812651-6.00001-X)
[22] A.H. Castro Neto, F. Guinea, N.M.R. Peres, K.S. Novoselov, A.K. Geim (2009), The electronic properties of graphene, Rev. Mod. Phys., 81, 109–162.
(DOI: https://doi.org/10.1103/RevModPhys.81.109)

[23] T. Christensen (2017), Electronic Properties of Graphene, in: T. Christensen (Ed.), From Classical to Quantum Plasmonics in Three and Two Dimensions, Springer International Publishing, Cham., pp (DOI: 83–96. https://doi.org/10.1007/978-3-319-48562-1_4)
[24] L.A. Falkovsky (2008), Optical properties of graphene, J. Phys.: Conf. Ser., 129, 012004 (DOI: https://doi.org/10.1088/1742-6596/129/1/012004)
[25] C. Lee, X. Wei, J.W. Kysar, J. Hone (2008), Measurement of the Elastic Properties and Intrinsic Strength of Monolayer Graphene, Science., 321, 385–388 (DOI: https://doi.org/10.1126/science.1157996)
[26] D.G. Papageorgiou, I.A. Kinloch, R.J. Young (2017), Mechanical properties of graphene and graphene-based nanocomposites, Progress in Materials Science., 90, 75–127 (DOI: https://doi.org/10.1016/j.pmatsci.2017.07.004)
[27] A.A. Balandin, S. Ghosh, W. Bao, I. Calizo, D. Teweldebrhan, F. Miao, C.N. Lau (2008), Superior Thermal Conductivity of Single-Layer Graphene, Nano Lett., 8, 902–907 (DOI: https://doi.org/10.1021/nl0731872)
[28] R. Rudrapati (2020), Graphene: Fabrication Methods, Properties, and Applications in Modern Industries, Graphene Production and Application (DOI: https://doi.org/10.5772/intechopen.92258)
[29] F. Bonaccorso, A. Lombardo, T. Hasan, Z. Sun, L. Colombo, A.C. Ferrari (2012), Production and processing of graphene and 2d crystals, Materials Today., 15, 564–589 (DOI: https://doi.org/10.1016/S1369-7021 (13)70014-2)
[30] P. Sutter (2009), How silicon leaves the scene, Nature Materials., 8, 171–172 (DOI: https://doi.org/10.1038/nmat2392)
[31] C. Mattevi, H. Kim, M. Chhowalla (2011), A review of chemical vapour deposition of graphene on copper, J. Mater. Chem., 21, 3324–3334 (DOI: https://doi.org/10.1039/C0JM02126A)
[32] W. Liu, H. Li, C. Xu, Y. Khatami, K. Banerjee (2011), Synthesis of high-quality monolayer and bilayer graphene on copper using chemical vapor deposition, Carbon., 49, 4122–4130 (DOI: https://doi.org/10.1016/j.carbon.2011.05.047)
[33] A.K. Geim, A.H. MacDonald (2007), Graphene: Exploring carbon flatland, Physics Today., 60, 35–41 (DOI: https://doi.org/10.1063/1.2774096)
[34] M. Cao, N. Wang, L. Wang, Y. Zhang, Y. Chen, Z. Xie, Z. Li, E. Pambou, R. Li, C. Chen, F. Pan, H. Xu, J. Penny, J.R.P. Webster, J.R. Lu (2015), Direct exfoliation of graphite into graphene in aqueous solutions of amphiphilic peptides, J. Mater. Chem. B., 4, 152–161 (DOI: https://doi.org/10.1039/C5TB02065D)
[35] R. Narayan, S.O. Kim (2015), Surfactant mediated liquid phase exfoliation of graphene, Nano Convergence., 2, 20

(DOI: https://doi.org/10.1186/s40580-015-0050-x)
[36] S. Goenka, V. Sant, S. Sant (2014), Graphene-based nanomaterials for drug delivery and tissue engineering, Journal of Controlled Release., 173, 75–88
(DOI: https://doi.org/10.1016/j.jconrel.2013.10.017)
[37] R.G. Mendes, B. Koch, A. Bachmatiuk, X. Ma, S. Sanchez, C. Damm, O.G. Schmidt, T. Gemming, J. Eckert, M.H. Rümmeli (2015), A size dependent evaluation of the cytotoxicity and uptake of nanographene oxide, J. Mater. Chem. B., 3, 2522–2529
(DOI: https://doi.org/10.1039/C5TB00180C)
[38] S. Vranic, A.F. Rodrigues, M. Buggio, L. Newman, M.R.H. White, D.G. Spiller, C. Bussy, K. Kostarelos (2018), Live Imaging of Label-Free Graphene Oxide Reveals Critical Factors Causing Oxidative-Stress-Mediated Cellular Responses, ACS Nano., 12, 1373–1389 (DOI: https://doi.org/10.1021/acsnano.7b07734)
[39] M. de Sousa, C.H.Z. Martins, L.S. Franqui, L.C. Fonseca, F.S. Delite, E.M. Lanzoni, D.S.T. Martinez, O.L. Alves (2018), Covalent functionalization of graphene oxide with D-mannose: evaluating the hemolytic effect and protein corona formation, J. Mater. Chem. B., 6, 2803–2812
(DOI: https://doi.org/10.1039/C7TB02997G)
[40] A. Pattammattel, C.V. Kumar (2015), Kitchen Chemistry 101: Multigram Production of High Quality Biographene in a Blender with Edible Proteins, Advanced Functional Materials., 25, 7088–7098 (DOI: https://doi.org/10.1002/adfm.201503247)
[41] S. Ahadian, M. Estili, V.J. Surya, J. Ramón-Azcón, X. Liang, H. Shiku, M. Ramalingam, T. Matsue, Y. Sakka, H. Bae, K. Nakajima, Y. Kawazoe, A. Khademhosseini (2015), Facile and green production of aqueous graphene dispersions for biomedical applications, Nanoscale., 7, 6436–6443
(DOI: https://doi.org/10.1039/C4NR07569B)
[42] J. Kim, S. Kwon, D.-H. Cho, B. Kang, H. Kwon, Y. Kim, S.O. Park, G.Y. Jung, E. Shin, W.-G. Kim, H. Lee, G.H. Ryu, M. Choi, T.H. Kim, J. Oh, S. Park, S.K. Kwak, S.W. Yoon, D. Byun, Z. Lee, C. Lee (2015), Direct exfoliation and dispersion of two-dimensional materials in pure water via temperature control, Nature Communications., 6, ncomms9294
(DOI: https://doi.org/10.1038/ncomms9294)
[43] Y. Ma, D. Bai, X. Hu, N. Ren, W. Gao, S. Chen, H. Chen, Y. Lu, J. Li, Y. Bai (2018), Robust and Antibacterial Polymer/Mechanically Exfoliated Graphene Nanocomposite Fibers for Biomedical Applications, ACS Appl. Mater. Interfaces., 10, 3002–3010
(DOI: https://doi.org/10.1021/acsami.7b17835)
[44] X. Xu, R. Ray, Y. Gu, H.J. Ploehn, L. Gearheart, K. Raker, W.A. Scrivens (2004), Electrophoretic Analysis and Purification of

Fluorescent Single-Walled Carbon Nanotube Fragments, J. Am. Chem. Soc., 126, 12736–12737
(DOI: https://doi.org/10.1021/ja040082h)
[45] Y.-P. Sun, B. Zhou, Y. Lin, W. Wang, K.A.S. Fernando, P. Pathak, M.J. Meziani, B.A. Harruff, X. Wang, H. Wang, P.G. Luo, H. Yang, M.E. Kose, B. Chen, L.M. Veca, S.-Y. Xie (2008), Quantum-Sized Carbon Dots for Bright and Colorful Photoluminescence, J. Am. Chem. Soc., 128, 7756–7757
(DOI: https://doi.org/10.1021/ja062677d)
[46] E. Ju, Z. Liu, Y. Du, Y. Tao, J. Ren, X. Qu (2014), Heterogeneous Assembled Nanocomplexes for Ratiometric Detection of Highly Reactive Oxygen Species in Vitro and in Vivo, ACS Nano., 8, 6014–6023 (DOI: https://doi.org/10.1021/nn501135m)
[47] A. Jaiswal, S.S. Ghosh, A. Chattopadhyay (2011), One step synthesis of C-dots by microwave mediated caramelization of poly(ethylene glycol), Chem. Commun., 48, 407–409
(DOI: https://doi.org/10.1039/C1CC15988G)
[48] Z. Yang, M. Xu, Y. Liu, F. He, F. Gao, Y. Su, H. Wei, Y. Zhang (2014), Nitrogen-doped, carbon-rich, highly photoluminescent carbon dots from ammonium citrate, Nanoscale., 6, 1890–1895
(DOI: https://doi.org/10.1039/C3NR05380F)
[49] H. Jiang, F. Chen, M.G. Lagally, F.S. Denes (2010), New Strategy for Synthesis and Functionalization of Carbon Nanoparticles, Langmuir., 26, 1991–1995
(DOI: https://doi.org/10.1021/la9022163)
[50] M. Vedamalai, A.P. Periasamy, C.-W. Wang, Y.-T. Tseng, L.-C. Ho, C.-C. Shih, H.-T. Chang (2014), Carbon nanodots prepared from o-phenylenediamine for sensing of Cu2+ ions in cells, Nanoscale., 6, 13119–13125
(DOI: https://doi.org/10.1039/C4NR03213F)
[51] L. Wang, Y. Bi, J. Gao, Y. Li, H. Ding, L. Ding (2016), Carbon dots based turn-on fluorescent probes for the sensitive determination of glyphosate in environmental water samples, RSC Adv., 6, 85820–85828
(DOI: https://doi.org/10.1039/C6RA10115A)
[52] T. Feng, X. Ai, H. Ong, Y. Zhao (2016), Dual-Responsive Carbon Dots for Tumor Extracellular Microenvironment Triggered Targeting and Enhanced Anticancer Drug Delivery, ACS Appl. Mater. Interfaces., 8, 18732–18740
(DOI: https://doi.org/10.1021/acsami.6b06695)
[53] V. Sharma, A.K. Saini, S.M. Mobin (2016), Multicolour fluorescent carbon nanoparticle probes for live cell imaging and dual palladium and mercury sensors, J. Mater. Chem. B., 4, 2466–2476
(DOI: https://doi.org/10.1039/C6TB00238B)

[54] W. Wang, Y. Li, L. Cheng, Z. Cao, W. Liu (2013), Water-soluble and phosphorus-containing carbon dots with strong green fluorescence for cell labeling, J. Mater. Chem. B., 2, 46–48
(DOI: https://doi.org/10.1039/C3TB21370F)
[55] J. Zhou, C. Booker, R. Li, X. Zhou, T.-K. Sham, X. Sun, Z. Ding (2007), An Electrochemical Avenue to Blue Luminescent Nanocrystals from Multiwalled Carbon Nanotubes (MWCNTs), J. Am. Chem. Soc., 129, 744–745
(DOI: https://doi.org/10.1021/ja0669070)
[56] H. Li, X. He, Y. Liu, H. Huang, S. Lian, S.-T. Lee, Z. Kang (2011), One-step ultrasonic synthesis of water-soluble carbon nanoparticles with excellent photoluminescent properties, Carbon., 49, 605–609
(DOI: https://doi.org/10.1016/j.carbon.2010.10.004)
[57] S.-T. Yang, L. Cao, P.G. Luo, F. Lu, X. Wang, H. Wang, M.J. Meziani, Y. Liu, G. Qi, Y.-P. Sun (2009), Carbon Dots for Optical Imaging in Vivo, J. Am. Chem. Soc., 131, 11308–11309
(DOI: https://doi.org/10.1021/ja904843x)
[58] Z.-A. Qiao, Y. Wang, Y. Gao, H. Li, T. Dai, Y. Liu, Q. Huo (2009), Commercially activated carbon as the source for producing multicolor photoluminescent carbon dots by chemical oxidation, Chem. Commun., 46, 8812–8814
(DOI: https://doi.org/10.1039/C0CC02724C)
[59] J.-Y. Li, Y. Liu, Q.-W. Shu, J.-M. Liang, F. Zhang, X.-P. Chen, X.-Y. Deng, M.T. Swihart, K.-J. Tan (2017), One-Pot Hydrothermal Synthesis of Carbon Dots with Efficient Up- and Down-Converted Photoluminescence for the Sensitive Detection of Morin in a Dual-Readout Assay, Langmuir., 33, 1043–1050
(DOI: https://doi.org/10.1021/acs.langmuir.6b04225)
[60] S.-L. Hu, K.-Y. Niu, J. Sun, J. Yang, N.-Q. Zhao, X.-W. Du (2009), One-step synthesis of fluorescent carbon nanoparticles by laser irradiation, J. Mater. Chem., 19, 484–488
(DOI: https://doi.org/10.1039/B812943F)
[61] Z.A.I. Mazrad, C.A. Choi, Y.M. Kwon, I. In, K.D. Lee, S.Y. Park (2017), Design of Surface-Coatable NIR-Responsive Fluorescent Nanoparticles with PEI Passivation for Bacterial Detection and Killing, ACS Appl. Mater. Interfaces., 9, 33317–33326
(DOI: https://doi.org/10.1021/acsami.7b10688)
[62] M.T. Hasan, R. Gonzalez-Rodriguez, C. Ryan, N. Faerber, J.L. Coffer, A.V. Naumov (2018), Photo-and Electroluminescence from Nitrogen-Doped and Nitrogen–Sulfur Codoped Graphene Quantum Dots, Advanced Functional Materials., 28, 1804337
(DOI: https://doi.org/10.1002/adfm.201804337)
[63] D. Shen, Y. Long, J. Wang, Y. Yu, J. Pi, L. Yang, H. Zheng (2019), Tuning the fluorescence performance of carbon dots with a reduction pathway, Nanoscale., 11, 5998–6003
(DOI: https://doi.org/10.1039/C8NR09587F)

[64] S. Liu, J. Tian, L. Wang, Y. Zhang, X. Qin, Y. Luo, A.M. Asiri, A.O. Al-Youbi, X. Sun (2012), Hydrothermal Treatment of Grass: A Low-Cost, Green Route to Nitrogen-Doped, Carbon-Rich, Photoluminescent Polymer Nanodots as an Effective Fluorescent Sensing Platform for Label-Free Detection of Cu(II) Ions, Advanced Materials., 24, 2037–2041. (DOI: https://doi.org/10.1002/adma.201200164)

[65] P.-C. Hsu, Z.-Y. Shih, C.-H. Lee, H.-T (2012), Chang, Synthesis and analytical applications of photoluminescent carbon nanodots, Green Chem., 14, 917–920 (DOI: https://doi.org/10.1039/C2GC16451E)

[66] V. Sharma, P. Tiwari, S.M. Mobin (2017), Sustainable carbon-dots: recent advances in green carbon dots for sensing and bioimaging, J. Mater. Chem. B., 5, 8904–8924. (DOI: https://doi.org/10.1039/C7TB02484C)

[67] S. Sahu, B. Behera, T.K. Maiti, S. Mohapatra (2012), Simple one-step synthesis of highly luminescent carbon dots from orange juice: application as excellent bio-imaging agents, Chem. Commun., 48, 8835–8837 (DOI: https://doi.org/10.1039/C2CC33796G)

[68] A.-M. Alam, B.-Y. Park, Z.K. Ghouri, M. Park, H.-Y. Kim (2015), Synthesis of carbon quantum dots from cabbage with down- and up-conversion photoluminescence properties: excellent imaging agent for biomedical applications, Green Chem., 17, 3791–3797 (DOI: https://doi.org/10.1039/C5GC00686D)

[69] M.K. Kumawat, M. Thakur, R.B. Gurung, R. Srivastava (2017), Graphene Quantum Dots from Mangifera indica: Application in Near-Infrared Bioimaging and Intracellular Nanothermometry, ACS Sustainable Chem. Eng., 5, 1382–1391 (DOI: https://doi.org/10.1021/acssuschemeng.6b01893)

[70] L. Zhu, Y. Yin, C.-F. Wang, S. Chen (2013), Plant leaf-derived fluorescent carbon dots for sensing, patterning and coding, J. Mater. Chem. C., 1, 4925–4932 (DOI: https://doi.org/10.1039/C3TC30701H)

[71] C. Frigerio, D.S.M. Ribeiro, S.S.M. Rodrigues, V.L.R.G. Abreu, J.A.C. Barbosa, J.A.V. Prior, K.L. Marques, J.L.M. Santos (2012), Application of quantum dots as analytical tools in automated chemical analysis: A review, Analytica Chimica Acta., 735, 9–22 (DOI: https://doi.org/10.1016/j.aca.2012.04.042)

[72] Y. Guo, L. Zhang, F. Cao, Y. Leng (2016), Thermal treatment of hair for the synthesis of sustainable carbon quantum dots and the applications for sensing Hg 2+, Scientific Reports., 6, 35795 (DOI: https://doi.org/10.1038/srep35795)

[73] S. Xu, Z. Su, Z. Zhang, Y. Nie, J. Wang, G. Ge, X. Luo (2017), Rapid synthesis of nitrogen doped carbon dots and their application as a label free sensor array for simultaneous discrimination of multiple proteins, J. Mater. Chem. B., 5, 8748–8753

(DOI: https://doi.org/10.1039/C7TB02129A)
[74] L.J. Mohammed, K.M. Omer (2020), Dual functional highly luminescence B, N Co-doped carbon nanodots as nanothermometer and Fe 3+ /Fe 2+ sensor, Scientific Reports., 10, 3028
(DOI: https://doi.org/10.1038/s41598-020-59958-5)
[75] C. D'Angelis do E. S. Barbosa, J.R. Corrêa, G.A. Medeiros, G. Barreto, K.G. Magalhães, A.L. de Oliveira, J. Spencer, M.O. Rodrigues, B.A.D. Neto (2015), Carbon Dots (C-dots) from Cow Manure with Impressive Subcellular Selectivity Tuned by Simple Chemical Modification, Chemistry – A European Journal., 21, 5055–5060. (DOI: https://doi.org/10.1002/chem.201406330)
[76] A. Sachdev, P. Gopinath (2015), Green synthesis of multifunctional carbon dots from coriander leaves and their potential application as antioxidants, sensors and bioimaging agents, Analyst., 140, 4260–4269 (DOI: https://doi.org/10.1039/C5AN00454C)
[77] J.-C. Jin, Z.-Q. Xu, P. Dong, L. Lai, J.-Y. Lan, F.-L. Jiang, Y. Liu (2015), One-step synthesis of silver nanoparticles using carbon dots as reducing and stabilizing agents and their antibacterial mechanisms, Carbon., 94, 129–141
(DOI: https://doi.org/10.1016/j.carbon.2015.05.084)
[78] T. Liu, J.X. Dong, S.G. Liu, N. Li, S.M. Lin, Y.Z. Fan, J.L. Lei, H.Q. Luo, N.B. Li (2017), Carbon quantum dots prepared with polyethyleneimine as both reducing agent and stabilizer for synthesis of Ag/CQDs composite for Hg2+ ions detection, Journal of Hazardous Materials. 322 (2017) 430–436.
(DOI: https://doi.org/10.1016/j.jhazmat.2016.10.034)
[79] B. Unnikrishnan, C.-W. Wu, I.-W.P. Chen, H.-T. Chang, C.-H. Lin, C.-C. Huang (2016), Carbon Dot-Mediated Synthesis of Manganese Oxide Decorated Graphene Nanosheets for Supercapacitor Application, ACS Sustainable Chem., Eng. 4, 3008–3016
(DOI: https://doi.org/10.1021/acssuschemeng.5b01700)

CHAPTER 2

High yield graphene production arising from synergistic effect of elevated temperature and gelatin offers higher stability and cellular compatibility

2.1. Introduction

Two-dimensional (2D) graphene (G) sheets have emerged as a backbone of material science in today's world. The extraordinary [1-3] properties of G not only attracted scientists but also to engineer for upcoming technologies. The G has been significantly utilised in the areas of electronic devices, energy generation, reinforced composite materials, biomaterials [4-8], antibacterial activities [9] and chemical sensing [10]. So far various approaches like epitaxial growth [11], CVD [12], and micromechanical cleavage [13,14] has been employed for the productions of high quality G. However, constraints like low yield, high cost of production, extensive time consumption, limits their large-scale applicability. On the other hand, the liquid phase exfoliation overcomes the above limitations with improved production yield [2,3] but due to conventional and tedious reduction of graphene oxide (GO) it suffers irregularities both in structure and properties and also restricts its extensive applicability [15-16]. Thus, the liquid phase direct exfoliation of graphite (Gr) using solvent or surfactant is a need of an hour to overcome the limitations of conventional methods in term of ease of synthesis and quality of G production [17-18]. A variety of surfactants and solvents were used to directly exfoliate Gr to G [19-21]. Recently Dong et al [22]., proposed a new synthesis method to produce high crystalline G with very concentration (50 mg/mL) by using alkaline water. The use of biomolecules as stabilizing agent has potential benefits in terms of availability, biocompatibility, hydrophilicity, minimization of safety

related issues and non-covalent functionalization with G layers [23-26]. The pioneer work on biomolecule based direct exfoliation using hydrophobins highlights the use of proteins in exfoliation [27-28]. Various other proteins like lysozyme, BSA etc. were used to directly exfoliate Gr to G but the yield offered was relatively low [29-33]. Recently Kim et al [34]., highlighted the effect of high temperature sonication on graphene yield. Kumar et al [35]., used BSA to directly exfoliate G using kitchen blender. Further, the use of amphiphilic peptides [36], lignin [37] ,Vmh2 [38],liposome [39] were also explored. Joseph et al., prepared double strand DNA-Graphene hybrid by directly exfoliating graphene using double strand DNA. Further, they studied the biological activates of the exfoliated graphene on NIH-3T3, HCT-116 cell lines [40]. The chemical composition of exfoliated Gr could be a bottleneck for bio-medical applications. Liao et al [41]., reported that oxygen content of rGO induces hemolysis, hence more biocompatible approaches needs to be sought for applications like theranostics [42-44]. So far no report consider the scalability and cost of the exfoliate involving biomolecules for the maximum yield with low-cost to cater the industrial demand. Gelatin is the hydrolysed form of collagen which obtained from boiling skin / tendons, bones with water and also found as a by-product from meat-leather industries. It was reported the worldwide production of gel is about 3.75-4.00 lakhs of tonnes every year [45]. Gelatin is widely used in food, cosmetic and pharmaceutical industries however, its applicability in exfoliating 2D-materials due to the presence of hydrophilic and hydrophobic segments given a way for new direction of research. Gelatin offers exclusive advantages like non toxicity, biodegradability, phenomenal likeness with protein, cheap and commercial availability [46]. Gelatin contains different amount of 18 polar and non-polar amino acids. The non-polar amino acids through hydrophobic-hydrophobic interactions interact with exfoliated sheets and form the stable dispersion. Further, it was reported that gelatin exhibit strong affinity towards GO as well as

graphene [47]. Presence of electro-negative atoms in its structure gelatin can provides more favourable interaction with graphene and allows more effective stabilizations of graphene [48]. As most of the earlier studies focussed on GO-gelatin which restricts the overall applications due to tedious synthesis conditions, presence of oxidative defects and toxicity. Thus, the quest for high yield, colloidal stability, biocompatibility and low toxic effects, lead to the anticipation of using gelatin as stabiliser and exploring the effect of varying exfoliation parameters.

Herein, we report direct exfoliation of G using gel followed by; the effect of exfoliation conditions such as temperature, pH, Gr to gelatin ratio and total particle concentration on G yield is examined. The exfoliated G dispersion was checked for its colloidal stability. Interestingly, compare to temperature~30^{o}C the higher G production was observed on increasing the temperature to 60^{o}C. Moreover, the exfoliated G was found to be highly bio and hemocompatible even at high concentration upto 10 mg/mL. All these findings opens a more environment friendly route to exfoliate graphite to graphene using a sustainable resource for many biological applications which so far was ignored and will enhance its applicability in a more practical capacity.

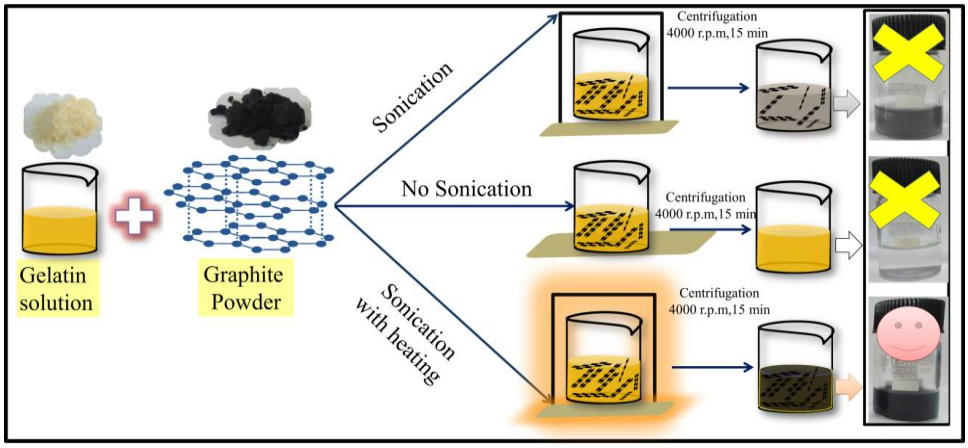

Scheme 2.1. Direct exfoliation of Gr to G with variation in exfoliation parameters. Non- sonicated (NS), sonication (S) at ~30^{0}C and sonication with heating (SH) at ~60^{0}C.

2.2. Results and discussion

A facile exfoliation of high quality, un-oxidized graphene (G) using gelatin as stabilizing agent from graphite powder (Gr) by employing ultrasonication technique has been reported (**Scheme 1**). The effects of exfoliation parameters such as sonication, temperature, pH, Gr to gelatin ratio etc., are meticulously examined for enhanced yield. The characterisation of G was performed using Raman spectroscopy, X-ray diffractometer (XRD), Transmission electron microscope (TEM) and Atomic force microscope (AFM). The colloidal stability and biological applicability of G has been investigated under varied conditions.

2.2.1. Parameters influencing graphitic exfoliation

The effect of sonication and temperature on exfoliation efficiency was first studied and the results are summarised (Figure **2.1**). The *Uv-vis* spectra of non-sonicated (NS) Gr shows least absorbance value, while the sonicated (S) and sonication with heating (SH) resulted in better dispersion and high absorption of Gr. However, SH shows significantly high absorption compare to S (Figure **2.1a-b**). The low absorption at RT can be attributed to the lower sonic pressure due to absorption of sonic energy by cold water in terms of heat, while high yield in SH may be due to higher sonic pressure [49]. A visible difference in G dispersion with varying exfoliation conditions can easily be seen in Figure **2.1c**.

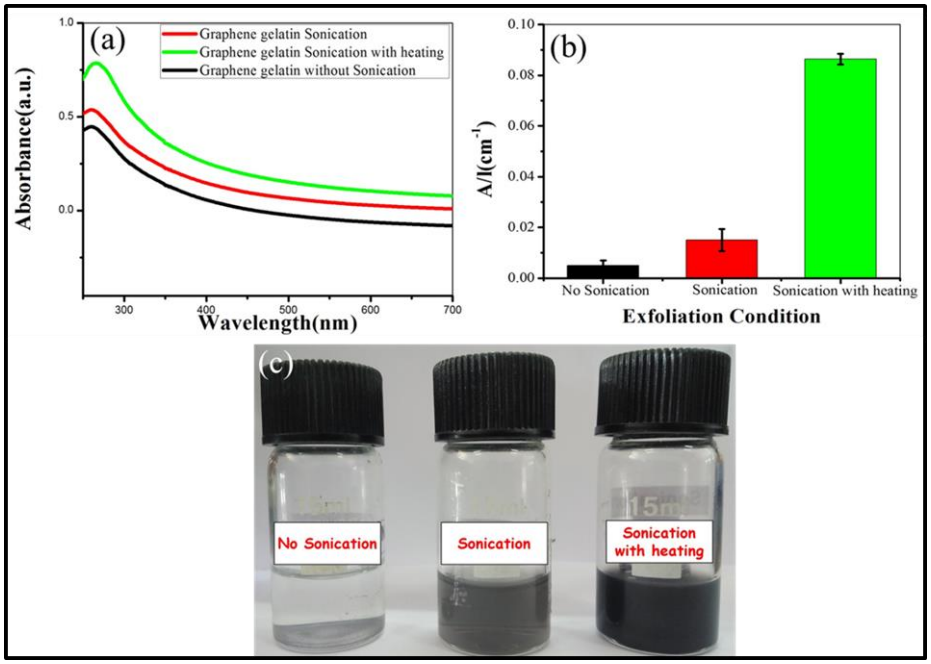

Figure 2.1. Effect of exfoliation condition on G production from unsonicated and sonicated Gr-gel dispersion (a) Absorption spectrum (b) A/l_{660} (cm^{-1}) value (c) Photograph of G dispersion. Gr-gelatin dispersion was subjected to ultrasonication for 2h and then centrifugation at 4000 r.p.m. for 15 minutes for the removal of excess Gr.

The sonication does not affect gelatin concentration validated by consistent absorption of gel post sonication (Figure **2.2a**). Gelatin lowers the surface tension between graphitic sheets and water (Figure **2.2b**). It was observed that surface tension of water at 24^{o}C is 72.05 mN/m whereas it gets reduced to 56.32 mN/m for water-gelatin system. Surface tension of water decreases with increase in temperature i.e. at 60^{o}C water exhibit surface tension of 66.180 mN/m. So, the lowering of water-gelatin system surface tension gets more efficient at higher temperature which may lead to more efficient exfoliation.

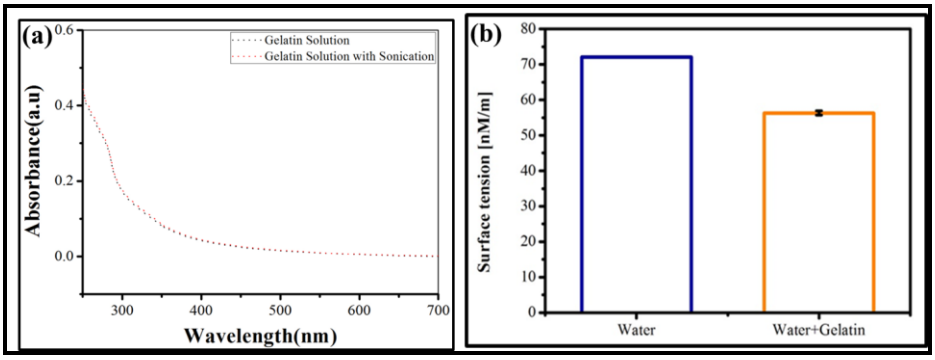

Figure 2.2. (a) Effect of sonication on gelatin (b) Surface tension of water and water+gelatin.

Further, gelatin interacts strongly with G via hydrophobic interactions and through the edges and stabilizes the exfoliated sheets [50]. To avoid the interference of gelatin in absorption values, absorbance at 660 nm was measured due to negligible absorption by gelatin at this wavelength. So sonication at temperature~60^{o}C was maintained in further experiments. It must be mentioned here that sonication at 70^{o}C& 80^{o}C were performed, however absorption value was increasing (Figure **2.3a-b**) highly distorted sheets were observed (Figure **2.4**) arising from very high shear forces at higher temperature. Thus, 60^{o}C temperature was chosen for further experiments.

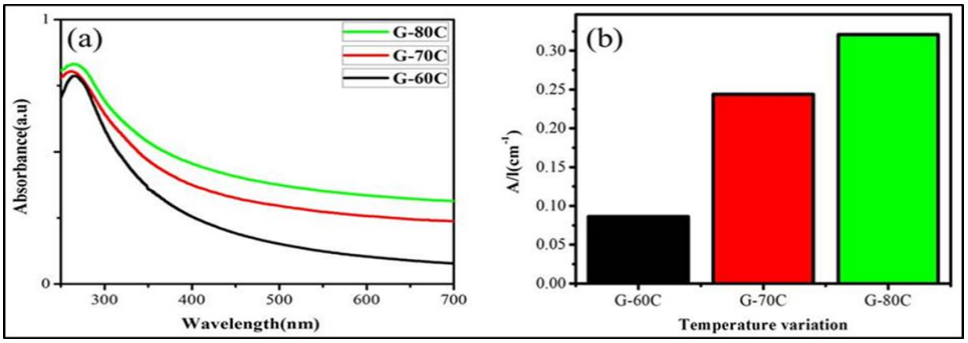

Figure 2.3. Effect of temperature increment on G production (a) *Uv-vis* spectra (b) A/l_{660} (cm^{-1}) value of G-80C, G-70C and G-60C.

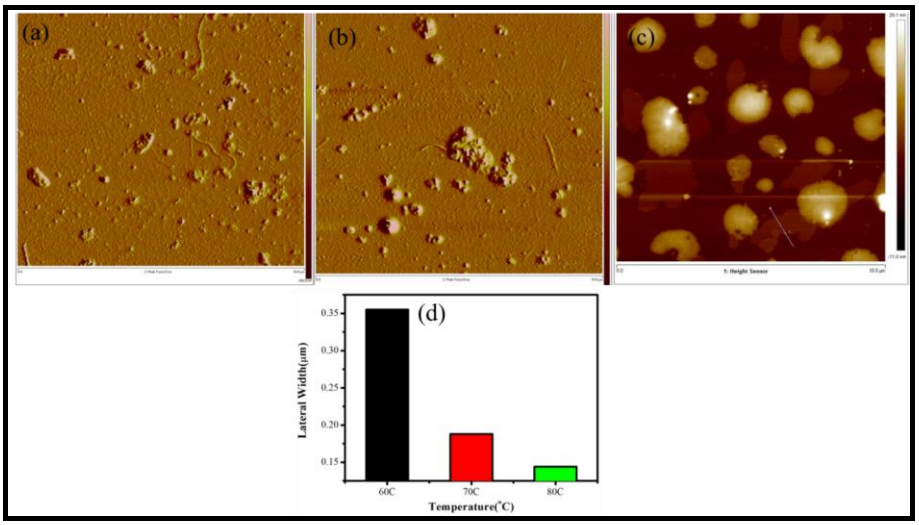

Figure 2.4. AFM image of exfoliated G sheets at various temperature (a) 80^{o}C (b) 70^{o}C (c) 60^{o}C (d) Lateral width of exfoliated G at varying temperature.

Further optimization of exfoliation parameters were performed on SH conditions. The effect of Gr to gelatin ratio on G yield was analysed with five different ratio i.e. Ggel1 (90% Gr, 10% gelatin); Ggel2 (80% Gr, 20% gelatin); Ggel3 (70% Gr, 30% gelatin); Ggel4 (60%Gr, 40% gelatin) and Ggel5 (50% Gr, 50% gelatin) and the total particle (Gr + gelatin) was fixed 1 gm /100 mL. The results exhibited in Figure **2.5a** shows the influence of Gr to gelatin ratio on the production yield of G, as maximum absorbance was observed for Ggel4 with value A/l_{660} (cm^{-1}) 0.16. Figure **2.5b** shows pictures of exfoliated G dispersion at different Gr to gel ratio which shows an evident higher exfoliation for Ggel4. These results highlight the importance of relative concentrations of interacting species for agreeable surface matching and effective exfoliation.

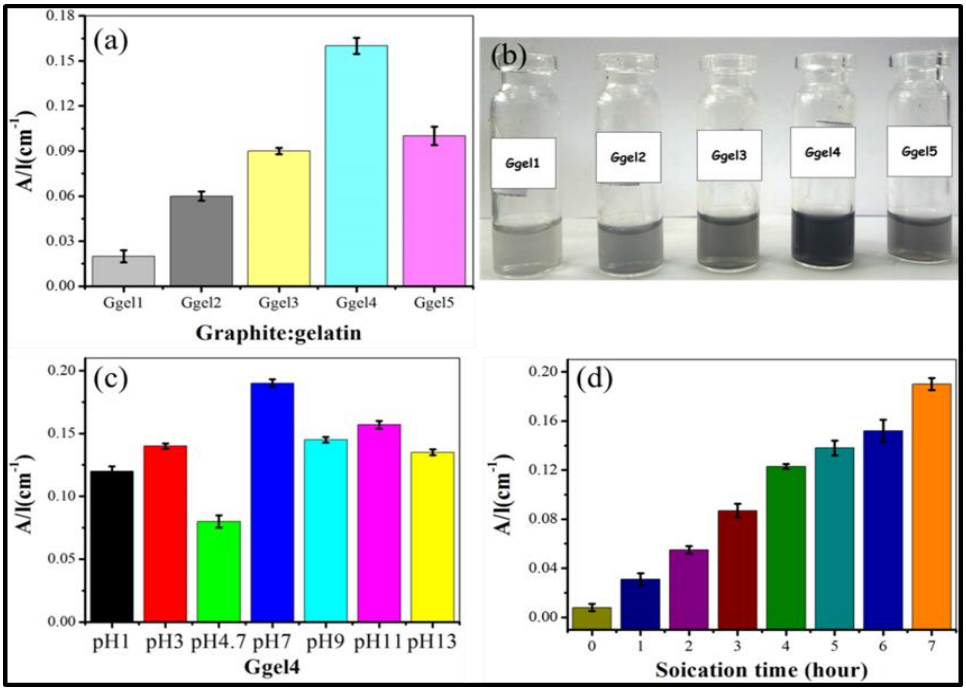

Figure 2.5. Effect of solution parameters on A/l_{660} (cm^{-1}) value of exfoliated G. (a) variation in Gr to gelatin ratio (b) Picture of G dispersion at different Gr to gelatin ratio (c) at different pH (d) at varied sonication time.

Similarly, the effect of total particles (Gr+gelatin) on production yield was analysed at varied total mass i.e. 1, 2, 4 and 6 gm/100mL, the Gr to gelatin ratio was maintained as per Ggel4 condition. The results depicted in Figure **2.6a** shows that increasing the total mass can result in higher yield as maximum A/l_{660} (cm^{-1}) value of 0.18 was observed at 6 gm/100mL just after 2 hrs of sonication. The above optimized Ggel4 (60%Gr: 40% gel) was considered for further studies. The colloidal stabilization of G depends on the net charge in the solution; hence pH is a crucial parameter. The effect of pH as exhibited in Figure **2.5c** shows least A/l_{660} (cm^{-1}) value at pH 4.7 which can be attributed to the isoelectric point of type b gelatin in pH range (4.7-5.4) leading to a net zero charge at pH 4.7, causing restacking of sheets.

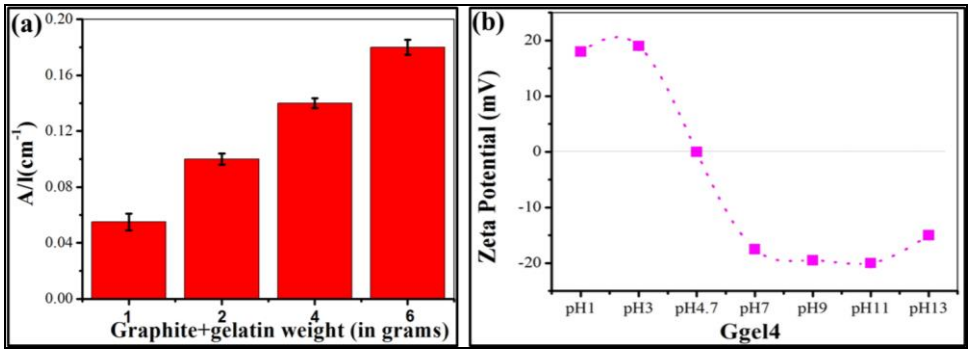

Figure 2.6. (a) Effect of Graphite+gelatin ration on G yields (b) Zeta Potential of Ggel4.

This presumption was further validated by measuring zeta potential of exfoliated G dispersion at various pH values (Figure **2.6b**). The zeta value at pH 4.7 was obtained to be zero and range ±20 mV for other pH values. The effect of sonication time shows more exfoliation with increase in sonication time upto 7 hrs (Figure **2.5d**). The prolonged sonicating force breaks the larger fraction of graphitic flakes into reduced fraction of smaller flakes depict the notable effect of sonicating force [51]. In order to quantify the yield of G production, the calibration plot (at 660 nm, pH 7, DI water) was used to calculate the extinction coefficient which was found to be 0.04338 mL mg^{-1} cm^{-1}. The calculated extinction coefficient and Beer-Lambert law ($A= \alpha_{660}lc$) was employed for determining G concentration. The yield obtained for Ggel4 conditions was 4.37 mg/mL for 1gm/100 mL (Gr+gelatin), after 7 hrs of sonication. However, at higher Gr+gelatin i.e. 6 gm/100mL; a concentration of 4.14 mg/mL G was obtained within 2 hr of sonication (Figure **2.6a**). It must be mentioned here that very low yield of 1mg/mL was achieved when Ggel4 were exfoliated at room temperature even after 7 hrs of sonication. The above results provide evidences for higher G production with tuning of exfoliation conditions which can lead to large scale production of unoxidized, high quality G.

2.2.2. Evidence and morphology of exfoliated G sheets

In order to characterize the exfoliated G, Raman spectroscopy, TEM and AFM were performed. Figure **2.7**, shows Raman spectra of Gr and Ggel4 after 1 and 7 hour of sonication. It is to be noted that the peak around 1580 cm^{-1} corresponds to G band, peak around 1360 cm^{-1} corresponds to D (defect) band and 2700 cm^{-1} corresponds to 2D band. The defect related peak was absent in control Gr however, D peak was appeared in Ggel4 samples. The appearance of this peak was due to edge defect occurred in exfoliated samples by sonicating force. A significant difference in peak intensities and shape were observed in Ggel4 samples as compared to control Gr.

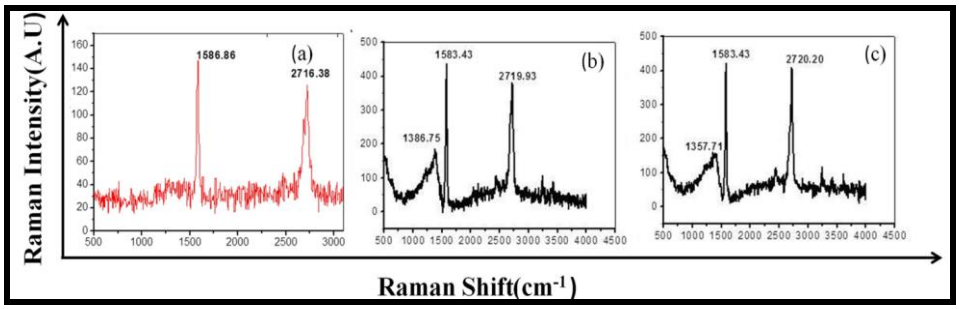

Figure 2.7. Raman spectra of (a) Gr powder, (b) Ggel4 after 1 hrs sonication, (c) Ggel4 after 7 hrs sonication.

Table 2.1. I_D/I_G, I_{2D}/I_G, Number of layers and lateral size of Gr powder and Ggel4 after 1hrs and 7 hrs of sonication.

S. no.	Samples	I_D/I_G	I_{2D}/I_G	Number of layers	Lateral size
1	Gr	0	-	-	-
2	Ggel4 (1 hrs sonication)	0.38	0.89	8	0.447 µm
3	Ggel4 (7 hrs sonication)	0.48	0.96	5	0.354 µm

As shown in Table **2.1**., I_D/I_G values of Ggel4 samples after 1 and 7 hrs of sonication is 0.38 and 0.48 respectively indicating exfoliated G has very less defect as compared to G obtained via reduction of GO due to the presence of oxygen atom [52,53]. These defects were arises from sp^3 hybridized graphitic atoms from edges of the sheets. The broadening of 2D peak and increase in I_{2D}/I_G value for Ggel4 samples with increase in sonication time, indicates breaking of sheets. It was reported that for single layer G the I_{2D}/I_G value was around 2.1±0.2 and gets decreased to 0.8±0.1 for quadruple layers [54]. For Ggel4 after 7 hrs sonication I_{2D}/I_G was 0.96 indicating 5 or fewer layers. The lateral thickness of sheets gets decreased to 0.354 µm after 7 hrs of sonication from 0.447 µm after 1 hrs of sonication, indicating the role of sonication time in the exfoliation process. The 2D peak of Ggel4 samples were deconvoluated into 4 components in range 2600-2800 cm^{-1} (Figure **2.8**). For Ggel4 after 1 hrs sonication the major peak was at ~2745 cm^{-1} and minor peaks were at ~2625 cm^{-1}, ~2638 cm^{-1} and ~2695 cm^{-1}. A similar trend was observed in Ggel4 sample after 7 hrs sonication. The peak broadening and peak shifting implies loss of ABAB stacking of graphitic layers occurred due to higher shear force.

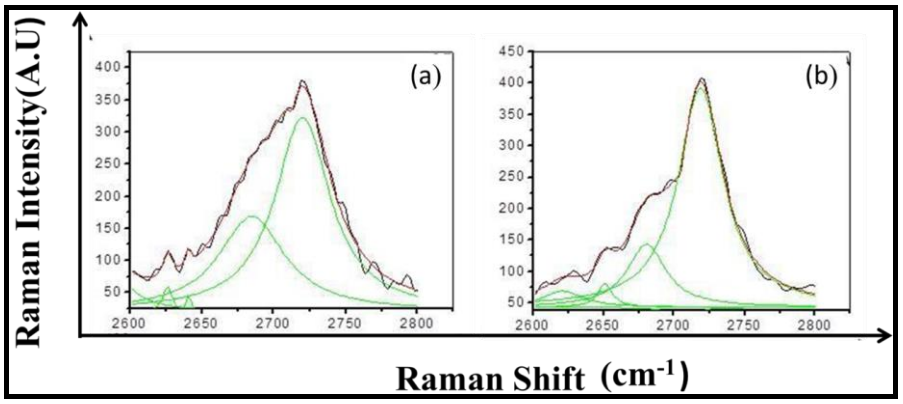

Figure 2.8. 2D deconvoluated peak of Ggel4 (a) after 1 hrs sonication (b) 7 hrs sonication.

TEM and AFM were performed for investigating morphology of the exfoliated sheets. Figure **2.9a-b** shows the lateral thicknesses of exfoliated G having size 0.249 µm with crumpled morphology, twisting and folding of layers. Although presence of crumpled morphology, no observable holes or other structural damage can be seen in the exfoliated sheets. The crumpled morphology was very well reported in earlier report [55] and arises from decrease in sheets thickness and number of layers. These irregularities in exfoliated sheets occurred due to high sonication force and lesser thickness. The irregularities in exfoliated sheets results in formation of asymmetric graphene flakes with aspect ratio of <L/w>=2.4. The SAED pattern (Figure **2.9c**) shows distorted electron diffraction pattern occurred due to exfoliation as compared to perfect hexagonal pattern of control Gr. The presence of more than one order of electron diffraction spots indicates multilayer G formation. These results support the successful exfoliation of Gr to G with no loss in crystallinity. Similarly, irregular morphology of exfoliated G sheets was observed by AFM having a horizontal distance of 134 nm and vertical distance of 1.42 nm corresponds to 4 layers.

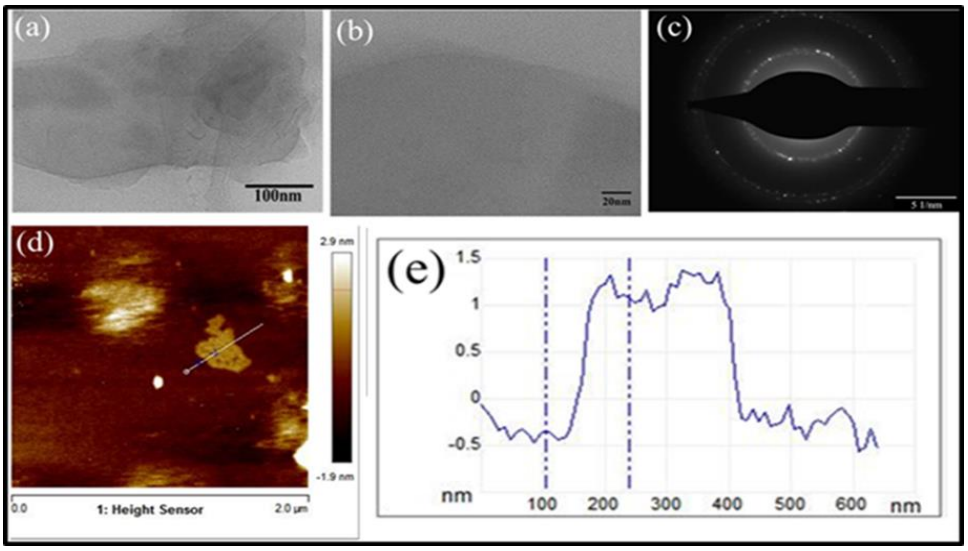

Figure 2.9. (a) Representative TEM images of multilayer exfoliated G sheets, (b) TEM images of bilayer G, (c) SAED pattern (d-e) AFM image of exfoliated G sheets along with its height profile.

2.2.3. Mechanism of gel towards direct exfoliation of Gr

The role of gelatin in stabilising exfoliated G was investigated using Fluorescence spectroscopy, fluorescence life time decay and dynamic light scattering. It is evident that both sonication and a stabilising agent are required for efficient exfoliation. As discussed earlier, no exfoliation was observed without sonication and absence of a stabiliser restricts the solubility in water [29]. Gelatin lowers the surface tension between water and Gr surface and sonication facilitates the exfoliation. The fluorescence spectra of gelatin solution and Ggel4 after 1 and 7 hrs sonication shows the fluorescence quenching of gel solution with exfoliation of G (Figure **2.10a**). The average life time decay of gelatin solution was 2.19 ns which was reduced to 0.86 ns and 0.43 ns in Ggel4 after 1 and 7 hrs sonication (Figure **2.10b**), respectively. This reduction in lifetime decay can be attributed to electron energy transfer between gelatin and exfoliated G [56-58]. The XRD pattern of Gr and Ggel4 shows peak at (θ=26.6^o) (Figure **2.10c**) corresponding to (002) plane. However, the intensity in Ggel4 was very less and a hump appeared around (θ=20^o) due to presence of gelatin. The presence of (002) plane with lesser intensity indicates exfoliation with retained crystallinity of exfoliated sheets.

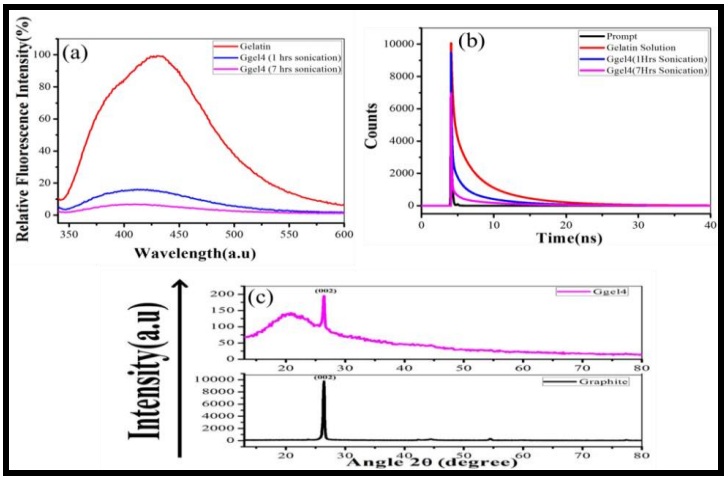

Figure 2.10. Characterization of the Gelatin and Ggel4 dispersions after 1 and 7 hrs sonication. (a) Relative fluorescence intensity, (b) fluorescence lifetime decay and (c) PXRD spectra of Ggel4 and Gr powder.

Table 2.2. PdI, D_H and zeta potential (mV) of gelatin solution and Ggel4 after 1 and 7 hrs of sonication.

Sl no.	Samples	PdI	D_H	Zeta Potential
1.	Gel	0.444	756.4nm	-24.44mV
2.	Ggel4 (1 hrs Sonication)	0.182	303.6nm	-9.38mV
3.	Ggel4 (7 hrs Sonication)	0.228	249.1nm	-12.16mV

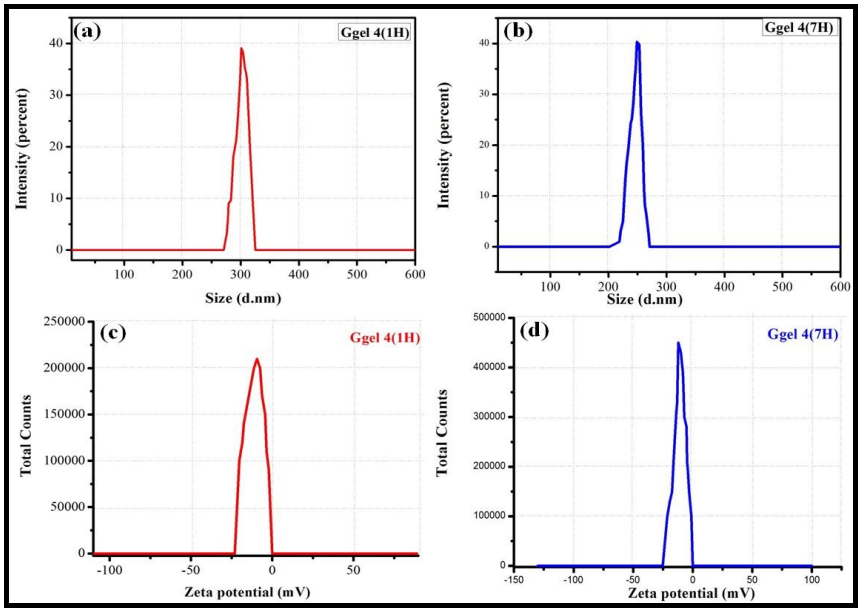

Figure 2.11. Traces (DLS and Zeta Potential) for Ggel4 after 1 and 7 hrs sonication (a) DLS of Ggel 4(1H) (b) DLS of Ggel4 (7H) (c) Zeta potential of Ggel 4(1H) (d) Zeta potential of Ggel4 (7H).

The dynamic light scattering was performed to measure hydrodynamic diameter (D_H), polydispersity index (PdI) and zeta potential and the results are summarised in Table **2.2**. The Traces (DLS and Zeta Potential) for

Ggel4 after 1 and 7 hrs sonication were given in (Figure **2.11**). The gel solution have PdI value of 0.444 and D_H 756.4 nm, which was reduced to PdI value of 0.182 and D_H 303.6 nm in Ggel 4 after 1 hr sonication (Figure **2.11a**). At 7 hr sonication the PdI gets increased to 0.228 and D_H value gets further decreased to 249.1 nm (Figure **2.11b**). The initial open structure of gelatin gets contracted due to Gr addition and leads to decrease in D_H with increase in sonication time. However, slight increase in PdI value after 7 hrs sonication attributes that few layer G was forming. It is worth noting that low PdI value of Ggel4 corresponds uniformity in thickness of exfoliated G. The zeta potential of gelatin at neutral pH shows negative charge which shows a further reduction with addition of Gr due to decrease of electrophoretic mobility of Ggel4. However, it remains well within the stable range i.e. -25 mV to + 25 mV. The lateral thickness measured from DLS, TEM and Raman was 0.249, 0.225 and 0.354 µm respectively. The lateral thickness measured was in agreement with earlier reports [59].

2.2.4. Colloidal Stability of Exfoliated G

The colloidal stability of exfoliated Ggel4 was studied under various physiological conditions like storage at 37^{o}C (RT@Ggel4) and at 5^{o}C (LT@Ggel4). The effect of bio- fluids like Fetal Bovine Serum (FBS) and Trypsin was also studied in Figure **2.12** shows consistent A/l_{660} (cm^{-1}) values over a period of 31 days, indicating high storage stability without temperature constraints. However, FBS and trypsin affects the stability as shown in Figure **2.12b-c**, the A/l_{660} (cm^{-1}) values show consistent decrease. The decrease in absorption of Ggel4 in FBS and trypsin can be attributed to deterioration of adsorbed gelatin due to the presence of protease, and subsequent re-aggregation of exfoliated sheets. On the other hand, the studied temperature variation doesn't affect gelatin degradation and a stable A/l_{660} (cm^{-1}) is obtained. The colloidal stability of biomolecule exfoliated G is scarcely reported [35]. The use of gelatin as

stabilizing agent offer advantage of low cost and convenient storage requirements as compared to other proteins like BSA, lysozymes and histone [30,31,60]. The role of gelatin in better cellular adhesion [61], makes gelatin a suitable candidate for benign approach towards direct exfoliation for biological applications.

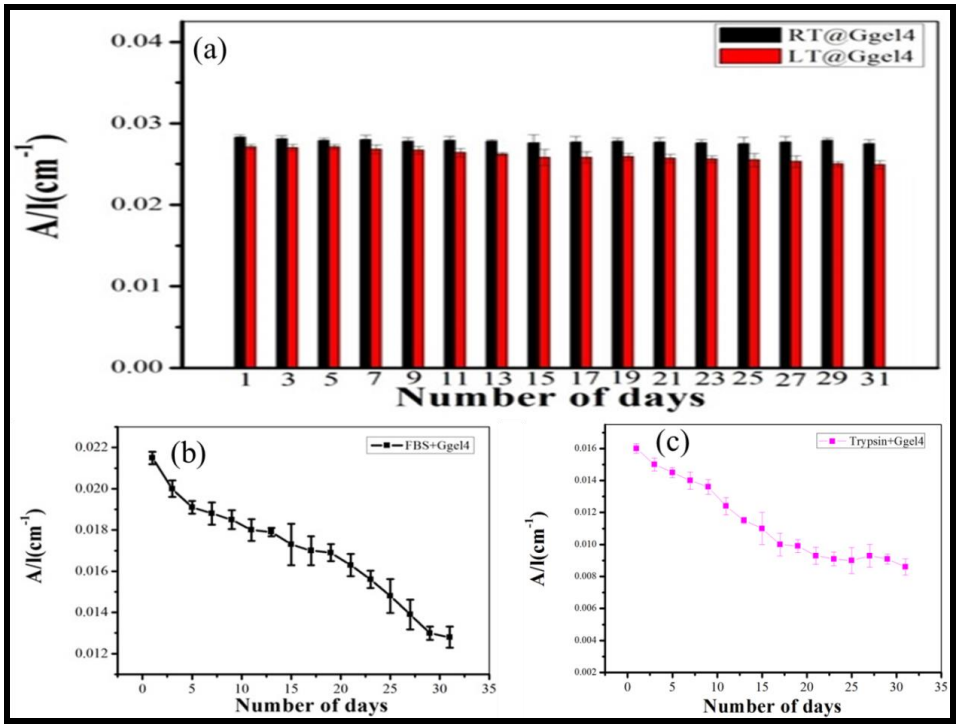

Figure 2.12. The colloidal stability of Ggel4 (a) Storage at room temperature (RT@Ggel4) and at 5^0C (LT@Ggel4), (b) With 50% (w/v) FBS and (c) trypsin.

2.2.5. Evaluation of biological potential of exfoliated G

The most crucial parameter for application of G in the area of biomedical applications is its biocompatibility hence, cyto and hemocompatibility studies were performed. The cellular viability of HeLa cells treated with Ggel4 was assessed by MTT assay [62]. The Figure **2.13a**, shows high cytocompatibility of Ggel4 even at a very high concentration of 1000 µg/mL attributed to the excellent hydrophilicity, less charged oxygen and presence of gelatin on G surface. Moreover, the presence of gelatin on G

minimizes direct contact between cells and G sheets, providing better adhesion sites with the presence of hydroxyl groups and creates a favourable surface topography which helps in the biocompatible nature as reported previously [63].

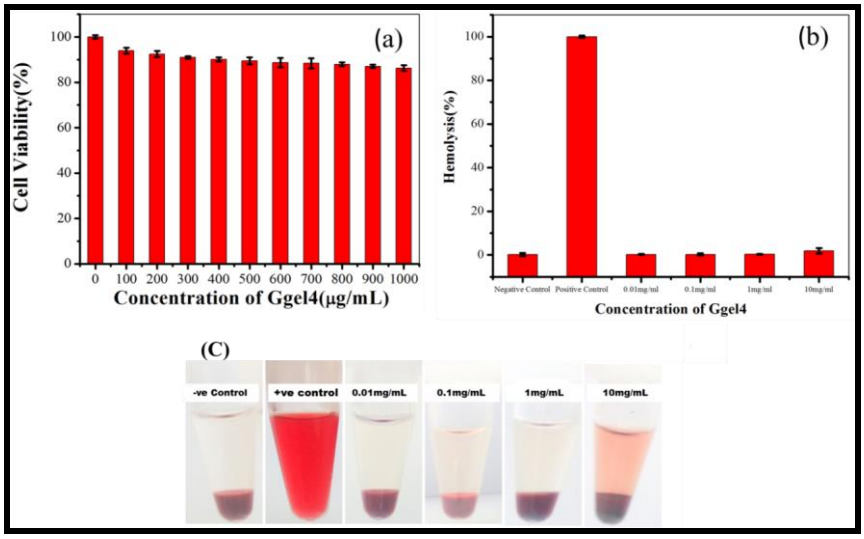

Figure 2.13. (a) Biocompatibility of Ggel4 after 24hour incubation via MTT assay (b) % hemolysis of RBCs after incubation with Ggel4 for 1 hour (c) Picture of hemolysis samples after treatment with Ggel4.

The application of materials for intravenous drug delivery systems requires them to be hemocompatible. The human RBC treated with Ggel4 in concentration range 0.01-10 mg/mL was quantified for hemolysis effect of Ggel4. The Figure **2.13b** shows that less than 2% hemolysis occurred upto 10 mg/mL which was well within the standard ASTM E2524-08 [64]. The visual appearance of treated RBC suspension is shown in Figure **2.13c**. Due to release of hemoglobin significant red colour was observed in positive control but, in rest other samples (-)ve control and Ggel4 (0.01-10 mg/mL), a colourless supernatant was observed which validates the hemocomptabile nature of Ggel4. Further, the scanning electron microscopy (SEM) was performed to check the morphology of RBCs after treatment with Ggel4. No change in cellular morphology was seen (Figure **2.14**) for the treated samples similar to control biconcave appearance. The

presence of lesser oxygen defects, suppression of cell membrane with G surface leads to less hemolysis of Ggel4 as compared to GO [65].

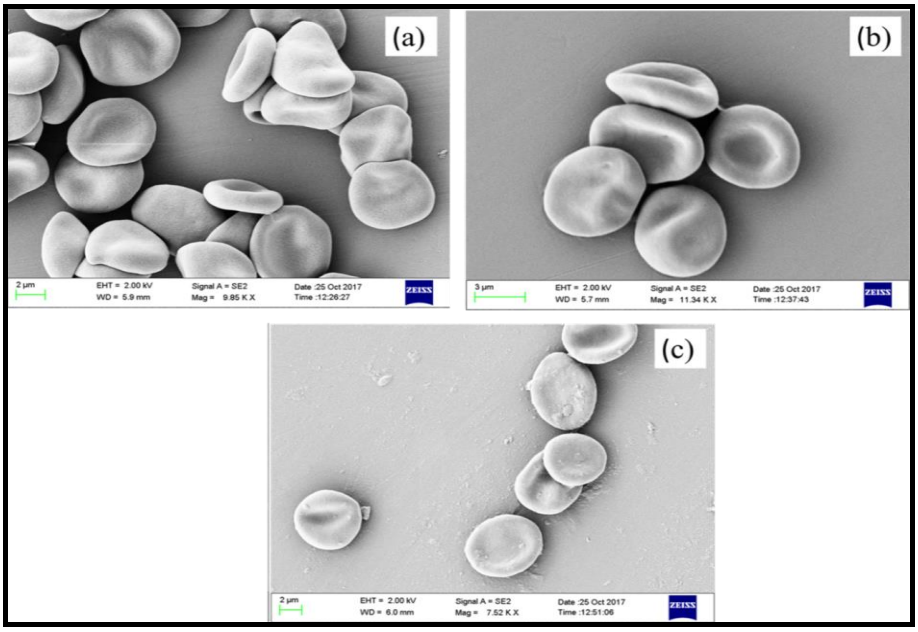

Figure 2.14 SEM images of (a) Control RBCs (b) Ggel4 (1mg/mL) with RBCs (c) Ggel4 (10mg/mL) with RBCs.

In current approach yield of 4.37 mg/mL graphene was obtained when sonication temperature was maintained at 60^{o}C and 1 mg/mL was obtained when sonication temperature was maintained at 30^{o}C. To the best of our knowledge, this is the highest yield obtained using proteins/peptides and sonication and infers the role of sonication temperature in the exfoliation (Table **2.3**).

Table 2.3. Comparison in G yields with variation in proteins and sonication condition.

Sln o	Biomolecules (Protein/Peptides)	Exfoliation condition	Concentration (mg/mL)	Applications	References
1.	HFBI	40 min Bath sonication/Tip sonication Temp= Not mentioned	0.04	-	*Angew. Chem. Int. Ed.*, 2010, 49, 4946–4949
2.	Vmh2	Probe Sonication Temp= Not mentioned	0.5	-	*Adv. Funct. Mater.*, 2015, 25, 2771–2779.
3.	BSA	48hrs Bath sonication	0.85	-	*J. Am. Chem. Soc.*, 2015, 137, 6152–6155
		Temp= Not mentioned 3hrs Probe Sonication Temp~25^{o}C	0.8	Biocompatible, Used to increase conductivity of hydrophilic hydrogels.	*Nanoscale*, 2015, 7, 6436–6443.
4.	Lysozyme	6 hrs Probe Sonication	2.09	*Anti-cancerous*	*RSC Adv.*, 2013, 4, 4085–4093
		Temp= Not mentioned 150 min Probe sonication	0.18	*Catalytic activity towards reduction of o-nitroaniline*	*Nano Res.*, 2013, 6, 693–702
5.	Calf histone	Not mentioned	Not mentioned	-	*RSC Adv.*, 2013, 4, 4085–4093
6.	Amphilic Peptides	24 hrs Bath Sonication Temp=<65^{O}C	0.03	-	*J. Mater. Chem. B*, 2015, 4, 152–161
7.	Liposomes	2 hrs Sonication Temp= Not mentioned	0.124±0.010	Anti-bacterial activities	*J. Mater. Chem. B,2015*,3,6520
8.	Gelatin	7 hrs Bath Sonication, (Gr: gel 60:40)total concentration(1gm/100mL)	4.37	Biocompatible and Hemocompatible	Present Work
		2hrs Bath Sonication, (Gr: gel 60:40)total concentration(6gm/100mL)	4.14		Present Work

2.3. Conclusion

High quality liquid phase exfoliated G with minimum defects has ample applications especially in the areas of biomedical and electronic industries. The biomedical applications of G requires aqueous solubility, stability and

biocompatibility, which is a known bottleneck for chemically exfoliated G. Various biomolecules like proteins, peptides were explored as exfoliating agent and as modifiers. Ultrasonic cavitation is the basic technique used so far to directly exfoliate G. Recently; Kim et al [34] explored effect of temperature on exfoliation process from ultrasonication. However, role of temperature increment in exfoliation process is still in very infant stage.

In this report exciting possibilities of combining synergistic effect of high temperature sonication and biopolymers like gelatin were explored for scalable G having lower defect and better solubility. Further, inherent heat generation from sonication bath was applied in the exfoliation process. The present exfoliation methods yields 4.37 mg/mL G which is highest till date with direct exfoliation using proteins and ultrasonication and have potential of scaling up. Gelatin plays two major roles in the exfoliation process: (i). Facilitating the exfoliation by lowering the surface tension of water-gel system (ii). Through favourable interaction towards G, gel stabilizes G and prevents them from aggregation. The exfoliated G shows better stability irrespective of temperature. Moreover, lesser defects and higher aqueous solubility provides bio and hemocompatibility to bioinspired G. This simple one-step exfoliation method utilizes low-cost, environment friendly sustainable exfoliant for exfoliating graphite to graphene. This improved synthetic route will help in easy functionalization of graphene and will remould its biomedical application.

2.4. Experimental section

2.4.1. Materials

Gr powder, Gelatin (Type B) from Thermo-fisher was used without further purification. Fetal bovine serum (FBS), 0.25% trypsin-EDTA solution, 3(4,5-dimethylthylazol-2-yl)-2,5-diphenyl tetrazolium bromide (MTT), Minimum essential medium (MEM) high media.

2.4.2. Gr Exfoliation

Initially gelatin powder was dissolved in DI water by providing magnetic stirring and temperature 50^{o}C. Then Gr powders were added in that gelatin solution. Then whole sample was applied for bath sonication prepares G dispersion. After that G dispersion was centrifuged at 4000 rpm for 15 minutes and stable exfoliated G dispersion were isolated from settled Gr powder. Further exfoliation parameters were varied like sonication temperatures, Gr: gelatin ratio in solution, total particle in solution and time in different experiments for maximum G yield. A/l_{660} (cm^{-1}) value was measured at 660 nm. A/l_{660} (cm^{-1}) value depends upon size, number of layers and functionalization of G exfoliated. The effect of Gr to gelatin ratio and pH on A/l_{660} (cm^{-1}) value was studied after 7 hrs of sonication whereas effect of exfoliation condition and effect of total weight concentration (Gr+gelatin) on A/l_{660} (cm^{-1}) value was studied after 2 hrs of sonication. All the experiments were performed in three trails.

2.4.3. Characterizations

G exfoliation was performed on bath sonicator. The Uv-vis spectroscopy was performed using Agilent Cary 60 UV-Visible spectrophotometer. Surface tension measurement was performed using Dynamic surface tensiometer purchased from Sensa dyne. The measurement was performed using “maximum bubble pressure method” at 24^{o}C. The hydrodynamic diameter, polydispersity index and zeta potential measurement was performed on Micromeritics Nanoplus 3 setup. The fluorescence measurement was performed using Fluoromax spectrofluorometer. The

fluorescence life time decay experiment was performed using TCSPC system from Horiba (Model: Fluorocube-01-NL). Samples were excited using picosecond diode laser having wavelength 280 nm (Model: Pico Brite-375L) having repetition rate 5MHz. The signals were collected at magic angle (54.70) on detector (TBX-07C). For our instrument response function was 150ps. IBH DAS software (version6, HORIBA, scientific Edison, NJ) was used for decay analysis. LabRAM HR (UV System) was used for raman measurement. 514 nm laser source was used for the measurement. Statistical analysis for number of layers ($<N_G>$) using equation [35]. PXRD was performed on Rigaku smart Lab X-ray diffractometer with wavelength (1.54 A).TEM images were analysed using TEM of maker PHILIPS with model- CM200 and operating voltages- 20-200 kV. Diluted sample were sonicated and then put on carbon coated copper grid and was vacuum dried before investigation. For determining secondary structure of gelatin with and without exfoliation circular dichroism (CD) spectra was performed using JASCO J-815CD spectropolarimeter. Samples were put in quartz cells of 1mm path length. Scans were performed with slit width 1mm and speed of 20 nm/min.

2.4.4. Biocompatibility and Hemocompatibility study of Ggel4

The biocompatibility study of Ggel4 was performed on HeLa cells, using MTT assay. Cells were seeded in 96 well plates, MEM media, 10% fetal bovine serum FBS and 1% penicillin streptomycin were used as nutrient media. For 24 hours cells were incubated with 5% CO_2 and at 37^{o}C with humid environment. Varying concentration of Ggel4 (100-1000) µg/mL were treated for 24 hours with the cells. After that, media containing Ggel4 were replaced with MEM media containing 3-(4,5-Dimethylthiazol-2-Yl)-2,5-Diphenyltetrazolium Bromide (MTT) (0.5mg/mL) and further incubated for four hours. After incubation MTT containing media were replaced with DMSO and plate was read under plate reader. Absorbance value was noted on Synergy H1 Biotek microplate reader. For hemocompatibility study of, Ggel4 were incubated with varying

concentration (0.01, 0.1,1 and 10) mg/mL in 1X PBS with fresh RBCs. Using TritonX100 (PBS) positive control was prepared and treating RBCs with 1X PBS negative control was prepared. The incubation time was for 1 hour. After that treated blood were centrifuged for 10 min at 1000Xg and absorbance of collected supernatant were taken at 540 nm in a plate reader. In order to study morphological changes in RBCs, treated RBCs pellet were fixed with 4% glutaraldehyde and dehydrated with serial dehydration using ethanol (30%, 50%, 70%, 100% v/v). After that samples were coated with gold using sputtering and imaged under scanning electron microscope. Scanning electron microscope study was performed on Carl Zeiss Supra 55 FE-SEM. From Institute Human Ethics Committee (IHEC), IIT Indore prior approval was taken for studying hemocompatibility. Standard procedure was followed from the guidelines of Indian Council of Medical Research (ICMR, New Delhi).

2.5. References

[1] K. I. Bolotin, K. J. Sikes, Z. Jiang, M. Klima, G. Fudenberg, J. Hone, P. Kim H. L. Stormer (2008), Ultrahigh electron mobility in suspended graphene, Solid State Commun., 146, 351–355 (DOI: https://doi.org/10.1016/j.ssc.2008.02.024)

[2] S. Stankovich, D. A. Dikin, G. H. B. Dommett, K. M. Kohlhaas, E. J. Zimney, E. A. Stach, R. D. Piner, S. T. Nguyen, R. S. Ruoff (2006), Graphene-based composite materials, Nature., 442, 282–286 (DOI: https://doi.org/10.1038/nature04969)

[3] A. K. Geim, K. S. Novoselov (2007), The rise of graphene, Nat. Mater., 6, 183–191 (DOI: https://doi.org/10.1038/nmat1849)

[4] H. Y. Mao, S. Laurent, W. Chen, O. Akhavan, M. Imani, A. A. Ashkarran, M. Mahmoudi (2013), Graphene: Promises, Facts, Opportunities, and Challenges in Nanomedicine, Chem. Rev.,113, 3407–3424 (DOI: https://doi.org/10.1021/cr300335p)

[5] W. Yang, K. R. Ratinac, S. P. Ringer, P. Thordarson, J. J. Gooding F. Braet (2010), Carbon Nanomaterials in Biosensors: Should You Use Nanotubes or Graphene?, Angew. Chem. Int. Ed., 49, 2114–2138 (DOI: https://doi.org/10.1002/anie.200903463)

[6] J. R. Potts, D. R. Dreyer, C. W. Bielawski, R. S. Ruoff (2011), Graphene-based polymer nanocomposites, Polymer., 52, 5–25 (DOI: https://doi.org/10.1016/j.polymer.2010.11.042)

[7] X. Zhang, P. Samorì (2017), Graphene/Polymer Nanocomposites for Supercapacitors, ChemNanoMat., 3, 362–372 (DOI:https://doi.org/10.1002/cnma.201700055)

[8] Feng Lingyan, Wu Li, Qu Xiaogang (2012), New Horizons for Diagnostics and Therapeutic Applications of Graphene and Graphene Oxide, Adv. Mater., 25, 168–186 (DOI:https://doi.org/10.1002/adma.201203229)

[9] H. Ji, H. Sun, X. Qu (2016), Antibacterial applications of graphene-based nanomaterials: Recent achievements and challenges, Adv. Drug Deliv. Rev., 105, 176–189 (DOI: https://doi.org/10.1016/j.addr.2016.04.009)

[10] V. Sharma, S. M. Mobin (2017), Cytocompatible peroxidase mimic CuO:graphene nanosphere composite as colorimetric dual sensor for hydrogen peroxide and cholesterol with its logic gate implementation., Sens. Actuators B Chem., 240, 338–348 (DOI: https://doi.org/10.1016/j.snb.2016.08.169)

[11] P. W. Sutter, J.-I. Flege, E. A. Sutter (2008), Epitaxial graphene on ruthenium, Nat. Mater.,7, 406–411 (DOI: https://doi.org/10.1038/nmat2166)

[12] X. Li, L. Colombo, R. S. Ruoff (2016), Synthesis of Graphene Films on Copper Foils by Chemical Vapor Deposition, Adv. Mater., 28, 6247–6252 (DOI: https://doi.org/10.1002/adma.201504760)

[13] B. Jayasena, S. Subbiah (2011), A novel mechanical cleavage method for synthesizing few-layer graphenes, Nanoscale Res. Lett., 6, 95(DOI: https://doi.org/10.1186/1556-276X-6-95)

[14] H. Tao, Y. Zhang, Y. Gao, Z. Sun, C. Y, J. Texter (2017), Scalable exfoliation and dispersion of two-dimensional materials – an update, Phys. Chem. Chem. Phys., 19, 921–960 (DOI: https://doi.org/10.1039/C6CP06813H)

[15] S. Park, R. S. Ruoff (2010), Chemical methods for the production of graphenes, Nat. Nanotechnol., 5, 309–309 (DOI: https://doi.org/10.1038/nnano.2009.58)

[16] A. R. Kamali (2016), Eco-friendly production of high quality low cost graphene and its application in lithium ion batteries, Green Chem., 18, 1952–1964 (DOI: https://doi.org/10.1039/C5GC02455B)

[17] W. Du, X. Jiang, L. Zhu (2013), From graphite to graphene: direct liquid-phase exfoliation of graphite to produce single- and few-layered pristine graphene, J. Mater. Chem. A., 1, 10592–10606 (DOI: https://doi.org/10.1039/C3TA12212C)

[18] M. Buzaglo, M. Shtein, S. Kober, R. Lovrinčić, A. Vilan, O. Regev (2013), Critical parameters in exfoliating graphite into graphene, Phys. Chem. Chem. Phys., 15, 4428–4435 (DOI: https://doi.org/10.1039/C3CP43205J)

[19] Y. Hernandez, V. Nicolosi, M. Lotya, F. M. Blighe, Z. Sun, S. De, I. T. McGovern, B. Holland, M. Byrne, Y. K. Gun'Ko, J. J. Boland, P. Niraj, G. Duesberg, S. Krishnamurthy, R. Goodhue, J. Hutchison, V. Scardaci, A. C. Ferrari, J. N. Coleman (2008), High-yield production of graphene by liquid-phase exfoliation of graphite, Nat. Nanotechnol., 3, 563–568 (DOI: https://doi.org/10.1038/nnano.2008.215)

[20] C. E. Hamilton, J. R. Lomeda, Z. Sun, J. M. Tour, A. R. Barron (2009), High-Yield Organic Dispersions of Unfunctionalized Graphene, Nano Lett., 9, 3460–3462 (DOI: https://doi.org/10.1021/nl9016623)

[21] M. P. Lavin-Lopez, J. L. Valverde, L. Sanchez-Silva, A. Romero (2016), Solvent-Based Exfoliation via Sonication of Graphitic Materials for Graphene Manufacture, Ind. Eng. Chem. Res., 55, 845–855 (DOI: https://doi.org/10.1021/acs.iecr.5b03502)

[22] L. Dong, Z. Chen, X. Zhao, J. Ma, S. Lin, M. Li, Y. Bao, L. Chu, K. Leng, H. Lu, K. P. Loh (2018), A non-dispersion strategy for large-scale production of ultra-high concentration graphene slurries in water., Nat. Commun., 9, 76 (DOI: https://doi.org/10.1038/s41467-017-02580-3)

[23] E. Satheeshkumar, A. Bandyopadhyay, M. B. Sreedhara, S. K. Pati, C. N. R. Rao, M. Yoshimura (2017), One-Step Simultaneous Exfoliation and Covalent Functionalization of MoS2 by Amino Acid Induced Solution Processes, ChemNanoMat., 3, 172–177

(DOI: https://doi.org/10.1002/cnma.201600363)
[24] Y. Zhang, J. Tian, H. Li, L. Wang, X. Qin, A. M. Asiri, A. O. Al-Youbi, X. Sun (2012), Biomolecule-Assisted, Environmentally Friendly, One-Pot Synthesis of CuS/Reduced Graphene Oxide Nanocomposites with Enhanced Photocatalytic Performance, Langmuir., 28, 12893–12900
(DOI: https://doi.org/10.1021/la303049w)
[25] F. Emadi, A. Amini, A. Gholami, Y. Ghasemi (2017), Functionalized Graphene Oxide with Chitosan for Protein Nanocarriers to Protect against Enzymatic Cleavage and Retain Collagenase Activity, Sci. Rep.,7, srep42258 (DOI: https://doi.org/10.1038/srep42258)
[26] L. Niu, J. N. Coleman, H. Zhang, H. Shin, M. Chhowalla, Z. Zheng (2016), Production of Two-Dimensional Nanomaterials via Liquid-Based Direct Exfoliation, Small., 12, 272–293
(DOI: https://doi.org/10.1002/smll.201502207)
[27] P. Laaksonen, M. Kainlauri, T. Laaksonen, A. Shchepetov, H. Jiang, J. Ahopelto, M. B. Linder (2010), Interfacial Engineering by Proteins: Exfoliation and Functionalization of Graphene by Hydrophobins, Angew. Chem. Int. Ed., 49, 4946–4949
(DOI: https://doi.org/10.1002/anie.201001806)
[28] J. Tao, Y. Wang, Y. Xiao, P. Yao, C. Chen, D. Zhang, W. Pang, H. Yang, D. Sun, Z. Wang, J. Liu (2017), One-step exfoliation and functionalization of graphene by hydrophobin for high performance water molecular sensing, Carbon., 116, 695–702
(DOI: https://doi.org/10.1016/j.carbon.2017.02.052)
[29] D. Joseph, N. Tyagi, A. Ghimire, K. E. Geckeler (2013), A direct route towards preparing pH-sensitive graphene nanosheets with anti-cancer activity, RSC Adv., 4, 4085–4093
(DOI: https://doi.org/10.1039/C3RA45984E)
[30] K. Qu, L. Wu, J. Ren, X. Qu (2013), Enzyme-directed pH-responsive exfoliation and dispersion of graphene and its decoration by gold nanoparticles for use as a hybrid catalyst, Nano Res., 6, 693–702 (DOI: https://doi.org/10.1007/s12274-013-0345-3)
[31] S. Ahadian, M. Estili, V. J. Surya, J. Ramón-Azcón, X. Liang, H. Shiku, M. Ramalingam, T. Matsue, Y. Sakka, H. Bae, K. Nakajima, Y. Kawazoe, A. Khademhosseini (2015), Facile and green production of aqueous graphene dispersions for biomedical applications, Nanoscale., 7, 6436–6443
(DOI: https://doi.org/10.1039/C4NR07569B)
[32] G. Guan, S. Zhang, S. Liu, Y. Cai, M. Low, C. P. Teng, I. Y. Phang, Y. Cheng, K. L. Duei, B. M. Srinivasan, Y. Zheng, Y.-W. Zhang, M.-Y. Han (2015), Protein Induces Layer-by-Layer Exfoliation of Transition Metal Dichalcogenides, J. Am. Chem. Soc., 137, 6152–6155 (DOI: https://doi.org/10.1021/jacs.5b02780)

[33] Y. Ge, J. Wang, Z. Shi, J. Yin (2012), Gelatin-assisted fabrication of water-dispersible graphene and its inorganic analogues, J. Mater. Chem., 22, 17619–17624 (DOI: https://doi.org/10.1039/C2JM33173J)

[34] J. Kim, S. Kwon, D.-H. Cho, B. Kang, H. Kwon, Y. Kim, S. O. Park, G. Y. Jung, E. Shin, W.-G. Kim, H. Lee, G. H. Ryu, M. Choi, T. H. Kim, J. Oh, S. Park, S. K. Kwak, S. W. Yoon, D. Byun, Z. Lee, C. Lee (2015), Direct exfoliation and dispersion of two-dimensional materials in pure water via temperature control, Nat. Commun., 6, ncomms9294 (DOI: https://doi.org/10.1038/ncomms9294)

[35] A. Pattammattel, C. V. Kumar (2015), Kitchen Chemistry 101: Multigram Production of High Quality Biographene in a Blender with Edible Proteins, Adv. Funct. Mater., 25, 7088–7098 (DOI: https://doi.org/10.1002/adfm.201503247)

[36] M. Cao, N. Wang, L. Wang, Y. Zhang, Y. Chen, Z. Xie, Z. Li, E. Pambou, R. Li, C. Chen, F. Pan, H. Xu, J. Penny, J. R. P. Webster, J. R. Lu (2015), Direct exfoliation of graphite into graphene in aqueous solutions of amphiphilic peptides, J. Mater. Chem. B., 4, 152–161 (DOI: https://doi.org/10.1039/C5TB02065D)

[37] W. Liu, R. Zhou, D. Zhou, G. Ding, J. M. Soah, C. Y. Yue, X. Lu (2015), Lignin-assisted direct exfoliation of graphite to graphene in aqueous media and its application in polymer composites, Carbon., 83, 188–197 (DOI: https://doi.org/10.1016/j.carbon.2014.11.036)

[38] A. M. Gravagnuolo, E. Morales-Narváez, S. Longobardi, E. T. da Silva, P. Giardina, A. Merkoçi (2015), In Situ Production of Biofunctionalized Few-Layer Defect-Free Microsheets of Graphene, Adv. Funct. Mater., 25, 2771–2779 (DOI: https://doi.org/10.1002/adfm.201500016)

[39] R. Zappacosta, M. D. Giulio, V. Ettorre, D. Bosco, C. Hadad, G. Siani, S. D. Bartolomeo, A. Cataldi, L. Cellini, A. Fontana (2015), Liposome-induced exfoliation of graphite to few-layer graphene dispersion with antibacterial activity, J. Mater. Chem. B., 3, 6520–6527 (DOI: https://doi.org/10.1039/C5TB00798D)

[40] D. Joseph, S. Seo, D. R. Williams, Kurt E. Geckeler (2014), Double-Stranded DNA-Graphene Hybrid: Preparation and Anti-Proliferative Activity, ACS Appl. Mater. Interfaces., 6,5, 3347-3356 (DOI: https://doi.org/10.1021/am405378x)

[41] K.-H. Liao, Y.-S. Lin, C. W. Macosko, C. L. Haynes (2011), Cytotoxicity of Graphene Oxide and Graphene in Human Erythrocytes and Skin Fibroblasts, ACS Appl. Mater. Interfaces., 3, 2607–2615 (DOI: https://doi.org/10.1021/am200428v)

[42] G. Reina, J. M. González-Domínguez, A. Criado, E. Vázquez, A. Bianco, M. Prato (2017), Promises, facts and challenges for graphene in biomedical applications, Chem. Soc. Rev., 46, 4400–4416 (DOI: https://doi.org/10.1039/C7CS00363C)

[43] S. Pattnaik, K. Swain, Z. Lin (2016), Graphene and graphene-based nanocomposites: biomedical applications and biosafety, J. Mater. Chem. B., 4, 7813–7831 (DOI: https://doi.org/10.1039/C6TB02086K)

[44] L. Wu, H. Ji, Y. Guan, X. Ran, J. Ren, X. Qu (2017), A graphene-based chemical nose/tongue approach for the identification of normal, cancerous and circulating tumor cells, NPG Asia Mater., 9, e356 (DOI: https://doi.org/10.1038/am.2017.11)

[45] Global Gelatin Market Projected to Reach $2.79 Billion in 2018, https://www.nutraceuticalsworld.com/contents/view_breaking-news/2013-07-15/global-gelatin-market-projected-to-reach-279-billion-in-2018/, (accessed February 28, 2018).

[46] K. Liu, J.-J. Zhang, F.-F. Cheng, T.-T. Zheng, C. Wang, J.-J. Zhu (2011), Green and facile synthesis of highly biocompatible graphene nanosheets and its application for cellular imaging and drug delivery, J. Mater. Chem., 21, 12034–12040 (DOI: https://doi.org/10.1039/C1JM10749F)

[47] M. Lian, J. Fan, Z. Shi, S. Zhang, H. Li, J. Yin (2015), Gelatin-assisted fabrication of graphene-based nacre with high strength, toughness, and electrical conductivity, Carbon, 89, 279–289 (DOI: https://doi.org/10.1016/j.carbon.2015.03.045)

[48] M. Zeng, S. A. Shah, D. Huang, D. Parviz, Y.-H. Yu, X. Wang, M. J. Green, Z. Cheng (2017), Aqueous Exfoliation of Graphite into Graphene Assisted by Sulfonyl Graphene Quantum Dots for Photonic Crystal Applications, ACS Appl. Mater. Interfaces., 9,36, 30797-30804 (DOI: https://doi.org/10.1021/acsami.7b06980)

[49] K. S. Suslick, D. A. Hammerton, R. E. Cline (1986), Sonochemical hot spot, J. Am. Chem. Soc., 108, 5641–5642 (DOI: https://doi.org/10.1021/ja00278a055)

[50] S. Bhattacharya, S. Mishra, P. Gupta, Pranav, M. Ghosh, A. Kumar Pramanick, D. Prasad Mishra, S. Nayar (2015), Liquid phase collagen modified graphene that induces apoptosis, RSC Adv., 5, 44447–44457 (DOI: https://doi.org/10.1039/C5RA06629H)

[51] A. V. Alaferdov, A. Gholamipour-Shirazi, M. A. Canesqui, Y. A. Danilov, S. A. Moshkalev (2014), Size-controlled synthesis of graphite nanoflakes and multi-layer graphene by liquid phase exfoliation of natural graphite, Carbon, 69, 525–535 (DOI: https://doi.org/10.1016/j.carbon.2013.12.062)

[52] H. Yu, B. Zhang, C. Bulin, R. Li, R. Xing (2016), High-efficient Synthesis of Graphene Oxide Based on Improved Hummers Method, Sci. Rep., 6, 36143 (DOI: https://doi.org/10.1038/srep36143)

[53] K. Savaram, M. Kalyanikar, M. Patel, R. Brukh, C. R. Flach, R. Huang, M. R. Khoshi, R. Mendelsohn, A. Wang, E. Garfunkel, H. He (2015), Synergy of oxygen and a piranha solution for eco-

friendly production of highly conductive graphene dispersions, Green Chem., 17, 869–881
(DOI: https://doi.org/10.1039/C4GC01752H)

[54] A. A. Green, M. C. Hersam (2009), Solution Phase Production of Graphene with Controlled Thickness via Density Differentiation, Nano Lett., 9, 4031–4036
(DOI: https://doi.org/10.1021/nl902200b)

[55] D. Liu, W. Lei, Y. Chen (2015), Scalable production of wrinkled and few-layered graphene sheets and their use for oil and organic solvent absorption, Phys. Chem. Chem. Phys., 17, 6913–6918
(DOI: https://doi.org/10.1039/C4CP05864J)

[56] S. Sampath, A. N. Basuray, K. J. Hartlieb, T. Aytun, S. I. Stupp, J. F. Stoddart (2013), Direct Exfoliation of Graphite to Graphene in Aqueous Media with Diazaperopyrenium Dications, Adv. Mater., 25, 2740–2745 (DOI: https://doi.org/10.1002/adma.201205157)

[57] S. Li, A. N. Aphale, I. G. Macwan, P. K. Patra, W. G. Gonzalez, J. Miksovska, R. M. Leblanc (2012), Graphene Oxide as a Quencher for Fluorescent Assay of Amino Acids, Peptides, and Proteins, ACS Appl. Mater. Interfaces., 4, 7069–7075
(DOI: https://doi.org/10.1021/am302704a)

[58] G. Liu, H. Qin, T. Amano, T. Murakami, N. Komatsu (2015), Direct Fabrication of the Graphene-Based Composite for Cancer Phototherapy through Graphite Exfoliation with a Photosensitizer, ACS Appl. Mater. Interfaces., 7,42, 23402-23406
(DOI: https://doi.org/10.1021/acsami.5b07432)

[59] M. Lotya, A. Rakovich, J. F. Donegan, J. N. Coleman (2013), Measuring the lateral size of liquid-exfoliated nanosheets with dynamic light scattering, Nanotechnology., 24, 265703
(DOI: https://doi.org/10.1088/0957-4484/24/26/265703)

[60] D. Joseph, N. Tyagi, A. Ghimire, K. E. Geckeler (2013), A direct route towards preparing pH-sensitive graphene nanosheets with anti-cancer activity, RSC Adv., 4, 4085–4093
(DOI: https://doi.org/10.1039/C3RA45984E)

[61] M. Kan, Y. Minamoto, S. Sunami, I. Yamam, M. Umeda (1982), The Effects on Cell Adhesion of Fibronectin and Gelatin in a Serum-Free, Bovine Serum Albumin Medium, Cell Struct. Funct., 7, 245–252 (DOI: https://doi.org/10.1247/csf.7.245)

[62] J. Carmichael, W. G. DeGraff, A. F. Gazdar, J. D. Minna, J. B. Mitchell (1987), Evaluation of a Tetrazolium-based Semiautomated Colorimetric Assay: Assessment of Chemosensitivity Testing, Cancer Res., 47, 936–942

[63] A. M. Pinto, I. C. Gonçalves, F. D. Magalhães (2013), Graphene-based materials biocompatibility: A review, *Colloids Surf. B Biointerfaces.*, 111, 188–202
(DOI: https://doi.org/10.1016/j.colsurfb.2013.05.022)

[64] M. Das Purkayastha, A. K. Manhar, V. K. Das, A. Borah, M. Mandal, A. J. Thakur, C. L. Mahanta (2014), Antioxidative, Hemocompatible, Fluorescent Carbon Nanodots from an "End-of-Pipe" Agricultural Waste: Exploring Its New Horizon in the Food-Packaging Domain., J. Agric. Food Chem., 62, 4509–4520 (DOI: https://doi.org/10.1021/jf500138f)

[65] B. Cai, K. Hu, C. Li, J. Jin, Y. Hu (2015), Bovine serum albumin bioconjugated graphene oxide: Red blood cell adhesion and hemolysis studied by QCM-D, Appl. Surf. Sci., 356, 844–851 (DOI: https://doi.org/10.1016/j.apsusc.2015.08.178)

CHAPTER 3

Insight into Protein Corona formation with Gelatin stabilized Graphene: Impact of Flake size, Incubation time and Concentration

3.1. Introduction

In recent year's significant interest have been given for understanding the influence of nanomaterial interactions with biomolecules and living systems [1–3]. Among various nanomaterials, graphene (G) and its derivative have gained significant attention as well as expectations in the areas of nanobiotechnology and biomedical engineering owing to its attractive properties [4–6]. The distinctive surface morphology, size, shape, surface functionalization of G offers different types of interactions with biomolecules and cells which leads to variation in cellular processing machinery [7–9]. When G and its derivative makes contact with biological media i.e. serum or plasma proteins, the surface of G induces an exchanging layer with these proteins and forms a biomolecular corona around the nanoflakes [10,11]. Because of these corona formations, the protein acts very critically in the early stages of biological interactions. Due to these protein corona formations the original surface attributes of G and their derivatives gets changed and for our biological entities, these changed G surfaces become the original surface and ultimately explored as first information center towards biological responses [12,13]. Because of this change, the *invivo* fate of G and their derivatives becomes very complicated and nullifies the role of initial designing and synthesis. Thus a significant portion of G and its derivatives for biomedical applications is based on molecular interaction that occurs between proteins and G sheets. As we know that proteins plays a very prominent role during various biological functions thus becomes one of the fundamental elements of the

physiological system. The molecular interactions between proteins and G sheets depend upon the surface charge, surface energy and degree of hydrophobicity so the whole biological responses from these G sheets comes a lot from the outcome of these molecular interactions. In earlier reports different surface bound proteins used for enhancing cellular uptakes and ultimately activates the intracellular signalling pathways [14,15]. Thus a comprehensive investigation on G nanoflakes- proteins interactions is out most important for establishing the effect of G sheets on the structure and physiological activities of proteins. Apart from protein interactions G sheets lateral size also plays a very prominent role in cellular toxicity. Marzi *et al* [16] discussed size dependent high genotoxic response on various cell lines with graphene oxide flakes and they conclude that flake size with size greater than 100 nm exhibited the highest genotoxic. Although reports about biocompatibility with graphene based material focused mainly with graphene oxide system only, however no detailed investigation between the flake sizes with biological responses were investigated. The earlier work on protein interactions and cellular toxicity were focused on "graphene oxide" [17–19]. The graphene oxide has limitations because of very high oxidative defects, safety related issues and toxicity thus direct exfoliation method came into existence to bypass the drawbacks of the existing method [20]. In the present work different lateral sized graphene (Ggel) was exfoliated using gelatin as an exfoliating agent along with high power sonicating forces [21]. Gelatin is a biopolymer synthesized by hydrolyzing collagen. Also, gelatin having worldwide production of around 3.75-4.00 lakhs tonnes every year makes it a sustainable source that too at low cost [22]. Gelatin provides advantages in terms of non-toxicity, commercial availability, biodegradability, phenomenal similarity with proteins. Also, it's very strong affinity towards graphene oxide/ G makes gelatin a perfect material for having stable colloidal dispersion of G sheets [23,24]. The protein interaction investigation was performed on bovine serum protein (BSA)

and fetal bovine serum (FBS) with varying lateral sizes of exfoliated sheets. Also the cell viability and hemocompatibility studies were performed with different lateral sized exfoliated sheets. The study was conducted with different incubation time and concentration. The present work provides information about molecular interactions, protein adsorption, corona formation between serum proteins and directly exfoliated graphene as well as size and concentration dependent toxicity studies. This work offers an insight for guiding directly exfoliated graphene for different biomedical applications.

3.2. Results and discussion

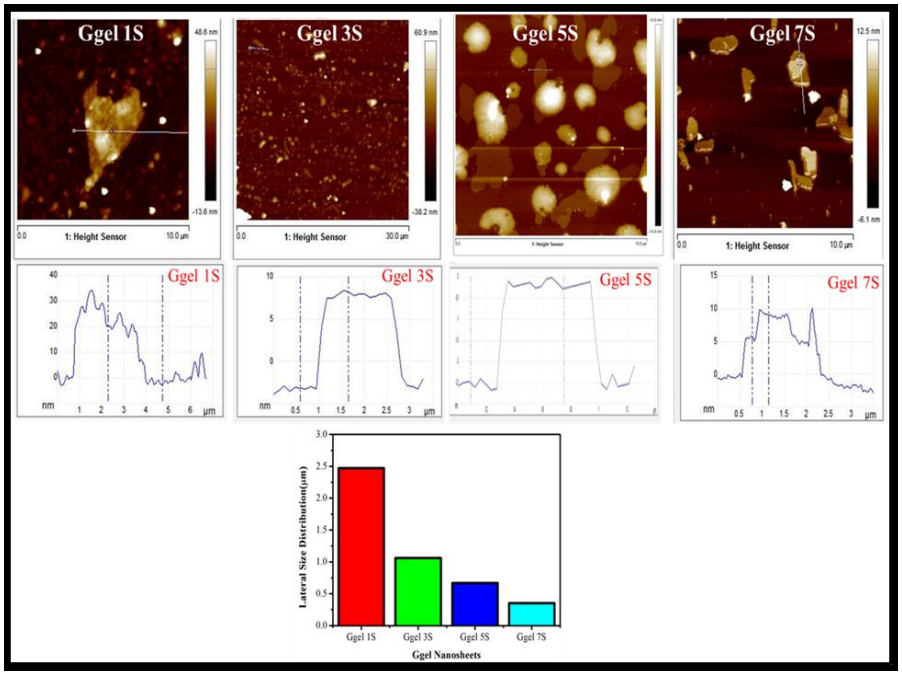

Figure 3.1. Lateral size and surface morphology of Ggel nanosheets.

The variation in the lateral size distribution of as prepared Ggel nanosheets were characterized using atomic force microscopy (Figure **3.1**). All Ggel nanosheets exhibited irregular morphologies. It must be mentioned here that exfoliation was performed as per earlier synthesized protocol [21] and to get different lateral size of nanosheets sonication time was varied i.e. for

Ggel1S, 3S, 5S and 7S sonication time was 1,3,5 and 7 h respectively. It is noteworthy that high shear forces and the stabilizing agents are needed for an efficient exfoliation. Further, as per an earlier report ultrasonication process doesn't inflict any variation in surface chemical properties with exfoliated sheets and only responsible for lateral size variation [25]. The lateral size of Ggel nanosheets were evaluated around 100 nanosheets. The lateral size for Ggel 1S, 3S, 5S and 7S was 2.47, 1.06, 0.667 and 0.355 µm respectively. Thus it is evident that all Ggel nanosheets possess significantly different lateral size with maximum size was obtained with minimum sonication time i.e. Ggel1S and minimum lateral size was obtained with maximum sonication time i.e. Ggel7S. This type of variation in lateral size was consistent with earlier reports [17,21]. Similar variation in lateral size with sonication time was supported from hydrodynamic diameter (D_H) variation with Ggel nanosheets subjected to different sonication time as shown in Figure **3.2.** The D_H value of Ggel1S, 3S, 5S and 7S was 639.8, 577.1, 404.9 and 248.3 nm respectively. Furthermore, the negative zeta potential values for all Ggel nanosheets confirm the presence of gelatin on exfoliated sheets.

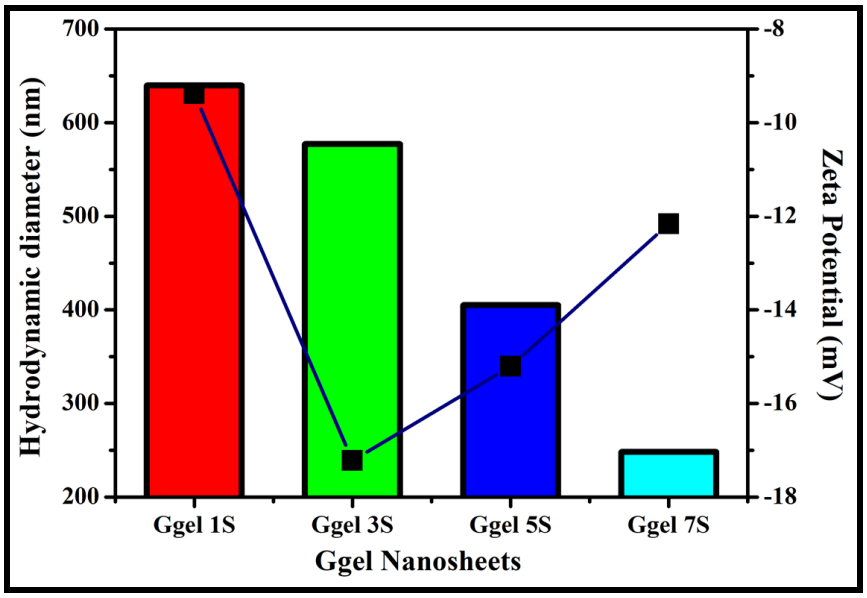

Figure 3.2. Hydrodynamic diameter and zeta potential values of Ggel nanosheets.

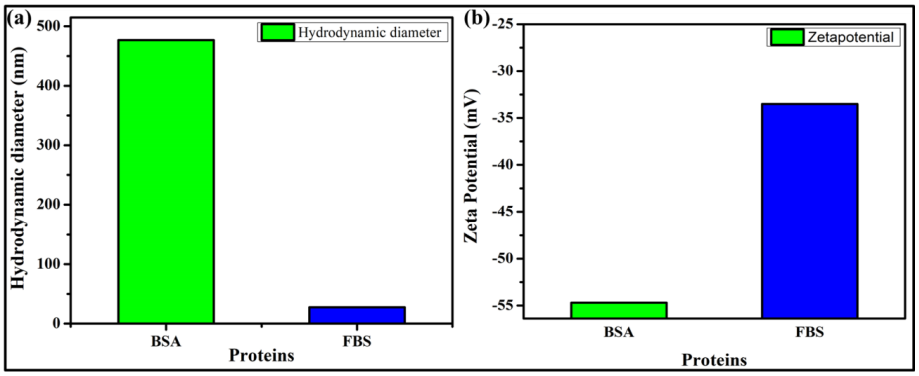

Figure 3.3. (a) Hydrodynamic diameter (b) Zeta potential of BSA and FBS.

The D_H value of BSA and FBS was 476.8 and 27.6 nm respectively as shown in Figure **3.3a** also both BSA and FBS showed negative zeta potential value i.e. -54.69 and -33.5 mV respectively shown in Figure **3.3b.**

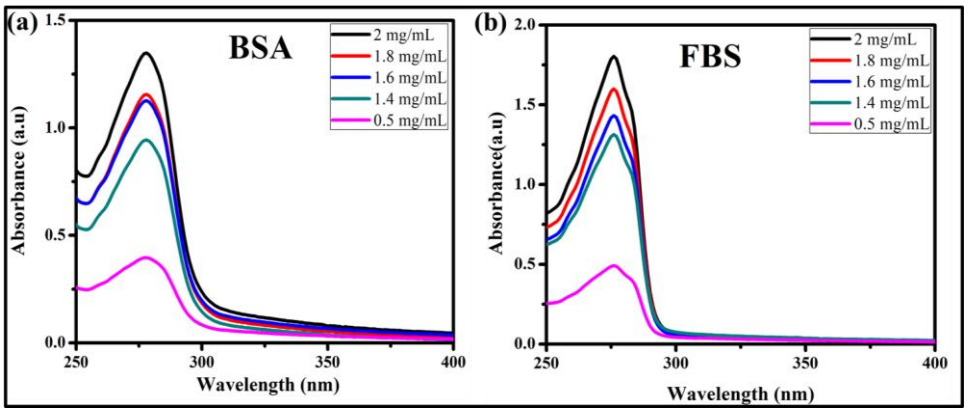

Figure 3.4. *UV-Vis* spectra of (a) BSA (b) FBS.

Similarly, both BSA and FBS exhibited signature absorbance peak at 280 nm arising from aromatic amino acid residue through π-π interactions. The free absorbance at different concentrations ranging from 2 mg/mL to 0.5 mg/mL was recorded in the wavelength range 250 to 400 nm (shown in Figure **3.4a-b**) and the concentration profile was plotted at absorbance 280 nm to measure the free absorbance prior to adsorption studies. Now to study and compare the ability of BSA and FBS adsorption on Ggel nanosheets their amount of protein adsorption was quantified. The protein concentration was fixed with 2 mg/mL and incubation time of 1 h however the concentration of Ggel nanosheets were varied i.e. 50, 100 and 200 µg/mL and results were summarized in Figure **3.5.**

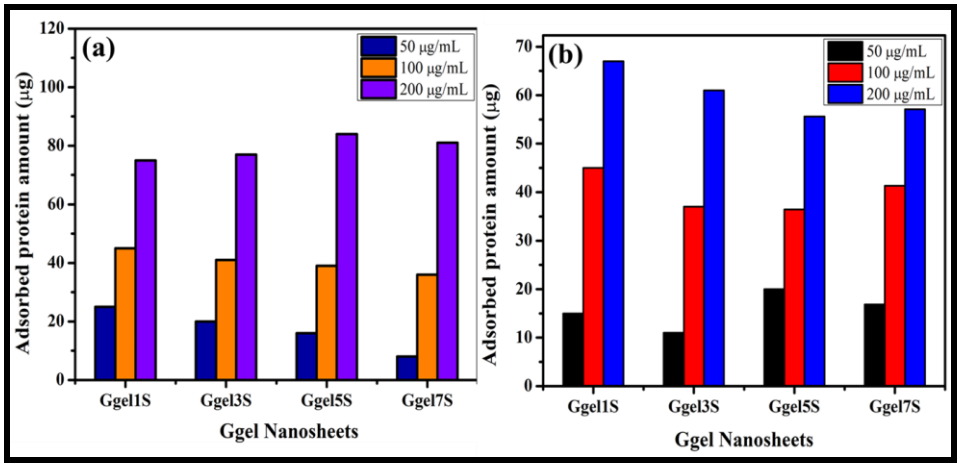

Figure 3.5. Absolute protein adsorbed on Ggel nanosheets at different concentration (a) BSA (b) FBS.

For BSA at lower concentration i.e. 50 µg/mL Ggel nanosheets having the highest lateral size (Ggel1S) showed the highest BSA adsorption among Ggel3S, 5S and 7S. However, as concentration increased i.e. for 100 µg/mL and 200 µg/mL the amount of protein adsorbed were almost similar suggesting lateral size independent adsorption behavior (Figure **3.5a**). Interestingly for FBS at low concentration (50 µg/mL) no uniform pattern for adsorption was observed w.r.to. lateral size however as concentration gets increased of Ggel nanosheets lateral size dependent adsorption behavior was found as shown in Figure **3.5b**. These result infers that protein concentration gradient, concentration of nanomaterials their lateral sizes significantly affects the protein adsorption further with different proteins the adsorption behavior will be different with same nanomaterials. Further the interaction between these proteins and Ggel nanosheets may occur via van der Waal's forces, electrostatic interactions, hydrophobic interactions, π-π interactions and hydrogen bonding and gets significantly affect by the surface properties such as charge and hydrophilicity factor of nanomaterials which contributes significantly for different adsorption behavior [26–28].

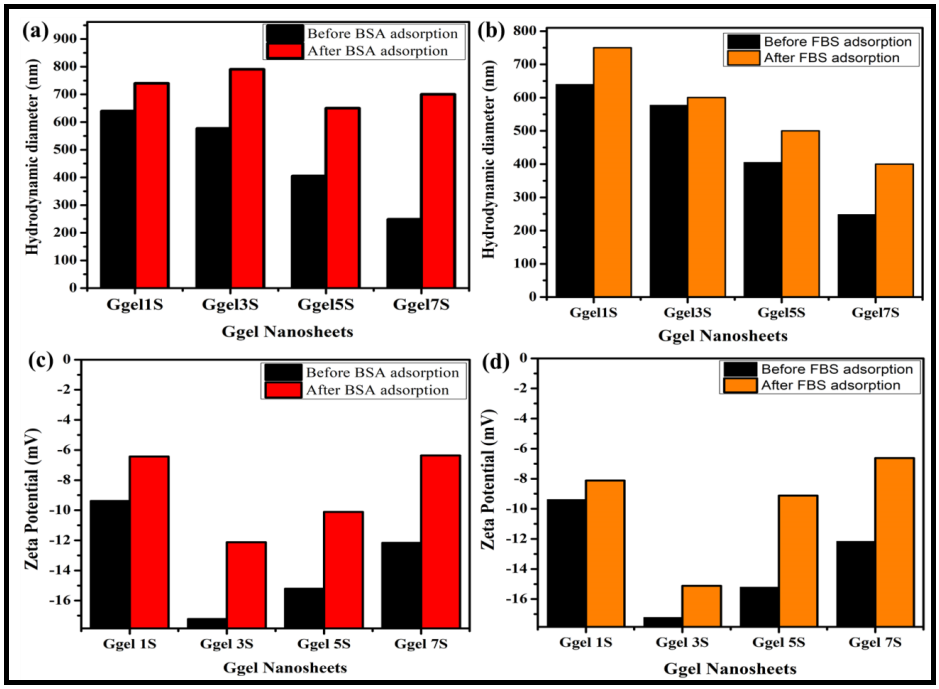

Figure 3.6. Hydrodynamic diameter of Ggel nanosheets before and after (a) BSA adsorption (b) FBS adsorption. Zeta potential value of Ggel nanosheets before and after (c) BSA adsorption (d) FBS adsorption.

Now, since these serum protein gets adsorbed onto Ggel nanosheets so their size and surface charges may get significantly changed. So, to verify this dynamic light scattering (DLS) was performed of these Ggel nanosheets before and after adsorption of BSA and FBS. As discussed earlier, Ggel1S showed the lateral size of 639.8 nm which gets decreased to 248.3 nm for Ggel7S. However, after adsorption significant changes both in D_H value and zeta potential were observed for both BSA and FBS as shown in Figure **3.6**. The change in D_H value was maximum post-protein adsorption i.e. for both BSA and FBS in Ggel7S as shown in Figure **3.6a-b**. The plausible reason behind this change includes due to prolonged sonication in Ggel7S the morphologies of exfoliated sheets also changed a lot along with lateral size which gets significantly changed after protein adsorption [19]. Similarly, the zeta potential value also gets increased after adsorption shown in Figure **3.6c-d**. It must be mentioned here that, zeta potential mainly derived from adsorbed protein located on

the surface of these Ggel nanosheets. Also, the significant difference both in D_H value and zeta potential value with Ggel7S (having the lowest lateral size) may attribute to the formation of protein corona surrounding around them [19]. So, this significant change in size and charges for Ggel nanosheets post protein adsorption must be taken into consideration for any biomedical application as, the real size of these nanomaterials is the size measured after the protein adsorption/corona formation.

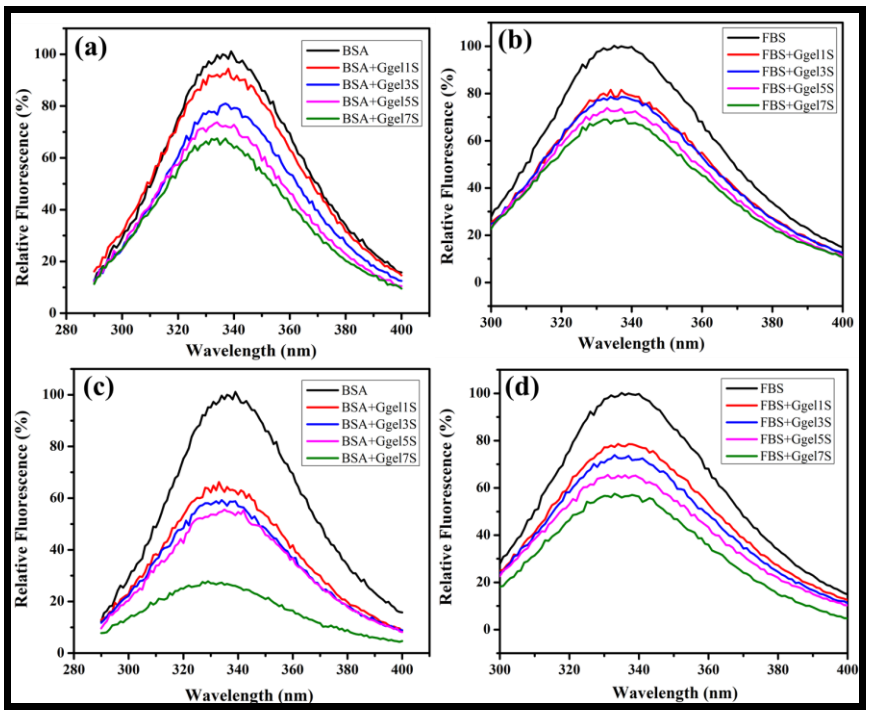

Figure 3.7. Relative fluorescence quenching after incubation with Ggel nanosheets (50µg/mL) (a) BSA (b) FBS, with Ggel nanosheets (200µg/mL) (c) BSA (d) FBS.

Now after investigating the size & charge variation the molecular interaction which involved the fluorescence tuning in proteins after adsorption was measured. As we know that proteins exhibit the inherent fluorescence nature all thanks to the contribution made by their aromatic amino acid present in them i.e. tryptophan; tyrosine and phenylalanine [29]. So the fluorescence behavior of BSA and FBS were measured in the presence of Ggel nanosheets having concentration of 50 and 200 µg/mL as

shown in Figure **3.7**. Now, it can easily be observed that irrespective of concentration for both BSA and FBS the maximum quenching was observed with Ggel7S. Also, as the concentration of Ggel7S gets increased quenching becomes more prominent in BSA (Figure **3.7a,c**). It must be mentioned here that G and their derivative have shown fluorescence quenching capability with proteins, peptides and amino acids [30,31]. The fluorescence quenching arises because of the generation of non-radiative transition between the exfoliated sheets and aromatic residues present in the proteins. Further, with decreased lateral size, more Ggel nanosheets gets confined in the closed proximity of the proteins which ultimately shortens the distance between intrinsic fluorescence emitter present in protein and exfoliated sheets and leads to fluorescence quenching. Thus, the fluorescence quenching phenomenon may act as an indicator of the change in the local environment of proteins due to adsorption which may lead to a change in their confirmations [32,33].

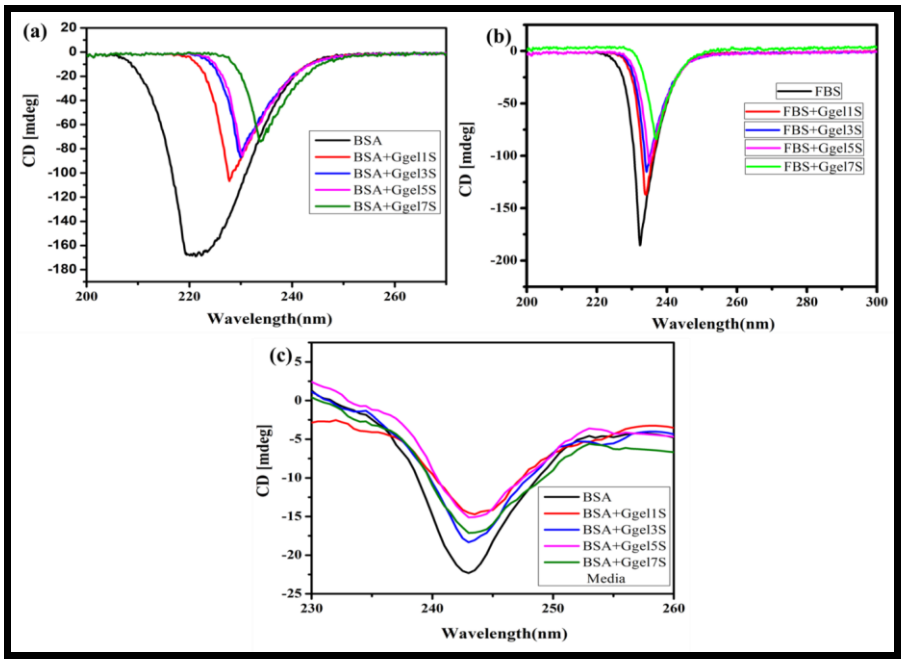

Figure 3.8. Secondary structure stability after incubation with Ggel nanosheets (a) BSA (b) FBS (c) BSA in DMEM media.

Circular dichroism (CD) spectroscopy was performed to assess the secondary structure of these proteins upon association with Ggel nanosheets. The spectra were recorded in the far UV range i.e. 190 to 260 nm. From the obtained result shown in Figure **3.8** it was observed that with decrease in lateral size of Ggel nanosheets the ellipticity value gets decreased also shift in band (red shift) was observed. The trends were similar with both BSA and FBS (shown in Figure **3.8a-b**). This result was in agreement with the fluorescence quenching behavior shown in Figure **3.7**. Furthermore, the progressive decrease in ellipticity with lateral size infers very strong; size dependent molecular interactions between Ggel nanosheets and these serum proteins. Also, the presence of a negative band even after Ggel nanosheets interaction suggesting its conformational stability upon interactions. Thus based on fluorescence spectra and CD spectra the existence of size and concentration dependent molecular interaction between Ggel nanosheets and BSA/FBS can easily be inferred.

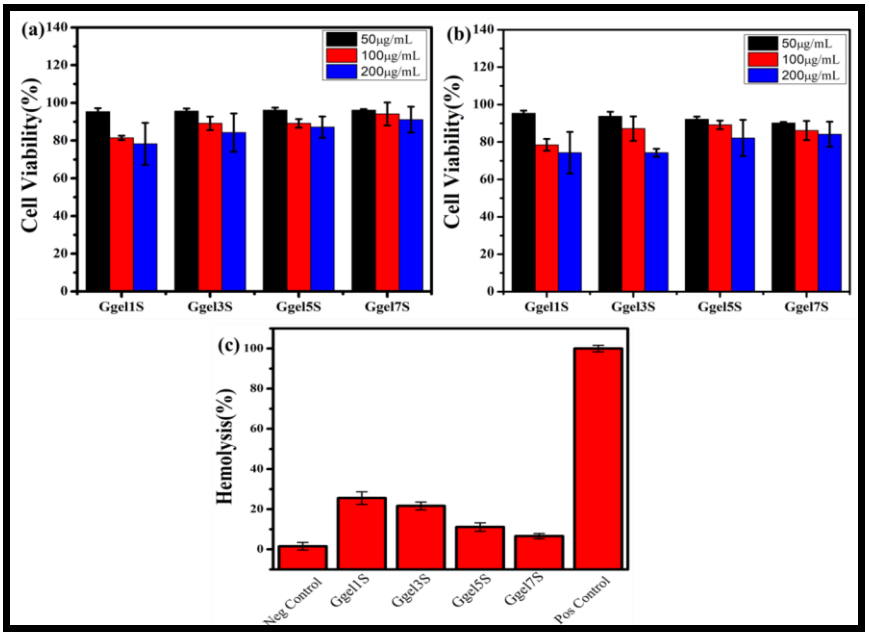

Figure 3.9. Panels (a) and (b) shows cell viability for HeLa cells after 24 h and 48 h (c) shows % hemolysis of RBCs (incubation time 2 h, concentration 200 µg/mL) for Ggel nanosheets.

After investigating size and concentration dependent protein interaction study these different laterals sized Ggel nanosheets were investigated for *invitro* toxicity using MTT assay. Herein cellular toxicity studies were performed on HeLa cells. The obtained data shown in Figure **3.9a-b** suggests the cytocompatible nature irrespective of lateral size as more than 90% viable cells were observed after 24 h and 48 h incubation with maximum concentration of 200 µg/mL. Similarly, these Ggel nanosheets were investigated for hemolysis and it was observed that with Ggel1S having maximum lateral size around 30% of RBCs gets lysed which gets decreased as the lateral size decreases i.e. with Ggel7S only 8% of RBCs gets lysed. The obtained results were compared with positive control and negative control. It must be mentioned here that % hemolysis value after Ggel interactions were well within the range of the standard ASTM E2524-08 [34]. Thus very good biocompatible and hemocompatible nature with these directly exfoliated Ggel nanosheets comes because of excellent hydrophilicity and very less oxidative defect. Also, the presence of gelatin on exfoliated sheet surface minimizes the direct interaction between cells and G sheets leads to better cellular adhesion and favourable surface topography which ultimately leads to excellent biocompatible nature [21,35] .

3.3. Conclusion

In summary, a detailed investigation has been made to study the interaction between serum proteins and different lateral sized directly exfoliated graphene. The exfoliation process and varying lateral size was attained just by varying the sonication time thus nullifies the use of conventional exfoliation method. The obtained results showed that due to protein adsorption the lateral size and zeta potential value of Ggel nanosheets gets significantly changed. Further, the adsorption leads to fluorescence quenching and change in the ellipticity of BSA and FBS proteins. The adsorption behaviour and molecular interaction showed

lateral size and concentration dependent nature and were different with both BSA and FBS. Thus, these protein adsorption phenomenons must be taken into account for utilizing G and their derivative for biomedical applications.

3.4. Experimental

3.4.1. Materials

Graphite powder and gelatin (type b) was purchased from Thermo-Fisher and were used without any further purification. Serum proteins BSA and FBS were purchased from Highmedia. Cells were grown in Minimum essential medium (MEM) high media and MTT assay (3(4,5-dimethylthylazol-2-yl)-2,5-diphenyl tetrazolium bromide) was done for cellular toxicity studies.

3.4.2. Direct exfoliation of Graphite

Gelatin powder was dissolved in DI water (pH7) by providing temperature~50^{o}C and magnetic stirring. Afterwards, graphite powder was added to gelatin solution. The whole solution was applied for bath sonication (temperature~60^{o}C). For obtaining different lateral size sonication time was varied i.e. Ggel1S (1 h sonication); Ggel3S (3 h sonication); Ggel5S (5 h sonication) and Ggel7S (7 h sonication). After sonication centrifugation was performed (time 15 min; 4000 r.p.m) to separate unexfoliated graphite powder from graphene dispersion.

3.4.3. Ggel nanosheets lateral size

Ggel (Ggel 1S, 3S, 5S and 7S) dispersions were dropped on a mica substrate and air dried. The surface morphology of Ggel nanosheets was characterized by atomic force microscopy (Model: Bruker, Billerica, MA) using tapping mode. The lateral size distribution and mean lateral size was calculated using the obtained AFM image (~100 sheets) analyzed by Image J software (NIH,US).

3.4.4 Hydrodynamic diameter and zeta potential

The hydrodynamic diameter and zeta potential were measured using dynamic light scattering (DLS) on a Micromeritics Nanoplus 3 setup. Post centrifuged samples of Ggel dispersion were used for the investigation (concentration~ 200 µg/mL). The serum proteins were incubated with Ggel nanosheets for 1 h and after those samples were centrifuged (time 10 min, 8000 r.p.m.) and supernatant was discarded the settled pallet was again redispersed for the measurement. The control Ggel nanosheets and proteins, hydrodynamic diameter and zeta potential were also measured for comparative study.

3.4.5. Quantification of adsorbed serum protein concentration on Ggel nanosheets

Absorption spectrum of BSA and FBS was recorded using *UV-Vis* spectrometer (Model: Aglient Cary 60 UV-visible spectrophotometer). Initially, the concentration profile of BSA and FBS was plotted by measuring the absorbance (absorbance was recorded~280 nm) at various concentrations. For the measurement of protein adsorption Ggel nanosheets having different lateral sizes and concentrations (50, 100 & 200 µg/mL) incubated with BSA and FBS (conecntration~2 mg/mL) for 1 h. Afterwards, the resultant suspension (0.5 mg/mL) was centrifuged for (8000 r.p.m, time~10 min) and supernatant was obtained and absorbance was recorded at 280 nm. The amount of protein adsorbed was quantified from variation in adsorption pre and post Ggel incubation.

3.4.6. Effect of Ggel nanosheets on fluorescence quenching in proteins

The fluorescence spectrum was recorded using a fluorescence spectrometer (Model: Fluoromax spectrometer) after incubating BSA and FBS with Ggel nanosheets. It must be mentioned here that protein concentration was fixed with 2 mg/mL however Ggel concentration was varied i.e. 50 µg/mL and 200 µg/mL. Furthermore, incubation time and centrifugation condition were similar to adsorption studies. For the

measurement, the excitation wavelength was fixed at 280 nm and emission was recorded between 290 nm- 400 nm.

3.4.7. Effect of Ggel nanosheets on secondary structure of proteins

To measure the secondary structure stability circular dichroism (CD) spectroscopy was performed. The CD spectrum was recorded between 190 to 260 nm using JASCO J-815CD spectropolarimeter. The scanning speed was fixed at 50 nm min^{-1}. CD spectrum were recorded and collected as the average of three consecutive scans at room temperature.

3.4.8. Effect of Ggel nanosheets on biocompatibility and hemocompatibility

The biocompatibility of Ggel nanosheets was determined on HeLa cells using MTT assay. Cells seeded in 96-well plates and were grown in nutrient media which contains MEM media; 1% penicillin streptomycin and 10% FBS. Cells were incubated for 24 h & 48 h after treatment with Ggel nanosheets (concentrations~ 50; 100 and 200 µg/mL). Subsequently, Ggel nanosheets were replaced with MTT containing media (~0.5 mg/mL) and further incubated for 4 h. Afterwards, MTT containing media were replaced with DMSO and absorbance was recorded using Synergy H1 Biotek microplate reader. For hemocompatibility study blood were incubated with Ggel nanosheets (concentration~ 200 µg/mL). TritonX 100 was treated with blood to make positive control and blood incubated with 1X PBS used as a negative control. The incubation was done for 2 h. After incubation RBCs were centrifuged for 10 min at 1000Xg and absorbance of supernatant was recorded at 540 nm.

3.5. References

[1] C. Röcker, M. Pötzl, F. Zhang, W.J. Parak, G.U. Nienhaus (2009), A quantitative fluorescence study of protein monolayer formation on colloidal nanoparticles, Nat. Nanotechnol., 4, 577–580 (DOI: https://doi.org/10.1038/nnano.2009.195)

[2] B. Pelaz, P. del Pino, P. Maffre, R. Hartmann, M. Gallego, S. Rivera-Fernández, J.M. de la Fuente, G.U. Nienhaus, W.J. Parak (2015), Surface Functionalization of Nanoparticles with Polyethylene Glycol: Effects on Protein Adsorption and Cellular Uptake, ACS Nano., 9, 6996–7008 (DOI: https://doi.org/10.1021/acsnano.5b01326)

[3] O. Vilanova, J.J. Mittag, P.M. Kelly, S. Milani, K.A. Dawson, J.O. Rädler, G. Franzese (2016), Understanding the Kinetics of Protein–Nanoparticle Corona Formation, ACS Nano., 10, 10842–10850 (DOI: https://doi.org/10.1021/acsnano.6b04858)

[4] C. Chung, Y.-K. Kim, D. Shin, S.-R. Ryoo, B.H. Hong, D.-H. Min (2013), Biomedical Applications of Graphene and Graphene Oxide, Acc. Chem. Res., 46, 2211–2224 (DOI: https://doi.org/10.1021/ar300159f)

[5] A.C. Ferrari, F. Bonaccorso, V. Fal'ko, K.S. Novoselov, S. Roche, P. Bøggild, S. Borini, F.H.L. Koppens, V. Palermo, N. Pugno, J.A. Garrido, R. Sordan, A. Bianco, L. Ballerini, M. Prato, E. Lidorikis, J. Kivioja, C. Marinelli, T. Ryhänen, A. Morpurgo, J.N. Coleman, V. Nicolosi, L. Colombo, A. Fert, M. Garcia-Hernandez, A. Bachtold, G.F. Schneider, F. Guinea, C. Dekker, M. Barbone, Z. Sun, C. Galiotis, A.N. Grigorenko, G. Konstantatos, A. Kis, M. Katsnelson, L. Vandersypen, A. Loiseau, V. Morandi, D. Neumaier, E. Treossi, V. Pellegrini, M. Polini, A. Tredicucci, G.M. Williams, B.H. Hong, J.-H. Ahn, J.M. Kim, H. Zirath, B.J. van Wees, H. van der Zant, L. Occhipinti, A.D. Matteo, I.A. Kinloch, T. Seyller, E. Quesnel, X. Feng, K. Teo, N. Rupesinghe, P. Hakonen, S.R.T. Neil, Q. Tannock, T. Löfwander, J. Kinaret (2015), Science and technology roadmap for graphene, related two-dimensional crystals, and hybrid systems, Nanoscale., 7, 4598–4810 (DOI: https://doi.org/10.1039/C4NR01600A)

[6] K.S. Novoselov, A.K. Geim, S.V. Morozov, D. Jiang, Y. Zhang, S.V. Dubonos, I.V. Grigorieva, A.A. Firsov (2004), Electric Field Effect in Atomically Thin Carbon Films, Science., 306, 666–669 (DOI: https://doi.org/10.1126/science.1102896)

[7] A. Bianco (2013), Graphene: Safe or Toxic? The Two Faces of the Medal, Angew. Chem. Int. Ed., 52, 4986–4997 (DOI: https://doi.org/10.1002/anie.201209099)

[8] A. Schinwald, F.A. Murphy, A. Jones, W. MacNee, K. Donaldson (2012), Graphene-Based Nanoplatelets: A New Risk to the

Respiratory System as a Consequence of Their Unusual Aerodynamic Properties, ACS Nano., 6, 736–746
(DOI: https://doi.org/10.1021/nn204229f)

[9] A. Sasidharan, L.S. Panchakarla, P. Chandran, D. Menon, S. Nair, C.N.R. Rao, M. Koyakutty (2011), Differential nano-bio interactions and toxicity effects of pristine versus functionalized graphene, Nanoscale., 3, 2461–2464
(DOI: https://doi.org/10.1039/C1NR10172B)

[10] L. Boselli, E. Polo, V. Castagnola, K.A. Dawson (2017), Regimes of Biomolecular Ultrasmall Nanoparticle Interactions, Angew. Chem. Int. Ed., 56, 4215–4218
(DOI: https://doi.org/10.1002/anie.201700343)

[11] M.P. Monopoli, C. Åberg, A. Salvati, K.A. Dawson (2012), Biomolecular coronas provide the biological identity of nanosized materials, Nat. Nanotechnol., 7, 779–786
(DOI: https://doi.org/10.1038/nnano.2012.207)

[12] D. Walczyk, F.B. Bombelli, M.P. Monopoli, I. Lynch, K.A. Dawson (2010), What the Cell "Sees" in Bionanoscience, J. Am. Chem. Soc., 132, 5761–5768
(DOI: https://doi.org/10.1021/ja910675v)

[13] M. Lundqvist, J. Stigler, G. Elia, I. Lynch, T. Cedervall, K.A. Dawson (2008), Nanoparticle size and surface properties determine the protein corona with possible implications for biological impacts, Proc. Natl. Acad. Sci., 105, 14265–14270
(DOI: https://doi.org/10.1073/pnas.0805135105)

[14] A. Lesniak, A. Campbell, M.P. Monopoli, I. Lynch, A. Salvati, K.A. Dawson (2010), Serum heat inactivation affects protein corona composition and nanoparticle uptake, Biomaterials., 31, 9511–9518
(DOI: https://doi.org/10.1016/j.biomaterials.2010.09.049)

[15] Z.J. Deng, M. Liang, M. Monteiro, I. Toth, R.F. Minchin (2011), Nanoparticle-induced unfolding of fibrinogen promotes Mac-1 receptor activation and inflammation, Nat. Nanotechnol., 6, 39–44
(DOI: https://doi.org/10.1038/nnano.2010.250)

[16] D.M. L, O. L, P. F, N. M, S. S, D.L. J, B. M, T. E, P. V, P. A (2014), Flake size-dependent cyto and genotoxic evaluation of graphene oxide on in vitro A549, CaCo2 and vero cell lines, J. Biol. Regul. Homeost. Agents., 28, 281–289

[17] Kenry, K.P. Loh, C.T. Lim (2016), Molecular interactions of graphene oxide with human blood plasma proteins, Nanoscale., 8, 9425–9441 (DOI: https://doi.org/10.1039/C6NR01697A)

[18] R.G. Mendes, B. Koch, A. Bachmatiuk, X. Ma, S. Sanchez, C. Damm, O.G. Schmidt, T. Gemming, J. Eckert, M.H. Rümmeli (2015), A size dependent evaluation of the cytotoxicity and uptake of nanographene oxide, J. Mater. Chem. B., 3, 2522–2529
(DOI: https://doi.org/10.1039/C5TB00180C)

[19] X.-Q. Wei, L.-Y. Hao, X.-R. Shao, Q. Zhang, X.-Q. Jia, Z.-R. Zhang, Y.-F. Lin, Q. Peng (2015), Insight into the Interaction of Graphene Oxide with Serum Proteins and the Impact of the Degree of Reduction and Concentration, ACS Appl. Mater. Interfaces., 7, 13367–13374 (DOI: https://doi.org/10.1021/acsami.5b01874)

[20] J.I. Paredes, S. Villar-Rodil (2016), Biomolecule-assisted exfoliation and dispersion of graphene and other two-dimensional materials: a review of recent progress and applications, Nanoscale., 8, 15389–15413 (DOI: https://doi.org/10.1039/C6NR02039A)

[21] P. Tiwari, N. Kaur, V. Sharma, S.M. Mobin (2018), High-yield graphene produced from the synergistic effect of inflated temperature and gelatin offers high stability and cellular compatibility, Phys. Chem. Chem. Phys., 20, 20096–20107 (DOI: https://doi.org/10.1039/C8CP02263A)

[22] Global Gelatin Market Projected to Reach $2.79 Billion in 2018, Nutraceuticals World. (n.d.). https://www.nutraceuticalsworld.com/contents/view_breaking-news/2013-07-15/global-gelatin-market-projected-to-reach-279-billion-in-2018/ (accessed February 28, 2018).

[23] K. Liu, J.-J. Zhang, F.-F. Cheng, T.-T. Zheng, C. Wang, J.-J. Zhu (2011), Green and facile synthesis of highly biocompatible graphene nanosheets and its application for cellular imaging and drug delivery, J. Mater. Chem., 21, 12034–12040 (DOI: https://doi.org/10.1039/C1JM10749F)

[24] M. Lian, J. Fan, Z. Shi, S. Zhang, H. Li, J. Yin (2015), Gelatin-assisted fabrication of graphene-based nacre with high strength, toughness, and electrical conductivity, Carbon., 89, 279–289 (DOI: https://doi.org/10.1016/j.carbon.2015.03.045)

[25] S. Liu, M. Hu, T.H. Zeng, R. Wu, R. Jiang, J. Wei, L. Wang, J. Kong, Y. Chen (2012), Lateral Dimension-Dependent Antibacterial Activity of Graphene Oxide Sheets, Langmuir., 28, 12364–12372 (DOI: https://doi.org/10.1021/la3023908)

[26] S. Li, J.J. Mulloor, L. Wang, Y. Ji, C.J. Mulloor, M. Micic, J. Orbulescu, R.M. Leblanc (2014), Strong and Selective Adsorption of Lysozyme on Graphene Oxide, ACS Appl. Mater. Interfaces., 6, 5704–5712 (DOI: https://doi.org/10.1021/am500254e)

[27] Y. Zhang, J. Zhang, X. Huang, X. Zhou, H. Wu, S. Guo (2012), Assembly of Graphene Oxide–Enzyme Conjugates through Hydrophobic Interaction, Small., 8, 154–159 (DOI: https://doi.org/10.1002/smll.201101695)

[28] L. Zhou, Y. Jiang, J. Gao, X. Zhao, L. Ma (2012), Graphene Oxide as a Matrix for the Immobilization of Glucose Oxidase, Appl. Biochem. Biotechnol., 168, 1635–1642 (DOI: https://doi.org/10.1007/s12010-012-9884-4)

[29] C.A. Royer (2006), Probing Protein Folding and Conformational Transitions with Fluorescence, Chem. Rev., 106, 1769–1784

(DOI: https://doi.org/10.1021/cr0404390)
[30] S. Li, A.N. Aphale, I.G. Macwan, P.K. Patra, W.G. Gonzalez, J. Miksovska, R.M. Leblanc (2012), Graphene Oxide as a Quencher for Fluorescent Assay of Amino Acids, Peptides, and Proteins, ACS Appl. Mater. Interfaces., 4, 7069–7075
` (DOI: https://doi.org/10.1021/am302704a)
[31] X. Ling, L. Xie, Y. Fang, H. Xu, H. Zhang, J. Kong, M.S. Dresselhaus, J. Zhang, Z. Liu (2010), Can Graphene be used as a Substrate for Raman Enhancement?, Nano Lett., 10, 553–561
(DOI: https://doi.org/10.1021/nl903414x)
[32] P. Roach, D. Farrar, C.C. Perry (2005), Interpretation of Protein Adsorption: Surface-Induced Conformational Changes, J. Am. Chem. Soc., 127, 8168–8173
(DOI: https://doi.org/10.1021/ja042898o)
[33] Q. Xiao, S. Huang, Z.-D. Qi, B. Zhou, Z.-K. He, Y. Liu (2008), Conformation, thermodynamics and stoichiometry of HSA adsorbed to colloidal CdSe/ZnS quantum dots, Biochim. Biophys. Acta BBA - Proteins Proteomics., 1784, 1020–1027
(DOI: https://doi.org/10.1016/j.bbapap.2008.03.018)
[34] M. Das Purkayastha, A.K. Manhar, V.K. Das, A. Borah, M. Mandal, A.J. Thakur, C.L. Mahanta (2014), Antioxidative, Hemocompatible, Fluorescent Carbon Nanodots from an "End-of-Pipe" Agricultural Waste: Exploring Its New Horizon in the Food-Packaging Domain, J. Agric. Food Chem., 62, 4509–4520
(DOI: https://doi.org/10.1021/jf500138f)
[35] A.M. Pinto, I.C. Gonçalves, F.D. Magalhães (2013), Graphene-based materials biocompatibility: A review, Colloids Surf. B Biointerfaces., 111, 188–202
(DOI: https://doi.org/10.1016/j.colsurfb.2013.05.022)

CHAPTER 4

Sustainable Graphene Production: New insights into *Cannabis Sativa* Engineered Carbon Dots based Exfoliating agent for Facile Production of Graphene

4.1. Introduction

Graphene (G) having sp^2 hybridized carbon atom exhibits honeycomb-like structure and serves as an elementary unit for other carbon forms like carbon dots (0D), carbon nanotube (1D) and graphite (3D) (Gr) [1]. Since its discovery in 2004 G has emerged as a wonder material due to its fascinating properties and potential applications especially in electronic devices, gas sensors, disease diagnosis, drug delivery etc. [2-5]. Various methods have been applied so far for G synthesis e.g. CVD, epitaxial growth, ball milling, micromechanical cleavage etc. [6-10]. However, high cost and scalability of G production were the major constraints so far. The liquid phase exfoliation of Gr to G was initially done using modified hummers method [11,12]. The uses of toxic reagents severely affect the G production [13]. Recently electrochemical methods with green approach, low cost, high efficiency and controllable production are developed [11, 14-20]. However, the presence of oxidative defects limits the applicability and can be overcome by direct exfoliation of Gr to G [21]. Direct exfoliation mainly used surfactant, solvents, polymers, proteins, silk fibres etc. [22-25]. The exfoliation process based on the reduction of the surface energy of liquid to match with that of Gr by getting adsorbed on Gr surface. The presence of functional groups on exfoliated G surface plays a predominant role in making high-quality graphene dispersions [26].

The past few years have witnessed the emergence of 0D carbon nanomaterials known as carbon dots (C-dots) because of its extraordinary

attributes like fluorescence, cytocompatibility, photostability, small particle size etc. [27-29]. Due to the fascinating properties C-dots were used in various applications like chemical sensing, bioimaging, solar cells, storage devices, drug delivery etc [30-35]. Recently the use of natural carbon sources for the synthesis of C-dots has been successfully introduced because of its sustainable nature [36].

The hydrophobic nature of G limits its applicability especially, in different biomedical applications. Earlier, Jiang et al [37]., demonstrated graphene quantum dots can act as a stabilizer for the aqueous dispersion of G with good stability. C-dots were used as a reducing agent to graphite oxide [38,39]. Zhang et al [40]., synthesized C-dots using citric acids and exfoliated Gr with lesser structural defects and lower oxidation. Despite these prior studies, exfoliation of Gr was done using citric acids as a sole carbon precursor. However, the C-dots prepared by employing a green source of carbon precursor are still unknown for exfoliation of 2D materials [41].

In the present work for the first time "*Cannabis Sativa*" was used as a green carbon source to synthesize C-dots (CSDs) and nitrogen doped C-dots (N@CSDs) using the hydrothermal method. The green sources offer an advantage in terms of cost, ease of availability & versatility. *Cannabis Sativa* possesses formidable features and is a great source of fibre and potential medicinal values. Further, it contains antibacterial cannabinoids which can become a potential candidate for the killing of antibiotic-resistant bacteria's [42]. The direct exfoliation of Gr to G was performed using high-temperature sonication; further CSDs and N@CSDs were explored as a stabilizing agent in the process. It was observed that nitrogen plays a crucial role in the stabilization process i.e. only N@CSDs was able to stabilize the exfoliated Gr into G (GN@CSDs) sheets. The as-prepared GN@CSDs was further investigated for antibacterial behaviour. The present method illustrates the potential of C-dots especially in exfoliating and stabilizing other 2D materials.

4.2. Results and discussion

We portray to exfoliate Gr into GN@CSDs by utilizing high sonicating forces to disrupt the bonds between the graphitic sheets and green C-dots for the very first time (here N@CSDs) as a stabilizing agent as shown in Scheme **4.1**. The exfoliation process follows a simple mathematical expression: 3+0⟶2. As synthesized N@CSDs and GN@CSDs were meticulously characterized using various analytical techniques like UV-Vis spectroscopy, Fluorescence spectroscopy, FTIR, Atomic Force Microscopy(AFM), PXRD, X-ray photoelectron spectroscopy, Scanning electron microscopy (SEM), raman spectroscopy and Transmission electron microscopy (TEM) were performed to gain insights about the exfoliation process and of exfoliated sheets. Additionally, stability and antibacterial activity of GN@CSDs were studied for its further applications.

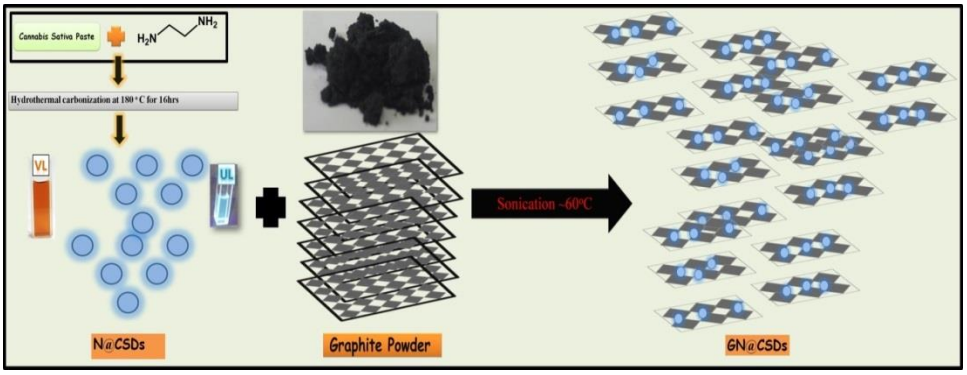

Scheme 4.1. The direct exfoliation of graphite (3D) using N@CSDs (0D) into graphene (2D).

4.2.1. Properties of as-synthesized N@CSDs

The Control C-dot sample was prepared without nitrogen doping (CSDs) and its UV-vis spectra and fluorescence spectra were recorded. The CSDs exhibit absorbance peaks around 280 nm and 320 nm which corresponds to π-π* and n- π* transitions respectively (Figure **4.1a**). The maximum

emission was observed around 412 nm with excitation wavelength at 330 nm (Figure **4.1b**).

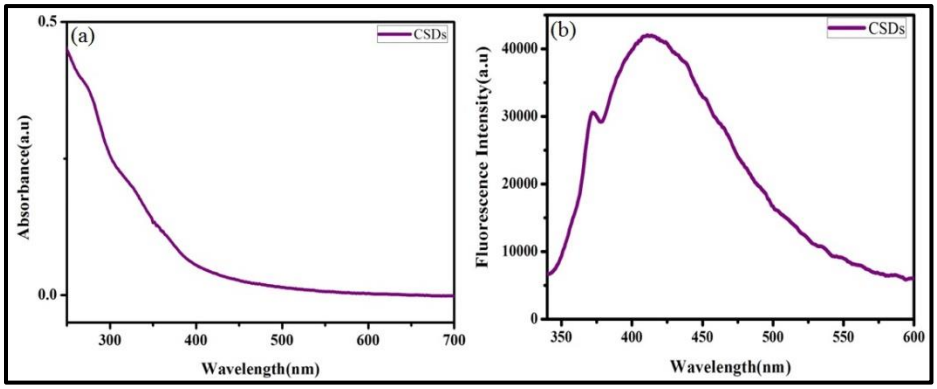

Figure 4.1. Optical properties of CSDs (a) *Uv-vis* spectra (b) Fluorescence spectra.

However, the fluorescence intensity was very low and exfoliation was not happening hence nitrogen was doped for enhancing the fluorescence intensity and facilitates the exfoliation process. The optical properties of N@CSDs were studied using absorption and fluorescence spectra. The absorption peak around 280 nm corresponds to π-π^* transition [43] (Figure **4.2a**) was observed. The fluorescence spectra of N@CSDs (Figure **4.2b**) exhibit wavelength tuned emission behaviour i.e. with an increase in excitation wavelength from 340 nm to 440 nm the emission maximum wavelength shifts towards longer wavelength. This emission nature of N@CSDs is a very common characteristic for c-dots and arises due to the quantum confinement effect. The optimal excitation and emission wavelength for N@CSDs were 360 nm and 460 nm respectively. For exploring N@CSDs as an exfoliant its stability was checked with the effect of sonication. N@CSDs was subjected to bath sonication for 3 hrs and the temperature was maintained~60 ^oC. A Slight decrease in the absorbance value (Figure **4.2c**) and fluorescence intensity (Figure **4.2d**) was observed due to sonication. However, no change in

absorbance peak position and emission spectra was observed which confirms the stability of N@CSDs towards high shear forces [44].

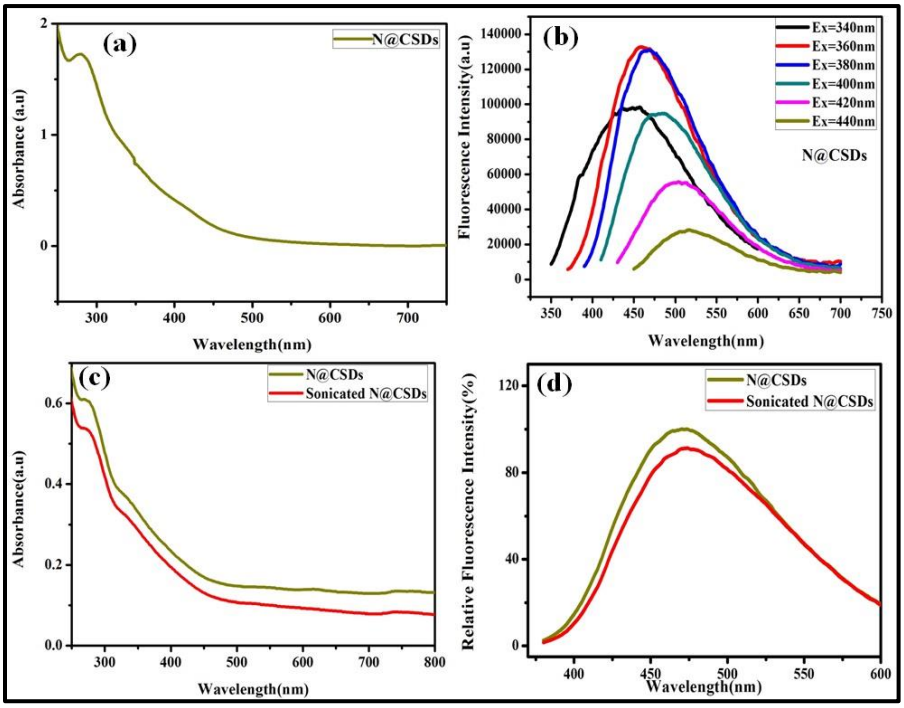

Figure 4.2. Optical characterization of N@CSDs (a) Absorption spectra (b) Fluorescence spectra with different excitation wavelength from 360 nm to 460 nm (c) Absorption spectra before and after sonication (d) Fluorescence spectra before and after sonication.

The structural characterizations of N@CSDs were studied using PXRD; Raman spectroscopy and FTIR spectra. N@CSDs exhibit amorphous nature as clear hump was observed at $2\theta = 23.91^{o}$ in PXRD (Figure **4.3a**). The amorphous nature confirms the formation of carbon dots. The Raman spectra of N@CSDs were shown in Figure **4.3b**. The G-bands correspond to sp^2 hybridized carbon network whereas D-bands correspond to the presence of defects in carbon lattice. N@CSDs exhibit structure analogous to graphite [41]. The I_D/I_G ratio of N@CSDs was around 0.32. The presence of D-band and I_D/I_G value correspond to the nitrogen-atom doping in the carbon lattice. However, lower I_D/I_G value infers the formation of high-quality carbon dots. The non-existence of 2D band in

the range 2700-2900 cm^{-1} stipulates the spherical structure of N@CSDs instead of layered one [41].

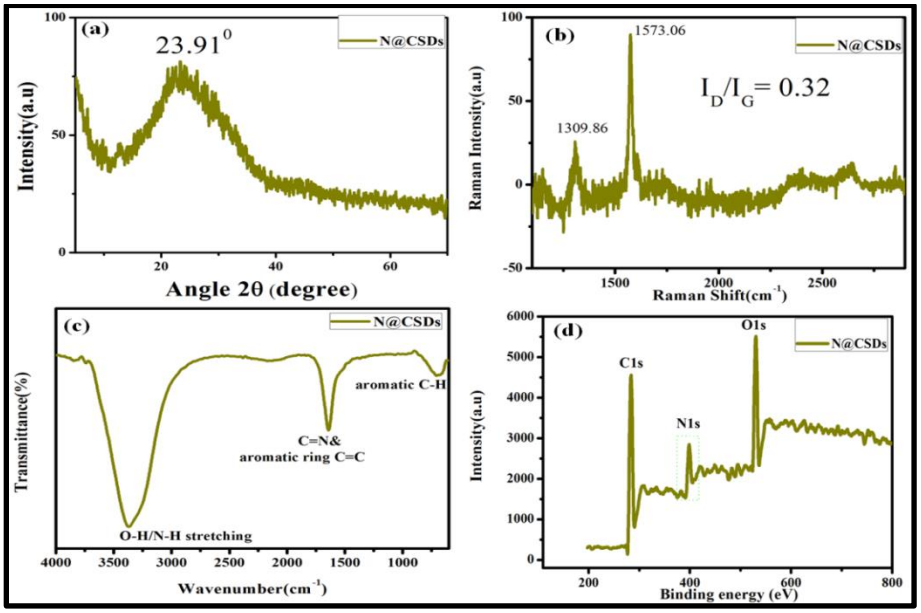

Figure 4.3. Structural characterization of N@CSDs (a) PXRD (b) Raman spectra (c) FTIR spectra (d) Survey XPS spectrum.

The FTIR spectrum of N@CSDs (Figure **4.3c**) indicates the presence of various surface functional groups. The vibration band around 3440 cm^{-1} indicates the O-H/N-H bond. The vibration band around 1639 cm^{-1} and 698 cm^{-1} indicates C=N/C=C (aromatic) and C-H bond respectively. The hydroxyl group presence enhances the solubility and stability of N@CSDs in an aqueous condition. The presence of various characteristics bands confirms the aromatic nature and successful grafting of nitrogen atom onto C-dots. To further investigate successful doping and chemical compositions present in N@CSDs, XPS was performed. Figure **4.3d** shows the survey scan having the presence of C1s (284.59 eV); N1s (399.3 eV) & O1s (531.3 eV) respectively. The survey spectrum confirms N@CSDs contain mainly carbon, nitrogen and oxygen in it. The FTIR & XPS spectrum were consistent on account of earlier reports [45].

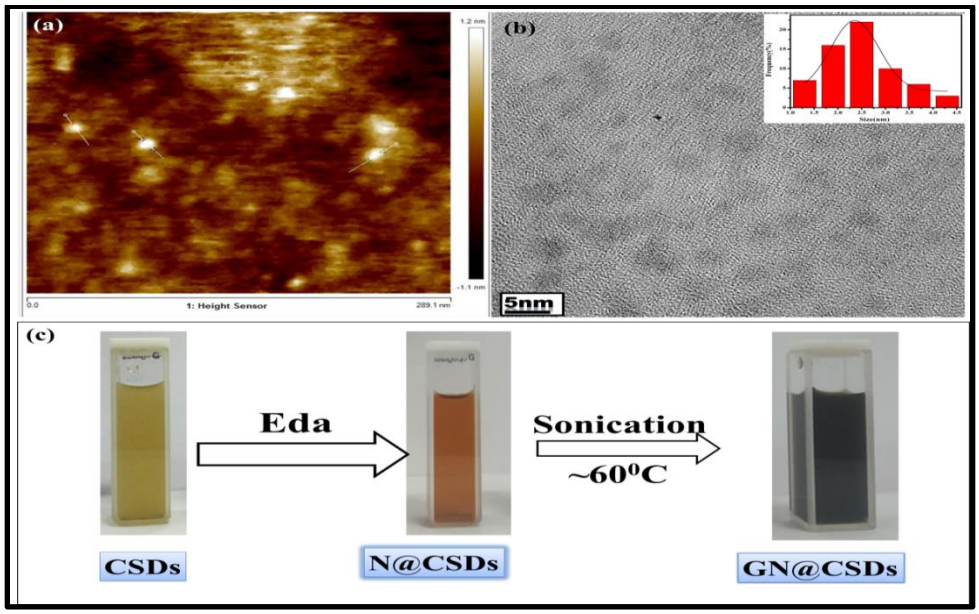

Figure 4.4. (a) AFM image of N@CSDs (b) TEM image of N@CSDs inset (size distribution) (c) Schematic representation of the production of GN@CSDs.

As depicted by AFM the synthesized N@CSDs exhibit spherical morphology (Figure **4.4a**). The narrow size distribution and continuous spherical morphologies observed from AFM images conclude the formation of isotropic C-dots with an overall size profile less than 10 nm. TEM image (as shown in Figure **4.4b**) confirms the ultra-small particles of N@CSDs. The particles were well dispersed without aggregation and having spherical morphologies. The average particle size was around 2-4 nm. Lattice fringes were absent in N@CSDs supports the amorphous nature of N@CSDs as shown in Figure **4.3a**. Successful nitrogen doping, excellent stability towards high sonication forces and lesser structural defects promoted us to employ N@CSDs as an exfoliant. The ultrasonication process was employed to direct exfoliation of Gr to G in aqueous solution (Figure **4.4c**). In the present work slurry of N@CSDs was mixed with Gr and sonicated. After the sonication, resultant colloidal solution was centrifuged and the supernatant was collected for study.

3.2.2. Evidence of N@CSDs as a successful exfoliating agent

It is evident that surface tension plays a very pivotal role in direct exfoliation of Gr. For a successful exfoliation to occur: (i) surface tension of aqueous system must match with Gr, and requirement of (ii) a suitable stabilizing agent to favorably interact with exfoliated sheets and prevent them from reaggregation. In general ultrasonication technique utilizes high- pressure jets that peel off graphitic sheets into G layers also; the high shear force intercalates bulky Gr sheets and minimizes the van der waal forces. N@CSDs contain various functional groups like (O-H, N-H, C=N, etc.) which may interact via non-covalent interactions and stabilizes the G sheets [41].

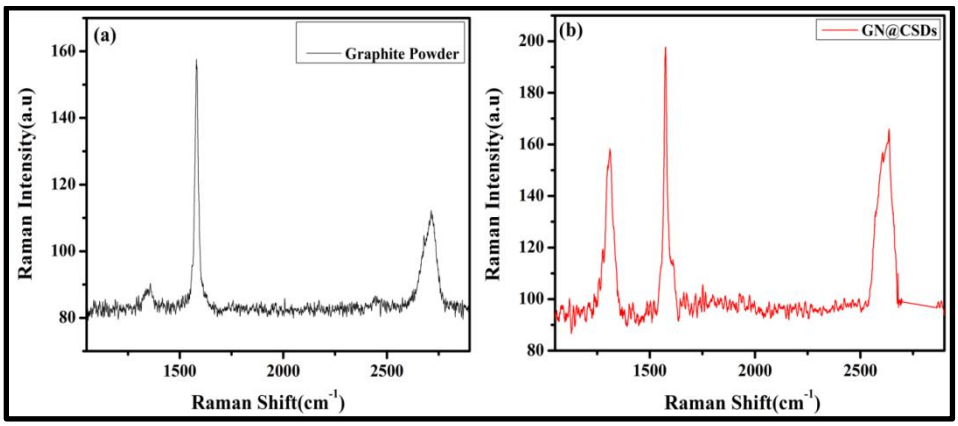

Figure 4.5. Raman Spectra of (a) Graphite (b) GN@CSDs.

To confirm the successful exfoliation raman spectra of Gr (Figure **4.5a**) and GN@CSDs (Figure **4.5b**) were recorded. Laser source of 785 nm was used for the measurement to minimize fluorescence of adsorbed N@CSDs and maximize the sensitivity of GN@CSDs [46]. The prominent "G" band at 1578 cm^{-1} corresponds sp^2 hybridized carbon atoms (graphitic band), "D" band at 1305 cm^{-1} corresponds to defect-related band and at 2631 cm^{-1} signifies "2D" band. The 2D band is the overtone of the D band. As expected, Gr does not contain any defect related band however it appeared prominently in GN@CSDs. As shown in Figure **4.5b** the I_D/I_G value and

I_{2D}/I_G of GN@CSDs were 0.85 and 0.89, respectively. The higher I_D/I_G value in GN@CSDs may arise due to edge defects from sonication and successful adsorption of N@CSDs onto GN@CSDs edges.

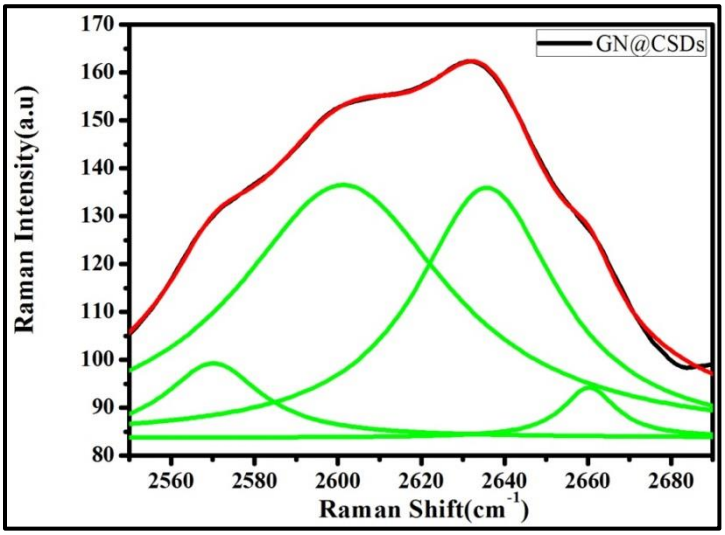

Figure 4.6. Deconvoluated 2D peak of GN@CSDs.

Further 2D peak broadening and higher I_{2D}/I_G value signifies the breaking of sheets and indicates successful exfoliation. The 2D peaks of GN@CSDs were deconvoluted in the range 2550-2700 cm^{-1} (Figure **4.6**) into 4 components. Two major peaks have appeared at 2600 & 2635 cm^{-1} and two minor peaks were at 2570 & 2660 cm^{-1}. The change in shape and 2D raman band width may occur due to the loss of bernal stacking sequence as a result of higher sonicating forces and interaction of N@CSDs. Furthermore, the loss in stacking results in the formation of partial dislocations and stacking fault formation on the basal planes and can be seen by twisting and rotation of GN@CSDs layers. [47] GN@CSDs show a signature absorbance peak around 280 nm (Figure **4.7a**) arising from the π-π^* transition. The peak position was analog to earlier values for directly exfoliated G. The G production gets affected from sonicating forces i.e. due to prolonged sonication, the higher sonicating force results in breaking of larger graphitic flakes into smaller G flakes. Hence continuous increment in absorbance value of GN@CSDs

was observed (Figure **4.7b**). Generally, absorbance value around 280 nm may get interfered from N@CSDs so absorbance values at 660 nm were recorded for GN@CSDs to circumvent the effect of N@CSDs. N@CSDs shows an absorbance value of 0.08 whereas GN@CSDs after 30 min shows absorbance value 0.144 and after 150 min it increased to 0.363. This difference was highly significant and gives a clearer idea about G production. It was reported earlier that initial Gr concentration and stabilizing agent concentration (here N@CSDs) severely affect G production [23]. The emission spectrum shows about 50% quenching in the fluorescent intensity of N@CSDs with the increase in sonication time to 150 min (Figure **4.7b**). The quenching arises due to the formation of G sheets with sonication time and was consistent with earlier reports [48]. The fluorescence quenching phenomenon portrays the interaction between N@CSDs and GN@CSDs. GN@CSDs acts as an electron acceptor and a non-radiative electron transfer occurs from N@CSDs to GN@CSDs which may lead to fluorescence quenching. The fluorescence quenching of N@CSDs with G formation can easily be visualized in Figure **4.8**. It was reported earlier that initial Gr concentration and stabilizing agent concentration (here N@CSDs) severely affect G production [23]. Thus, by fixing N@CSDs concentration (30 mg) Gr concentration was varied and absorbance was recorded at 660 nm (Figure **4.7d**). It was observed that the concentration of the stabilizing agent significantly affects the final G production as not much considerable difference in absorbance at 660 nm was found. Hence, an equal ratio of N@CSDs (mg): Gr (mg) were used for further experiment. The yield of 0.08 mg/mL was achieved after 150 min of sonication.

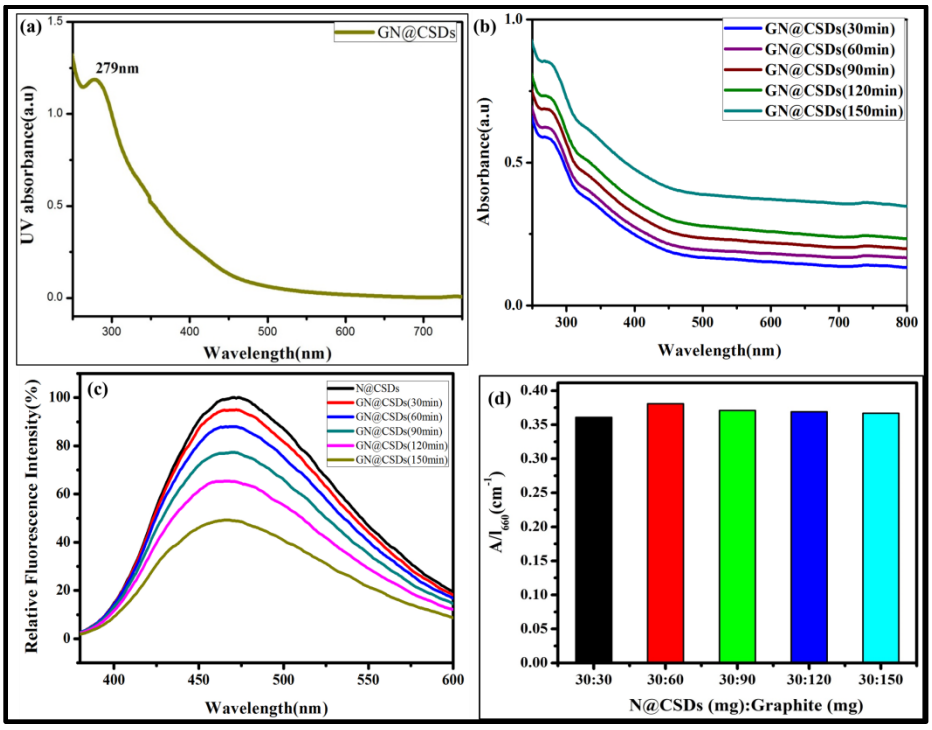

Figure 4.7. (a) *Uv-vis* spectra of GN@CSDs (b) Absorption spectra of GN@CSDs with sonication time (c) Fluorescence spectra of GN@CSDs with sonication time (d) Effect of ratio of N@CSDs: Graphite.

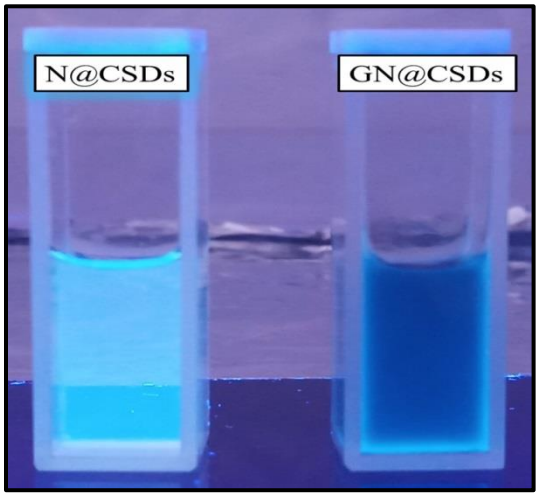

Figure 4.8. Pictorial representation of N@CSDs and GN@CSDs under UV light.

Figure **4.9a** illustrates the survey scan of GN@CSDs showing the presence of C1s, N1s& O1s core peaks at 284.7 eV, 397.91 eV& 530.29 eV respectively. An XPS spectrum reveals the interaction between N@CSDs and graphitic atoms. The interaction causes a slight shift in the binding energies of core peaks (C1s, N1s & O1s). N@CSDs contains an electron donating group like NH_2, OH^- etc. These groups interact with sp^2 carbon atoms and increase the binding energy of exfoliated GN@CSDs. Ideally, N1s peak was not found in Gr powder [49] and was observed in GN@CSDs confirming successful exfoliation and stabilization of N@CSDs on the exfoliated sheets. The deconvoluted C1s spectrum of GN@CSDs (Figure **4.9b**) shows an intense peak at 284.7 eV which corresponds to C-C/C=C bond. This bond corresponds to sp^2 hybridized graphitic atoms. The peak at 285.9 eV corresponds the C-O/C-OH bond which infers adsorption of hydroxyl molecule present in N@CSDs onto exfoliated sheets. The peak at 288.1 is for C=O/C-NH bond. The presence of –NH bond arises due to N@CSDs present onto GN@CSDs. Further, the sp^2/sp^3 ratio of GN@CSDs was around 1.47 which well matches with earlier reports on exfoliated G sheets [49]. GN@CSDs exhibited approximately 20 atom% oxygen content onto it. Higher oxygen content in GN@CSDs may arise from the oxygen atom present in N@CSDs which is acting as a stabilizing agent and present onto the exfoliated sheets. The C/O ratio of GN@CSDs was calculated from the survey scan and was around 4.003. The higher oxygen content and lower C/O ratio were well supported from a higher “D” band shown in Figure **4.5b**.

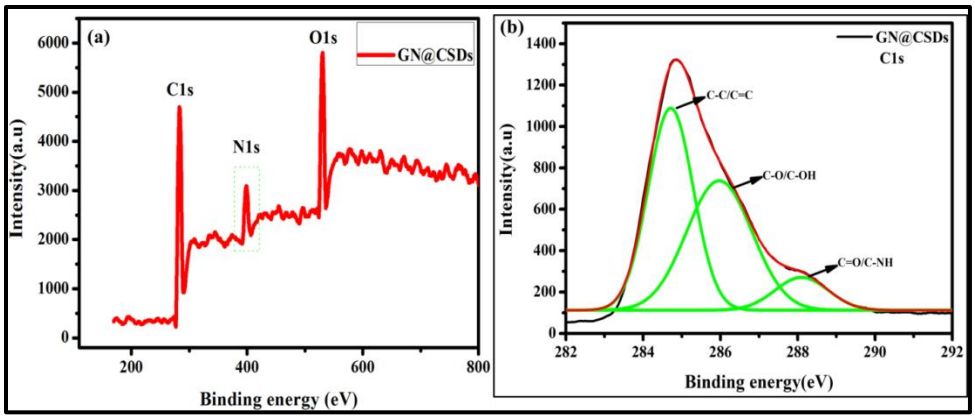

Figure 4.9. (a) Survey XPS spectra of GN@CSDs (b) Deconvoluated C1s spectrum of GN@CSDs.

AFM of GN@CSDs was performed and its lateral dimensions and edge thicknesses were measured. GN@CSDs dispersions were deposited and dried on the mica substrate. The cross-sectional view of GN@CSDs indicates lateral dimension in the range (180-220 nm) with the thickness of 2 nm indicating the formation of few-layer exfoliated sheets. GN@CSDs showed irregular edges with asymmetric flakes (Figure **4.10a**) size arising due to high sonicating forces. To gain insight about GN@CSDs sheets more than 100 G flakes were evaluated to obtain average lateral thickness which was around 188 nm (Figure **4.10c**). Also, most of the exfoliated sheets exhibited flake thickness of around 2 nm inferring 2-4 layer thick exfoliated sheets formation [50]. Further, it can be seen from (Figure **4.10a**) that GN@CSDs exhibited crumpled morphology with foldable and wrinkled layers and were consistent with earlier reports [51]. Apparently, some macroscopic aggregates can easily be observed with the smaller sizes for exfoliated GN@CSDs. Further from Figure **4.10a** presence of smaller c-dots (N@CSDs) onto the exfoliated sheets can be observed having the horizontal distance in the range 12-13 nm with spherical morphology, which confirms that high sonicating force does not affect the morphology of N@CSDs and supports its stability as discussed earlier in Figure **4.4a**. Also, N@CSDs

was partially adsorbed onto the exfoliating sheets which have potential in securing inherent properties of G [52].

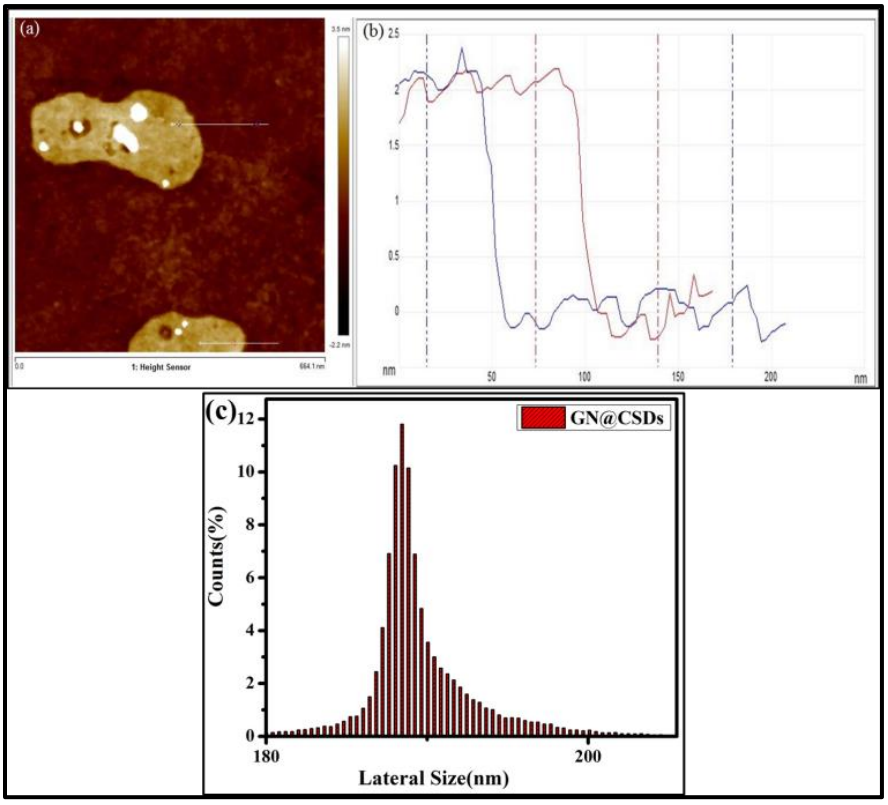

Figure 4.10. (a) AFM image of GN@CSDs (b) Height profile of GN@CSDs (c) Histogram of lateral size distribution of GN@CSDs from AFM image.

To further authenticate G formation TEM of GN@CSDs dispersion was performed. Production of few-layer G sheets can easily be observed in Figure **4.11a-b**. Formations of disordered sheets with sharp edges were observed. However, no distinct holes and structural damages were found suggesting no structural damage with high sonicating forces. At higher magnification (Figure **4.11b**) asymmetric G flakes were observed which confirms the AFM data shown in Figure **4.10a**. In Figure **4.11c** presence of N@CSDs was observed on exfoliated GN@CSDs sheets confirm the direct evidence of N@CSDs adsorption on exfoliated sheets. Further, the SAED pattern of GN@CSDs as shown in Figure **4.11d** shows the

distorted electron diffraction pattern from the perfect hexagonal pattern of Gr. The distortion occurs because of sonication which leads to disturbance in bernal stacking and formation of various sextets from differently oriented layers. [49,54].

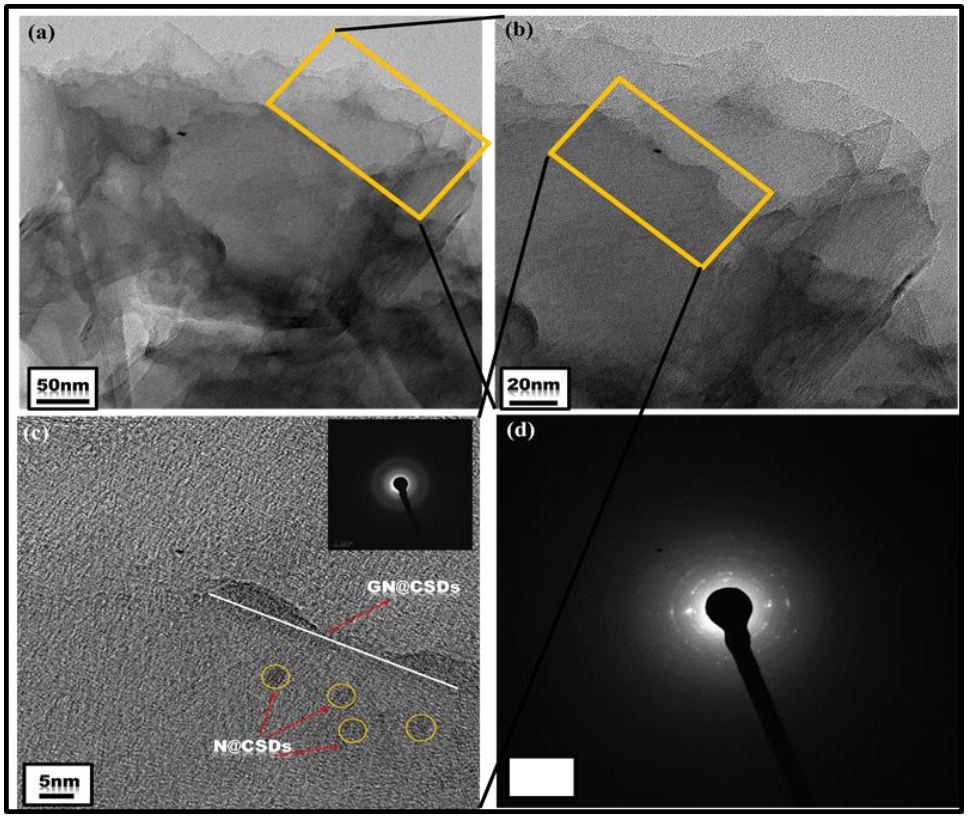

Figure 4.11 (a-c) Representative TEM image of GN@CSDs (inset: SAED of N@CSDs) (d) SAED pattern of GN@CSDs.

4.2.3. Mechanism of N@CSDs towards direct exfoliation & colloidal stability of GN@CSDs

The earlier reports suggest that high shear forces and stabilizing agents are essential traits needed for direct exfoliation to occur [55,56]. In the present work shear forces were applied via high-temperature sonication (~60^{o}C) and stabilization was attained via adsorption of N@CSDs on exfoliated sheets. High-temperature sonication was given to lower the surface tension of water and to provide sufficient energy to break graphitic layers by

cavitation process [57] (i.e. at 60°C the surface tension water decreases to 66.180 mN/m) [22,58]. The lowering of surface tension facilitates the exfoliation process by disrupting the van der Waals interaction between the graphitic sheets [59]. It must be mentioned here that no observable difference in surface tension of water and N@CSDs was observed suggesting no role of it in lowering of surface tension. Further, to investigate the dispersing mechanism zeta potential of N@CSDs and GN@CSDs were measured at pH=7. As shown in Figure **4.12a** both N@CSDs (30.60 mV) and GN@CSDs (44.20 mV) exhibit positive charges. It was worth mentioning that positive potential value arises from amino functional group present in N@CSDs [40]. Also, it is known that pure G sheet doesn't exhibit any charge thus any charge on the exfoliated sheets must get originated from adsorbed C-dots through π-π interaction and stabilizes GN@CSDs via electrostatic interactions [37]. The interaction between G sheets and C-dots occurs through the edges of the sheets having presence of dangling atoms which have easy affinity to reacts with the stabilizing agents [60]. The amount of N@CSDs adsorbed on GN@CSDs surface was determined from TGA spectra (Figure **4.12b**) and was approximate ~30wt%. The adsorbed quantity of N@CSDs was lower compared to gum-arabic assisted exfoliation [61-63].

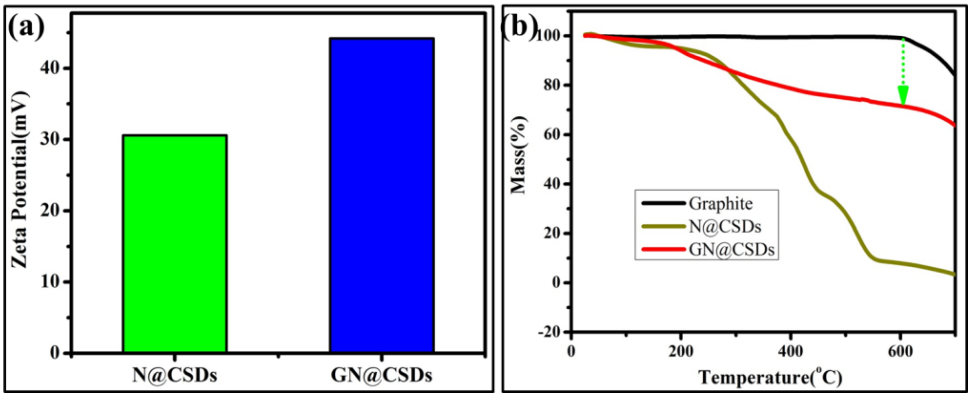

Figure 4.12 (a) Zeta potential value of N@CSDs and GN@CSDs at pH=7 (b) TGA curve of Graphite, N@CSDs and GN@CSDs.

Colloidal stability of G dispersion depends upon the stabilizing agent and its degree of functionalization [23,64]. As discussed earlier, here N@CSDs acts as the stabilizing agent for the exfoliated sheets; thus, any structural change in N@CSDs due to varying harsh conditions i.e. salt, pH & temperature may influence the stability of GN@CSDs. Thus, an aqueous dispersion of GN@CSDs was analysed by *UV-Vis* spectrometer for its colloidal stability study. GN@CSDs exhibit stable colloidal solution for more than a month as no significant change in absorbance value@660 nm was observed (Figure **4.13a**). Further it was observed that GN@CSDs (Figure **4.13b-d**) were quite stable at various harsh conditions like very high (1M NaCl) salt concentrations, different pH and storage temperatures (-80^{o}C, -20^{o}C, 5^{o}C, 27^{o}C &37^{o}C). These results imply very good colloidal stability of GN@CSDs under varying harsh conditions by using N@CSDs as an exfoliating agent.

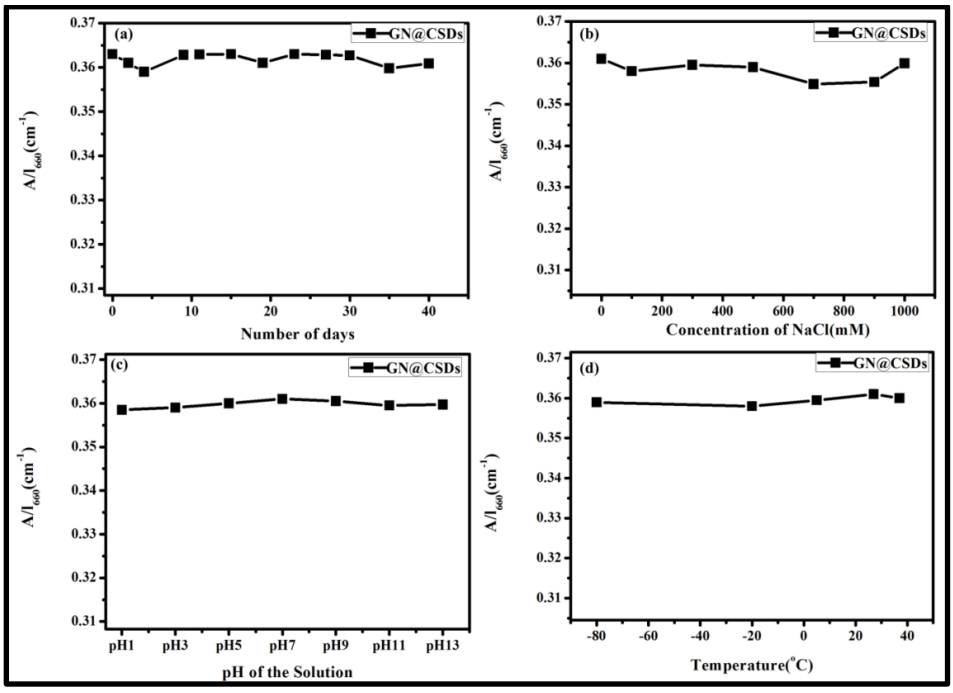

Figure 4.13 Colloidal stability of GN@CSDs (a) effect of the number of days (b) effect of salt concentration (c) effect of pH of the solution (d) effect of storage temperature.

4.2.4. Antibacterial activity of GN@CSDs

The antibiotic-resistant bacteria such as *E.coli* cause a severe threat to public health, especially in hospitals. Carbon nanomaterials especially G and C-dots cause antibacterial activity by damaging bacterial cell walls by interacting physically with them. The orientations, morphologies, defects, and presence of surface functional groups affect the antibacterial efficacy of G based materials. Most of the works on antibacterial activity of G were studied on graphene oxide (GO) [65]. Jijie et al [66]; synthesized amine-functionalized C-dots immobilized on ampicillin. Ampicillin conjugated C-dots used for antibacterial activity by combining the antibacterial nature of ampicillin and the photodynamic nature of C-dots. C-dots have a greater affinity towards the *E coli* cell wall. Despite the great potential of G and C-dots towards antibacterial activity G-C-dots combinations have seldom been used so far for antibacterial activity. In the present work effect of GN@CSDs on the growth of *E Coli* was investigated. The growth inhibition studies were performed using the disk diffusion test and media turbidity assay. From the disc diffusion test it was observed (Figure **4.14a-b**) GN@CSDs shows concentration-dependent size inhibition behaviour and is very potent against bacteria's growth. Various concentrations of GN@CSDs were incubated for 24 h and results were summarised in Figure **4.15**. The size of the zone of inhibition increases gradually with an increase in concentration as a maximum diameter of 24 mm was found with a concentration of100 µg/mL. In media turbidity assay GN@CSDs were tested with different concentration (20 µg mL^{-1}-100 µg mL^{-1}). A gradual decrease in OD_{600} (as shown in Figure **4.14c**) value infers growth inhibition as concentration was increased from 20 µg mL^{-1} to 100 µg mL^{-1}). The MIC & MBC were not observed for concentration to 100 µg mL^{-1} after 7h of incubation. As discussed, earlier GN@CSDs exhibit intense "D" bands (Figure **4.5b**) and higher oxygen content (~20 atom %) as shown in Figure **4.9a**. This leads to a lesser C/O ratio (4.003) and enhanced oxygen functionality. Thus, the plausible

mechanism for the antibacterial nature of GN@CSDs towards *E Coli* arises from the generation of reactive oxygen species which provokes the cells to enter in the oxidative stress [65,67] and results into damaging of cellular components such as lipid, DNA etc. Which further leads to the disintegration of cellular membrane followed by cell death [68] also the sharp edges and corner sites of GN@CSDs interacts with bacterial membrane and may cause its cell membrane to get disrupted [69,70].

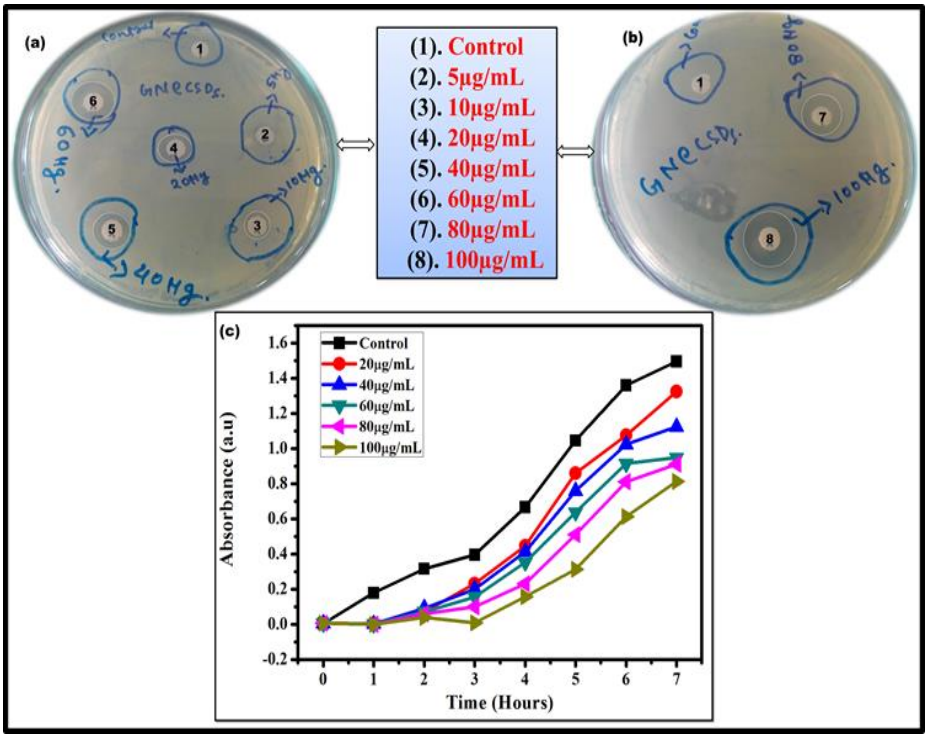

Figure 4.14. Antibacterial activity of GN@CSDs (a-b) Zone of inhibition formed by GN@CSDs in disk diffusion test (c) growth curve of *Escherichia Coli* post incubation with GN@CSDs at various concentrations.

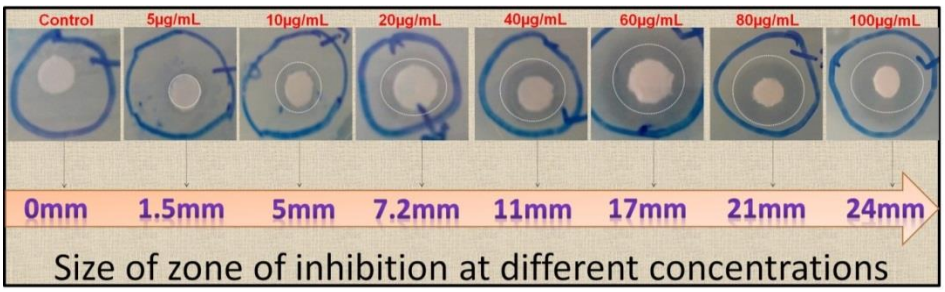

Figure 4.15. Size of zone of inhibition (mm) due to GN@CSDs varying concertation by disk diffusion test.

4.3. Conclusion

To conclude, the direct exfoliation method has drawn significant attention because of its easy synthesis condition; facile and large-scale production. Earlier mainly surfactants; proteins; polymers and solvents were explored for direct exfoliation [71]. However, facing grueling in removing these exfoliating agents from the exfoliated sheets severely limits its properties [7]. C-dots having similar conjugated carbon in its structure provide strong adsorption and have more potential as a stabilizing agent. Thus, exploring sustainable sources reduces our dependence on chemicals and may open a new avenue for green C-dots inspired exfoliating agents. In the present work for the very first time, sustainable source "*Cannabis Sativa*" engineered carbon dots (N@CSDs) were explored as an exfoliating agent to directly exfoliate Gr to G sheets (GN@CSDs) in a facile manner. N@CSDs exhibit only partial coverage onto the exfoliated sheets which provide attaining the pristine properties of G. GN@CSDs exhibit irregular morphology arising from high sonication forces and formation of few-layer sheets. Further, I_D/I_G and I_{2D}/I_G values were quite high (i.e. 0.85 & 0.89 respectively). The higher I_{2D}/I_G value arises from the recovery for C=C bonds (sp^2) in the graphitic structures [18]. Also, the pronounced "D" band and C/O value may occur from the oxygen atom present in N@CSDs adsorbed onto the exfoliated sheets. The exfoliation mechanism involves, lowering of surface tension due to high-temperature sonication and

stabilization via electrostatic interactions. The as-synthesized GN@CSDs was stable at various conditions such as pH, storage temp, number of days & salt concentration. GN@CSDs then exhibit antibacterial activity by inhibiting the growth of bacteria. The present method opens a new avenue of exploring 0D materials (carbon dots) to interact with a 3D material (graphite) and exfoliate it into a 2D material (graphene) and henceforth making it applicable for various industrial applications like solar cells, biomedical and photonic devices. Further, the present work is expected to attract attention towards exploring C-dots as an exfoliating agent for other 2D materials like WS_2, MoS_2, BN etc.

4.4. Experimental section

4.4.1. Materials

Gr powder was purchased from Thermo-Fisher. "*Cannabis Sativa*" was purchased from the local market and used without any further purification. Ethylene diamine was purchased from sigma-aldrich. All the chemicals used in the experiments were of analytical grade and used without any further purification. Deionized water (DI) from Sartorius milli-Q system was used throughout the study.

4.4.2. Synthesis of CSDs and N@CSDs

CSDs & N@CSDs were synthesized using the hydrothermal method. Typically, 250 mg paste from *Cannabis Sativa* (Family: Cannabaceae Genus: Cannabis Species: Sativa) was mixed in 50 mL water and 9 mL of ethylenediamine were added in the reaction mixture for nitrogen doping (N@CSDs). The reaction mixture was then transferred into an autoclave for hydrothermal treatments at 180^{o}C for 16 h. Undoped samples (CSDs) were synthesized at a similar reaction condition without adding ethylenediamine. After completion, the reaction product was centrifuged, and the supernatant was lyophilized to obtain N@CSDs and CSDs.

4.4.3. Direct exfoliation of graphite using N@CSDs

As synthesized N@CSDs (30 mg) and graphite (30 mg) were mixed in an equal ratio in 5 mL DI water. The mixture was then subjected for ultrasonication in a sonication bath at the temperature (~60^{o}C) for 150 minutes. The as-prepared aqueous dispersion was then centrifuged at 4000 rpm for 15 min. The exfoliated graphene was then isolated from settled larger graphite particles. The stable supernatant was used for further characterization.

4.4.4. Characterization

Absorbance spectra of CSDs, N@CSDs and GN@CSDs were studied from UV-Vis spectroscopy using an instrument Agilent Cary 60 UV-Visible spectrometer. The fluorescence nature of CSDs and N@CSDs were studied using the fluoromax spectrofluorometer. Raman measurement was performed with a 785 nm laser source using a LabRAM HR (UV System). The powder x-ray diffraction (PXRD) was performed on a Rigaku Smart Lab X-ray diffractometer using CuK_{α} as a radiation source (1.54 Å). FTIR spectra measured in the range [4000-400 cm^{-1}] using instrument Bio-Rad FTS 3000MX. X-ray photoelectron spectroscopy (XPS) was performed on instrument AXIS ULTRA with model: PHI 5000Versa ProbeII. Morphologies and lateral size of N@CSDs and GN@CSDs were measured using AFM (Bruker, Billerica; MA). Samples were drop cast and air dried on mica sheets. Tapping mode of AFM was performed for the measurement. Scanning electron microscopy was performed on Carl Zeiss Supra 55 FE-SEM. TEM was performed on “JEOL JEM 2200FS” with an acceleration voltage of 200 kV. Cyclic voltammetry was performed on AUTOLAB PGSTAT 204N.

4.4.5. Bactericidal studies of GN@CSDs

For investigating the antibacterial nature of GN@CSDs growth inhibition studies were carried out for gram-negative bacteria *Escherichia Coli* strain

DH5α. Luria Broth medium was used for culturing DH5α bacteria at 37 ^{o}C. A single colony of bacteria was extracted in LB broth at 37^{o}C for the investigation. Two different tests were performed for studying antibacterial activity. The first test was the disc diffusion test. Different concentrations of GN@CSDs (5 µg/mL, 10µg/mL, 20 µg/mL, 40 µg/mL, 60 µg/mL, 80 µg/mL &100 µg/mL) were applied to sterile discs. These discs were then placed on inoculated plates. The zones of inhibition were then measured in "mm" after incubating the plates at 37^{o}C for 24 h. The second test was a media turbidity assay. 50 mL LB broth media were incubated with GN@CSDs with varying concentrations (20 µg/mL, 40 µg/mL, 60 µg/mL, 80 µg/mL &100 µg/mL) in a 250 mL flask. 500 µL of bacterial suspension was added in all flasks for maintaining uniform concentrations of bacteria. A negative control (bacterial+ media) & positive control (media+ GN@CSDs) were maintained along with experimental flask. Culture flasks were placed in an incubator shaker at 220 rpm and 37^{o}C. Absorbance was recorded at 600 nm for measuring growth kinetics.

4.5. References

[1] A.K.Geim, K.S.Novoselov (2007), K. S. The Rise of Graphene, Nat. Mater., 6 (3), 183–191 (DOI: https://doi.org/10.1038/nmat1849)

[2] J.-H.Ahn, B.H. Hong (2014), Graphene for Displays That Bend, Nat. Nanotechnol., 9, 737–738 (DOI: https://doi.org/10.1038/nnano.2014.226)

[3] B. Cho, J.Yoon, M.G. Hahm, D.H Kim, Y.H. Kahng, S.W. Park, Y.J. Lee, S.G Park, J.D. Kwon (2014), Graphene-Based Gas Sensor: Metal Decoration Effect and Application to a Flexible Device, J. Mater. Chem. C., *2* (27), 5280–5285 (DOI: https://doi.org/10.1039/C4TC00510D)

[4] J. Liu, J.Dong, T. Zhang, Q. Peng (2018), Graphene-Based Nanomaterials and Their Potentials in Advanced Drug Delivery and Cancer Therapy, J. Controlled Release., *286*, 64–73 (DOI: https://doi.org/10.1016/j.jconrel.2018.07.034)

[5] A.Arvinte, A.M. Sesay (2017) Graphene Applications in Biosensors and Diagnostics. In *Biosensors and Nanotechnology*; Wiley-Blackwell., pp 297–326. (DOI: https://doi.org/10.1002/9781119065036.ch13)

[6] A.Alnuaimi, I. Almansouri, I. Saadat, A. Nayfeh (2017), Toward Fast Growth of Large Area High Quality Graphene Using a Cold-Wall CVD Reactor, RSC Adv., *7* (82), 51951–51957 (DOI: https://doi.org/10.1039/C7RA10336K)

[7] F. Bonaccorso, A. Lombardo, T. Hasan, Z. Sun, L. Colombo, A.C. Ferrari, A. C (2012), Production and Processing of Graphene and 2d Crystals, Mater. Today., 15 (12), 564–589 (DOI: https://doi.org/10.1016/S1369-7021(13)70014-2)

[8] W. Strupinski, K. Grodecki, K.; Wysmolek, A.; Stepniewski, R.; Szkopek, T.; Gaskell, P. E.; Grüneis, A.; Haberer, D.; Bozek, R.; Krupka, J.; (2012), Graphene Epitaxy by Chemical Vapor DepositiononSiC, NanoLett., 11(4), 1786–1791 (DOI: https://doi.org/10.1021/nl200390e)

[9] H.Wang, C. Wei, K. Zhu, Y. Zhang, C. Gong, Yu. Zhang, J. Zhang (2017), J. Preparation of Graphene Sheets by Electrochemical Exfoliation of Graphite in Confined Space and Their Application in Transparent Conductive Films, ACS Appl. Mater. Interfaces, 2017, *9* (39), 34456–34466(DOI: https://doi.org/10.1021/acsami.7b09891)

[10] C. Teng, D. Xie, J. Wang, Z. Yang, G. Ren, Y. Zhu (2017), Ultrahigh Conductive Graphene Paper Based on Ball-Milling Exfoliated Graphene, Adv. Funct. Mater., 27 (20), 1700240. (DOI: https://doi.org/10.1002/adfm.201700240)

[11] H. Yu, B. Zhang, C. Bulin, R. Li, R. Xing (2016), High-Efficient Synthesis of Graphene Oxide Based on Improved Hummers Method, Sci.Rep., 6, 36143.

(DOI: https://doi.org/10.1038/srep36143)
[12] A. Ejigu, K. Fujisawa, B.F. Spencer, B. Wang, M. Terrones, I.A. Kinloch, R.A.W. Dryfe (2018), On the Role of Transition Metal Salts During Electrochemical Exfoliation of Graphite: Antioxidants or Metal Oxide Decorators for Energy Storage Applications, Adv. Funct. Mater., 0 (0), 1804357.
(DOI: https://doi.org/10.1002/adfm.201804357)
[13] Z.Y Xia, S. Pezzini, E. Treossi, G. Giambastiani, F. Corticelli, V. Morandi, A. Zanelli, V. Bellani, V. Palermo (2013), The Exfoliation of Graphene in Liquids by Electrochemical, Chemical, and Sonication-Assisted Techniques: A Nanoscale Study. Adv. Funct. Mater., 23 (37), 4684–4693
(DOI: https://doi.org/10.1002/adfm.201203686)
[14] S.Pei, Q. Wei, K. Huang, H.-M. Cheng, W. Ren (2018), Green Synthesis of Graphene Oxide by Seconds Timescale Water Electrolytic Oxidation, Nat. Commun., 9 (1), 145
(DOI: https://doi.org/10.1038/s41467-017-02479-z)
[15] J.M. Munuera, J.I. Paredes, M. Enterría, A. Pagán, S. Villar-Rodil, M.F.R. Pereira, J.I.Martins, J.L. Figueiredo, J.L. Cenis, A. Martínez-Alonso (2017), Electrochemical Exfoliation of Graphite in Aqueous Sodium Halide Electrolytes toward Low Oxygen Content Graphene for Energy and Environmental Applications, ACS Appl. Mater. Interfaces., 9 (28), 24085–24099
(DOI: https://doi.org/10.1021/acsami.7b04802)
[16] S.Yang, M.R. Lohe, K. Müllen, X. Feng (2016), New-Generation Graphene from Electrochemical Approaches: Production and Applications, Adv. Mater.,28 (29), 6213–6221
(DOI: https://doi.org/10.1002/adma.201505326)
[17] A.M. Abdelkader, A.J. Cooper, R.a.W Dryfe, I.A. Kinloch (2015), How to Get between the Sheets: A Review of Recent Works on the Electrochemical Exfoliation of Graphene Materials from Bulk Graphite, Nanoscale., 7 (16), 6944–6956.
(DOI: https://doi.org/10.1039/C4NR06942K)
[18] C.-Y. Su, A.-Y. Lu, Y. Xu, F.-R Chen, A.N. Khlobystov, L.-J. Li (2011), High-Quality Thin Graphene Films from Fast Electrochemical Exfoliation, ACS Nano., 5 (3), 2332–2339
(DOI: https://doi.org/10.1021/nn200025p)
[19] L.-J. Li, C.-Y Su (2014), Preparation of Graphene Sheets, US8858776B2, October 14, 2014.
[20] S. Yang, S. Brüller, Z.-S. Wu, Z. Liu, K. Parvez, R. Dong, F. Richard, P. Samorì, X. Feng, K. Müllen (2015), Organic Radical-Assisted Electrochemical Exfoliation for the Scalable Production of High-Quality Graphene, J. Am. Chem. Soc., 137 (43), 13927
(DOI:13932. https://doi.org/10.1021/jacs.5b09000)

[21] L. Niu, J.N. Coleman, H. Zhang, H. Shin, M. Chhowalla, Z. Zheng (2016), Production of Two-Dimensional Nanomaterials via Liquid-Based Direct Exfoliation, Small., 12 (3), 272–293 (DOI: https://doi.org/10.1002/smll.201502207)

[22] P. Tiwari, N. Kaur, V. Sharma, S.M. Mobin (2018), High-Yield Graphene Produced from the Synergistic Effect of Inflated Temperature and Gelatin Offers High Stability and Cellular Compatibility, Phys. Chem. Chem. Phys., 20 (30), 20096–20107 (DOI: https://doi.org/10.1039/C8CP02263A)

[23] A. Pattammattel, C.V. Kumar (2015), Kitchen Chemistry 101: Multigram Production of High Quality Biographene in a Blender with Edible Proteins, Adv. Funct. Mater., 25 (45), 7088–7098 (DOI: https://doi.org/10.1002/adfm.201503247)

[24] X. Zhang, L. Wang, Q. Lu, D.L. Kaplan (2018), Mass Production of Biocompatible Graphene Using Silk Nanofibers, ACS Appl. Mater. Interfaces., 10 (27), 22924–22931 (DOI: https://doi.org/10.1021/acsami.8b04777)

[25] H. Zhuo, X. Zhang, L. Wang, Q. Lu, D.L. Kaplan (2018), Sonication Exfoliation of Defect-Free Graphene in Aqueous Silk Nanofiber Solutions, ACS Sustain. Chem. Eng., 6(9), 12261–12267 (DOI: https://doi.org/10.1021/acssuschemeng.8b02644)

[26] S. Zhao, S. Xie, Z. Zhao, J. Zhang, L. Li, Z. Xin (2016), Green and High-Efficiency Production of Graphene by Tannic Acid-Assisted Exfoliation of Graphite in Water, ACS Sustain.Chem.Eng., 6(6), 7652–7661 (DOI:https://doi.org/10.1021/acssuschemeng.8b00497)

[27] V. Sharma, N. Kaur, P. Tiwari, S.M. Mobin (2018), S. M. Full Color Emitting Fluorescent Carbon Material as Reversible PH Sensor with Multicolor Live Cell Imaging, J. Photochem. Photobiol. B., 182, 137–145 (DOI: https://doi.org/10.1016/j.jphotobiol.2018.04.006)

[28] Y.Wang, A. Hu (2014), Carbon Quantum Dots: Synthesis, Properties and Applications, J. Mater. Chem. C., 2 (34), 6921–6939 (DOI: https://doi.org/10.1039/C4TC00988F)

[29] V. Sharma, A.K. Saini, S.M. Mobin (2016), Multicolour Fluorescent Carbon Nanoparticle Probes for Live Cell Imaging and Dual Palladium and Mercury Sensors, J. Mater. Chem. B., 4 (14), 2466–2476 (DOI: https://doi.org/10.1039/C6TB00238B)

[30] Q. Zeng, D. Shao, X, He, Z. Ren, W. Ji, C. Shan, S. Qu, J. Li, L. Chen, Q. Li (2016), Carbon Dots as a Trackable Drug Delivery Carrier for Localized Cancer Therapy in Vivo, J. Mater. Chem. B., 4 (30), 5119–5126 (DOI: https://doi.org/10.1039/C6TB01259K)

[31] J. Zhang, S.-H. Yu (2016), Carbon Dots: Large-Scale Synthesis, Sensing and Bioimaging, Mater. Today.,19 (7), 382–393. (DOI: https://doi.org/10.1016/j.mattod.2015.11.008)

[32] X. Lin, G. Gao, L. Zheng, Y. Chi, G. Chen (2014), Encapsulation of Strongly Fluorescent Carbon Quantum Dots in Metal–Organic Frameworks for Enhancing Chemical Sensing, Anal. Chem., 86 (2), 1223–1228 (DOI: https://doi.org/10.1021/ac403536a)

[33] H.Wang, P. Sun, S. Cong, J. Wu, L. Gao, Y. Wang, X. Dai, Q. Yi, Z. Zou (2016), Nitrogen-Doped Carbon Dots for "Green" Quantum Dot Solar Cells, Nanoscale Res. Lett., 11 (1), 27 (DOI: https://doi.org/10.1186/s11671-016-1231-1)

[34] D. Carolan, C.Rocks, D.B. Padmanaban, P. Maguire, V. Svrcek, D. Mariotti (2017), Environmentally Friendly Nitrogen-Doped Carbon Quantum Dots for next Generation SolarCells, Sustain.EnergyFuels., 1(7),1611–1619 (DOI: https://doi.org/10.1039/C7SE00158D)

[35] W. Li, S. Wu, H. Zhang, X. Zhang, J. Zhuang, C. Hu, Y. Liu, B. Lei, L. Ma, X. Wang (2018), Enhanced Biological Photosynthetic Efficiency Using Light-Harvesting Engineering with Dual-Emissive Carbon Dots, Adv. Funct. Mater., 28 (44), 1804004 (DOI: https://doi.org/10.1002/adfm.201804004)

[36] V. Sharma, P. Tiwari, S.M. Mobin (2017), Sustainable Carbon-Dots: Recent Advances in Green Carbon Dots for Sensing and Bioimaging, J. Mater. Chem. B., 5 (45), 8904–8924 (DOI: https://doi.org/10.1039/C7TB02484C)

[37] P. He, J. Sun, S. Tian, S.Yang, S. Ding, G. Ding, X. Xie, M. Jiang (2015), Processable Aqueous Dispersions of Graphene Stabilized by Graphene Quantum Dots, Chem. Mater., 27 (1), 218–226 (DOI: https://doi.org/10.1021/cm503782p)

[38] A. Konwar, U. Baruah, M.J. Deka, A.A. Hussain, S.R. Haque, A.R. Pal, D. Chowdhury (2017), Tea-Carbon Dots-Reduced Graphene Oxide: An Efficient Conducting Coating Material for Fabrication of an E-Textile, ACS Sustain. Chem. Eng., 5 (12), 11645–11651 (DOI: https://doi.org/10.1021/acssuschemeng.7b03021)

[39] H.Xu, L.Xie, M. Hakkarainen (2017), Coffee-Ground-Derived Quantum Dots for Aqueous Processable Nanoporous Graphene Membranes, ACS Sustain. Chem. Eng., 5 (6), 5360–5367 (DOI: https://doi.org/10.1021/acssuschemeng.7b00663)

[40] M. Zeng, S.A. Shah, D. Huang, D. Parviz, Y.-H. Yu, X. Wang, M.J. Green, Z. Cheng (2017), Aqueous Exfoliation of Graphite into Graphene Assisted by Sulfonyl Graphene Quantum Dots for Photonic Crystal Applications, ACS Appl. Mater. Interfaces., 9 (36), 30797–30804 (DOI: https://doi.org/10.1021/acsami.7b06980)

[41] M. Xu, W. Zhang, Z. Yang, F. Yu, Y. Ma, N. Hu, D. He, Q. Liang, Y. Su, Y. Zhang (2015), Y. One-Pot Liquid-Phase Exfoliation from Graphite to Graphene with Carbon Quantum Dots, Nanoscale., 7 (23), 10527–10534 (DOI: https://doi.org/10.1039/C5NR02198G)

[42] G. Appendino, S. Gibbons, A. Giana, A. Pagani, G. Grassi, M. Stavri, E. Smith, M.M. Rahman (2008), Antibacterial Cannabinoids

from Cannabis Sativa: A Structure−Activity Study, J. Nat. Prod., 71 (8), 1427–1430 (DOI: https://doi.org/10.1021/np8002673)
[43] X. Yang, Y. Zhuo, S. Zhu, Y. Luo, Y. Feng, Y. Dou (2014), Novel and Green Synthesis of High-Fluorescent Carbon Dots Originated from Honey for Sensing and Imaging, Biosens. Bioelectron., 60, 292–298 (DOI: https://doi.org/10.1016/j.bios.2014.04.046)
[44] M. Zeng, S.A. Shah, D. Huang, D. Parviz, Y.-H Yu, X. Wang, M.J. Green, Z. Cheng (2017), Aqueous Exfoliation of Graphite into Graphene Assisted by Sulfonyl Graphene Quantum Dots for Photonic Crystal Applications, ACS Appl. Mater. Interfaces., 9 (36), 30797–30804 (DOI: https://doi.org/10.1021/acsami.7b06980)
[45] S. Xu, Z. Su, Z. Zhang, Y. Nie, J. Wang, G. Ge, X. Luo (2017), Rapid Synthesis of Nitrogen Doped Carbon Dots and Their Application as a Label Free Sensor Array for Simultaneous Discrimination of Multiple Proteins, J. Mater. Chem. B., 5 (44), 8748–8753 (DOI: https://doi.org/10.1039/C7TB02129A)
[46] P. Wang, D. Zhang, L. Zhang, Y. Fang (2013), The SERS Study of Graphene Deposited by Gold Nanoparticles with 785nm Excitation, Chem. Phys. Lett., 556, 146–150 (DOI: https://doi.org/10.1016/j.cplett.2012.11.018)
[47] L.Gong, R.J. Young, I.A. Kinloch, S.J. Haigh, J.H. Warner, J.A. Hinks, Z. Xu, L. Li, F. Ding, I. Riaz (2013), Reversible Loss of Bernal Stacking during the Deformation of Few-Layer Graphene in Nanocomposites, ACS Nano., 7 (8), 7287–7294 (DOI: https://doi.org/10.1021/nn402830f)
[48] S. Sampath, A.N. Basuray, K.J. Hartlieb, T. Aytun, S.I. Stupp, J.F. Stoddart (2013), Direct Exfoliation of Graphite to Graphene in Aqueous Media with Diazaperopyrenium Dications, Adv.Mater., 25 (19), 2740–2745 (DOI: https://doi.org/10.1002/adma.201205157)
[49] S. Bhattacharya, S. Mishra, P. Gupta, P.; Pranav; M. Ghosh, A.K. Pramanick, D.P. Mishra, S. Nayar (2015), Liquid Phase Collagen Modified Graphene That Induces Apoptosis, RSC Adv, 5(55), 44447–44457 (DOI: https://doi.org/10.1039/C5RA06629H)
[50] B.-H. Wee, T.-F Wu, J.-D. Hong (2017), Facile and Scalable Synthesis Method for High-Quality Few-Layer Graphene through Solution-Based Exfoliation of Graphite, ACS Appl. Mater. Interfaces., 9 (5), 4548–4557 (DOI: https://doi.org/10.1021/acsami.6b11771)
[51] J. Malig, C. Romero-Nieto, N. Jux, D.M. Guldi (2012), Integrating Water-Soluble Graphene Into PorphyrinNanohybrids, Adv.Mater. 24(6), 800–805 (DOI: https://doi.org/10.1002/adma.201103697)
[52] P. He, J. Sun, S. Tian, S. Yang, S. Ding, G. Ding, X. Xie, M. Jiang, (2015), Processable Aqueous Dispersions of Graphene Stabilized by Graphene Quantum Dots, Chem. Mater., *27*(1), 218–226 (DOI: https://doi.org/10.1021/cm503782p)

[53] S. Gurunathan, J.W. Han, J.H. Park, J. H. Kim (2014), An in Vitro Evaluation of Graphene Oxide Reduced by Ganoderma Spp. in Human Breast Cancer Cells (MDA-MB-231), Int. J. Nanomedicine., 1783 (DOI: https://doi.org/10.2147/IJN.S57735)

[54] M. Lotya, Y. Hernandez, P.J. King, R.J. Smith, V. Nicolosi, L.S. Karlsson, F.M. Blighe, S. De, Z. Wang, I.T. McGovern (2009), Liquid Phase Production of Graphene by Exfoliation of Graphite in Surfactant/Water Solutions, J. Am. Chem. Soc., 131(10), 3611–3620 (DOI: https://doi.org/10.1021/ja807449u)

[55] M. Cao, N. Wang, L. Wang, Y. Zhang, Y. Chen, Z. Xie, Z. Li, E. Pambou, R. Li, C. Chen (2015),. Direct Exfoliation of Graphite into Graphene in Aqueous Solutions of Amphiphilic Peptides, J. Mater. Chem. B., 4(1), 152–161 (DOI: https://doi.org/10.1039/C5TB02065D)

[56] A. Ciesielski, P. Samorì (2013), Graphene via Sonication Assisted Liquid-Phase Exfoliation, Chem. Soc. Rev., 43 (1), 381–398. (DOI: https://doi.org/10.1039/C3CS60217F)

[57] J. Kim, S. Kwon, D.-H Cho, B. Kang, H. Kwon, Y. Kim, S.O. Park, G.Y. Jung, E. Shin, W.-G Kim (2015), Direct Exfoliation and Dispersion of Two-Dimensional Materials in Pure Water via Temperature Control, Nat. Commun., 6, 8294 (DOI: https://doi.org/10.1038/ncomms9294)

[58] F.A. Gonçalves, J. Kestin, J.V. Sengers (1991), Surface-Tension Effects in Suspended-Level Capillary Viscometers, Int. J. Thermophys., 12 (6), 1013–1028 (DOI: https://doi.org/10.1007/BF00503516)

[59] M. Cai, D.H. Thorpe, D.C. Adamson, H. Schniepp (2012), Methods of Graphite Exfoliation, J. Mater. Chem., 22(48), 24992–25002 (DOI: https://doi.org/10.1039/C2JM34517J)

[60] N. Rosenkranz, C. Till, C. Thomsen, J. Maultzsch (2011), J. Ab Initio Calculations of Edge-Functionalized Armchair Graphene Nanoribbons: Structural, Electronic, and Vibrational Effects, Phys.Rev.B., 84(19), 195438 (DOI: https://doi.org/10.1103/PhysRevB.84.195438)

[61] V. Chabot, B. Kim, B. Sloper, C. Tzoganakis, A. Yu (2013), High Yield Production and Purification of Few Layer Graphene by Gum Arabic Assisted Physical Sonication, Sci. Rep., 3, 1378 (DOI: https://doi.org/10.1038/srep01378)

[62] J. Fan, Z. Shi, Y. Ge, J. Wang, Y. Wang, J. Yin (2012), Gum Arabic Assisted Exfoliation and Fabrication of Ag–Graphene-Based Hybrids, J. Mater. Chem., 22 (27), 13764–13772 (DOI: https://doi.org/10.1039/C2JM31437A)

[63] J. Fan, Z. Shi, J. Wang, J. Yin (2013), Glycidyl Methacrylate-Modified Gum Arabic Mediated Graphene Exfoliation and Its Use for Enhancing Mechanical Performance of Hydrogel, Polymer., 54 (15), 3921–3930.

(DOI: https://doi.org/10.1016/j.polymer.2013.05.057)
[64] V. Georgakilas, M. Otyepka, A.B. Bourlinos, V. Chandra, N. Kim, K.C. Kemp, P. Hobza, R. Zboril, K.S. Kim (2012), Functionalization of Graphene: Covalent and Non-Covalent Approaches, Derivatives and Applications, Chem. Rev., 112(11), 6156–6214 (DOI: https://doi.org/10.1021/cr3000412)
[65] S. Szunerits, R. Boukherroub (2014), Antibacterial Activity of Graphene-Based Materials, J. Mater. Chem. B., 4(43), 6892–6912 (DOI: https://doi.org/10.1039/C6TB01647B)
[66] R. Jijie, A. Barras, J. Bouckaert, N. Dumitrascu, S. Szunerits, R. Boukherroub (2018), Enhanced Antibacterial Activity of Carbon Dots Functionalized with Ampicillin Combined with Visible Light Triggered Photodynamic Effects, Colloids Surf. B Biointerfaces., *170*, 347–354 (DOI: https://doi.org/10.1016/j.colsurfb.2018.06.040)
[67] S. Gurunathan, J. Woong Han, A. Abdal Daye, V. Eppakayala, J. Kim (2012), J. Oxidative Stress-Mediated Antibacterial Activity of Graphene Oxide and Reduced Graphene Oxide In PseudomonasAeruginosa, Int.J.Nanomedicine., 5901 (DOI: https://doi.org/10.2147/IJN.S37397)
[68] K. Krishnamoorthy, M. Veerapandian, L.-H. Zhang, K. Yun, S.J. Kim (2012), Antibacterial Efficiency of Graphene Nanosheets against Pathogenic Bacteria via Lipid Peroxidation, J. Phys. Chem. C., 116 (32), 17280–17287 (DOI: https://doi.org/10.1021/jp3047054)
[69] Y. Li, H. Yuan, A. Bussche, R.H. Hurt, A.B. Kane, H. Gao (2013), Graphene Microsheets Enter Cells through Spontaneous Membrane Penetration at Edge Asperities and Corner Sites, Proc. Natl. Acad. Sci., 110 (30), 12295–12300 (DOI: https://doi.org/10.1073/pnas.1222276110)
[70] L. Hui, J.-G. Piao, J. Auletta, K. Hu, Y. Zhu, T. Meyer, H. Liu, L. Yang (2014), Availability of the Basal Planes of Graphene Oxide Determines Whether It Is Antibacterial, ACS Appl. Mater. Interfaces., 6 (15), 13183–13190 (DOI: https://doi.org/10.1021/am503070z)
[71] J.I. Paredes, S. Villar-Rodil (2016), Biomolecule-Assisted Exfoliation and Dispersion of Graphene and Other Two-Dimensional Materials: A Review of Recent Progress and Applications, Nanoscale., 8(34), 15389–15413. (DOI: https://doi.org/10.1039/C6NR02039A)

CHAPTER 5

Cannabis Sativa derived carbon dots with N-S co-doped: highly efficient nanosensors for temperature and vitamin B_{12}

5.1. Introduction

Temperature, as we know is an elemental framework and any change in temperature may affect the biological, physical and chemical behaviour of the entities. The thermal monitoring is important in many existing fields ranging from electronic devices; medical diagnostics; biochemical reactions etc. [1–4]. Over the last decade, the nanomaterials inspired thermal sensing using semiconducting nanocrystals [5], rare earth doped nanoparticles [6–10], organic compounds [11], metal nanoparticles [12–14] etc. have gained much attention. However, low quantum yield; high toxicity; poor photostability were the major drawbacks [15]. Nucleic acids based thermal sensing offers advantages in terms of ease of synthesis and detection using common bioanalytical techniques. Grass et al [16]., encapsulated nuclei acid in silica for temperature sensing by analyzing damages in nucleic acid through qPCR because of accumulated temperature. Recently carbon nanoparticles, which have potential as an alternative to inorganic semiconducting nanomaterials have been investigated for detecting temperature, particular for cell line works or living cells [17–23].

Cobalamin or vitamin B_{12} (VB_{12}) is a water-soluble vitamin which can be easily found in various food sources like meat, dairy products and eggs [24]. Further, VB_{12} is critical in the metabolism of cells and in myelin synthesis which is needed for normal functioning of nervous system [25] and it contains “Co” in the centre of its corrin ring [26]. So, VB_{12} plays an essential role in a human healthy body. Regular monitoring of VB_{12} is essential because of the presence of excessive VB_{12} causes toxic effects

leading to shortage of folic acid [27]. Initially, several analytical methods such as HPLC-UV, atomic absorption spectroscopy, microbological assay etc. have been applied for its monitoring, however high cost; complicated sample preparation and time consumption limited its applicability [28]. Calorimetric detection of VB_{12} provides advantages compared with other methods due to its uncomplicated, subtle & selective nature. Recently, organic dyes [29]; metallic nanoclusters [30] & semiconducting quantum dots [31] were used to sense VB_{12} based on the fluorometric assay. However, toxicity and complex operational process were a major concern. Hence, exploration of biocompatible sensors forVB_{12} is imperative [32,33].

Zero-dimensional carbon nanomaterial (C-dots) having size ≤ 10 nm exhibits excellent optical properties like excitation dependent multi-colour emission; very high fluorescence; significant quantum yield; very stable photoluminescence and resistance to photobleaching [34]. The facile synthesis of C-dots using green carbon precursor provides advantages like cheapness; ease of availability and substantial cellular compatibility [35–37]. C-dots have opened a new avenue in biosensing and biomedical applications [38–42]. Further, tedious synthesis protocol, poor photostability and toxicity were the major concerned associated with the earlier method used for temperature sensing thus; motivated us to explore C-dots based calorimetric sensing.

Herein, in the present work, we focussed on "*Cannabis Sativa*" leaves as a green precursor and synthesized N-S heteroatom-doped carbon dots **N-S@CsCD**. *Cannabis Sativa* offers great medicinal values and its carbon dots were earlier used for direct exfoliation of graphite [43]. Heteroatom doping provides an efficient way to improve the fluorescent property of C-dots and also increases the solubility and photophysical properties [44]. Nitrogen having similar electronic structure to that of carbon can contribute their unpaired electron as an electron donor to carbon and improve the emission nature of C-dots [45]. Further, sulphur the fifth

most common element present on earth also has similar electronegativity to that of carbon [46]. Also, the atomic radius of sulphur is much bigger than that of carbon hence will make the electronic transition easier. N-S heteroatom doping increases the fluorescent nature of C-dots [47,48]. Further, the synthesized **N-S@CsCD** was used as a nanosensor for temperature and VB_{12}.

5.2. Results and discussion

Highly fluorescent nitrogen and sulphur co-doped C-dots (**N-S@CsCD**) were synthesized using the hydrothermal method by employing *Cannabis sativa*, ethylene diamine and glutathione as a carbon, nitrogen and sulphur precursors, respectively (**Scheme 1**). **N-S@CsCD** was extensively characterised using techniques like *UV-vis* spectroscopy, fluoresecence spectroscopy, XPS, TEM and AFM microscopy to gain insight about its structural and optical characteristics. As synthesized **N-S@CsCD** offers good quantum yield; high photostability and cytocompatibility. Further, the multifunctional characteristics of **N-S@CsCD** were investigated as a nanosensor by getting fluorescence "turn-off" with temperature and VB_{12}.

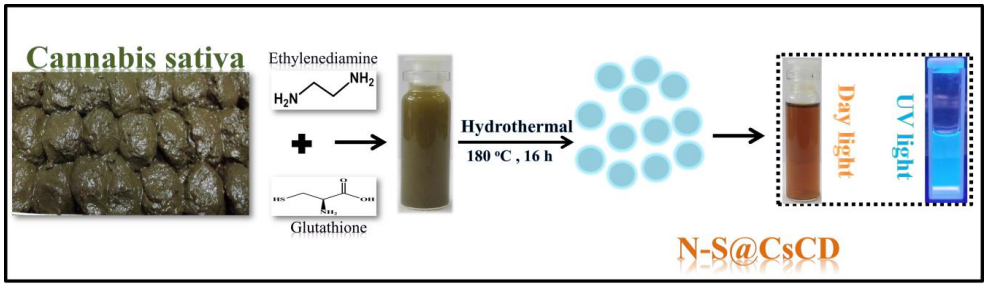

Scheme 5.1. Schematic representation of **N-S@CsCD** preparation.

5.2.1. Morphological and structural characterization of N-S@CsCD

The structural and morphological characterizations of N-S@CsCD were investigated using TEM and AFM. From TEM micrograph (Figure **5.1a**) ultra-small particles with size range (4-6 nm) were found. AFM micrograph (Figure **5.1b**) reveals the presence of smaller particles with

spherical morphologies. However, some agglomerated particles were also observed which may arise due to smaller particle size and high dangling bonds. AFM line scanning revels horizontal distance between 8.3 nm and 9.4 nm and height range from 1.5 to 2.7 nm. The origination of these C-dots formation involves carbonization present in *cannabis* [50]. The carbonization process starts with the decomposition of *cannabis sativa* constituents because of hydrothermal treatment which further leads to polymerization and polycondensation of decomposed carbon [34] and then during polymerization small carbon nuclei gets emerged. Afterwards, with the continuous increase in temperature, the carbon nuclei grew further and form amorphous dots. The PXRD spectrum of **N-S@CsCD** (Figure **5.1c**) confirms the amorphous characteristics by exhibiting the signature broader hump at $2\theta = 24.3^{o}$. The corresponding interlayer spacing was calculated and was around 0.61 nm and was higher than the corresponding graphitic layer spacing at (002) plane. The increased interlayer spacing and broader hump supports the amorphous nature of **N-S@CsCD** and arises because of oxygen containing functional groups [51].

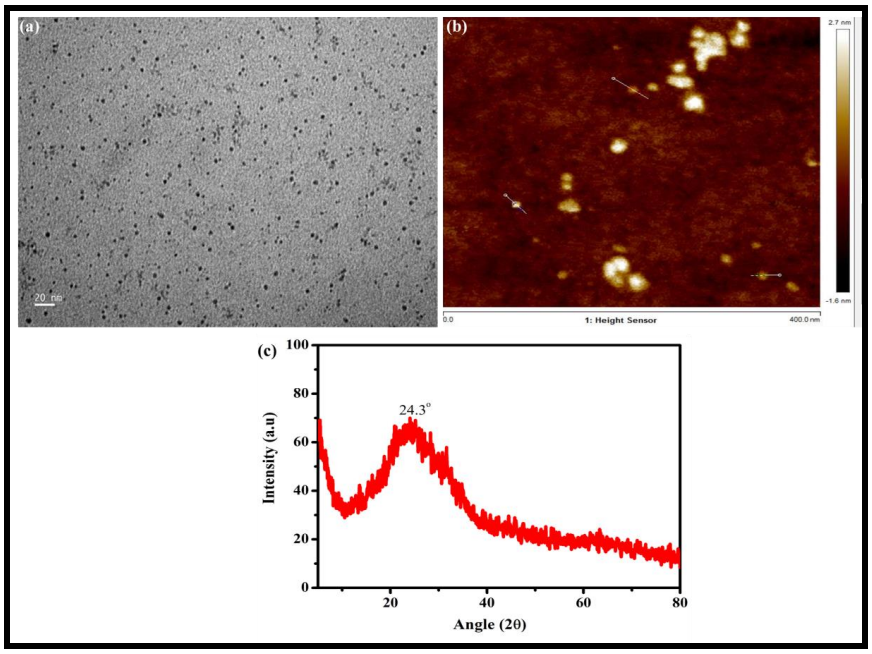

Figure 5.1. Structural characterization of **N-S@CsCD** (a) TEM micrograph (b) AFM micrograph (c) PXRD.

5.2.2. Optical and surface characterization of N-S@CsCD

For investigating the optical behavior of **N-S@CsCD** its *UV-Vis* and fluorescence spectroscopy were performed. The *UV-Vis* spectra peaks correspond to π–π* and n–π* transitions occur around 280 nm and 320 nm (Figure **5.2a**) [52]. The **N-S@CsCD** exhibits the maximum emission at 384 nm when it was excited with 320 nm wavelength light. Furthermore, Figure **5.2b** shows the excitation independent emission behavior of the **N-S@CsCD** between the wavelength range of 280 nm-340 nm. The fluorescence intensity almost gets diminished with a further excitation wavelength and with a shift in its emission wavelength as shown in the emission spectrum of the Figure **5.2b**. Thus, the emission spectrum supports the degeneracy in emission behavior which originates from a uniform emissive energy level [53]. The absolute quantum yield of **N-S@CsCD** was investigated by taking quinine sulphate as a reference and was found to be around 14% under an excitation wavelength of 320 nm. **N-S@CsCD** shows highly intense cyan colour under UV lamp thus, making it an excellent luminescent probe. The average lifetime of **N-S@CsCD** was calculated using TCSPC technique by exciting at 320 nm diode laser and monitored at 384 nm bandpass filter. The average lifetime was around 3.07 ns after tri-exponential fitting (as shown in Figure **5.2c**).

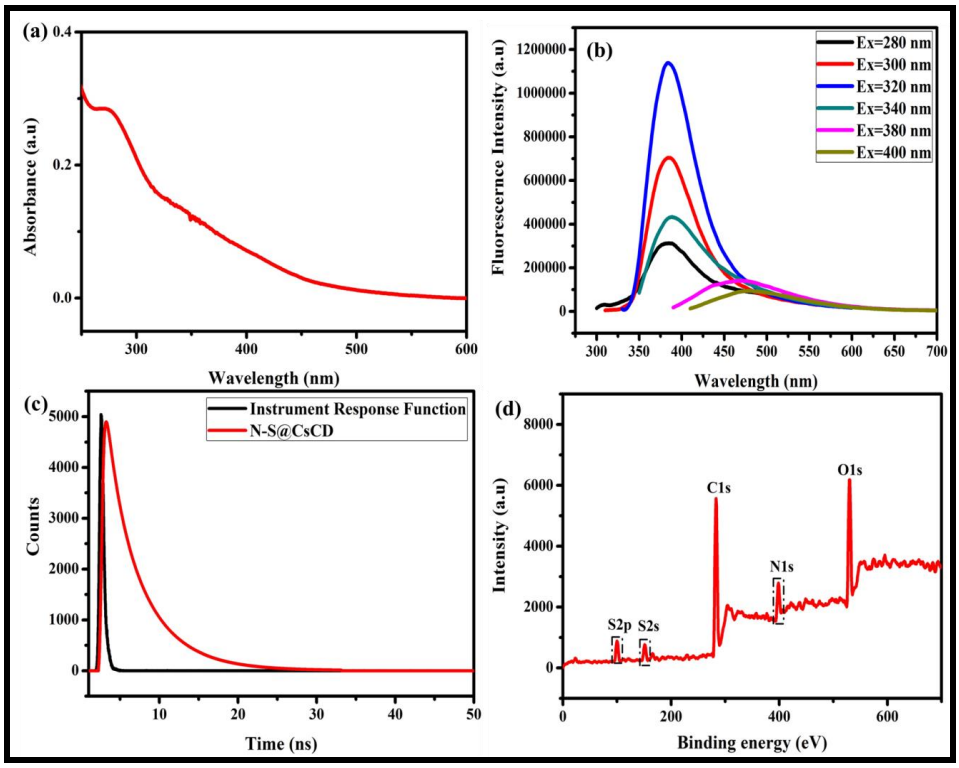

Figure 5.2. Optical and surface characterization of **N-S@CsCD** (a) *UV-Vis* spectra (b) emission spectra with variation in excitation wavelength (c) TCSPC (d) XPS survey spectrum.

XPS spectra give insights about chemical bonding and elemental composition of **N-S@CsCD** (Figure **5.2d**). The survey scan of XPS confirms the presence of carbon; nitrogen; sulphur and oxygen with concentrations 66.55, 10.71, 1.94and 20.79% respectively. Further, deconvolution of C1s, O1s, N1s and S2p was done to explore the various chemical bonds present in **N-S@CsCD**. The deconvoluated peak of C1s confirms the presence of C-C; C-O/C-S and C-NH bond at 284.7 eV, 286 eV and 288 eV as shown in Figure **5.3a**. Similarly, the presence of C-O and N-O was observed with O1s deconvoluated peak at 528.2 and 531.9 eV (Figure **5.3b**). The presence of N1s and S2p peak confirms the successful doping of nitrogen and sulphur. Also, the deconvoluted peaks and the presence of various bands were consistent with earlier reports [54,55].

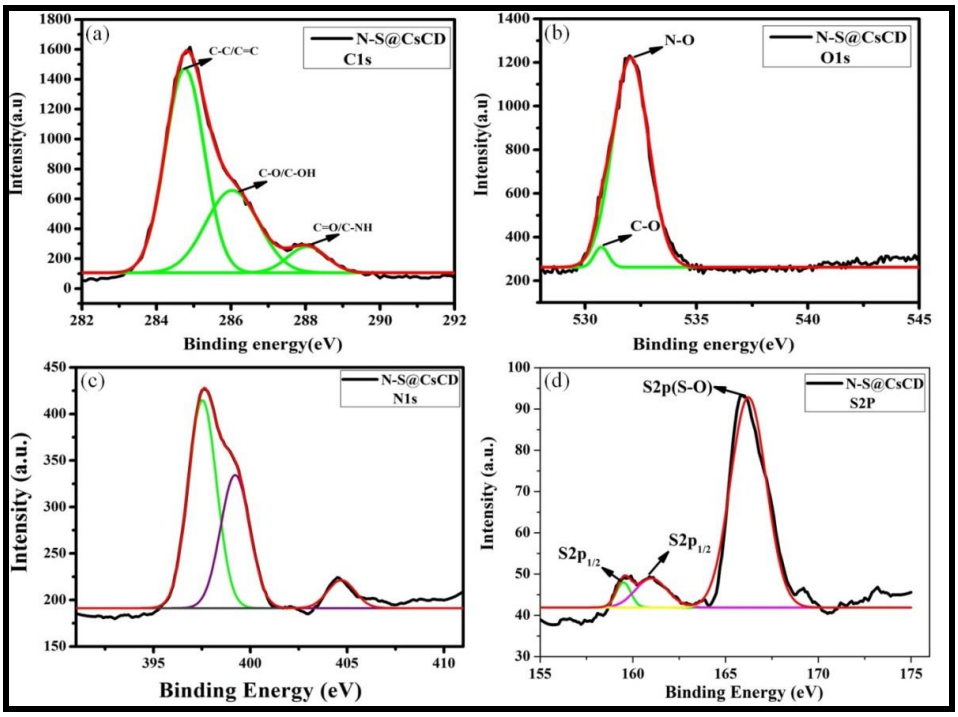

Figure 5.3. Deconvoluated XPS peak of **N-S@CsCD** (a) C1s (b) O1s (c) N1s (d) S2p.

The FTIR spectrum of **N-S@CsCD** shown in **Figure 5.4** displays –OH/-NH groups at 3364 cm^{-1}. Also, the band around 2878 and 2831 cm^{-1} corresponds to C-H stretching. The band at 1640, 1517, 1474 & 1230 cm^{-1} corresponds C=C, N-O stretching, C-H bending and C-O stretching respectively.

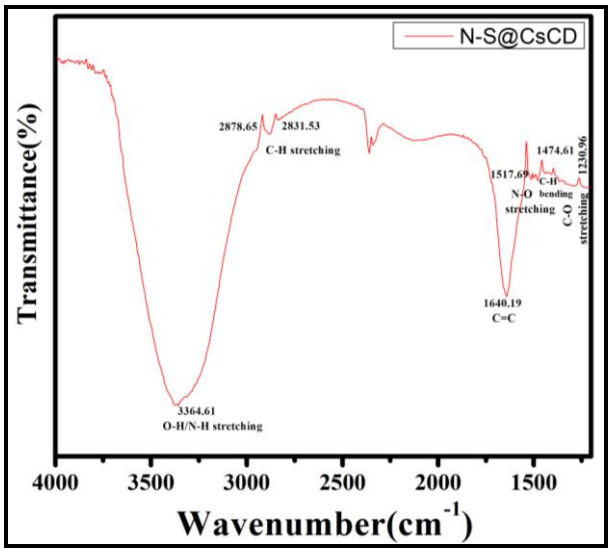

Figure 5.4. FTIR spectra of **N-S@CsCD**.

The fluorescence stability of **N-S@CsCD** was investigated on the number of days; different pH and NaCl concentration. As shown in Figure **5.5a** for over a period of month the fluorescence intensity was almost constant. Similarly, **N-S@CsCD** shows considerable stability under very high concentration of NaCl (1 M) as shown in Figure **5.5b**. The fluorescence intensity of **N-S@CsCD** was quite stable in the pH range (1-13) as shown in Figure **5.5c**. Further, to check the stability of **N-S@CsCD** in the different simulated biological fluid it was subjected to water, phosphate buffer saline (PBS) and Dulbecco's modified Eagle's medium (DMEM). As depicted in Figure **5.5d** the fluorescence intensity of **N-S@CsCD** was almost constant in water & PBS whereas around 25% decrease in fluorescence intensity was observed when **N-S@CsCD** fluorescence was measured in DMEM media. To further confirm the fluorescence characteristics of **N-S@CsCD** in different biological fluid its lifetime was measured using TCSPC and the results were summarized in Figure **5.5e**. The lifetime of **N-S@CsCD** in water and PBS were 3.07 and 2.82 ns respectively. Whereas it gets decreased to 0.37 ns for DMEM media as shown in Figure **5.5e**. **N-S@CsCD** shows high quantum yield, decent fluorescence lifetime and excellent fluorescence stability and thus can become an exciting candidate for nanosensors and biomedical applications.

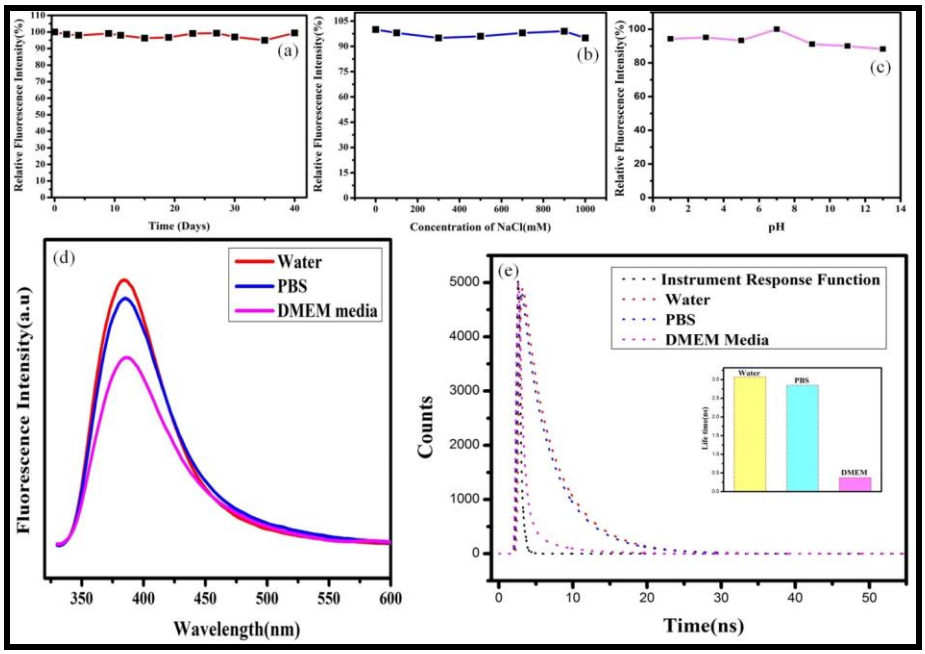

Figure 5.5. Fluorescence stability of **N-S@CsCD** with (a) number of days (b) Salt concentration (c) pH (d) fluorescence intensity of **N-S@CsCD** in varying fluids (e) fluorescence life time decay of **N-S@CsCD** in varying fluid.

5.2.3. Effect of temperature on fluorescence behavior of N-S@CsCD

N-S@CsCD absorbance spectrum was recorded between temperatures 25^{o}C - 80^{o}C and shown in Figure **5.6a**. No observable change in absorption band and intensity was found with an increase in temperature. The results were consistent with earlier C-dots synthesized from glucose [56]. Further, the fluorescence emission of **N-S@CsCD** was recorded with an increase in temperature from 15^{o}C to 80^{o}C. As with the increase in temperature, the fluorescence intensity gets quenched by around 74% at temperature 80^{o}C (Figure **5.6b**). A very good linear relation between temperature and fluorescence intensity was found as a gradual decrease in F/F_o can easily be detected in Figure **5.6c**. To further investigate N-S@CsCD fluorescence lifetime at temperature between 15^{o}C-60^{o}C TCSPC of **N-S@CsCD** was performed (Figure **5.7d**). It was observed that **N-S@CsCD** shows a strong effect on fluorescence emission nature and life time with temperature. The average lifetime of 4.2 ns was found for

N-S@CsCD at temperature 15^{o}C whereas it gets decreased to 1.47 ns as temperature increased to 60^{o}C. The χ^2 value for each fitted sample was closer to 1 suggesting the fitted curve fairly matched with the theoretical curve and were consistent with earlier reports [57,58].

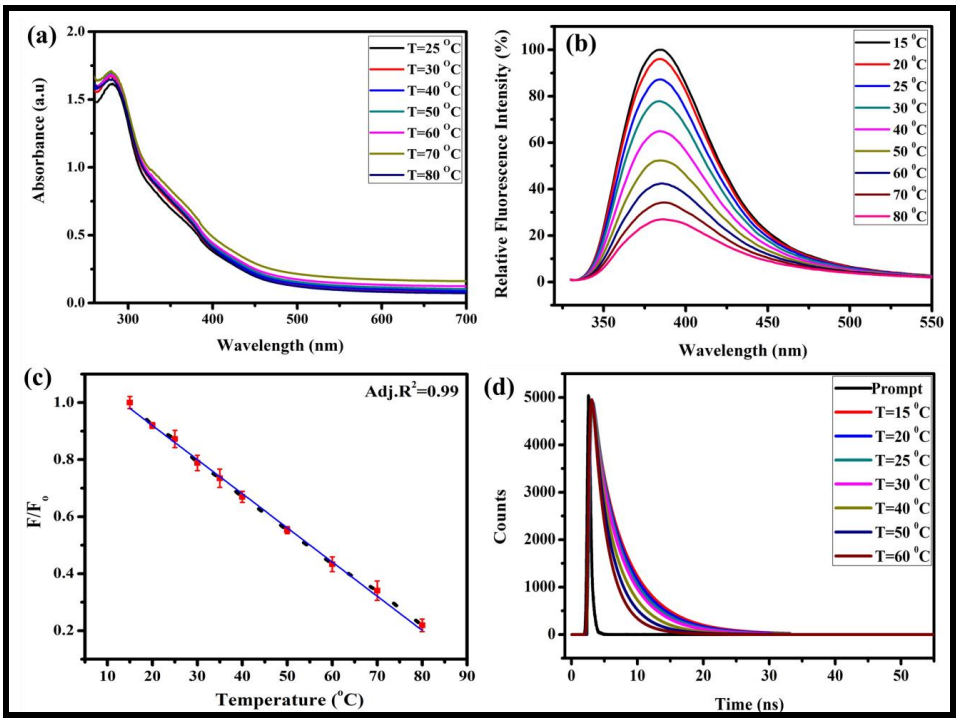

Figure 5.6. N-S@CsCD steady state optical characterization (a) *UV-vis* spectra with temperature increment (b) Fluorescence spectra with temperature increment (c) Linearity plot of temperature dependent fluorescence emission (d) Temperature dependent life time value.

Further, the change in average lifetime value with temperature can easily be fitted using 3rd order polynomial curve, as shown in Figure 5.7 and follows the following equation:-

$$T= 148.75-95.25\tau + 26.20\ \tau^2 -2.62\ \tau^3$$

Here R^2=0.99, T is for temperature (^{o}C) and τ is life time (nS) at T.

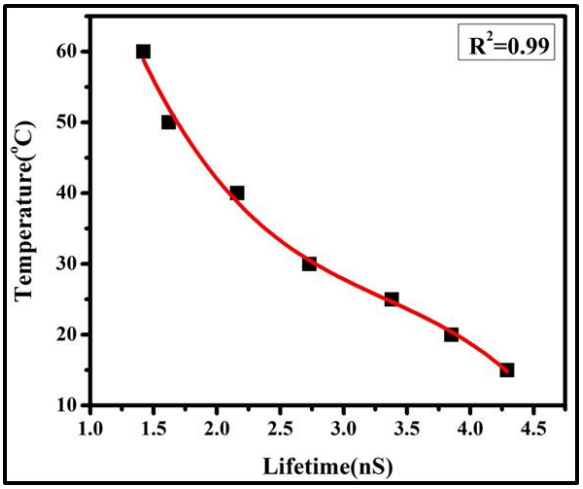

Figure 5.7. Polynomial calibration curve for N-S@CsCD life time value with temperature.

To better understand the quantum efficiency of **N-S@CsCD** with temperature radiative and non-radiative recombination rates were calculated at different temperature. Quantum yield at various temperatures was calculated and plotted as shown in Figure **5.8a**. With the increase in temperature continuous decrease in quantum yield was observed. Further, radiative & nonradiative recombination rates were calculated and plotted shown in Figure **5.8b**. Radiative recombination rate was nearly constant with temperature increment however monotonic increase was easily observed with nonradiative recombinations rate [53]. At higher temperature, thermal activation of nonradiative channel enhances because of trapping by various surface/defects or ionized impurity states which leads to thermal quenching. Thus, the quantum efficiency of **N-S@CsCD** gets decreased with increase in temperature [59].

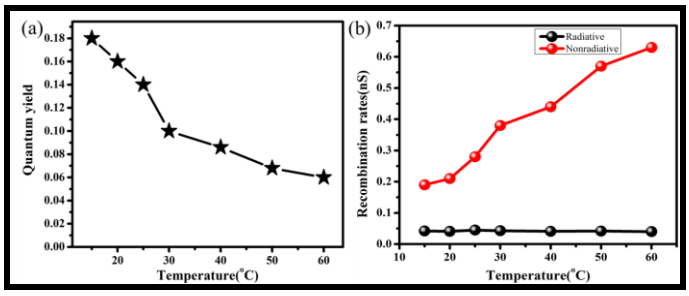

Figure 5.8. Effect of temperature (a) Quantum yield (b) Radiative and nonradiative recombination rates.

The temperature sensing ability of **N-S@CsCD** demonstrates biologically relevant as well as electronic devices operating temperatures which prove its versatility and further applications [53]. To further check temperature sensing capability of N-S@CSDs for biological applications **N-S@CsCD** was kept in simulated biological fluids i.e. PBS and DMEM. The sensing behaviour of **N-S@CsCD** was similar in water, PBS and DMEM as shown in Figure **5.9**. However, the fluorescence quenching was observed in all three fluids but in DMEM around 67% intensity gets quenched whereas in water and PBS around 75% fluorescence intensity gets quenched.

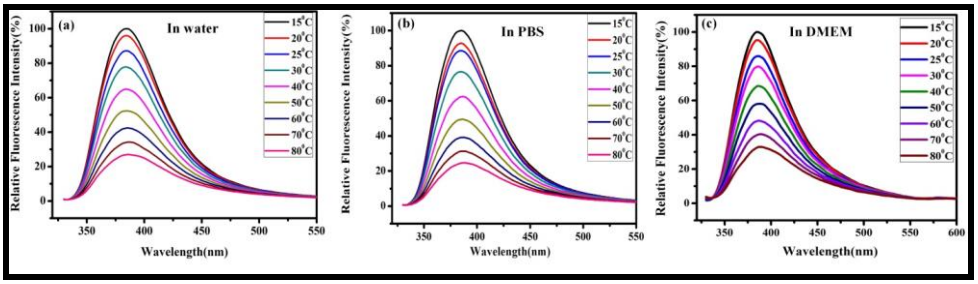

Figure 5.9. Temperature dependent fluorescence changes in **N-S@CsCD** with varying fluid (a) water (b) PBS (c) DMEM.

To further investigate the sensing quality of **N-S@CsCD** its sensing response time was investigated between temperature range = 25°C-15°C (shown in Figure **5.10a**) and temperature range = 25°C-80°C (shown in Figure **5.10b**). From Figure **5.10a** as the temperature gets decreased from 25°C to 15°C the relative fluorescence intensity of **N-S@CsCD** gets increases monotonically however it gets constant after 300 sec. Whereas as temperature increases from 25°C to 80°C within 60 sec the relative fluorescence intensity shows a steep decrease whereas after 60 sec gentle decrease was observed and after 300 sec it becomes almost constant. Thus, for both temperature ranges after 300 sec not much considerable change in relative fluorescence intensity was observed suggesting the sensing response time of **N-S@CsCD** towards temperature was around 300 sec. To further asses the reversible nature of **N-S@CsCD** towards temperature its reversibility study was performed in temp range (15°C-25°C) and

(25°C-80°C) shown in Figure **5.10c** and Figure **5.10d**. The reversible nature of **N-S@CsCD** was consistent even after 4 cycles which proves the robustness of **N-S@CsCD** as a nanosensor for temperature.

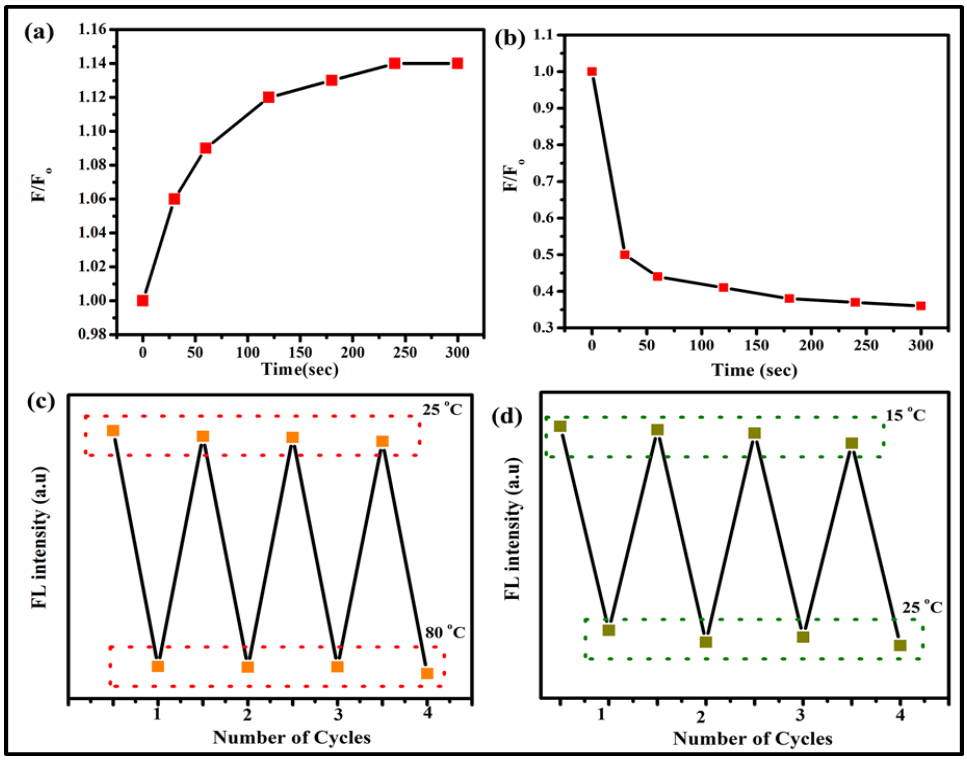

Figure 5.10. (a) Sensing response time of **N-S@CsCD** with temperature range from 25°C to 15°C (b) Sensing response time of **N-S@CsCD** with temperature range from 25°C to 80°C (c) Reversibility in temperature range from 15°C to 25°C (d) Reversibility in temperature range from 25°C to 80°C.

To further evaluate the sensing mechanism, fluorescence spectra of **N-S@CsCD** were deconvoluated using multi-Gaussian function and results were summarized in Figure **5.11** and Table **5.1**. With each temperature increment, the fluorescence spectra can easily be fitted into two- Gaussian functions (R^2=0.99). The peak around 380 nm corresponds to peak 1 and peak around 414 nm corresponds to peak 2. The peak 1 exhibits a larger area with respect to peak 2 (as shown in Figure **5.11a-b**). Interestingly it was observed that both the deconvoluated spectra exhibit very small redshift i.e. 5 nm for peak 1 and 13 nm for peak 2.

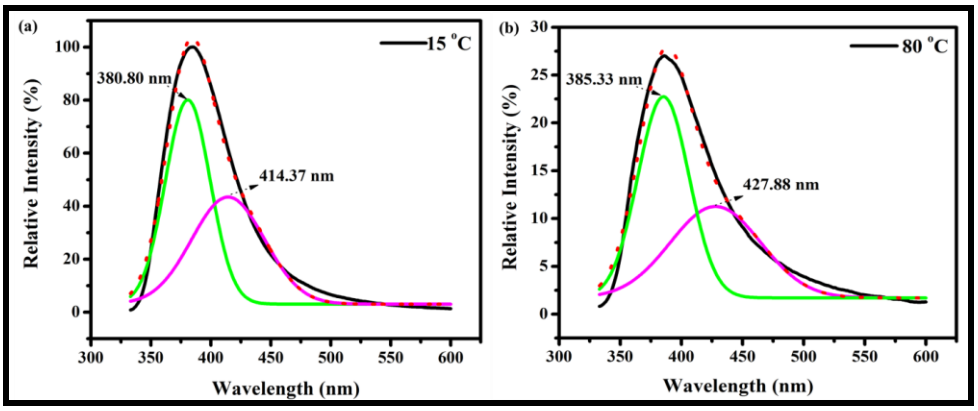

Figure 5.11. Deconvoluated fluorescence spectra with temperature increment (a) Temp~15^{o}C (b) Temp~80^{o}C.

Table **5.1.** Deconvoluated fluorescence spectra with temperature increment.

Sl no	Temp(^{o}C)	FWHM	Peak1(nm)	Peak2(nm)
1	15	43.94	380.80	414.37
2	20	44.05	380.86	414.33
3	25	44.23	381.13	415.20
4	30	44.61	381.33	415.80
5	40	45.37	381.97	417.58
6	50	45.96	382.53	419.17
7	60	47.15	383.46	421.98
8	70	48.09	384.51	424.94
9	80	49.23	385.33	427.88

As, no considerable changes in emission wavelength and absorbance spectrum (Figure **5.6a**) were observed suggesting the weak dependence of **N-S@CsCD** band gap with temperatures [56,60]. Thus, the deconvoluated spectrum, small redshift and weak band gap dependence with temperature suggest **N-S@CsCD** exhibits similar temperature dependency like metallic nanoclusters and were significantly different from semiconducting and inorganic quantum dots [61].

5.2.4. Effect of VB_{12} on fluorescence behavior of N-S@CsCD

As discussed earlier C-dots have become a strong candidate for chemical and biosensing applications and were already used in detecting L-cyestine, messenger RNA (mRNA), DNA etc [62–64]. Thus, in present study the fluorescent stability of **N-S@CsCD** was assessed with different biomolecules (especially vitamins) and strong optical response was found with VB_{12} i.e. fluorescence "turn-off" was observed as shown in Figure **5.12a**. Further, with the addition of VB_{12} in range (0-550 µg/mL) consistent quenching in fluorescence intensity was observed and almost 92% decay of initial fluorescence intensity was found shown in Figure **5.12b**. A linear response was found between 20-100 µg/mL (Figure **5.12c**) and the limit of detection (LOD) was around 7.87 µg/mL.

The limit of detection was calculated using following equation [65]:

$$LOD = 3.3(\sigma/S)$$

Here, σ corresponds to standard error and S corresponds to the slope of the calibration curve. Further to gain more insight about the sensing behaviour, TCSPC of **N-S@CsCD** was performed with and without the addition of VB_{12} (Figure **5.12d**). Interestingly no change in the lifetime value of **N-S@CsCD** was found with and without VB_{12}. As no detectable change in lifetime was found suggesting static quenching mechanism [66]. To further check the versatility of **N-S@CsCD** towards VB_{12} sensing, **N-S@CsCD** fluorescence intensity was recorded in presence of VB_{12} in water, PBS and DMEM as shown in Figure **5.13**. It can easily be seen that decay of 46%, 42% and 39% was observed in water, PBS and DMEM respectively.

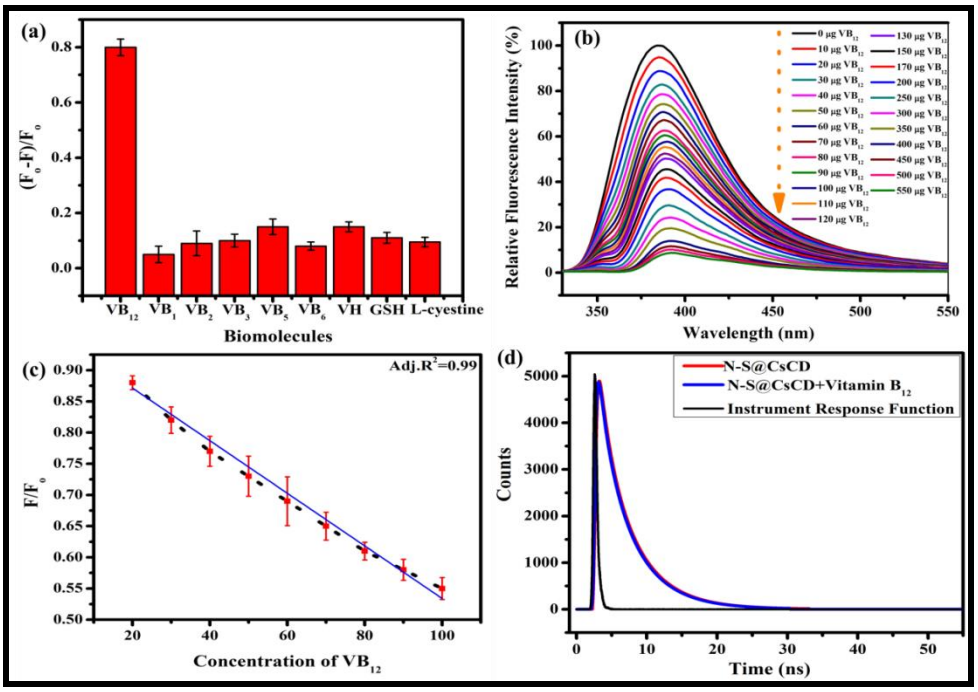

Figure 5.12. (a) Selectivity of sensing behavior towards VB_{12} (b) Fluorescence spectra of **N-S@CsCD** with addition of VB_{12} (Concentration: 10 µg/mL-550 µg/mL) (c) Linear relation with concentration of VB_{12} and F/F_o (d) Fluorescence lifetime decay in absence and presence of VB_{12} of **N-S@CsCD**.

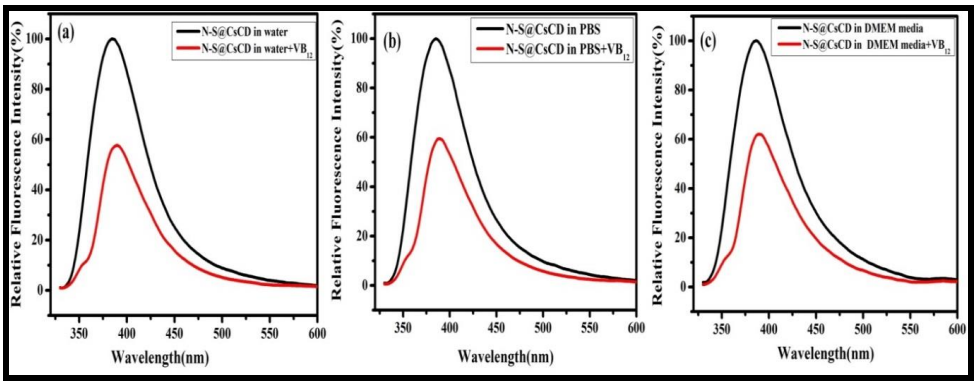

Figure 5.13. Vitamin sensing with **N-S@CsCD** with varying fluid (a) water (b) PBS (c) DMEM.

The sensing response time of **N-S@CsCD** towards VB_{12} was around 25 sec (Figure **5.14a**). Moreover, to check the competitive nature of the sensing system, sensing of VB_{12} was carried out in the presence of other

biomolecules especially vitamins shown in Figure **5.14b**. As elucidated the presence of other biomolecules such as (vitamins, cysteine etc.) does not cause any considerable change in the fluorescence intensity of **N-S@CsCD** whereas the "turn-off" in fluorescence intensity in presence of VB_{12} was not affected with other biomolecules. The performance comparison for VB_{12} sensing (Table **5.2**) based on fluorescence sensing method supports the supremacy of **N-S@CsCD** especially because of its preparation using sustainable carbon source, broader linearity and low LOD value.

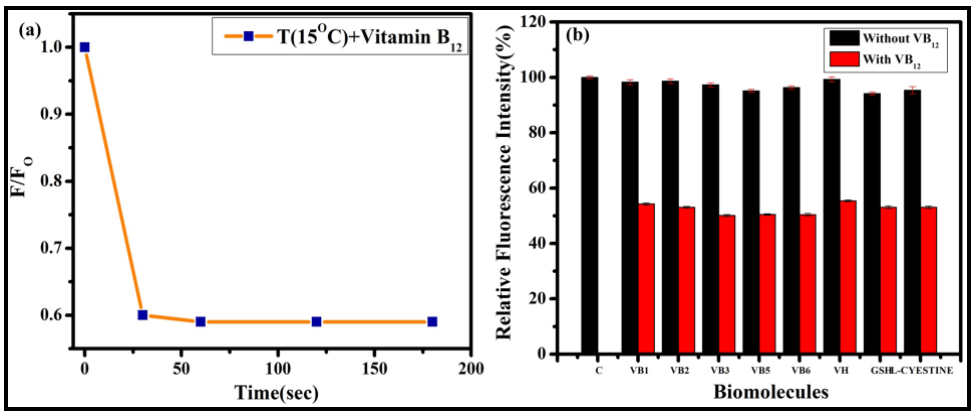

Figure 5.14. (a) Sensing response time of **N-S@CsCD** with VB_{12} (b) Effect of interfering species.

To further determine the practical applicability of **N-S@CsCD** its sensing behaviour was investigated with vitamin B_{12} injection (label value: 1000 mcg/mL). 100 µL of VB_{12} injection were mixed with **N-S@CsCD** solution and fluorescence spectra was recorded. To determine quantitatively the sensing response with real pharmaceutical injections varying known concentrations of VB_{12} was injected in **N-S@CsCD** solution and results were summarized in Table **5.3**. Very high recovery with quite low standard deviation value with real samples supports the practical suitability of **N-S@CsCD** for developing nanosensor for VB_{12} sensing.

Table 5.2. Performance comparison for VB_{12} sensing based on fluorescence sensing method.

Sl no	Sensing element	Linearity	LOD	Ref
1.	Hydroxypropyl-β-cyclodextrin	0–2.1 $\times 10^{-5}$ M	1.8 $\times 10^{-7}$ M	[29]
2.	CdTe QDs	$7x10^{-7}$-$1.8x10^{-5}$ M	$1x10^{-7}$ M	[31]
3.	Carbon dots(Citric acid)	$0.6x10^{-5}$ M	$1x10^{-7}$ M	[67]
4.	t-CD(Citric acid)	1-12 µg/mL	0.1 µg/mL	[68]
5.	Carbon dots (ammonium citrate)	0.3-15 µM	93 nM	[27]
6.	BCQDs (cytidine diphosphate choline)	0-50 mM	81 nM	[33]
7.	Silk Fibroin	-	0.003×10−6 g/µL	[69]
8.	**N-S@CsCD (*Cannabis sativa*)**	**20-100 µg/mL**	**7.87 µg/mL**	**Present work**

Table 5.3. Determination of VB_{12} in real pharmaceutical injections (n=4).

Sample	Claimed Concentration (µg)	Found Concentration (µg)	Recovery (%)	SD
Injection1	20	18.75±0.14	93.75	0.28
Injection2	40	39.28±0.26	98.2	0.53
Injection3	60	57.91±0.53	96.51	1.07
Injection4	80	77.83±0.54	97.28	1.09

5.2.5. Cell viability and bioimaging with N-S@CsCD

After exploring the extraordinary photophysical properties; sensing behaviour of **N-S@CsCD** it's *in vitro* cytotoxicity was investigated. It's very crucial to know the cytocompatibility of any material for its practical applicability, especially for biomedical applications [70]. The toxicity profile of **N-S@CsCD** was studied by MTT assay on HeLa cells with concentrations in the range 20-1200 µg/mL. After 24 h of incubation, the cells were viable as shown in Figure **5.15a**. It can be seen that more than 90% cells were viable at concentration 1200 µg/mL. The non-toxic nature and inherent fluorescent behaviour of **N-S@CsCD** make it an ideal candidate for cell labelling. Before exploring the bioimaging studies phototoxicity of **N-S@CsCD** was investigated on HeLa cells with above mentioned incubation condition and concentrations.

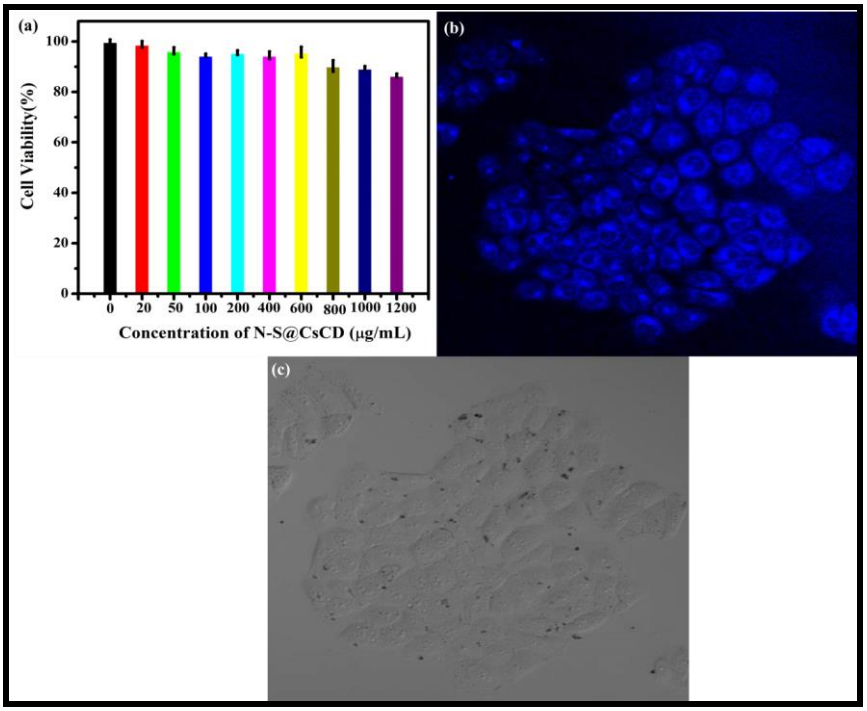

Figure 5.15. (a) Cell viability of HeLa cells after 24 h with varying concentration of **N-S@CsCD** (20-1200 µg/mL) (b) Cellular imaging of HeLa cells at 37^{o}C with **N-S@CsCD** (c) Bright field image of HeLa cells with **N-S@CsCD**.

In order to explore the ability of **N-S@CsCD** for bioimaging HeLa and A375 cells were incubated with **N-S@CsCD** for 3 h and their live cell imaging was performed as shown in Figure **5.15b-c**. As illustrated with excitation of 405 nm laser light blue colour fluorescence signal was observed from confocal microscope. The fluorescence signalling arises because of the internalization of **N-S@CsCD** particles inside the cells through the uptaking process. The uptaking of **N-S@CsCD** occurs because of small size (≤10 nm) and hydrophilic nature via endocytosis [71]. Also, from bright field image (Figure **5.15c**) intact morphology of healthy cells can easily be seen, which supports the non-toxic nature of **N-S@CsCD**.

5.3. Conclusion

In conclusion, N-S doped carbon dots (**N-S@CsCD**) was synthesized using *cannabis sativa* as a carbon precursor. The hetero-atom doped **N-S@CsCD** showed an excellent quantum yield of 14% and photostability with excitation independent emission behaviour. Further, the **N-S@CsCD** exhibited ultrafast dual sensing behaviour towards temperature and VB_{12} by getting fluorescence "turn-off". Importantly, the **N-S@CsCD's** sensing behaviour was reversible for at least 4 cycles in the temperature range (15^oC-25^oC and 25^oC-80^oC) which covers physiological temperature needed for both biological investigations and electronic devices. Further, the limit of detection and linear range of **N-S@CsCD** for VB_{12} sensing was 7.87 µg/mL and 20-100 µg/mL respectively. The practical applicability of VB_{12} was strongly supported by real sample analysis with very high recovery of more than 90%. The sensing behaviour of the **N-S@CsCD** for temperature and VB_{12} was consistent in water, PBS and DMEM. The **N-S@CsCD** exhibited very high cellular uptake and excellent biocompatibility and demonstrated for intracellular imaging. Thus, green carbon precursor, **N-S@CsCD,** with good quantum yield, excellent stability, biocompatibility and strong fluorescence response to

temperature and VB_{12} has potential as a nanosensor in biomedical applications.

5.4. Experimental section

5.4.1. Materials

"*Cannabis Sativa*" paste was procured from the market. Ethylenediamine and Glutathione were purchased from sigma-aldrich and SRL chemicals. The vitamins were purchased from SRL chemicals. All chemicals were of analytical grade. Deionized water (DI) by Sartorius milli-Q system was used for all experiments.

5.4.2. Characterizations

High resolution images of the C-dots were taken by transmission electron microscope (TEM) (JEM-1400, JEOL. Co.). To explore the morphology of N-S@CsCD tapping mode of atomic force microscopy (AFM) (Bruker, Billerica, MA) was used. The powder X-ray diffraction (PXRD) was performed using CuK_{α} radiation (1.54 Å) using Rigaku Smart Lab X-ray diffractometer. The UV-absorbance spectra studies were carried on Cary 100 Bio UV-Visible spectrophotometer. Fluorescence spectrum was recorded on fluoromax spectrofluorometer. The fluorescence lifetime study was conducted on time correlated single photon counting (TCSPC) system (model: Fluorocube-01-NL). The X-ray photoelectron spectra (XPS) were recorded on AXIS ULTRA. Fourier-transform infrared spectroscopy (FTIR) spectra were recorded on Bio-Rad FTS 3000MX instrument. Cell viability was studied using MTT assay and was performed on Synergy H1 Biotek microplate reader. For cellular imaging study an Olympus confocal laser scanning microscope was used.

5.4.3. Synthesis of N-S@CsCD

The synthesis of **N-S@CsCD** was carried on one-step hydrothermal method. 250 mg *Cannabis sativa* paste (Family: Cannabaceae Genus: Cannabis Species: Sativa) was mixed with 50 mL water. In this solution 9 mL ethylenediamine and 300 mg glutathione were added for nitrogen and sulphur doping respectively. Mixed solution was then hydrothermally treated at 180^{o}C for 16 h.

5.4.4. Quantum yield calculation

Fluorescence quantum yield (ϕ) of **N-S@CsCD** was calculated using following equation…. (1)

$\phi = \phi_{st} \times S/S_{st} \times A/A_{st} \times n^2/n^2_{st}$ …… (1)

ϕ_{st} = quantum yield of standard, ϕ = quantum yield of **N-S@CsCD**, quinine sulphate was chosen as standard ($\phi_{st} = 0.54$)

A= absorbance of **N-S@CsCD**, A_{st} = Absorbance of standard at excitation wavelength

n= refractive index of **N-S@CsCD**, n_{st} = solvent refractive index

N-S@CsCD and quinine sulphate was dissolved in DI water and in 0.1 M H_2SO_4.

5.4.5. Temperature sensing experiments

The temperature controlled UV absorption spectra was collected on Perkin Elmer Lambda 35 spectrophotometer equipped with PCB-1500 circulating water Bath. The temperature accuracy of ±0.1^{o}C with reproducibility of ±0.05^{o}C was attained in the thermoelectrically temperature controlled cell holder. The temperature dependent fluorescence measurement was performed on fluomax-4 spectrometer. Temperature controlled cell holder was attached with spectrometer equipped with peltier system (Escy IC 201) with the stability of ±0.03^{o}C (measured over 5 min). The

fluorescence emission was measured at 384 nm with excitation at 320 nm. Temperature dependent fluorescence life time was investigated on TCSPC system (model: fluorescence-01-NL) equipped with temperature controlled cell holder. For analysing the lifetime decay data IBH DAS6.0 software was used. For analysing the lifetime decay data IBH DAS6.0 software[49]. The iterative reconvoluation method measured the fluorescence life time decay and fit value was judged by reduced χ-square (χ^2) value. The decay values were fitted using the following equation with a three-exponential function:

$F(t)= \Sigma a_i \exp(-\tau / \tau_i)$……(2)

Here $F(\tau)$ denotes normalized PL decay; a represents amplitude of decay component τ. Further, the average lifetime was obtained using the following equation:

$< \tau >=\Sigma a_i \tau_i$……..(3)

N@CSDs concentration of 20 µg/mL was used for thermal sensing study by heating and cooling the N@CSDs dispersion.

5.4.6. Vitamin B_{12} sensing and interference studies

Different concentrations of VB_{12} were added systemically in 2 mL to **N-S@CsCD** having a concentration of 20 µg/mL and the fluorescence intensity changes were recorded. The selectivity of **N-S@CsCD** towards VB_{12} was checked with other vitamins under identical conditions. To investigate the effect of interference of some vitamins and amino acids (VB_1; VB_2; VB_3; VB_5; VB_6; VH; Glutathione; L-Cysteine; Methionine) were added to **N-S@CsCD** solution containing VB_{12}. The vitamins concentration was fixed at 100 µg/mL.

5.4.7. Biocompatibility & Bioimaging studies

Cellular compatibility of **N-S@CsCD** was explored on cervical cancerous cell line HeLa by employing MTT assay. Complete nutrient media of (DMEM, Himedia) supplemented with 10% fetal bovine serum (FBS) &

1% antibiotics were supplied to HeLa cells seeded in a 96 well plate. Cells were incubated at $37^{o}C$ and 5% CO_2 for 24 h. **N-S@CsCD** varying concentration 100-1000 µg/mL was given for 24 h. Afterwards, media containing **N-S@CsCD** was replaced with 3-(4,5-dimethylthiazol-2-Yl)-2,5-diphenyltetrazolium bromide (MTT) contained media and incubated for 4 h. Then, DMSO replaced MTT containing media. Absorbance was noted by putting a plate in microplate reader under synergy H1 Biotek microplate reader.

5.5. References

[1] M. Mecklenburg, W.A. Hubbard, E.R. White, R. Dhall, S.B. Cronin, S. Aloni, B.C. Regan (2015), Nanoscale temperature mapping in operating microelectronic devices, Science., 347, 629–632 (DOI: https://doi.org/10.1126/science.aaa2433)

[2] G. Kucsko, P.C. Maurer, N.Y. Yao, M. Kubo, H.J. Noh, P.K. Lo, H. Park, M.D. Lukin (2013), Nanometre-scale thermometry in a living cell., Nature., 500, 54–58 (DOI: https://doi.org/10.1038/nature12373)

[3] U. Lucia, G. Grazzini, B. Montrucchio, G. Grisolia, R. Borchiellini, G. Gervino, C. Castagnoli, A. Ponzetto, F. Silvagno (2015), Constructal thermodynamics combined with infrared experiments to evaluate temperature differences in cells, Sci.Rep., 5, 11587 (DOI: https://doi.org/10.1038/srep11587)

[4] C.D.S. Brites, X. Xie, M.L. Debasu, X. Qin, R. Chen, W. Huang, J. Rocha, X. Liu, L.D. Carlos (2016), Instantaneous ballistic velocity of suspended Brownian nanocrystals measured by upconversion nanothermometry, Nat.Nanotechnol., 11, 851–856 (DOI: https://doi.org/10.1038/nnano.2016.111)

[5] D. Zhou, M. Lin, X. Liu, J. Li, Z. Chen, D. Yao, H. Sun, H. Zhang, B. Yang (2013), Conducting the Temperature-Dependent Conformational Change of Macrocyclic Compounds to the Lattice Dilation of Quantum Dots for Achieving an Ultrasensitive Nanothermometer, ACS Nano., 7, 2273–2283 (DOI: https://doi.org/10.1021/nn305423p)

[6] F. Vetrone, R. Naccache, A. Zamarrón, A. Juarranz de la Fuente, F. Sanz-Rodríguez, L. Martinez Maestro, E. Martín Rodriguez, D. Jaque, J. García Solé, J.A. Capobianco (2010), Temperature Sensing Using Fluorescent Nanothermometers, ACS Nano., 4, 3254–3258 (DOI: https://doi.org/10.1021/nn100244a)

[7] Y. Gao, F. Huang, H. Lin, J. Zhou, J. Xu, Y. Wang (2016), A Novel Optical Thermometry Strategy Based on Diverse Thermal Response from Two Intervalence Charge Transfer States, Adv. Funct. Mater., 226, 3139–3145 (DOI: https://doi.org/10.1002/adfm.201505332)

[8] X. Wang, Y. Wang, J. Yu, Y. Bu, X. Yan (2018), Modifying phase, shape and optical thermometry of $NaGdF_4$:2%Er^{3+} phosphors through Ca^{2+} doping, Opt. Express., 26, 21950–21959 (DOI: https://doi.org/10.1364/OE.26.021950)

[9] A. Maurya, A. Bahadur, A. Dwivedi, A.K. Choudhary, T.P. Yadav, P.K. Vishwakarma, S.B. Rai (2019), Optical properties of Er3+, Yb3+ co-doped calcium zirconate phosphor and temperature sensing efficiency: Effect of alkali ions (Li+, Na+ and K+)., J. Phys. Chem. Solids., 119, 228–237 (DOI: https://doi.org/10.1016/j.jpcs.2018.04.004)

[10] X. Wang, Y. Wang, Y. Bu, X. Yan, J. Wang, P. Cai, T. Vu, H.J. Seo (2017), Influence of Doping and Excitation Powers on Optical

Thermometry in Yb^{3+}-Er^{3+} doped $CaWO_4$., Sci. Rep., 7, 43383 (DOI: https://doi.org/10.1038/srep43383)

[11] J. Feng, K. Tian, D. Hu, S. Wang, S. Li, Y. Zeng, Y. Li, G. Yang (2011), A Triarylboron-Based Fluorescent Thermometer: Sensitive Over a Wide Temperature Range, Angew. Chem. Int. Ed., 50, 8072–8076 (DOI: https://doi.org/10.1002/anie.201102390)

[12] L. Shang, F. Stockmar, N. Azadfar, G.U. Nienhaus (2013), Intracellular Thermometry by Using Fluorescent Gold Nanoclusters, Angew. Chem. Int. Ed., 52, 11154–11157 (DOI: https://doi.org/10.1002/anie.201306366)

[13] D. Cauzzi, R. Pattacini, M. Delferro, F. Dini, C. Di Natale, R. Paolesse, S. Bonacchi, M. Montalti, N. Zaccheroni, M. Calvaresi, F. Zerbetto, L. Prodi (2012), Temperature-Dependent Fluorescence of Cu5 Metal Clusters: A Molecular Thermometer, Angew. Chem. Int. Ed., 51, 9662–9665 (DOI: https://doi.org/10.1002/anie.201204052)

[14] P. Cai, X. Wang, H.J. Seo (2018), Excitation power dependent optical temperature behaviors in Mn4+ doped oxyfluoride Na2WO2F4, Phys. Chem. Chem. Phys., 20, 2028–2035 (DOI: https://doi.org/10.1039/C7CP07123J)

[15] T. Bai, N. Gu (2016), Micro/Nanoscale Thermometry for Cellular Thermal Sensing, Small., 12, 4590–4610 (DOI: https://doi.org/10.1002/smll.201600665)

[16] M. Puddu, G. Mikutis, W.J. Stark, R.N. Grass (2016), Submicrometer-Sized Thermometer Particles Exploiting Selective Nucleic Acid Stability., Small, 12, 452–456. (DOI: https://doi.org/10.1002/smll.201502883)

[17] Z. Song, F. Quan, Y. Xu, M. Liu, L. Cui, J. Liu (2016), Multifunctional N,S co-doped carbon quantum dots with pH- and thermo-dependent switchable fluorescent properties and highly selective detection of glutathione, Carbon., 104, 169–178 (DOI: https://doi.org/10.1016/j.carbon.2016.04.003)

[18] H.K. Sadhanala, S. Senapati, K.K. Nanda (2018), Temperature sensing using sulfur-doped carbon nanoparticles, Carbon., 13313, 200–208 (DOI: https://doi.org/10.1016/j.carbon.2018.03.039)

[19] C. Wang, H. Lin, Z. Xu, Y. Huang, M.G. Humphrey, C. Zhang (2016), Tunable Carbon-Dot-Based Dual-Emission Fluorescent Nanohybrids for Ratiometric Optical Thermometry in Living Cells, ACSAppl.Mater.Interfaces., 8, 6621–6628 (DOI: https://doi.org/10.1021/acsami.5b11317)

[20] Y. Yang, W. Kong, H. Li, J. Liu, M. Yang, H. Huang, Y. Liu, Z. Wang, Z. Wang, T.-K. Sham, J. Zhong, C. Wang, Z. Liu, S.-T. Lee, Z. Kang (2015), Fluorescent N-Doped Carbon Dots as in Vitro and in Vivo Nanothermometer, ACS Appl. Mater. Interfaces., 7, 27324–27330 (DOI: https://doi.org/10.1021/acsami.5b08782)

[21] C. Wang, Z. Xu, H. Cheng, H. Lin, M.G. Humphrey, C. Zhang (2015), A hydrothermal route to water-stable luminescent carbon dots as nanosensors for pH and temperature, Carbon., 82, 87–95 (DOI: https://doi.org/10.1016/j.carbon.2014.10.035)

[22] X. Cui, Y. Wang, J. Liu, Q. Yang, B. Zhang, Y. Gao, Y. Wang, G. Lu (2017), Dual functional N- and S-co-doped carbon dots as the sensor for temperature and Fe3+ ions, Sens. Actuators B Chem., 242, 1272–1280 (DOI: https://doi.org/10.1016/j.snb.2016.09.032)

[23] G. Liu, S. Li, M. Cheng, L. Zhao, B. Zhang, Y. Gao, Y. Xu, F. Liu, G. Lu (2018), Facile synthesis of nitrogen and sulfur co-doped carbon dots for multiple sensing capacities: alkaline fluorescence enhancement effect, temperature sensing, and selective detection of Fe3+ ions, New J. Chem., 42, 13147–13156 (DOI: https://doi.org/10.1039/C8NJ02086H)

[24] K. Yamada (2013), Cobalt: Its Role in Health and Disease, in: A. Sigel, H. Sigel, R.K.O. Sigel (Eds.), Interrelat. Essent. Met. Ions Hum. Dis, Springer Netherlands., Dordrecht, pp. 295–320 (DOI: https://doi.org/10.1007/978-94-007-7500-8_9)

[25] A. Miller, M. Korem, R. Almog, Y. Galboiz (2005), Vitamin B12, demyelination, remyelination and repair in multiple sclerosis, J.Neurol.Sci., 233, 93–97 (DOI: https://doi.org/10.1016/j.jns.2005.03.009)

[26] Z. Rzepka, M. Respondek, J. Rok, A. Beberok, K. Ó Proinsias, D. Gryko, D. Wrześniok (2018), Vitamin B12 Deficiency Induces Imbalance in Melanocytes Homeostasis—A Cellular Basis of Hypocobalaminemia Pigmentary Manifestations, Int. J. Mol. Sci., 19, 2845 (DOI: https://doi.org/10.3390/ijms19092845)

[27] X.Y. Sun, M.J. Yuan, B. Liu, J.S. Shen (2018), Carbon dots as fluorescent probes for detection of VB12 based on the inner filter effect, RSC Adv., 8, 19786–19790 (DOI: https://doi.org/10.1039/C8RA03070G)

[28] B. Brunetti (2016), Recent Advances in Electroanalysis of Vitamins, Electroanalysis., 28, 1930–1942 (DOI: https://doi.org/10.1002/elan.201600097)

[29] J. Sun, X. Zhu, M. Wu (2007), Hydroxypropyl-β-Cyclodextrin Enhanced Determination for the Vitamin B12 by Fluorescence Quenching Method, J. Fluoresc., 17, 265–270 (DOI: https://doi.org/10.1007/s10895-007-0168-2)

[30] F. Samari, B. Hemmateenejad, Z. Rezaei, M. Shamsipur (2012), A novel approach for rapid determination of vitamin B12 in pharmaceutical preparations using BSA-modified gold nanoclusters, Anal. Methods., 4, 4155–4160 (DOI: https://doi.org/10.1039/C2AY25196E)

[31] E. Vaishnavi, R. Renganathan (2013), CdTe quantum dot as a fluorescence probe for vitamin B12 in dosage form, Spectrochim. Acta, A. Mol. Biomol. Spectrosc., 115, 603–609

(DOI: https://doi.org/10.1016/j.saa.2013.06.068)
[32] S. Chakravarty, B. Gogoi, B.B. Mandal, N. Bhardwaj, N.S. Sarma (2018), Silk fibroin as a platform for dual sensing of vitamin B12 using photoluminescence and electrical techniques, Biosens.Bioelectron., 112, 18–22 (DOI: https://doi.org/10.1016/j.bios.2018.03.057)
[33] M. Wang, Y. Liu, G. Ren, W. Wang, S. Wu, J. Shen (2018), Bioinspired carbon quantum dots for sensitive fluorescent detection of vitamin B12 in cell system, Anal. Chim. Acta., 1032, 154–162 (DOI: https://doi.org/10.1016/j.aca.2018.05.057)
[34] M.L. Liu, B.B. Chen, C.M. Li, C.Z. Huang (2019), Carbon dots: synthesis, formation mechanism, fluorescence origin and sensing applications, Green Chem., 21, 449–471 (DOI: https://doi.org/10.1039/C8GC02736F)
[35] V. Sharma, P. Tiwari, S.M. Mobin (2017), Sustainable carbon-dots: recent advances in green carbon dots for sensing and bioimaging, J. Mater. Chem. B., 5, 8904–8924 (DOI: https://doi.org/10.1039/C7TB02484C)
[36] N. Kaur, V. Sharma, P. Tiwari, A.K. Saini, S.M. Mobin (2019), "Vigna radiata" based green C-dots: Photo-triggered theranostics, fluorescent sensor for extracellular and intracellular iron (III) and multicolor live cell imaging probe, Sens. Actuators B Chem., 291, 275–286 (DOI: https://doi.org/10.1016/j.snb.2019.04.039)
[37] Z. Wei, B. Wang, Y. Liu, Z. Liu, H. Zhang, S. Zhang, J. Chang, S. Lu (2019), Green synthesis of nitrogen and sulfur co-doped carbon dots from Allium fistulosum for cell imaging, New J. Chem., 43, 718–723 (DOI: https://doi.org/10.1039/C8NJ05783D)
[38] Z.A.I. Mazrad, K. Lee, A. Chae, I. In, H. Lee, S.Y. Park (2018), Progress in internal/external stimuli responsive fluorescent carbon nanoparticles for theranostic and sensing applications, J. Mater. Chem. B., 6, 1149–1178 (DOI: https://doi.org/10.1039/C7TB03323)
[39] S. Konar, B.N.P. Kumar, M.Kr. Mahto, D. Samanta, M.A.S. Shaik, M. Shaw, M. Mandal, A. Pathak (2019), N-doped carbon dot as fluorescent probe for detection of cysteamine and multi color cell imaging, Sens.ActuatorsBChem., 2019, 286, 77–85 (DOI: https://doi.org/10.1016/j.snb.2019.01.117)
[40] S. Venkatesan, A.J. Mariadoss, K. Arunkumar, A. Muthupandian (2019), Fuel waste to fluorescent carbon dots and its multifarious applications, Sens. Actuators B Chem., 282, 972–983 (DOI: https://doi.org/10.1016/j.snb.2018.11.144)
[41] P. Das, S. Ganguly, S. Mondal, M. Bose, A.K. Das, S. Banerjee, N.C. Das (2018), Heteroatom doped photoluminescent carbon dots for sensitive detection of acetone in human fluids, Sens. Actuators B Chem., 266, 583–593 (DOI: https://doi.org/10.1016/j.snb.2018.03.183)

[42] P. Das, S. Ganguly, M. Bose, D. Ray, S. Ghosh, S. Mondal, V.K. Aswal, A.K. Das, S. Banerjee, N.C. Das (2019), Surface quaternized nanosensor as a one-arrow-two-hawks approach for fluorescence turn "on–off–on" bifunctional sensing and antibacterial activity, New J. Chem., 43, 6205–6219 (DOI: https://doi.org/10.1039/C8NJ06308G)

[43] P. Tiwari, V. Sharma, N. Kaur, K. Ahmad, S.M. Mobin (2019), Sustainable Graphene Production: New Insights into Cannabis sativa Engineered Carbon Dots Based Exfoliating Agent for Facile Production of Graphene, ACS Sustain. Chem. Eng., 7, 11500–11510 (DOI: https://doi.org/10.1021/acssuschemeng.9b01353)

[44] Q. Xu, T. Kuang, Y. Liu, L. Cai, X. Peng, T.S. Sreeprasad, P. Zhao, Z. Yu, N. Li (2016), Heteroatom-doped carbon dots: synthesis, characterization, properties, photoluminescence mechanism and biological applications., J. Mater. Chem. B., 4, 7204–7219 (DOI: https://doi.org/10.1039/C6TB02131J)

[45] X. Liu, J. Liu, B. Zheng, L. Yan, J. Dai, Z. Zhuang, J. Du, Y. Guo, D. Xiao (2017), N-Doped carbon dots: green and efficient synthesis on a large-scale and their application in fluorescent pH sensing, New J. Chem., 4, 10607–10612 (DOI: https://doi.org/10.1039/C7NJ01889D)

[46] W. Kwon, J. Lim, J. Lee, T. Park, S.-W. Rhee (2013), Sulfur-incorporated carbon quantum dots with a strong long-wavelength absorption band, J. Mater. Chem.C., 1, 2002–2008 (DOI: https://doi.org/10.1039/C3TC00683B)

[47] Y. Xu, D. Li, M. Liu, F. Niu, J. Liu, E. Wang (2017), Enhanced-quantum yield sulfur/nitrogen co-doped fluorescent carbon nanodots produced from biomass Enteromorpha prolifera : synthesis, posttreatment, applications and mechanism study, Sci. Rep., 7, 4499 (DOI: https://doi.org/10.1038/s41598-017-04754-x)

[48] H. Ding, J.-S. Wei, H.-M. Xiong (2014), Nitrogen and sulfur co-doped carbon dots with strong blue luminescence, Nanoscale., 6, 13817–13823 (DOI: https://doi.org/10.1039/C4NR04267K)

[49] R. Prajapati, S. Chatterjee, A. Bhattacharya, T.K. Mukherjee (2015), Surfactant-Induced Modulation of Nanometal Surface Energy Transfer from Silicon Quantum Dots to Silver Nanoparticles, J. Phys. Chem. C., 119, 13325–13334 (DOI: https://doi.org/10.1021/acs.jpcc.5b02903)

[50] V. Sharma, S.K. Singh, S.M. Mobin (2019), Bioinspired carbon dots: from rose petals to tunable emissive nanodots, Nanoscale Adv., 1, 1290–1296. (DOI: https://doi.org/10.1039/C8NA00105G)

[51] J. Peng, W. Gao, B.K. Gupta, Z. Liu, R. Romero-Aburto, L. Ge, L. Song, L.B. Alemany, X. Zhan, G. Gao, S.A. Vithayathil, B.A. Kaipparettu, A.A. Marti, T. Hayashi, J.-J. Zhu, P.M. Ajayan (2012), Graphene Quantum Dots Derived from Carbon Fibers, Nano Lett., 12, 844–849 (DOI: https://doi.org/10.1021/nl2038979)

[52] V. Sharma, N. Kaur, P. Tiwari, A.K. Saini, S.M. Mobin (2018), Multifunctional fluorescent "Off-On-Off" nanosensor for Au3+ and S2− employing N-S co-doped carbon–dots, Carbon., 139, 393–403 (DOI: https://doi.org/10.1016/j.carbon.2018.07.004)
[53] S. Kalytchuk, K. Poláková, Y. Wang, J.P. Froning, K. Cepe, A.L. Rogach, R. Zbořil (2017), Carbon Dot Nanothermometry: Intracellular Photoluminescence Lifetime Thermal Sensing, ACS Nano., 11, 1432–1442 (DOI: https://doi.org/10.1021/acsnano.6b06670)
[54] S.-S. Liu, C.-F. Wang, C.-X. Li, J. Wang, L.-H. Mao, S. Chen (2014), Hair-derived carbon dots toward versatile multidimensional fluorescent materials, J. Mater. Chem. C., 2, 6477–6483 (DOI: https://doi.org/10.1039/C4TC00636D)
[55] D. Rodríguez-Padrón, M. Algarra, L.A.C. Tarelho, J. Frade, A. Franco, G. de Miguel, J. Jiménez, E. Rodríguez-Castellón, R. Luque (2018), Catalyzed Microwave-Assisted Preparation of Carbon Quantum Dots from Lignocellulosic Residues, ACS Sustain. Chem. Eng., 26, 7200–7205 (DOI: https://doi.org/10.1021/acssuschemeng.7b03848)
[56] C. Wang, Z. Xu, H. Cheng, H. Lin, M.G. Humphrey, C. Zhang (2015), A hydrothermal route to water-stable luminescent carbon dots as nanosensors for pH and temperature, Carbon., 82, 87–95 (DOI: https://doi.org/10.1016/j.carbon.2014.10.035)
[57] X. Li, X. Wei, Y. Qin, Y. Chen, C. Duan, M. Yin (2016), The emission rise time of BaY2ZnO5:Eu3+ for non-contact luminescence thermometry, J. Alloys Compd., 657, 353–357 (DOI: https://doi.org/10.1016/j.jallcom.2015.10.101)
[58] V. Lojpur, Ž. Antić, M.D. Dramićanin (2014), Temperature sensing from the emission rise times of Eu3+ in SrY2O4, Phys. Chem. Chem. Phy., 2014, 16, 25636–25641 (DOI: https://doi.org/10.1039/C4CP04141K)
[59] P. Yu, X. Wen, Y.-R. Toh, J. Tang (2012), Temperature-Dependent Fluorescence in Carbon Dots, J. Phys. Chem. C., 116, 25552–25557 (DOI: https://doi.org/10.1021/jp307308z)
[60] A. Narayanaswamy, L.F. Feiner, A. Meijerink, P.J. van der Zaag (2009), The Effect of Temperature and Dot Size on the Spectral Properties of Colloidal InP/ZnS Core−Shell Quantum Dots, ACS Nano., 3, 2539–2546 (DOI: https://doi.org/10.1021/nn9004507)
[61] S. Kalytchuk, O. Zhovtiuk, S.V. Kershaw, R. Zbořil, A.L. Rogach (2016), Temperature-Dependent Exciton and Trap-Related Photoluminescence of CdTe Quantum Dots Embedded in a NaCl Matrix: Implication in Thermometry, Small., 12, 466–476 (DOI: https://doi.org/10.1002/smll.201501984)
[62] H. Xu, S. Huang, C. Liao, Y. Li, B. Zheng, J. Du, D. Xiao (2015), Highly selective and sensitive fluorescence probe based on

thymine-modified carbon dots for Hg2+ and L-cysteine detection, RSC Adv., 5, 89121–89127
(DOI: https://doi.org/10.1039/C5RA18432K)

[63] F. Khakbaz, M. Mahani (2017), Micro-RNA detection based on fluorescence resonance energy transfer of DNA-carbon quantum dots probes, Anal. Biochem., 2017, 523, 32–38
(DOI: https://doi.org/10.1016/j.ab.2017.01.025)

[64] J. Kudr, L. Richtera, K. Xhaxhiu, D. Hynek, Z. Heger, O. Zitka, V. Adam (2017), Carbon dots based FRET for the detection of DNA damage, Biosens. Bioelectron., 92, 133–139
(DOI: https://doi.org/10.1016/j.bios.2017.01.067)

[65] A. Shrivastava, V. Gupta (2011), Methods for the determination of limit of detection and limit of quantitation of the analytical methods., Chron. Young Sci., 2, 21
(DOI: https://doi.org/10.4103/2229-5186.79345)

[66] V. Sharma, A.K. Saini, S.M. Mobin (2016), Multicolour fluorescent carbon nanoparticle probes for live cell imaging and dual palladium and mercury sensors, J. Mater. Chem. B., 4, 2466–2476 (DOI: https://doi.org/10.1039/C6TB00238B)

[67] L. Ding, H. Yang, S. Ge, J. Yu (2018), Fluorescent carbon dots nanosensor for label-free determination of vitamin B12 based on inner filter effect, Spectrochim. Acta. A. Mol. Biomol. Spectrosc., 19, 305–309 (DOI: https://doi.org/10.1016/j.saa.2017.12.015)

[68] J. Wang, J. Wei, S. Su, J. Qiu (2014), Novel fluorescence resonance energy transfer optical sensors for vitamin B12 detection using thermally reduced carbon dots, New J. Chem., 39, 501–507
(DOI: https://doi.org/10.1039/C4NJ00538D)

[69] S. Chakravarty, B. Gogoi, B.B. Mandal, N. Bhardwaj, N.S. Sarma (2018), Silk fibroin as a platform for dual sensing of vitamin B12 using photoluminescence and electrical techniques, Biosens. Bioelectron., 112, 18–22
(DOI: https://doi.org/10.1016/j.bios.2018.03.057)

[70] K.-T. Yong, W.-C. Law, R. Hu, L. Ye, L. Liu, M.T. Swihart, P.N. Prasad (2013), Nanotoxicity assessment of quantum dots: from cellular to primate studies, Chem. Soc. Rev., 42, 1236–1250
(DOI: https://doi.org/10.1039/C2CS35392J)

[71] P.G. Luo, S. Sahu, S.-T. Yang, S.K. Sonkar, J. Wang, H. Wang, G.E. LeCroy, L. Cao, Y.-P. Sun (2013), Carbon “quantum” dots for optical bioimaging, J. Mater. Chem. B., 1, 2116–2127
(DOI: https://doi.org/10.1039/C3TB00018D)

CHAPTER 6

A spectroscopic investigation of Carbon dots and its reduced state towards fluorescence performance

6.1. Introduction

The development of highly fluorescent and robust luminescence material offers significant advantages especially in different practical applications such as displays; sensing; light emitters, solar concentrators, cellular imaging, and photodynamic therapies [1–8]. Traditionally, semiconducting quantum dots and organic dyes were used for these applications however inherent toxicity, tedious processing methods and fast photobleaching limits their applicability [9,10]. Since after its discovery carbon dots (CDs) have proven as one of the most promising alternate materials among carbon materials families [11,12] due to its fascinating attributes such as small size (≤10 nm), excellent optical properties like excitation dependent multi-colour emission; very high fluorescence quantum yield, broad optical absorption, good water solubility and the capacity to withstand photobleaching [13–17]. Moreover, most sought after biological properties like good biocompatibility, hemocompatibility, rapid cellular uptake along with simple and inexpensive processing method makes them an ideal candidate to substitute conventional organic dyes and semiconducting quantum dots [18,19]. The thrust for further improving and customizing the fluorescence properties of CDs leads to efforts like passivation [20,21] and doping [22]. Different types of polymers, diamine compounds were explored to passivate CDs [23,24]. It has been seen that the doping of nitrogen in CDs enhances the quantum yield and fluorescent behaviour of CDs [25–27]. However, the post-synthetic modification process, increment in defects often makes the whole preparation process highly unfeasible at a large

scale. Thus, the explorations of advanced and innovative strategies are needed for making multifunctional fluorescent CDs. The tailoring of the functional group on CDs can have the potential to modulate the fluorescence nature and enhances the quantum yield [28]. The tailored functional group can swap the optical and physical properties of CDs without disturbing the interference of heterogeneity [29]. The reduction is one of the prominent ways to tailor the functional group of CDs. The use of hydrazine hydrate [30–32] and sodium borohydride ($NaBH_4$) [33,34] as a reducing agent result in enhanced photoluminescence property. The reduced CDs have the potential to dramatically enhance the optical properties of the CDs and can open new avenues in optical performances and may be used for different applications [35,36].

In the present work, carbon dots were synthesized using citric acid as a sole carbon precursor and nitrogen, boron and fluorine were used as dopants to prepare CNBF. Nitrogen plays a very critical role for CDs both structurally and optically [37]. The emission behaviour of CDs gets modified through nitrogen doping because new trapping states of electron created because of nitrogen doping and ultimately facilitates the radiative recombination rates with high yield in CDs [38,39]. On the other hand, boron gets incorporated into CDs via covalent bonding thus, altering the electronic structure and offering more active sites that rendered excellent optical and electronic properties of CDs [40]. Fluorine, one of the most common elements present in the world and contains very high electronegativity thus fluorine moiety strongly absorbs adjacent electrons and may increase the separation between negative and positive charges which leads to modification in the electronic structure and excitation-emission nature in CDs [41]. So, the heteroatom doping improves fluorescence behaviour, solubility, and photophysical properties of CDs [26,42]. Further, $NaBH_4$ was employed as a reducing agent to prepare reduced carbon dots (rCNBF). The change in the fluorescence behaviour

of CNBF and rCNBF were evaluated comparatively using different spectroscopic techniques.

6.2. Results and discussion

Nitrogen, boron and fluorine codoped C-dots (CNBF) were prepared hydrothermally using citric acid as sole carbon precursor. The as-synthesized CNBF were reduced to rCNBF using $NaBH_4$ to alter optical properties of CDs. Further, CNBF and rCNBF were investigated and compared thoroughly through different spectroscopic and microscopic techniques to determine excitation-emission wavelength, quantum yield, lifetime values, morphology and particle size.
(Scheme **6.1**).

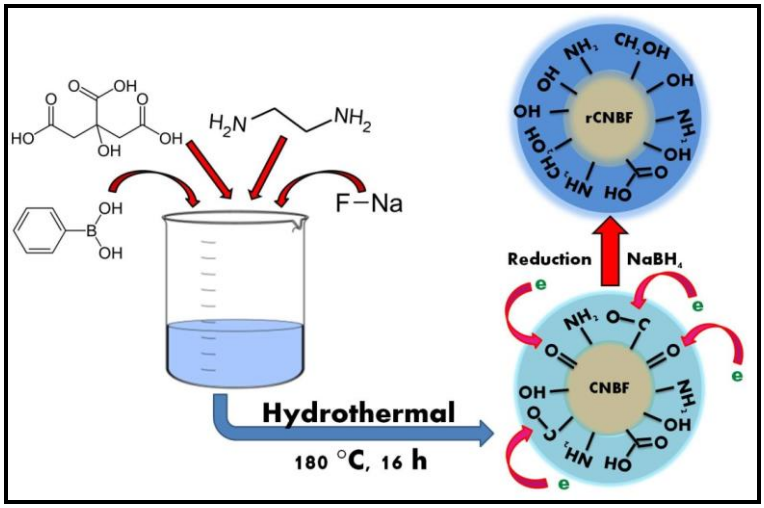

Scheme 6.1. Synthesis scheme for preparation of CNBF and rCNBF.

The absorption and emission behaviour of CNBF and rCNBF were studied using UV-vis and fluorescence spectroscopy. The absorption spectrum for both CNBF and rCNBF exhibited a prominent peak around 350 nm shown in Figure **6.1a-b**. This peak arises from the superposition of imidazo[1,2a]pyridine-7-carboxylic acid (IPCA) [45] present in CNBF. It must be mentioned that typically CDs exhibits absorption band around 280 nm and 320 nm attributes to π-π^* and n- π^* transitions [19,36]. However,

in present spectra, bands at ~280 nm and 320 nm were not discernible suggesting the absorption characteristics of CNBF and rCNBF occur mainly from their molecular state [45]. The excitation spectra show blue shift with reduction, the excitation peak for CNBF was found to be at 380 nm while a 20 nm blue shift is observed for rCNBF with excitation peak at 360 nm. Interestingly, both CNBF and rCNBF exhibited emission peak at 440 nm (Figure **6.1c-d**).

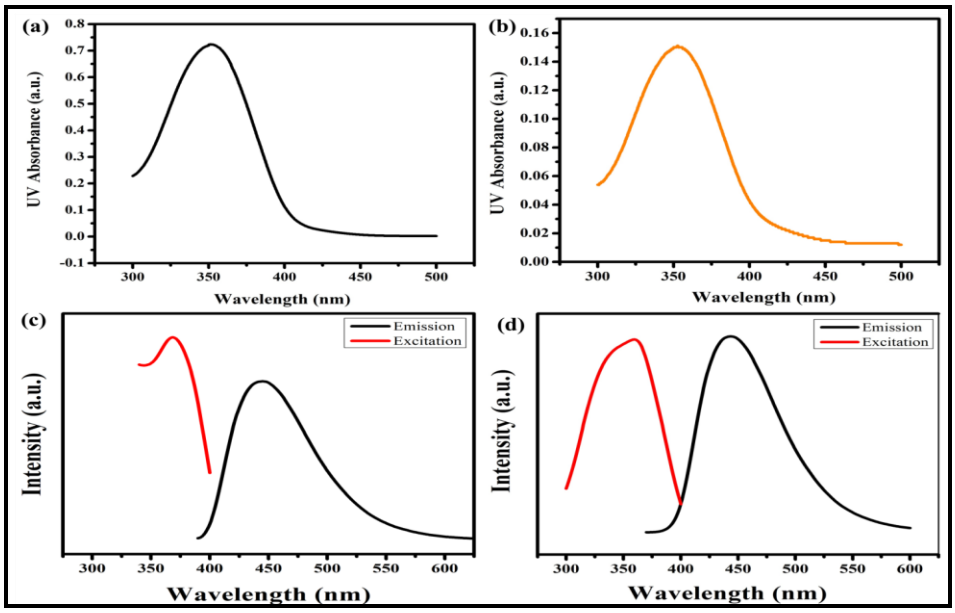

Figure 6.1. (a) *Uv-vis* spectra of CNBF (b) *Uv-vis* spectra of rCNBF (c) Excitation-emission spectra of CNBF (d) Excitation-emission spectra of rCNBF.

As seen in Figure **6.2**, for both CNBF & rCNBF excitation independent emission behaviour was observed in the excitation wavelength range of 280 nm to 400 nm. The excitation-independent emission behaviour results in the degeneracy, which may arise from the invariable emissive band.[46] Interestingly, the fluorescence excitation spectra of CNBF show two peaks located around ~320 nm and ~380 nm whereas the rCNBF shows only one band around ~360 nm and the band around ~320 nm were significantly suppressed. It can be concluded that due to the presence of lesser multi-chromic units the emissive nature was wavelength independent in the case of both CNBF and rCNBF [45]. Notably, the quantum yields of rCNBF

were increased as compared to CNBF. Moreover, the full width at half maxima (FWHM) decreases with increase in concentration of $NaBH_4$. The increase in quantum yield (Table **6.1**) infers that with the increase in concentration of reducing agent (rCNBF1= 0.15 g, rCNBF2=0.25 g and rCNBF3=0.35 g) the electron withdrawing group gets replaced by electron donating group leading to increase in π-electron density and ultimately results in increased radiative recombination rates and enhanced fluorescence [33,47,48].

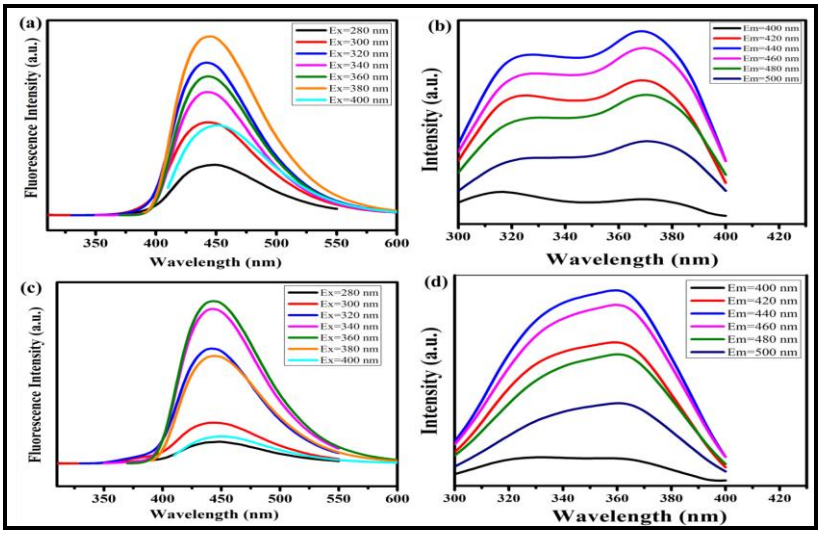

Figure 6.2. (a) Emission spectra of CNBF with varying excitation wavelength (b) Excitation spectra of CNBF with varying emission wavelength (c) Emission spectra of rCNBF with varying excitation wavelength (d) Excitation spectra of rCNBF with varying emission wavelength.

Table 6.1. Optical behavior of CNBF, rCNBF1, rCNBF2 and rCNBF3.

Samples	Excitation (nm)	Emission (nm)	Quantum Yield (%)
CNBF	**380**	**440**	**35.73**
rCNBF1	**360**	**440**	**39.14**
rCNBF2	**360**	**440**	**41.73**
rCNBF3	**360**	**440**	**44.61**

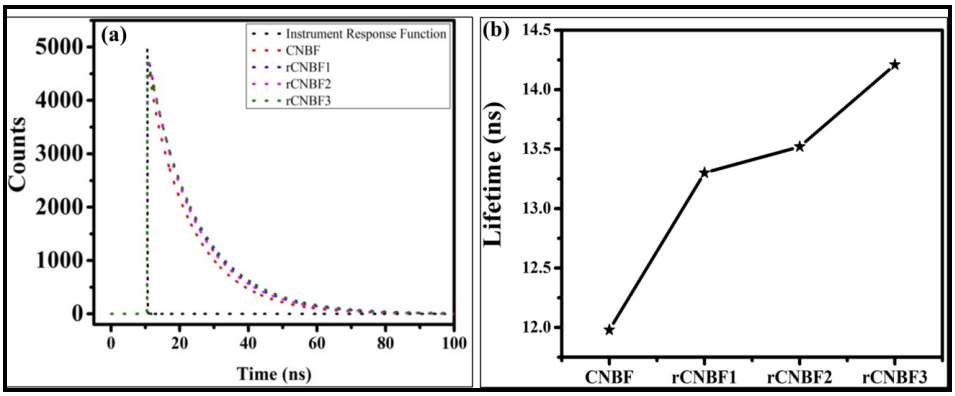

Figure 6.3. (a) Comparative TCSPC spectra of CNBF and rCNBF1,2,3 (b) Comparative lifetime values.

The fluorescence lifetime of CNBF, rCNBF1, rCNBF2 and rCNBF3 were measured with TCSPC. The CNBF was excited at 380 nm whereas rCNBF1, rCNBF2 and rCNBF3 were excited at 360 nm and emission was recorded at 440 nm. The data were fitted and summarized in Figure **6.3**. The fluorescence lifetime of CNBF was 11.98 nS, while the lifetime of rCNBF1, rCNBF2 and rCNBF3 shows continuous increase and determined to be 13.30 nS, 13.52 nS and 14.21 nS, respectively. So, after reduction the fluorescence performance gets significantly enhanced in rCNBF while the emission spectral pattern remains constant with CNBF. These results were in accordance with the earlier reports exhibiting similar spectral trend [31]. The time resolved fluorescence profile of CNBF, rCNBF1, rCNBF2 and rCNBF3 at several representative wavelengths (400 nm, 420 nm, 440 nm, 460 nm, 480 nm, 500 nm) was recorded. The increase in emissive wavelength results in the decrease of decay time for CNBF while the rCNBF shows weaker dependence on the probe wavelength (Table **6.2**). To study the dynamic behaviour of all the samples, decay profiles were fitted using the following equation [49]:

$$F(\tau) = \sum a_i \exp(-\tau/\tau_i) \quad \text{.....(5)}$$

$$\langle \tau \rangle = \sum a_i \tau_i \quad \text{.....(6)}$$

Here, F(τ) represents normalized fluorescence decay whereas <τ> represents the average lifetime. Due to the possible role of the emissive state and molecular state in fluorescence decay two stretched exponential components were considered during fitting [45]. To further, understand the dynamics of fluorescence lifetime, the excitation wavelength was fixed i.e. ~380 nm for CNBF and ~360 nm for rCNBF1, rCNBF2 and rCNBF3 and decay profile were recorded around 400-500 nm (Figure **6.4-6.5**, Table **6.2**). Here τ_1 represents short decay time which originates from surface states in CNBF and rCNBF and tells about non-radiative recombination. Whereas τ_2 represents the longest lifetime component which attributes to a molecule like state in CNBF and rCNBF [50,51]. It must be mentioned here that τ_1 origination involves n-π^* transitions occurs because of non-bonding electrons present in surface functional groups and τ_2 originates from a molecular state containing IPCA molecule [52,53].

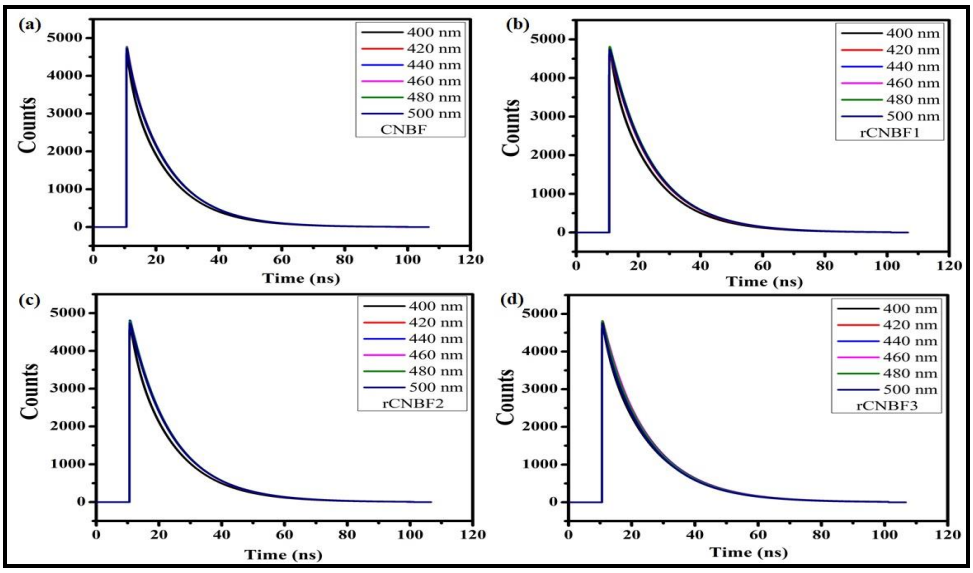

Figure 6.4. Fluorescence decay dynamics at various emission wavelength (a) CNBF (b) rCNBF1 (c) rCNBF2 (d) rCNBF3.

The τ_1 and τ_2 lifetime values in CNBF as shown in Table **6.2** exhibited nearly constant values with varying emission wavelength. However, the reduced samples, i.e. rCNBF1, rCNBF2 and rCNBF3 show drastic change

in τ_1 lifetime as compared to unreduced samples. Further, by comparing the τ_1 lifetime value among rCNBF1, rCNBF2 and rCNBF3, it was found that in rCNBF1 and rCNBF3 the lifetime pattern was irregular whereas in rCNBF2 the lifetime value increases from 400 nm to 420 nm and after that, it becomes nearly constant. Furthermore, the τ_2 lifetime values were nearly constant irrespective of emission wavelength. The variation in τ_1 lifetime value in all the reduced samples infers the heterogeneity in surface functional groups which may arise from the degree of reduction [45]. The short decay time portion of τ_1 in CNBF was highest i.e. 5.24% and with reduced samples this portion gets reduced as minimum was observed in rCNBF3 with 2.23%. This reduction in short decay time portion of τ_1 indicates that after the reduction of CNBF into rCNBF, the energy level became more simplified due to the tailored functional groups which lead to suppression in trap states [28]. Thus, it can be concluded that reducing agent concentration significantly affects the fluorescence lifetime and quantum yield of CDs. The average lifetime value was shorter for CNBF than for their reduced states which was in accordance with lower quantum yield of CNBF and were similar with earlier reports [51]. Furthermore, the maximum lifetime and quantum yield among the reduced CDs were observed in case of rCNBF3, hence further studies were performed on rCNBF3 and results were compared with CNBF.

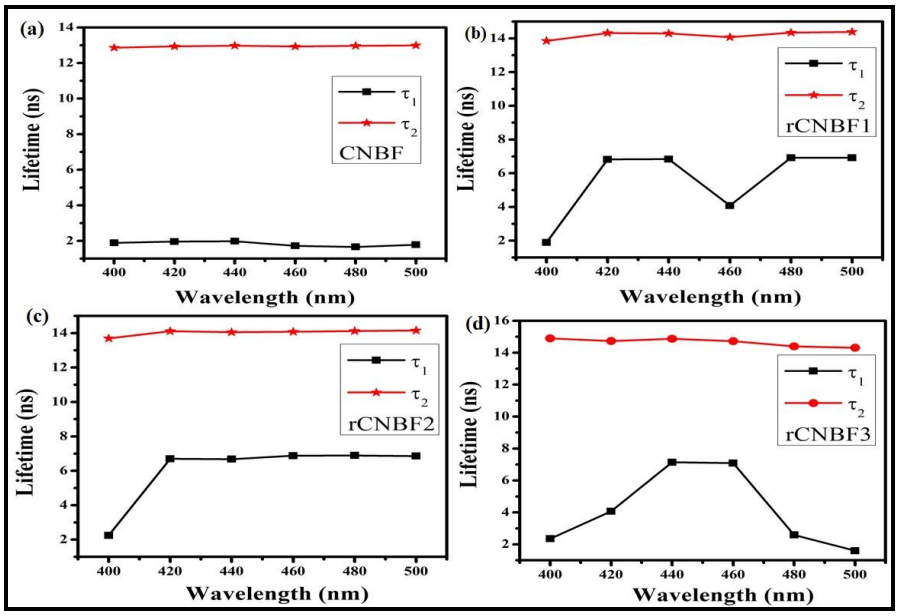

Figure 6.5. Lifetime values at various emission wavelength (a) CNBF (b) rCNBF1 (c) rCNBF2 (d) rCNBF3.

Table 6.2. Fluorescence lifetime calculated from the stretched exponential function.

Sample	λ_{ex} (nm)	λ_{em} (nm)	τ_1 (nS)	τ_2 (nS)	τ_{ave} (nS)
CNBF	380	400	1.99±0.11	12.86±0.02	10.78±0.11
		420	1.91±0.30	12.94±0.02	11.8±0.30
		440	1.88±0.32	12.98±0.02	11.98±0.32
		460	1.72±0.22	12.93±0.02	11.85±0.22
		480	1.66±0.22	12.97±0.02	11.85±0.22
		500	1.78±0.19	12.99±0.02	11.90±0.19
rCNBF1	360	400	1.89±0.16	13.85±0.02	11.92±0.16
		420	6.82±0.19	14.32±0.04	13.48±0.19
		440	6.84±0.18	14.29±0.04	13.35±0.19
		460	4.08±0.64	14.07±0.02	13.42±0.64
		480	6.92±0.16	14.34±0.04	13.54±0.17
		500	6.92±0.16	14.38±0.04	13.56±0.17
rCNBF2	360	400	2.25±0.13	13.69±0.02	11.82±0.13
		420	6.70±0.19	14.11±0.04	13.27±0.19
		440	6.68±0.19	14.05±0.04	13.52±0.20
		460	6.88±0.14	14.08±0.04	13.35±0.15
		480	6.89±0.14	14.12±0.04	13.37±0.15
		500	6.86±0.15	14.15±0.04	13.40±0.16
rCNBF3	360	400	2.35±0.17	14.90±0.02	13.09±0.17
		420	4.07±0.64	14.73±0.02	14.01±0.64
		440	7.14±0.20	14.87±0.04	14.21±0.21
		460	7.09±0.18	14.72±0.04	13.94±0.18
		480	2.59±0.48	14.40±0.02	13.63±0.48
		500	1.60±0.25	14.31±0.02	13.20±0.25

It has been reported that due to surface modification, intrinsic state emission plays a very critical role in fluorescence behaviour. CDs have functional groups such as carbonyl, amide and epoxy moieties present in it. This functional group after reduction gets transformed to –OH groups [54]. To discern the fluorescence tuning mechanism in CNBF & rCNBF3 their HOMO, LUMO and energy bandgap were measured using CV spectra (shown in Figure **6.7a-b**). As depicted in table **6.3**, CNBF exhibited a bandgap of 1.08 eV whereas for rCNBF3 it increased to 1.78 eV. Due to the reduction process, CNBFs surface chemistry gets tailored. Plausibly, rCNBF exhibited a higher bandgap as compared to CNBF due to enhanced π-electron density and suppression in the non-radiative decaying process caused because of –OH functional group. Further, rCNBF3 showed significantly larger quantum yield as a comparison to CNBF which bolstered enriched electron density [34,54]. According to advanced unified defect model (AUDM) the increase in photo fluorescence may occurs because of band bending as a result of reduction of density of midgap states [55]. Also, as midgap states decreases the amount of non-radiative transitions centers also gets decreased. Furthermore, the radiative rate constants of CNBF and rCNBF3 were calculated using following equation [56]:

$$k_F=\Phi_F/T_F \quad \text{.....(7)}$$

Here, k_F implies radiative rate constant, Φ_F is quantum yield and T_F represents lifetime. The value of k_F for CNBF & rCNBF3 were $0.02ns^{-1}$ & $0.03ns^{-1}$ respectively. The higher k_F value in rCNBF3 indicates higher radiative transition centers and supports enhanced fluorescence performance in accord with the AUDM theory [56].

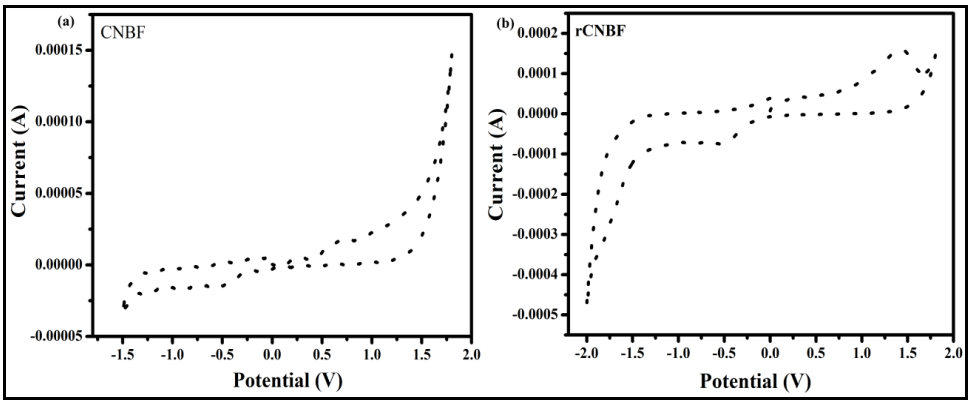

Figure 6.6. CV of (a) CNBF (b) rCNBF3.

Table 6.3. Energy states of CNBF and rCNBF3.

	HOMO/eV	LUMO/eV	Energygap
CNBF	**- 4.26 eV**	**-5.34 eV**	**1.08 eV**
rCNBF3	**- 4.36 eV**	**-6.14 eV**	**1.78 eV**

The hydrothermal synthesis process of CDs starts with the carbonization of citric acid [57]. Initially, citric acid entities get decomposed due to high temperature and pressure arises from hydrothermal treatment. After decomposition, polymerization occurs in which the formation of new nuclei takes place. Further, with subsequent increase in temperature, formed carbon nuclei grow and lead to the formation of nanodots [58,59]. Further to understand the morphological nature of CNBF, its TEM was performed. As depicted in Figure **6.7(a)** at lower magnification CNBF exhibited random network like structure. As the magnification was increased, homogeneous particles with size 4-6 nm with spherical morphology were further shown in Figure **6.7b**. Evidently from Figure **6.7c** lattice fringes of distance 0.21 nm were observed suggesting graphene like framework [60,61]. The SAED pattern of CNBF clearly showed crystalline nature and was consistent with earlier literatures [28,62,63]. The TEM of rCNBF as shown in Figure **6.8a-c**, the particles

were monodisperse without any aggregation with size in the range of 3.5 - 6 nm. However, the absence of lattice fringes comprehends the amorphous characteristics of rCNBF particles. However, the crystallinity gets affected due to the tailoring of surface functional groups [35,64,65]. These results indicates, the reduction process did not alter the particle morphology and size thus confirming fluorescence enhancement in rCNBF arises solely because of surface functional group alteration rather than their size variation [31].

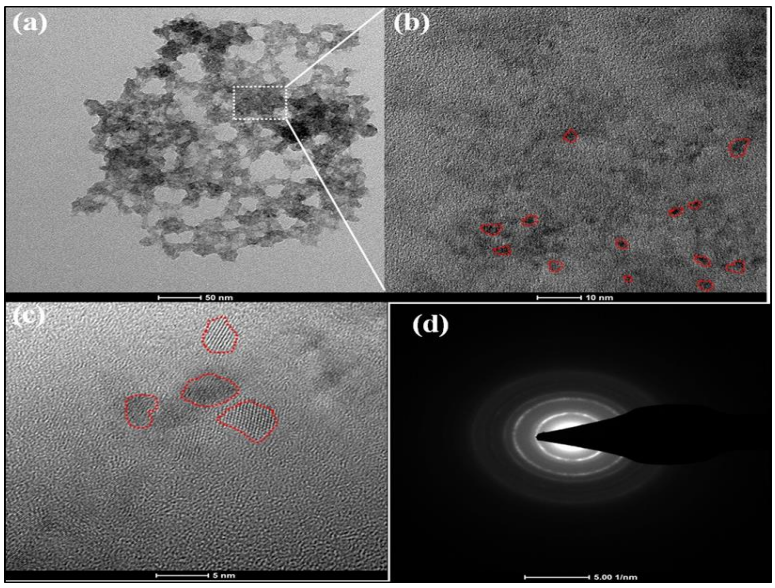

Figure 6.7. (a-c) Representative TEM image of CNBF (d) SAED pattern of CNBF.

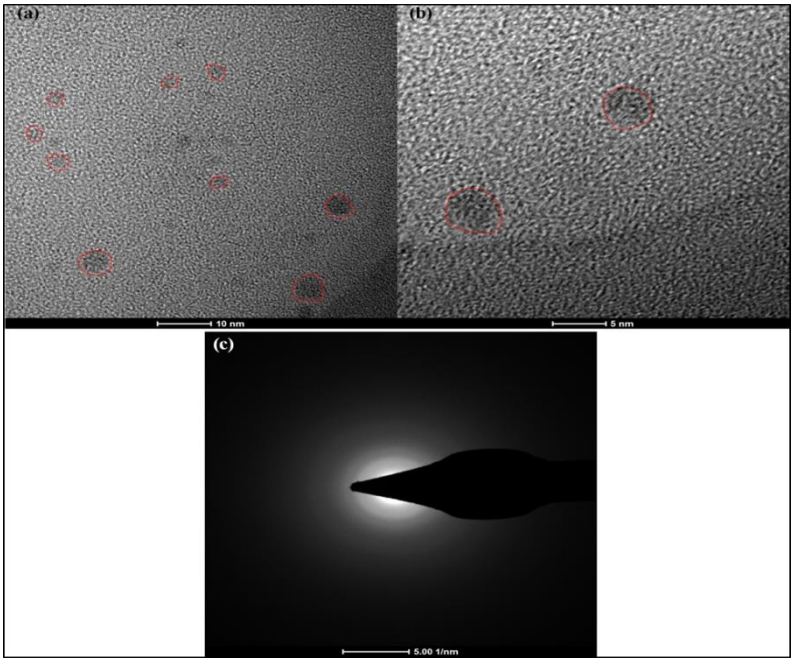

Figure 6.8. (a-b) Representative TEM image of rCNBF3 (c) SAED pattern of rCNBF3.

The functional groups present on CDs surface significantly influence its fluorescence behaviour [34]. So, XPS was performed to study the chemical structure and surface composition of CNBF and rCNBF. The survey scan of CNBF as shown in Figure **6.9a** confirms the element presents i.e. carbon, oxygen, nitrogen, boron and fluorine with concentrations 55.2%, 21.6%, 15.3%, 6.9% and 1.1% respectively. Although the presence of all the elements was observed from the survey scan of rCNBF shown in Figure **6.9b** however, after reduction from $NaBH_4$ the oxygen content gets increased to 28.5% in rCNBF whereas the nitrogen content gets decreased to 10.9%. The carbon, boron and fluorine content in rCNBF were 53.1%, 6.7% and 0.7% respectively. The variation in elemental composition after reduction was similar to earlier reports [54]. Further, the high resolution C1s spectra of CNBF and rCNBF showed in Figure **6.10** revels the disappearance of C-NH bonds which was present in CNBF at 287.6 eV. As presented the O/C atomic ratio of CNBF was 39.13% which gets increased drastically to 52.91% in rCNBF.

Meanwhile, the N/C atomic ratio of CNBF i.e. 27.71% gets decreased to 20.52% in rCNBF indicating that reduction results in the removal of nitrogen containing functional groups. Thus, the variation in functional group binding energies, increase in oxygen and decrease in nitrogen composition substantiating the successful reduction process of CNBF to rCNBF [31,54].

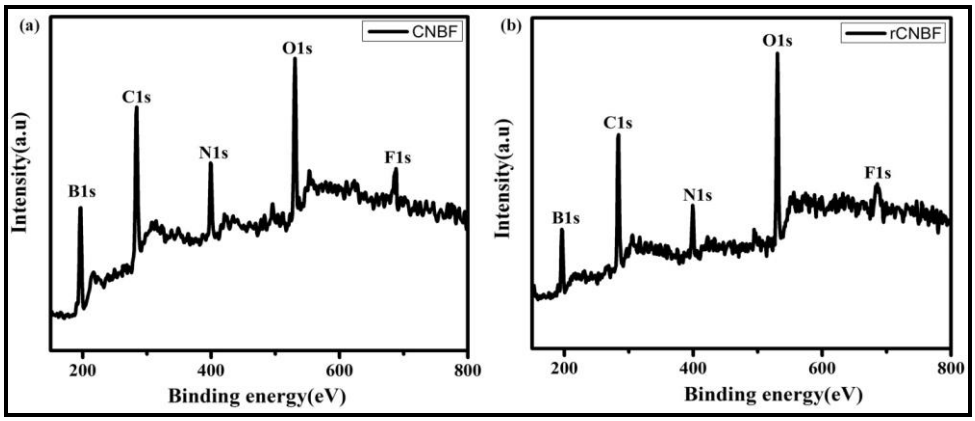

Figure 6.9. (a) XPS survey spectrum of CNBF (b) XPS survey spectrum of rCNBF3.

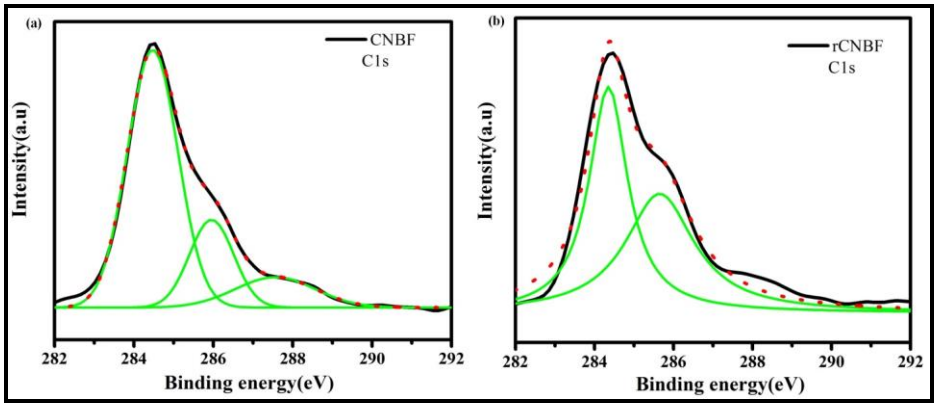

Figure 6.10. Deconvoluated C1s spectra of (a) CNBF (b) rCNBF3.

FTIR spectroscopy was used to investigate the functional groups present on CNBF and rCNBF surface shown in Figure **6.11**. CNBF showed intense FTIR band at 3365.33 cm^{-1} and 1686.63 cm^{-1}. The peak at 3365.33 cm^{-1} corresponds to stretching vibration of hydroxyl group (-OH band) [43]. Further, the band at 1686.63 cm^{-1} corresponds C=O & C=C bands.

For rCNBF bands at 3321.33 cm^{-1} and 2925.33 cm^{-1} corresponds to O-H and C-H bands. However band corresponding C=O/ C=C band at 1686.63cm^{-1} in CNBF shifted to 1638.31 cm^{-1}. The shift in band indicates that C=O was reduced [34]. Also, new bands at 1410 cm^{-1}, 1329.33 cm^{-1} and new intense band at 1051 cm^{-1} corresponding to O-H and C-O bands respectively attribute reduction of carbonyl and amide moieties to O-H groups [65–67]. Due to reduction by $NaBH_4$ the appearance of hydroxyl groups may lead to more defects in rCNBF electronic structure [33]. Furthermore, due to the appearance of these defects the non-radiative recombination rates get suppressed which leads an increase in fluorescence lifetime and quantum yield in rCNBF3 w.r.to CNBF as shown in Table **6.1**. Also based on the earlier report [68] the observed fluorescence response in CDs occurs because of the combination of two mechanisms: 1. Intrinsic energy quantization effects 2. Surface properties which ensembles surface functional groups and surface defects. So, the fluorescence characteristics in CNBF and rCNBF occur due to quantum confinement and surface properties. For CNBF the surface properties occur from carbonyl, hydroxyl etc. groups. However, because of reduction these carbonyl groups get reduced into hydroxyl groups that emerge at rCNBF surfaces. The emergence of these hydroxyl groups leads to an increase in surface defects in rCNBF, instigating different electron relaxation mode [69]. So, tuning of these surface states because of reduction plays a major role in improved fluorescence behaviour (quantum yield and lifetime values) in rCNBF and was consistent with earlier reports [33,54,70].

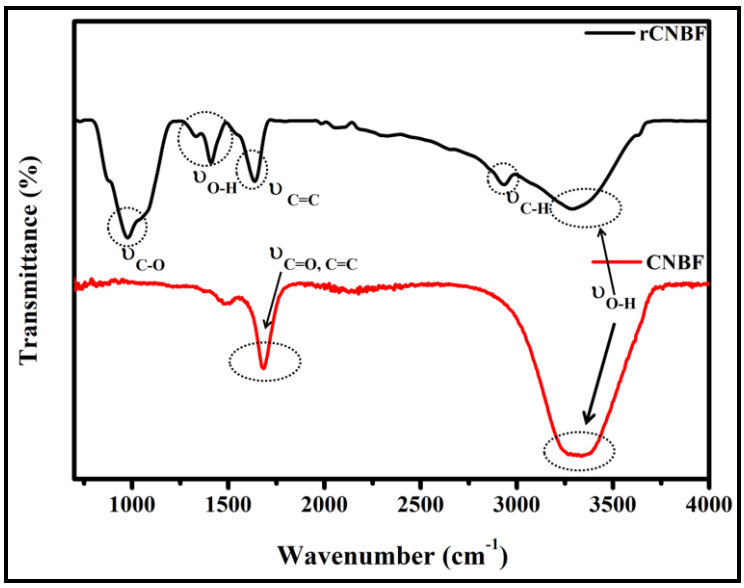

Figure 6.11. FTIR spectra of CNBF and rCNBF.

6.3. Conclusion

The heteroatom doped carbon dot was prepared (CNBF) via the hydrothermal method. Further, the optical characteristics of CNBF were tuned by varying the concentration of $NaBH_4$ i.e. the excitation wavelength gets blue shifted from 380 nm for CNBF to 360 nm in rCNBF. Moreover, the quantum yield and fluorescence life time values also get enhanced with an increase in $NaBH_4$ concentration. The maximum quantum yield and lifetime value of 44.61% and 14.21 nS was observed with rCNBF3 which was significantly higher than CNBF. This significant change in excitation wavelength, quantum yield and lifetime values pertained with energy bandgap values as with rCNBF3 the band gap gets increased to 1.78 eV from 1.08 eV for CNBF. Also, the crystallinity presented in CNBF gets diminished with the reduction. Thus, the change in band gap values and fluorescence nature attributed to modification in the functional groups with reduction. Our study provides conclusive evidence related to functional group modifications, suppression in non-radiative decaying process for enhanced fluorescence in rCNBF. It also

provides foundations in fabricating tuned fluorescent material from the CDs. Further, it can have potential applications in bioimaging and electronic devices.

6.4. Experimental section

6.4.1. Materials

Citric acid, sodium fluoride and ethylenediamine were purchased from SRL chemicals. Phenyl Boronic acid and sodium borohydride were purchased from Spectrochem. Chemicals were of analytical grade and were used without any further purification. Throughout the experiment Deionized water (DI) was used, obtained from Sartorius Milli-Q system.

6.4.2. Characterizations

The fluorescence spectra of as synthesized CNBF and rCNBF were recorded on FluoroMax spectrofluoromter. Time-correlated single photon counting from IBH corporation (Jobin Yvon Horiba) used to record fluorescence decays. Picosecond-pulsed diode lasers were used as an excitation source. IBH DAS 6.0 software was used to measure lifetime decay data using iterative reconvoluation method. The decay values were fitted with bi-exponential function. *Uv-Vis* absorption spectra were recorded on UV-1900 (Shimadzu, Japan). The size and high resolution images of CNBF and rCNBF were recorded using transmission electron microscope (FEI Tecnai G2-F20, Transmission electron microscope). The powder X-ray (PXRD) was performed on Bruker D2 phaser. For investing about elemental composition level X-ray photoelectron spectra (XPS) was recorded on model: PHI 5000 Versa Probe-II. A Fourier-transform infrared spectrum (FTIR) was recorded on Bio-Rad FTS 3000MX instrument in ATR mode.

6.4.3. Preparation of CNBF and rCNBF

CNBF was prepared from the one-step hydrothermal method. Briefly, 1 gram of citric acid was dissolved in 20 mL DI water. Further, phenyl boronic acid (0.08 M), sodium fluoride (0.4 M) and ethylene diamine (Eda) (5 mL) were mixed in citric acid solution. The resulting mixture was hydrothermally treated at 180^{o}C for 16 h. The resultant solution was centrifuged (10000 rpm; 10 min) to remove large particles. The obtained brown sticky product (CNBF) was lyophilized and resuspended in DI water. The rCNBF were prepared based on the previous report[37]. Briefly, different quantities of $NaBH_4$ (0.15 g, 0.25 g, 0.35 g) was mixed with CNBF (1×10-5 g/mL) and stirred for 24 h at ambient conditions. The unreacted $NaBH_4$ was removed by heating at 80^{o}C as reported previously.

6.4.4. Quantum yield measurements

The calculation of the fluorescence quantum yields (Φ) of CNBF and rCNBF was performed as per procedure suggested in "Guide to Recording Fluorescence Quantum Yields" by HORIBA Jobin Yvon IBH Ltd. and also to the published procedure" [38]. Quinie sulphate was chosen as standard (Φ_{st}=0.54) and following equation was used:

$$\Phi = \Phi st \text{ X } S_s/S_{st} \text{ X } A_s/A_{st} \text{ X } n^2_s/n^2_{st} \quad \text{..... (1)}$$

Here Φ is the quantum yield of fluorophore. A_s and A_{st} represents the absorbance of standard and samples. S_s and S_{st} are integrated intensity of sample and standard. The n_s and n_{st} represents the refractive index of standard and sample. The qunine sulphate was dissolved in 0.1M H_2SO_4 (n_{st} =1.33) and CNBF, rCNBF was dissolved in DI water.

6.4.5. Energy level calculation for CNBF and rCNBF using cyclic voltammetry

Cyclic voltammetry was performed on AutoLab PGSTAT 204N electrochemical workstation to measure the highest occupied molecular orbital (HOMO) and lowest unoccupied molecular orbital (LUMO) of CNBF and rCNBF. The scanning was performed in the range (-1.5 V to 2 V) with the scan rate of 0.05 Vs^{-1}. Throughout the measurement three-electrode system was used in which a glassy carbon electrode was used as a working electrode. 0.1 M PBS was used as an electrolyte. Further, HOMO and LUMO energy level and bandgap were calculated using the following equation [37].

$$HOMO = -e(E_{ox}+4.74)V \quad \text{.....(2)}$$

$$LUMO = -e(E_{red}+4.74)V \quad \text{.....(3)}$$

$$E_g = LUMO-HOMO \quad \text{.....(4)}$$

Here, E_{ox}, E_{red} was oxidation and reduction potential.

6.5. References

[1] D.H. Kim, T.W. Kim (2017), Ultrahigh current efficiency of light-emitting devices based on octadecylamine-graphene quantum dots, Nano Energy., 32, 441–447
(DOI: https://doi.org/10.1016/j.nanoen.2017.01.002)

[2] J. Xu, Y. Miao, J. Zheng, Y. Yang, X. Liu (2018), Ultrahigh Brightness Carbon Dot–Based Blue Electroluminescent LEDs by Host–Guest Energy Transfer Emission Mechanism, Adv. Opt. Mater., 6, 1800181
(DOI: https://doi.org/10.1002/adom.201800181)

[3] Y. Chen, M. Zheng, Y. Xiao, H. Dong, H. Zhang, J. Zhuang, H. Hu, B. Lei, Y. Liu (2016), A Self-Quenching-Resistant Carbon-Dot Powder with Tunable Solid-State Fluorescence and Construction of Dual-Fluorescence Morphologies for White Light-Emission, Adv. Mater., 28, 312–318
(DOI: https://doi.org/10.1002/adma.201503380)

[4] Y. Wu, H. Zhang, A. Pan, Q. Wang, Y. Zhang, G. Zhou, L. He (2019), White-Light-Emitting Melamine-Formaldehyde Microspheres through Polymer-Mediated Aggregation and Encapsulation of Graphene Quantum Dots, Adv. Sci., 6, 1801432
(DOI: https://doi.org/10.1002/advs.201801432)

[5] F. Mateen, M. Ali, H. Oh, S.-K. Hong (2019), Nitrogen-doped carbon quantum dot based luminescent solar concentrator coupled with polymer dispersed liquid crystal device for smart management of solar spectrum, Sol. Energy., 178, 48–55
(DOI: https://doi.org/10.1016/j.solener.2018.12.013)

[6] N. Kaur, V. Sharma, P. Tiwari, A.K. Saini, S.M. Mobin (2019), “Vigna radiata” based green C-dots: Photo-triggered theranostics, fluorescent sensor for extracellular and intracellular iron (III) and multicolor live cell imaging probe, Sens. Actuators B Chem., 291, 275–286 (DOI: https://doi.org/10.1016/j.snb.2019.04.039)

[7] S. Saeed, P.A. Channar, F.A. Larik, A. Saeed, M.A. Nadeem, A. Iqbal (2019), Charge/energy transfer dynamics in CuO quantum dots attached to photoresponsive azobenzene ligand, J. Photochem. Photobiol. Chem., 371, 44–49
(DOI: https://doi.org/10.1016/j.jphotochem.2018.10.055)

[8] I. Kaur, V. Sharma, S.M. Mobin, P. Kaur, K. Singh (2019), Excitation wavelength based reversible multicolour photoluminescence by a single chromophore upon aggregation: Detection of picric acid-application in bioimaging, Sens. Actuators B Chem., 281, 613–622
(DOI: https://doi.org/10.1016/j.snb.2018.10.161)

[9] W. Zhou, J.J. Coleman (2016), Semiconductor quantum dots, Curr. Opin. Solid State Mater. Sci., 20, 352–360
(DOI: https://doi.org/10.1016/j.cossms.2016.06.006)

[10] F.J. Duarte (2013), 7 - Liquid and solid-state tunable organic dye lasers for medical applications, in: H. Jelínková (Ed.), Lasers Med. Appl., Woodhead Publishing, pp. 203–221 (DOI: https://doi.org/10.1533/9780857097545.2.203)

[11] V. Sharma, P. Tiwari, S.M. Mobin (2017), Sustainable carbon-dots: recent advances in green carbon dots for sensing and bioimaging, J. Mater. Chem. B., 5, 8904–8924 (DOI: https://doi.org/10.1039/C7TB02484C)

[12] C. Zhao, Y. Jiao, Z. Gao, Y. Yang, H. Li (2018), N, S co-doped carbon dots for temperature probe and the detection of tetracycline based on the inner filter effect, J. Photochem. Photobiol. Chem., 367, 137–144 (DOI: https://doi.org/10.1016/j.jphotochem.2018.08.023)

[13] R.M.S. Sendão, D.M.A. Crista, A.C.P. Afonso, M. del V.M. de Yuso, M. Algarra, J.C.G.E. da Silva, L.P. da Silva (2019), Insight into the hybrid luminescence showed by carbon dots and molecular fluorophores in solution, Phys. Chem. Chem. Phys., 21, 20919–20926 (DOI: https://doi.org/10.1039/C9CP03730F)

[14] H. Ding, Y. Ji, J.-S. Wei, Q.-Y. Gao, Z.-Y. Zhou, H.-M. Xiong (2017), Facile synthesis of red-emitting carbon dots from pulp-free lemon juice for bioimaging, J. Mater. Chem. B., 5, 5272–5277 (DOI: https://doi.org/10.1039/C7TB01130J)

[15] Z. Peng, X. Han, S. Li, A.O. Al-Youbi, A.S. Bashammakh, M.S. El-Shahawi, R.M. Leblanc (2017), Carbon dots: Biomacromolecule interaction, bioimaging and nanomedicine, Coord. Chem. Rev., 343, 256–277 (DOI: https://doi.org/10.1016/j.ccr.2017.06.001)

[16] S. Ying Lim, W. Shen, Z. Gao (2015), Carbon quantum dots and their applications, Chem. Soc. Rev., 44, 362–381 (DOI: https://doi.org/10.1039/C4CS00269E)

[17] K. Wang, Z. Gao, G. Gao, Y. Wo, Y. Wang, G. Shen, D. Cui (2013), Systematic safety evaluation on photoluminescent carbon dots, Nanoscale Res. Lett., 8, 122 (DOI: https://doi.org/10.1186/1556-276X-8-122)

[18] B. Yao, H. Huang, Y. Liu, Z. Kang (2019), Carbon Dots: A Small Conundrum, Trends Chem., 1, 235–246 (DOI: https://doi.org/10.1016/j.trechm.2019.02.003)

[19] H. Yang, Y. Liu, Z. Guo, B. Lei, J. Zhuang, X. Zhang, Z. Liu, C. Hu (2019), Hydrophobic carbon dots with blue dispersed emission and red aggregation-induced emission, Nat. Commun., 10, 1–11 (DOI: https://doi.org/10.1038/s41467-019-09830-6)

[20] Y.-P. Sun, B. Zhou, Y. Lin, W. Wang, K.A.S. Fernando, P. Pathak, M.J. Meziani, B.A. Harruff, X. Wang, H. Wang, P.G. Luo, H. Yang, M.E. Kose, B. Chen, L.M. Veca, S.-Y. Xie (2006), Quantum-Sized Carbon Dots for Bright and Colorful

Photoluminescence, J. Am. Chem. Soc., 128, 7756–7757 (DOI: https://doi.org/10.1021/ja062677d)

[21] S.-T. Yang, X. Wang, H. Wang, F. Lu, P.G. Luo, L. Cao, M.J. Meziani, J.-H. Liu, Y. Liu, M. Chen, Y. Huang, Y.-P. Sun (2009), Carbon Dots as Nontoxic and High-Performance Fluorescence Imaging Agents, J. Phys. Chem. C., 113, 18110–18114 (DOI: https://doi.org/10.1021/jp9085969)

[22] Y. Duan, Y. Huang, S. Chen, W. Zuo, B. Shi (2019), Cu-Doped Carbon Dots as Catalysts for the Chemiluminescence Detection of Glucose, ACS Omega., 4, 9911–9917 (DOI: https://doi.org/10.1021/acsomega.9b00738)

[23] Z. Wang, P. Long, Y. Feng, C. Qin, W. Feng (2017), Surface passivation of carbon dots with ethylene glycol and their high-sensitivity to Fe3+, RSC Adv., 7, 2810–2816 (DOI: https://doi.org/10.1039/C6RA25465A)

[24] L. Li, T. Dong (2018), Photoluminescence tuning in carbon dots: surface passivation or/and functionalization, heteroatom doping, J. Mater. Chem. C., 6, 7944–7970 (DOI: https://doi.org/10.1039/C7TC05878K)

[25] Y. Liu, L. Jiang, B. Li, X. Fan, W. Wang, P. Liu, S. Xu, X. Luo (2019), Nitrogen doped carbon dots: mechanism investigation and their application for label free CA125 analysis, J. Mater. Chem. B., 7, 3053–3058 (DOI: https://doi.org/10.1039/C9TB00021F)

[26] P. Tiwari, N. Kaur, V. Sharma, H. Kang, J. Uddin, S.M. Mobin (2019), Cannabis sativa-derived carbon dots co-doped with N–S: highly efficient nanosensors for temperature and vitamin B12, New J. Chem., 43, 17058–17068 (DOI: https://doi.org/10.1039/C9NJ04061G)

[27] K. Zhang, Y. Shi, Y. Jia, P. Li, X. Zhang, X. Feng, L. Zhu, Y. Sun, W. Hu, G. Zhao (2020), Tunable dual fluorescence emissions with high photoluminescence quantum yields modulated by Na ion dispersion method for purely solid state N-doped carbon dots, J. Photochem. Photobiol. Chem., 397, 112548 (DOI: https://doi.org/10.1016/j.jphotochem.2020.112548)

[28] M. Kim, P.W. Kang, S. Park, D.Y. Jeon, H. Lee (2019), Enhancing the luminescence of carbon nanodots in films by tailoring the functional groups through alkylamine-functionalization and reduction, Phys. Chem. Chem. Phys., 21, 26095–26101 (DOI: https://doi.org/10.1039/C9CP05241K)

[29] W. Kwon, Y.-H. Kim, J.-H. Kim, T. Lee, S. Do, Y. Park, M.S. Jeong, T.-W. Lee, S.-W. Rhee (2016), High Color-Purity Green, Orange, and Red Light-Emitting Diodes Based on Chemically Functionalized Graphene Quantum Dots, Sci. Rep., 6, 1–10 (DOI: https://doi.org/10.1038/srep24205)

[30] M.T. Hasan, R. Gonzalez-Rodriguez, C. Ryan, N. Faerber, J.L. Coffer, A.V. Naumov (2018), Photo-and Electroluminescence

from Nitrogen-Doped and Nitrogen–Sulfur Codoped Graphene Quantum Dots, Adv. Funct. Mater., 28, 1804337 (DOI: https://doi.org/10.1002/adfm.201804337)

[31] Y. Feng, J. Zhao, X. Yan, F. Tang, Q. Xue (2014), Enhancement in the fluorescence of graphene quantum dots by hydrazine hydrate reduction, Carbon., 66, 334–339 (DOI: https://doi.org/10.1016/j.carbon.2013.09.008)

[32] B. Ahmed, S. Kumar, A.K. Ojha, F. Hirsch, S. Riese, I. Fischer (2018), Facile synthesis and photophysics of graphene quantum dots, J. Photochem. Photobiol. Chem., 364, 671–678 (DOI: https://doi.org/10.1016/j.jphotochem.2018.07.006)

[33] P. Dong, B.-P. Jiang, W.-Q. Liang, Y. Huang, Z. Shi, X.-C. Shen (2017), Synthesis of white-light-emitting graphene quantum dots via a one-step reduction and their interfacial characteristics-dependent luminescence properties, Inorg. Chem. Front., 4, 712–718 (DOI: https://doi.org/10.1039/C6QI00587J)

[34] H. Zheng, Q. Wang, Y. Long, H. Zhang, X. Huang, R. Zhu (2011), Enhancing the luminescence of carbon dots with a reduction pathway, Chem. Commun., 47, 10650–10652 (DOI: https://doi.org/10.1039/C1CC14741B)

[35] Y. Xu, M. Wu, X.-Z. Feng, X.-B. Yin, X.-W. He, Y.-K. Zhang (2013), Reduced Carbon Dots versus Oxidized Carbon Dots: Photo- and Electrochemiluminescence Investigations for Selected Applications, Chem. – Eur. J., 19, 6282–6288 (DOI: https://doi.org/10.1002/chem.201204372)

[36] T. Wang, A. Wang, R. Wang, Z. Liu, Y. Sun, G. Shan, Y. Chen, Y. Liu (2019), Carbon dots with molecular fluorescence and their application as a “turn-off” fluorescent probe for ferricyanide detection, Sci. Rep., 9, 1–9 (DOI: https://doi.org/10.1038/s41598-019-47168-7)

[37] L. Sciortino, A. Sciortino, R. Popescu, R. Schneider, D. Gerthsen, S. Agnello, M. Cannas, F. Messina (2018), Tailoring the Emission Color of Carbon Dots through Nitrogen-Induced Changes of Their Crystalline Structure, J. Phys. Chem. C., 122, 19897–19903 (DOI: https://doi.org/10.1021/acs.jpcc.8b04514)

[38] Y.H. Yuan, Z.X. Liu, R.S. Li, H.Y. Zou, M. Lin, H. Liu, C.Z. Huang (2016), Synthesis of nitrogen-doping carbon dots with different photoluminescence properties by controlling the surface states, Nanoscale., 8, 6770–6776 (DOI: https://doi.org/10.1039/C6NR00402D)

[39] L. Guo, J. Ge, W. Liu, G. Niu, Q. Jia, H. Wang, P. Wang (2015), Tunable multicolor carbon dots prepared from well-defined polythiophene derivatives and their emission mechanism, Nanoscale., 8, 729–734 (DOI: https://doi.org/10.1039/C5NR07153D)

[40] A.B. Bourlinos, G. Trivizas, M.A. Karakassides, M. Baikousi, A. Kouloumpis, D. Gournis, A. Bakandritsos, K. Hola, O. Kozak, R. Zboril, I. Papagiannouli, P. Aloukos, S. Couris (2015), Green and simple route toward boron doped carbon dots with significantly enhanced non-linear optical properties, Carbon., 83, 173–179 (DOI: https://doi.org/10.1016/j.carbon.2014.11.032)

[41] G. Zuo, A. Xie, J. Li, T. Su, X. Pan, W. Dong (2017), Large Emission Red-Shift of Carbon Dots by Fluorine Doping and Their Applications for Red Cell Imaging and Sensitive Intracellular Ag+ Detection, J. Phys. Chem. C., 121, 26558–26565 (DOI: https://doi.org/10.1021/acs.jpcc.7b10179)

[42] Y. Zhang, J. He (2015), Facile synthesis of S, N co-doped carbon dots and investigation of their photoluminescence properties, Phys. Chem. Chem. Phys., 17, 20154–20159 (DOI: https://doi.org/10.1039/C5CP03498A)

[43] D. Shen, Y. Long, J. Wang, Y. Yu, J. Pi, L. Yang, H. Zheng (2019), Tuning the fluorescence performance of carbon dots with a reduction pathway, Nanoscale., 11, 5998–6003 (DOI: https://doi.org/10.1039/C8NR09587F)

[44] L. Bao, Z.-L. Zhang, Z.-Q. Tian, L. Zhang, C. Liu, Y. Lin, B. Qi, D.-W. Pang (2011), Electrochemical Tuning of Luminescent Carbon Nanodots: From Preparation to Luminescence Mechanism, Adv. Mater., 23, 5801–5806 (DOI: https://doi.org/10.1002/adma.201102866)

[45] S. Kim, B.-K. Yoo, Y. Choi, B.-S. Kim, O.-H. Kwon (2018), Time-resolved spectroscopy of the ensembled photoluminescence of nitrogen- and boron/nitrogen-doped carbon dots, Phys. Chem. Chem. Phys., 20, 11673–11681 (DOI: https://doi.org/10.1039/C8CP01619D)

[46] S. Kalytchuk, K. Poláková, Y. Wang, J.P. Froning, K. Cepe, A.L. Rogach, R. Zbořil (2017), Carbon Dot Nanothermometry: Intracellular Photoluminescence Lifetime Thermal Sensing, ACS Nano., 11, 1432–1442 (DOI: https://doi.org/10.1021/acsnano.6b06670)

[47] R. Tian, S. Hu, L. Wu, Q. Chang, J. Yang, J. Liu (2014), Tailoring surface groups of carbon quantum dots to improve photoluminescence behaviors, Appl. Surf. Sci., 301, 156–160 (DOI: https://doi.org/10.1016/j.apsusc.2014.02.028)

[48] F. Yuan, T. Yuan, L. Sui, Z. Wang, Z. Xi, Y. Li, X. Li, L. Fan, Z. Tan, A. Chen, M. Jin, S. Yang (2018), Engineering triangular carbon quantum dots with unprecedented narrow bandwidth emission for multicolored LEDs, Nat. Commun., 9, 1–11 (DOI: https://doi.org/10.1038/s41467-018-04635-5)

[49] R. Prajapati, S. Chatterjee, A. Bhattacharya, T.K. Mukherjee (2015), Surfactant-Induced Modulation of Nanometal Surface

Energy Transfer from Silicon Quantum Dots to Silver Nanoparticles, J. Phys. Chem. C., 119, 13325–13334 (DOI: https://doi.org/10.1021/acs.jpcc.5b02903)

[50] W. Choi, D. Kim, H. Cho, M. Kim, J. Choi, D. Young Jeon (2019), A highly luminescent quantum dot/mesoporous TiO 2 nanocomplex film under controlled energy transfer, Nanoscale., 11, 13219–13226 (DOI: https://doi.org/10.1039/C9NR01044K)

[51] Y. Choi, B. Kang, J. Lee, S. Kim, G.T. Kim, H. Kang, B.R. Lee, H. Kim, S.-H. Shim, G. Lee, O.-H. Kwon, B.-S. Kim (2016), Integrative Approach toward Uncovering the Origin of Photoluminescence in Dual Heteroatom-Doped Carbon Nanodots, Chem. Mater., 28, 6840–6847 (DOI: https://doi.org/10.1021/acs.chemmater.6b01710)

[52] J. Schneider, C.J. Reckmeier, Y. Xiong, M. von Seckendorff, A.S. Susha, P. Kasák, A.L. Rogach (2017), Molecular Fluorescence in Citric Acid-Based Carbon Dots, J. Phys. Chem. C., 121, 2014–2022 (DOI: https://doi.org/10.1021/acs.jpcc.6b12519)

[53] Y. Song, S. Zhu, S. Zhang, Y. Fu, L. Wang, X. Zhao, B. Yang (2015), Investigation from chemical structure to photoluminescent mechanism: a type of carbon dots from the pyrolysis of citric acid and an amine, J. Mater. Chem. C., 3, 5976–5984 (DOI: https://doi.org/10.1039/C5TC00813A)

[54] S. Zhu, J. Zhang, S. Tang, C. Qiao, L. Wang, H. Wang, X. Liu, B. Li, Y. Li, W. Yu, X. Wang, H. Sun, B. Yang (2012), Surface Chemistry Routes to Modulate the Photoluminescence of Graphene Quantum Dots: From Fluorescence Mechanism to Up-Conversion Bioimaging Applications, Adv. Funct. Mater., 22, 4732–4740 (DOI: https://doi.org/10.1002/adfm.201201499)

[55] C.J. Spindt, R.S. Besser, R. Cao, K. Miyano, C.R. Helms, W.E. Spicer (1989), Photoemission study of the band bending and chemistry of sodium sulfide on GaAs (100), Appl. Phys. Lett., 54, 1148–1150 (DOI: https://doi.org/10.1063/1.100744)

[56] R. Shen, K. Song, H. Liu, Y. Li, H. Liu (2012), Dramatic Fluorescence Enhancement of Bare Carbon Dots through Facile Reduction Chemistry, ChemPhysChem., 13, 3549–3555 (DOI: https://doi.org/10.1002/cphc.201200018)

[57] V. Sharma, S.K. Singh, S.M. Mobin (2019), Bioinspired carbon dots: from rose petals to tunable emissive nanodots, Nanoscale Adv., 1, 1290–1296 (DOI: https://doi.org/10.1039/C8NA00105G)

[58] B. De, N. Karak (2013), A green and facile approach for the synthesis of water soluble fluorescent carbon dots from banana juice, RSC Adv., 3, 8286–8290 (DOI: https://doi.org/10.1039/C3RA00088E)

[59] S. Sahu, B. Behera, T. K. Maiti, S. Mohapatra (2012), Simple one-step synthesis of highly luminescent carbon dots from orange

juice: application as excellent bio-imaging agents, Chem. Commun., 48, 8835–8837
(DOI: https://doi.org/10.1039/C2CC33796G)
[60] H. Cheng, Y. Zhao, Y. Fan, X. Xie, L. Qu, G. Shi (2012), Graphene-Quantum-Dot Assembled Nanotubes: A New Platform for Efficient Raman Enhancement, ACS Nano., 6, 2237–2244 (DOI: https://doi.org/10.1021/nn204289t)
[61] C. Yuan, X. Qin, Y. Xu, X. Li, Y. Chen, R. Shi, Y. Wang (2020), Carbon quantum dots originated from chicken blood as peroxidase mimics for colorimetric detection of biothiols, J. Photochem. Photobiol. Chem., 396, 112529
(DOI: https://doi.org/10.1016/j.jphotochem.2020.112529)
[62] F. Messina, L. Sciortino, R. Popescu, A.M. Venezia, A. Sciortino, G. Buscarino, S. Agnello, R. Schneider, D. Gerthsen, M. Cannas, F.M. Gelardi (2016), Fluorescent nitrogen-rich carbon nanodots with an unexpected β-C3N4 nanocrystalline structure, J. Mater. Chem. C., 4, 2598–2605
(DOI: https://doi.org/10.1039/C5TC04096E)
[63] T.N.J.I. Edison, R. Atchudan, M.G. Sethuraman, J.-J. Shim, Y.R. Lee (2016), Microwave assisted green synthesis of fluorescent N-doped carbon dots: Cytotoxicity and bio-imaging applications, J. Photochem. Photobiol. B., 161, 154–161
(DOI: https://doi.org/10.1016/j.jphotobiol.2016.05.017)
[64] Y. Tang, M. Ouyang, Tailoring properties and functionalities of metal nanoparticles through crystallinity engineering (2007), Nat. Mater., 6, 754–759 (DOI: https://doi.org/10.1038/nmat1982)
[65] W. Zhang, Y. Liu, X. Meng, T. Ding, Y. Xu, H. Xu, Y. Ren, B. Liu, J. Huang, J. Yang, X. Fang (2015), Graphenol defects induced blue emission enhancement in chemically reduced graphene quantum dots, Phys. Chem. Chem. Phys., 17, 22361–22366 (DOI: https://doi.org/10.1039/C5CP03434E)
[66] S. Zhu, J. Shao, Y. Song, X. Zhao, J. Du, L. Wang, H. Wang, K. Zhang, J. Zhang, B. Yang (2015), Investigating the surface state of graphene quantum dots, Nanoscale., 7, 7927–7933
(DOI: https://doi.org/10.1039/C5NR01178G)
[67] L. Wang, S.-J. Zhu, H.-Y. Wang, S.-N. Qu, Y.-L. Zhang, J.-H. Zhang, Q.-D. Chen, H.-L. Xu, W. Han, B. Yang, H.-B. Sun (2014), Common Origin of Green Luminescence in Carbon Nanodots and Graphene Quantum Dots, ACS Nano., 8, 2541–2547 (DOI: https://doi.org/10.1021/nn500368m)
[68] A. Cayuela, M.L. Soriano, C. Carrillo-Carrión, M. Valcárcel (2016), Semiconductor and carbon-based fluorescent nanodots: the need for consistency, Chem. Commun., 52, 1311–1326
(DOI: https://doi.org/10.1039/C5CC07754K)
[69] S. Hu, A. Trinchi, P. Atkin, I. Cole (2015), Tunable Photoluminescence Across the Entire Visible Spectrum from

Carbon Dots Excited by White Light, Angew. Chem. Int. Ed., 54, 2970–2974 (DOI: https://doi.org/10.1002/anie.201411004)

[70] H. Nie, M. Li, Q. Li, S. Liang, Y. Tan, L. Sheng, W. Shi, S.X.-A. Zhang (2014), Carbon Dots with Continuously Tunable Full-Color Emission and Their Application in Ratiometric pH Sensing, Chem. Mater., 26, 3104–3112 (DOI: https://doi.org/10.1021/cm5003669)

CHAPTER 7

Conclusions and Future Outlook

The present thesis work ensembles synthesis of graphene and carbon dots by exploring green synthetic approach than focusing on their synthesis mechanism; its biomolecular interactions; responses and lastly employing these carbon nanomaterials for various applications such as carbon dots mediated synthesis of nanostructured materials; antibacterial; optical sensing and bioimaging. Furthermore, surface functional group tuning is performed to modulate the fluorescence performance of carbon dots.

Considering the robustness of directly exfoliated graphene using biopolymers, gelatin is explored as a surfactant as well as stabilizing agents for direct exfoliation purposes. The yield of 4.37 mg mL^{-1} is achieved using temperature elevation sonication condition. These exfoliated graphenes exhibited very high colloidal stability irrespective of conditions. Furthermore, the exfoliated graphene showed very low defects, gelatin based exfoliant used (a very cheap source) and the whole exfoliation process is very facile which eliminates drawbacks of existing methods. Thus, this improved synthesis route will be very helpful in the easy synthesis and functionalization of graphene and can be used to make its composites for different types of biomedical applications ranging from wound healing, scaffold materials to drug delivery.

In recent years, graphene based nanomaterial has gained significant attention in the biomedical field thus, their toxicity and protein adsorption study is of paramount importance for the advancement in the field of nanotherapeutics. It has been demonstrated that when any nanomaterial gets coated with various biomolecules after it enters into physiological conditions. This interaction/adsorption gets significantly affects the surface charge, morphology, sizes of the nanomaterials and ultimately affects the protein structures and leads to change in biological responses.

Thus, graphene nanosheets having varying lateral sizes are synthesized by varying the sonication time. In this work also gelatin is chosen as an exfoliating agent. The protein interaction study is performed on Bovine serum albumin (BSA) and fetal bovine serum (FBS). The lateral size of graphene nanoflakes plays a significant role in protein interaction i.e. different lateral sized graphene nanoflakes gets interacted with BSA and FBS differently. Also after adsorption, the size of graphene nanoflakes and their charge gets changed. Thus, protein adsorption is needed to be investigated in detail before employing it for biomedical application as the actual size of graphene nanoflakes are the size measured after the corona formation. Further due to molecular interaction between graphene and protein, the secondary structure of protein gets changed. The change in protein conformation can affect the cellular responses and ultimately the immune system. Thus, a detailed investigation is needed for understanding these molecular interactions. The graphene nanoflakes irrespective of lateral size are biocompatible and hemocompatible in nature. The compatibility arises because of gelatin adsorption onto exfoliated nanosheets which restricts direct interaction between cells and nanosheets. This finding provides a pathway to design graphene based nanomaterials for a plethora of biological and biomedical applications.

The carbon dot mediated synthesis of nanostructured materials especially their dispersing capabilities have been explored for 2D materials. Further bioinspired carbon dots have the potential to eliminate the requirement of chemical passivation because of the presence of carbohydrates and proteins in them. Thus, carbon dots are used as a dispersing agent to directly exfoliate graphite to graphene. Further, since these carbon dots have the size (less than 10 nm) thus, coverage on the exfoliated sheets will be less w.r.to. surfactant mediated synthesis, maintain the inherent property of graphene. Also, the rise in multi-drug resistant pathogens makes it inevitable to explore these multifunctional nanomaterials for bacterial elimination. The exploration of 0D (carbon dots) for exfoliating

3D (graphite) into 2D (graphene) opens a new avenue for synthesizing 2D nanomaterials making it applicable for designing more advanced material and their industrial applications ranging from solar cells to biomedical devices. Carbon dots have been used as optical sensors owing to their fluorescence nature and cover cations, anions, biomolecules and physical entity for sensing. So far very less work towards biomolecules such as vitamins and physical entity (temperature, pressure) sensing is done. Thus, utilizing these green sources derived carbon dots for vitamin sensing. As we know that vitamins such as Vitamin B12 help in maintaining the body's blood and nerve cells healthy and helps in making DNA. Also, excessive Vitamin B12 causes the toxic effect, leading to a shortage of folic acid. Thus, its continuous monitoring is needed for health related issue. Also, the temperature sensing capability of carbon dots can be used to fabricate the devices for temperature monitoring with applicability in biomedical devices and electronic industries. Although carbon dots have become a wonder material its fluorescence performance (quantum yield, lifetime value) is still not very high in comparison to semiconducting quantum dots. Thus, functional group modification through reduction pathway offers advantages in comparison to surface passivation and heteroatom doping. These reduced carbon dots can be explored for cellular targeting. The composites of graphene and carbon dots can be explored for theranostics and agriculture related applications.

ANNEXURE 1

Tables A1

Table A1. Permissions for re-producing the materials

Figure 1.1	Comparison of nanoparticles based on size w.r.to other common materials.	Reproduced from Ref. [1]: Chapter 1, with permission from the MDPI.
Figure 1.2	Representative images of various types of carbon nanomaterials.	Reproduced from Ref. [16]: Chapter 1, with permission from the Royal Society of Chemistry
Figure 1.3	Graphene as mother of all forms of carbon materials.	Reproduced from Ref. [19]: Chapter 1, with permission from the Nature publishing group.
Figure 1.4	A production mechanism for CVD graphene growth on Cu.	Reproduced from Ref. [32]: Chapter 1, with permission from the Elsevier.
Figure 1.5	The graphene production method via top-down approach.	Reproduced from Ref. [37]: Chapter 1, with permission from the Elsevier.
Figure 1.6	Graphene based material for biomedical applications.	Reproduced from Ref. [36]: Chapter 1, with permission from the Elsevier.
Figure 1.7	Schematic representation of size dependent toxicity.	Reproduced from Ref [37]: Chapter 1, with permission from the Royal Society of Chemistry
Figure 1.8	Effect of lateral size and serum coating on cellular toxicity.	Reproduced from Ref. [38]: Chapter 1, with permission from the American Chemical Society.
Figure 1.9	Effect of covalent functionalization on blood cells.	Reproduced from Ref. [39]: Chapter 1, with permission from the Royal Society of Chemistry.
Figure 1.10	(a) Shear exfoliation of graphite using bovine serum albumin (b) types of blades used to generate turbulence (c) visualization of graphene formed by laser light scattering (d) Scalability of the method.	Reproduced from Ref. [40]: Chapter 1, with permission from the John Wiley and Sons.
Figure 1.11	Direct exfoliation of graphite to graphene using BSA.	Reproduced from Ref. [41]: Chapter 1, with permission from Royal

		Society of Chemistry.
Figure 1.12	Photographs of 2D materials dispersed in water.	Reproduced from Ref. [42]: Chapter 1, with permission from Nature publishing group.
Figure 1.13	Mechanically exfoliated graphene nanocomposite fibers as medical suture.	Reproduced from Ref. [43]: Chapter 1, with permission from American Chemical Society.
Figure 1.14	C-dots fabrication using citric acid and polyethyleneimine.	Reproduced from Ref. [59]: Chapter 1, with permission from American Chemical Society.
Figure 1.15	Schematic representation of the (a) N-GQDS and (b) NS-GQDs.	Reproduced from Ref. [59]: Chapter 1, with permission from the John Wiley and Sons.
Figure 1.16	Illustration of sustainable sources derived c-dots.	Reproduced from Ref. [66]: Chapter 1, with permission from Royal Society of Chemistry.
Figure 1.17	Hydrothermal synthesis of c-dots using orange juice.	Reproduced from Ref. [67]: Chapter 1, with permission from Royal Society of Chemistry.
Figure 1.18	Cabbage derived hydrothermally synthesized c-dots.	Reproduced from Ref. [68]: Chapter 1, with permission from Royal Society of Chemistry.
Figure 1.19	*Mangifera indica* derived graphene quantum dots showing selective bioimaging and intracellular nanothermometry applications.	Reproduced from Ref. [69]: Chapter 1, with permission from American Chemical Society.
Figure 1.20	Plant leaf used c-dots synthesis.	Reproduced from Ref. [70]: Chapter 1, with permission from Royal Society of Chemistry.
Figure 1.21	Schematic representation of label free sensor array	Reproduced from Ref. [73]: Chapter

	for protein discrimination.	1, with permission from Royal Society of Chemistry.
Figure 1.22	Representative fluorescence imaging of A549 and L-132 cells incubated with 0.5 mg mL-1 CDs.	Reproduced from Ref. [76]: Chapter 1, with permission from Royal Society of Chemistry.
Figure 1.23	Schematic representation CDs based reductant and stabilizing agent.	Reproduced from Ref. [79]: Chapter 1, with permission from American Chemical Society.